EXPERIMENTS INVESTIGATING THE EFFECTS OF FLUID ELASTICITY ON LAMINAR VORTEX SHEDDING FROM A CYLINDER

THÈSE N^{O} 3347 (2005)

PRÉSENTÉE À LA FACULTÉ SCIENCES ET TECHNIQUES DE L'INGÉNIEUR

Institut des sciences de l'énergie

SECTION DE GÉNIE MÉCANIQUE

ÉCOLE POLYTECHNIQUE FÉDÉRALE DE LAUSANNE

POUR L'OBTENTION DU GRADE DE DOCTEUR ÈS SCIENCES

PAR

Christopher PIPE

Master of Engineering, University of London, Royaume-Uni
et de nationalité britannique

acceptée sur proposition du jury:

Prof. P.A. Monkewitz, directeur de thèse
Prof. C. Ancey, rapporteur
Prof. J. Hinch, rapporteur
Dr P. Le Gal, rapporteur

Lausanne, EPFL
2005

Abstract

Experiments on vortex shedding from a cylinder placed in uniform flows of low concentration polymer solutions are reported for Reynolds numbers from 50 to 150. The fluids used were aqueous solutions of polyethylene oxide (PEO) and rheological characterization showed them to have a constant viscosity over a wide range of shear rates. Using the Zimm model relaxation time the Deborah numbers calculated for the cylinder wake are $O(10^{-3})$. Parallel vortex shedding was induced with a combination of end-cylinders and end-plates and the resulting nominally two-dimensional cylinder wake was investigated using LDA, PIV, hydrogen bubble visualizations and hot film anemometry.

The characteristics of the von Kármán instability are presented as a function of PEO concentration. It is shown that even small amounts of polymers, corresponding to low Deborah numbers, have a significant stabilizing effect which is only counteracted by shear-thinning at higher concentrations. The presence of PEO is also observed to reduce the saturated vortex shedding frequency and cause a redistribution of velocity fluctuations in the attached shear layers. Shear-thinning is found to decrease velocity fluctuations in the wake. Downstream of the cylinder a velocity overshoot is measured for the polymer solutions and an analogy is drawn to the negative wake behind a sphere falling in a viscoelastic fluid.

Version abrégée

Des expériences de lâcher de tourbillons depuis un cylindre placé au sein d'écoulements uniformes de solutions polymères faiblement concentrées sont présentées pour des nombres de Reynolds variant de 50 à 150. Les fluides utilisés sont des solutions aqueuses d'oxyde de polyéthylène (PEO). La caractérisation rhéologique de ces fluides met en évidence une viscosité constante sur une large plage de taux de cisaillement. Utilisant le modèle de Zimm pour le temps de relaxation, les nombres de Deborah pour le sillage du cylindre sont d'ordre $O(10^{-3})$. Une allée de tourbillons parallèles est générée par un dispositif de type « end-cylinders and end-plates » et le sillage bidimensionnel résultant à l'arrière du cylindre est étudié en utilisant les techniques LDA, PIV, visualisations de bulles d'hydrogène et anémométrie à film chaud.

Les propriétés caractéristiques de l'instabilité de von Kármán sont présentées en fonction de la concentration de PEO. Il est montré que même de faibles quantités de polymère, correspondant à de faibles nombres de Deborah, ont un important effet stabilisant. Ce dernier est contrecarré par la pseudoplasticité (« shear-thinning ») pour les solutions de concentrations plus élevées. La présence de PEO réduit la fréquence de saturation du lâcher de tourbillons et entraîne une redistribution des fluctuations de vitesse dans les couches de cisaillement attachées. La viscosité rhéofluidifiante a pour effet de réduire les fluctuations du champ de vitesse dans le sillage. En aval du cylindre, un excès local de vitesse est mesuré pour les solutions de polymère permettant d'établir une analogie avec le sillage négatif derrière une sphère en chute libre dans un fluide viscoélastique.

Acknowledgements

I would first and foremost like to thank Prof. P. A. Monkewitz who has supervised this work. His guidance and support have been invaluable and immensely enriching.

To everyone at the LMF I express my appreciation for their time and assistance, and in particular: Dr. T. V. Truong for his help with everything experimental; Mr. G. Grandjean and Mr. B. Savary for their patience and expertise in the workshop; Dr. N. Borhani, Dr. D. Lo Jacono and Asst. Prof. R. Owens for their useful and thought-provoking discussions; Mr. E. Grandjean for lending a hand on countless occasions; and Dr. B. Ugurtas and Mr. R. Vonlanthen for being exemplary office-mates. Dr. D. Lo Jacono deserves a special mention for having put up with sharing a flat with me.

Elsewhere at the EPFL, I would like to extend my gratitude to Dr. T. Ursenbacher (STI-ISE-LTCM) for introducing me to the technique of PIV and the use of his code for generating synthetic PIV images, Dr. C. Wandrey (SB-ISIC-LBCH) for introducing me to the chemistry of polymer solutions, and Dr. K. Agebeviade (STI-IPR-LCSM) and Mr. R. Mottier (STI-ISE-LENI) for the extended loan of capillary viscometers.

I am very grateful to Asst. Prof. C. Ancey, Prof. J. Hinch and Dr. P. Le Gal for their participation in the thesis committee and taking the time to read through the manuscript and attend the private defense. Their comments and suggestions have been greatly appreciated. I would also like to thank Prof. J. Thome for presiding over the committee.

I would like to acknowledge the Swiss National Science Foundation for its financial support.

Last but certainly not least, I reserve my deepest thanks for my family and friends who have helped make the past four years so highly enjoyable.

Contents

List of Figures

List of Tables

Nomenclature

Greek letters

$\dot{\boldsymbol{\gamma}}, \dot{\gamma}_{ij}$	Rate of strain tensor, where i=j for extensional strain rates and i≠j for shear rates	1/s
Γ_1	Vortex centre identification function	
δ	Boundary layer thickness	m
δ^*	Boundary layer displacement thickness	m
δ_ω	Vorticity thickness	m
$[\eta]$	Intrinsinc viscosity	ml/g
η	Dynamic viscosity	Pa.s
η_{red}	Reduced viscosity defined as $(\eta_{rel} - 1)/c$	mol/g
η_{rel}	Relative viscosity	Pa.s
η_{inh}	Inherent viscosity	mol/g
Λ	Velocity ratio defined as $(\bar{u}_{CL} - \bar{u}_{max})/(\bar{u}_{CL} + \bar{u}_{max})$	
λ	Relaxation time	s
μ^*	Diffusion coefficient, which can be written as $\mu^* = \mu_r^* + i\mu_i^*$	m^2/s
ν	Kinematic viscosity	m^2/s
ρ	Density	kg/m^2
$\boldsymbol{\sigma}, \sigma_{ij}$	Fluid stress tensor, where i=j for extensional stresses and i≠j for shear stresses	Pa
σ_r, σ_i	Linear growth rate and frequency	1/s, Hz

ϕ	Phase	rad
Ψ	Stream function	m^2/s
Ψ_0	Vortex strength	m^2/s
Ψ_1, Ψ_2	1st and 2nd normal stress coefficient	$Pa.s^2$
$\boldsymbol{\omega}$	Vorticity field	1/s
ω^*	Perturbation frequency	Hz

Roman letters

b_{eff}	Effective blockage ratio	
c	Concentration	g/ml or wt%
c_{v}	Vortex convection speed	m/s
d	Cylinder diameter	m
De	Deborah number $= U_\infty \lambda / d$	
El	Elasticity number $= \text{De}/\text{Re} = \eta\rho\lambda/d^2$	
f	Vortex shedding frequency	Hz
G', G''	Storage and loss modulus	Pa
K	Mark-Houwink constant	
k	Bolzman constant $= 1.380650524 \times 10^{-23}$	J/K.molecules
k', k''	Huggins and Kraemer coefficients	
k_1, k_2	Coefficients in the Stuart-Landau model	
L	Cylinder length	m
L^*	Cylinder aspect ratio $= L/d$	
l^*	Landau constant, $l^* = l_{\text{r}}^* + \text{i}l_{\text{i}}^*$	1/s
M_{v}	Viscosity average molecular weight	g/mol
$\tilde{N}$	Avogadro's number $= 6.02214199 \times 10^{23}$	molecules/mol
N_1, N_2	1st and 2nd normal stress difference	Pa

R	Molar gas constant = 8.314	J/K.mol
Re	Reynolds number based on cylinder diamter = $\rho U_\infty d/\eta$	
St	Strouhal number = df/U_∞	
T	Temperature	K or °C
u, v	Streamwise and transverse velocities	m/s
U_∞	Freestream velocity	m/s
U_e	Local velocity external to the boundary layer	m/s
$\mathbf{u}$	Velocity field	m/s
x, y, z	Test section coordinate system	m

Subscripts

0	Zero shear value
c	Critical
CL	Centreline
M	Maxwell
N	Newtonian
OB	Oldroyd-B
P	Polymer
R	Rouse
VK	von Kármán
Z	Zimm

Superscripts

$\widehat{\ }$	Reduced quantity
*	Non-dimensional quantity
–	Time averaged quantity

LIST OF TABLES

Chapter 1

Introduction

The purpose of this thesis is to examine the effects of weak fluid elasticity on two dimensional laminar vortex shedding from a cylinder in a uniform flow. This introductory chapter will set out the problem under consideration and review previous research that is relevant.

1.1 Problem overview

Vortex shedding from a bluff body belongs to the family of flows collectively known as shear layer instabilities. The abundance of situations where understanding and manipulating vortex shedding are of considerable practical importance has motivated many studies into this type of flow. Furthermore, the rich mix of flow phenomena combined with the simplicity of the set up has attracted much research of a fundamental nature. Uniform flow past a cylinder is a benchmark configuration for investigating vortex shedding and is well documented experimentally for Newtonian fluids at low Reynolds numbers. However, although the ideal Newtonian fluid model accurately describes the behaviour of many fluids in many types of flow, there are fluids which exhibit significant deviations in certain circumstances. Fluids that do not obey the Newtonian model are referred to as being *non-Newtonian* and experiments leading to more accurate descriptions of their behaviour are clearly important. There are various types of non-Newtonian behaviour and in this study the role of fluid elasticity will be explored.

1.2 Newtonian flow past a cylinder

The formation of vortices behind a bluff body in a fluid flow takes its name from the work of von Kármán (1911) who analyzed the wake behind a cylin-

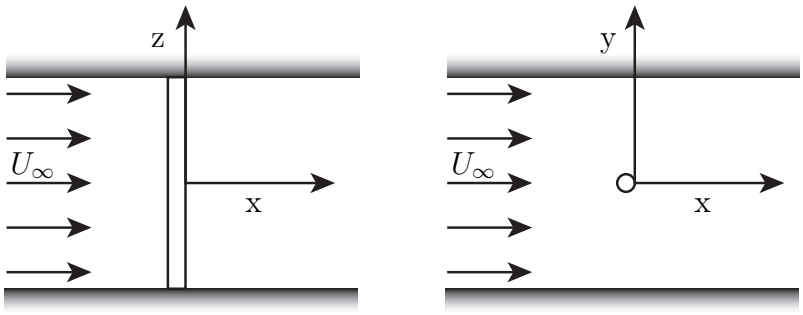

Fig. 1.1: Plan view (left) and side view (right) of a typical set up for investigating the flow past a cylinder in a uniform flow.

der. Since then much research has been directed at elucidating the underlying physical mechanisms of vortex shedding and a solid base of experimental work has led to the development of successful theoretical and numerical models. Figure 1.1 shows a typical set up for investigating the flow past a cylinder in a uniform flow where x is the streamwise coordinate, y is the transverse coordinate, z is the spanwise coordinate and the free stream velocity U_∞ has a 'top-hat' profile. The blockage ratio, the cylinder diameter divided by the tunnel height, is small and the aspect ratio, the cylinder length divided by the cylinder diameter, is large.

To characterize the uniform flow of an incompressible Newtonian fluid past a cylinder it is useful to introduce the classical Reynolds number Re:

$$\mathrm{Re} = \frac{\rho U_\infty d}{\eta}, \tag{1.1}$$

where U_∞ is the free stream velocity, d is the cylinder diameter, ρ is the fluid density and η is the dynamic viscosity of the fluid. The Reynolds number is a ratio of the fluid inertia forces to the viscous dissipation and governs the flow that is established. A comprehensive guide to flow regimes in the cylinder wake as a function of the Reynolds number is given in Williamson (1996) and the related stability aspects are reviewed by Oertel (1990). Here, the discussion is limited to a brief overview of the principle flow regimes followed by a detailed description of the regime of primary interest in this work, laminar 2D vortex shedding.

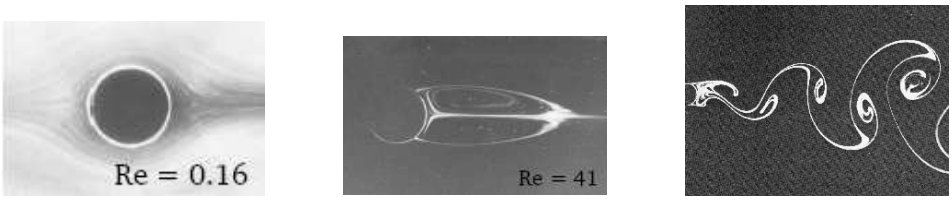

(a) (b) (c)

Fig. 1.2: Experimental visualizations of flow past a cylinder: (a) steady creeping flow, Re = 0.16, (b) downstream separation bubble, Re = 41, (c) two-dimensional laminar vortex shedding (the von Kármán vortex street), Re = 48-181.

1.2.1 Overview of regimes

Steady laminar flow, Re < 48

For Reynolds numbers less than 1 the flow past a cylinder is steady and without recirculation as shown in Fig. 1.2 (a). At Re ≈ 5 two attached counter-rotating vortices become visible downstream of the cylinder (Taneda, 1956), an example of which is shown in Fig. 1.2 (b) and as the Reynolds number increases so the length of the recirculation zone grows (Taneda, 1956; Gerrard, 1978). The wake becomes convectively unstable at Re ≈ 5, whereby selected perturbations are amplified and convected downstream but ultimately leave the flow undisturbed (Monkewitz, 1988). The locally most unstable part of the wake becomes absolutely unstable at Re ≈ 25 (Nishioka & Sato, 1978; Monkewitz, 1988), although this is not sufficient for self-sustained oscillations of the wake (Chomaz *et al.*, 1988). After Re ≈ 35 the approach of vortex shedding is signaled by the presence of 'gathers' or small disturbances which convect downstream on the side of the recirculation bubble and into the wake (Gerrard, 1978).

Laminar two-dimensional vortex shedding, $48 <$ **Re** < 180

At Re ≈ 48 the region of absolute instability in the wake is large enough for the whole wake to sustain time-amplified oscillations and the onset of the laminar two-dimensional (2-D) von Kármán instability occurs (Chomaz *et al.*, 1988; Monkewitz, 1988). Vortices are generated alternately on either side of the cylinder and are convected downstream, as shown in Fig. 1.2 (c). The vortex shedding frequency increases with increasing Reynolds number (Roshko, 1954). This regime will be treated in greater detail in Section 1.2.2.

Three-dimensional vortex shedding, $180 < \mathbf{Re} < 1000$

The laminar 2-D vortex shedding regime becomes three-dimensional (3-D) when Re is somewhere between 140 and 194, depending on the experimental set up. Spanwise vortex loops, termed 'mode A' vortices, occur initially and these are replaced by the appearance of finer scale 'mode B' vortices when Re is between 230 and 250 (Williamson, 1988*b*). The two 3-D modes are accompanied by changes in the vortex shedding frequency. As the Reynolds number increases further, the initial 2-D shedding mode persists while the finer scale 3-D structure becomes increasingly disordered.

Transition to turbulence and turbulent cylinder wake, $\mathbf{Re} > 1000$

For Reynolds numbers greater than 1000 the flow past a cylinder continues to undergo significant changes in behaviour (Williamson, 1996). These changes include alterations to the boundary layer and shear layer configuration and accompanying modifications to the base pressure. The fundamental vortex shedding phenomena, however, continues to be recognizable and has been shown to still exist at Reynolds numbers above 10^6 (Roshko, 1961).

1.2.2 Laminar Two-dimensional vortex shedding

The early experiments of Roshko (1954, 1955) provided a reference point for many investigations into the cylinder wake that were to follow. Using cylinders with very high aspect ratios $L^* = L/d$, where L is the cylinder length and d the diameter, Roshko examined the relationship between the drag, pressure, vortex shedding frequency and flow stability. Of particular note were the observations of a critical Reynolds number $\mathrm{Re_c} \approx 50$ for the onset of vortex shedding and a continuous relationship between the Reynolds number and the non-dimensional vortex shedding frequency given by the Strouhal number St:

$$\mathrm{St} = \frac{df}{U_\infty}, \tag{1.2}$$

where f is the vortex shedding frequency, from the onset of vortex shedding up to Re=150. This second point gave rise to a certain amount of debate as subsequent investigations were unable to fully reproduce this aspect of vortex shedding. For example, Tritton (1959) reported a discontinuous Re-St relationship, with frequency measurements showing both a 'high speed' mode similar to the results of Roshko and a 'low speed' mode occurring for $\mathrm{Re} \in [80, 105]$ where the vortex shedding frequency was reduced. Many

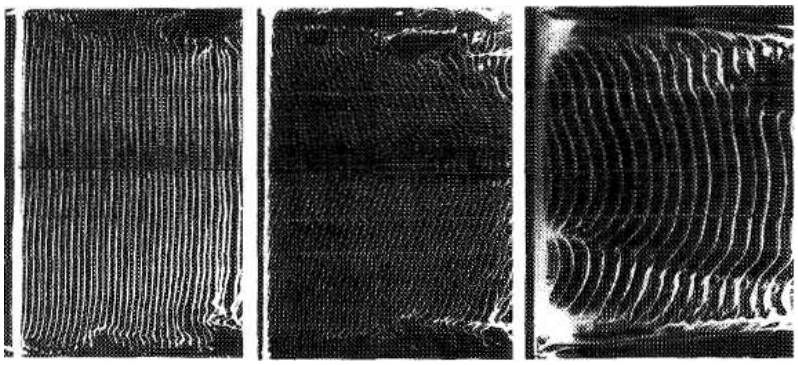

Fig. 1.3: Plan view of vortex shedding patterns downstream of a cylinder in cross flow, flow is from left to right. Images from left to right: parallel vortex shedding, 'chevron' vortex shedding and oblique vortex shedding. From Williamson (1988*a*).

hypotheses were advanced as to why different facilities should produce different Re-St relationships, including non-uniformities in the upstream flow, freestream turbulence and vibrations of the cylinder. The issue was finally resolved when Williamson (1988*a*) showed that vortices should be shed parallel to the cylinder axis to ensure a continuous Re-St curve as illustrated in Fig. 1.3. This was achieved by fine tuning the end conditions using endplates (Williamson, 1988*a*), end-cylinders (Eisenlohr & Eckelmann, 1989) or perpendicular control cylinders (Hammache & Gharib, 1989).

In the mean time, advances in the understanding of other aspects of cylinder wakes were being made. Investigations into the dynamics of the mean recirculation region downstream of the cylinder (Roshko, 1954; Taneda, 1956; Grove *et al.*, 1964; Coutanceau & Bouard, 1977*a*,*b*; Gerrard, 1978) underlined the importance of this area in the generation of vortices behind a cylinder. Nishioka & Sato (1978) described vortex shedding from a vibrating cylinder at Reynolds numbers as low as 20 and this was followed by the discovery of Mathis *et al.* (1984) and Provansal *et al.* (1987) that von Kármán vortex shedding was a manifestation of a limit cycle oscillation of the whole flow reached via a Hopf bifurcation and could be characterized by the Stuart–Landau model (Stuart, 1958, 1960). These experimental investigations provided support for theoretical studies (Monkewitz & Nguyen, 1987; Chomaz *et al.*, 1988; Monkewitz, 1988) which were able to apply to bluff body wakes the concepts of convective and absolute instability, originally borrowed from plasma physics (Briggs, 1964).

Experiments on the 3-D nature of the cylinder wake (Williamson, 1989; Lee & Budwig, 1991; Norberg, 1994) showed that the cylinder aspect ratio played an important role in the stability and the development of the von Kármán vortex street. These observations were well described by the spanwise complex Ginzburg–Landau model introduced by Albarède & Monkewitz (1992). Further experimental studies (e.g. Schumm *et al.*, 1994; Goujon-Durand *et al.*, 1994; Monkewitz *et al.*, 1996) contributed to the understanding of the stability and development of the flow downstream of a cylinder. The evolution of measuring techniques has given cause to re-visit the flow past a cylinder (Peschard *et al.*, 1999; Paranthoën *et al.*, 1999) and provide increasingly accurate observations.

1.3 Non-Newtonian fluids

Fluid flows exhibiting non-Newtonian behaviour range from micro-scale biological processes up to interstellar flows of fundamental particles. They are pertinent to many fluids which are within our sphere of everyday experience including foodstuffs, medicine, paints, inks, plastic, etc.

Initially a non-Newtonian fluid will be defined and this is followed by a brief overview of principle non-Newtonian behaviours. Finally the polymer fluids that will be used in this thesis will be introduced.

1.3.1 Definition of a non-Newtonian fluid

The stress in a fluid $\boldsymbol{\sigma}$ can be written as the sum of an isotropic part $-p\mathbf{I}$ due to hydrostatic pressure and the deviatoric stress $\mathbf{d}$ which is non-isotropic and due to motion of the fluid (Batchelor, 1967):

$$\boldsymbol{\sigma} = -p\mathbf{I} + \mathbf{d}. \tag{1.3}$$

For an incompressible fluid with an isotropic molecular structure, $\mathbf{d}$ is written:

$$\mathbf{d} = \eta\dot{\boldsymbol{\gamma}} = \frac{1}{2}\eta(\nabla\mathbf{u} + \nabla\mathbf{u}^T), \tag{1.4}$$

where η is a function of the fluid and the thermodynamic state, $\dot{\boldsymbol{\gamma}}$ is the rate of strain and $\mathbf{u}$ is the velocity. Fluids which are accurately described by Eq. (1.4) follow Newton's model for the relationship between the shear stress and the applied strain and are said to be Newtonian. For liquids with a heterogeneous molecular structure this model may cease to be realistic however, and these fluids are called non-Newtonian.

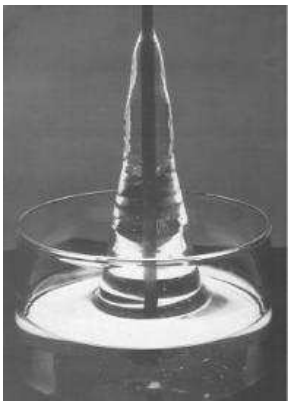

Fig. 1.4: Demonstration of non-Newtonian normal stresses in the rod climbing experiment. From Barnes *et al.* (1989).

1.3.2 Description of non-Newtonian fluid behaviour

There are various categories of non-Newtonian behaviour and excellent introductions to the subject are provided by Bird *et al.* (1987*a*,*b*) and Barnes *et al.* (1989). A short guide to those relevant is given below.

Shear rate dependent viscosity

Perhaps the most common non-Newtonian behaviour is a shear viscosity that is dependent on the applied shear rate, i.e. $\eta(\dot{\gamma}_{xy})$. This includes behaviours described by shear-thinning (or pseudoplasticity), shear-thickening (or dilatancy), thixotropy, and fluids with a yield stress (Bingham fluid). The shear viscosity at $\dot{\gamma}_{xy} = 0\ \mathrm{s}^{-1}$ is written η_0.

Normal stresses

The generation of stresses normal to the principle direction of motion is characteristic of viscoelastic non-Newtonian fluids. The normal stresses are proportional to the applied shear rates and are expressed as the normal stress differences N_1 and N_2:

$$N_1 = \sigma_{xx} - \sigma_{yy} = \dot{\gamma}_{xy}^2 \Psi_1, \tag{1.5}$$

$$N_2 = \sigma_{yy} - \sigma_{zz} = \dot{\gamma}_{xy}^2 \Psi_2, \tag{1.6}$$

where Ψ_1 and Ψ_2 are the first and second normal stress coefficients respectively. Normal stresses are a second order effect and are small at low shear rates. Ψ_1 is in practice always positive and greater in magnitude than Ψ_2

which is either zero or negative. When the fluid microstructure becomes anisotropic, normal stresses arise to balance the restoring forces of the deformed molecules. This is illustrated in Fig. 1.4 by the canonical rod climbing experiment for polymer solutions. The rotating rod aligns the polymer chains tangentially to the direction of rotation creating hoop stresses which contract around the axis of rotation and cause the fluid to climb up the rod.

Change in extensional viscosity

The extensional viscosity η_{ext} is three times the shear viscosity η for a Newtonian fluid, as given by the Trouton ratio. For a fluid with an anisotropic microstructure the behaviour under extension and compression can deviate from this significantly. Figure 1.5 shows that the height of a liquid column created after a drop impinges into a volume of fluid is dramatically altered when polymer additives are present. Although increases in η_{ext} are well documented, accurately measuring the change in extensional viscosity in a purely extensional flow still remains a challenge, especially for mobile solutions.

Viscoelasticity

Fluids which exhibit a combination of viscous (Newtonian fluid) and elastic (Hookean solid) behaviour are said to be viscoelastic. Viscoelastic fluids may demonstrate any of the previously described effects. Any fluid that has a deformable microstructure with a preferred undisturbed state will by definition 'remember' this state. The behaviour of a fluid is then also governed by the restoring forces and not just the instantaneous applied forces and therefore the behaviour at time t is dependent on all previous states since $t = -\infty$. The influence of past deformation is characterized by the relaxation time λ. This gives rise to the non-dimensional Deborah number De and elasticity number El:

$$\text{De} = \frac{U_\infty \lambda}{d}, \tag{1.7}$$

$$\text{El} = \frac{\text{De}}{\text{Re}} = \frac{\eta \lambda}{\rho d^2}. \tag{1.8}$$

The Deborah number is a ratio between a characteristic time for the fluid and a characteristic flow time while the elasticity number is the ratio of viscoelastic to inertial forces.

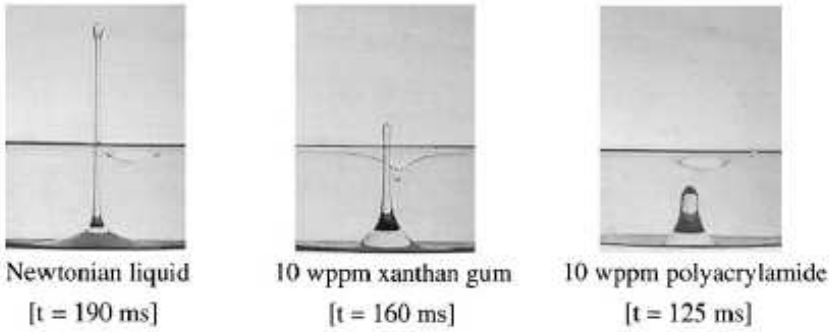

Fig. 1.5: Changes in the formation of the Worthington jet due to non-Newtonian extensional viscosity. From Cheny & Walters (1998).

1.3.3 Polymer solutions

For a detailed guide to polymer solution properties, the reader is referred to Bird *et al.* (1987*a*,*b*).

The dynamics of polymer solutions are highly dependent on the polymer concentration as well as the molecular structure of the polymer. However, even small amounts of polymer additive (concentration $c < 0.1$ wt%) in a Newtonian solvent can produce readily observable non-Newtonian behaviour. It is useful to isolate the influence of a specific non-Newtonian effect and this led to the advent of 'Boger' fluids (Boger, 1976). A Boger fluid is a highly elastic fluid with a constant viscosity over a large range of shear rates and is typically a solution of small amounts of high molecular weight polymer chains dissolved in a viscous solvent. This has the advantage of rendering changes in shear viscosity insignificant and revealing the elastic nature of the fluid. Low viscosity solvents such as water can be used, although to avoid shear-thinning, lower molecular weight (M)polymer chains must be used and the elastic forces are therefore typically lower.

1.4 Non-Newtonian flow past a cylinder

The original motivations for studying the viscoelastic flow past a cylinder were threefold: firstly, small amounts of polymer additive were seen to alter turbulent flow (Gadd, 1966*b*); secondly, measurements using hotfilm anemometers in polymer solutions were different compared to Newtonian fluids (Smith *et al.*, 1967); and thirdly was the need to understand viscoelas-

tic flow past submerged objects, a common situation in polymer processing. For obvious reasons, these different phenomena gave rise to a wide variety of geometric configurations and fluid rheologies for the study of viscoelastic flow past a cylinder. In the following survey the focus will be on investigations into flows with moderate amounts of fluid inertia.

Early studies of the viscoelastic vortex street showed that for low-concentration aqueous polyethylene oxide (PEO) solutions the vortex shedding frequency and the vorticity of the shed vortices were reduced for increasing polymer concentration (Gadd, 1966*a*; Kalashnikov & Kudin, 1970). Kalashnikov & Kudin also showed that the critical Reynolds number decreased for higher concentrations of PEO but when the solutions were mechanically degraded they exhibited properties closer to the Newtonian solvent. Other work on wakes behind cylinders and spheres also highlighted the importance of polymer solution degradation in relation to the effects observed (e.g. Brennen, 1970; Sarpkaya *et al.*, 1973)

Before the onset of vortex shedding, also for flows of low-concentration aqueous PEO solutions past a cylinder, dye streak visualizations showed that the boundary layer and shear layers thickened (James & Accosta, 1970; Konuita *et al.*, 1980) and this was attributed to the presence of normal forces. James & Gupta (1975) suggested that the increase in drag past a cylinder could be scaled with the elasticity number up to Reynolds numbers of 150. Konuita *et al.* also performed velocity measurements at $\mathrm{Re} = 5$ showing that downstream of the cylinder the centreline velocity was significantly reduced and the wider wake region also had higher velocity gradients $\mathrm{d}U/\mathrm{d}y$.

Further investigations into the vortex shedding frequency f by Usui *et al.* (1980) showed that St decreased for increasing polymer concentration. In addition, their Fig. 3 indicates a reduction in the value of $\mathrm{Re_c}$ although this is not discussed explicitly. The Deborah number and elasticity number were found to collapse the change in f. At high Reynolds numbers, Kim & Telionis (1989) showed that the reduction in f for dilute aqueous solutions of PEO ($M = 0.9 \times 10^6$ g/mol) and polyacrylamide ($M = 1 \times 10^6$ g/mol) compared to the Newtonian case disappears at $\mathrm{Re} = 1.8 \times 10^4$.

McKinley *et al.* (1993) showed that flow instability could be induced by fluid elasticity for flows of highly elastic viscoelastic liquids past a confined cylinder at Reynolds numbers much less than 1. This new instability was qualitatively different to the von Kármán vortex street, with initially a cellular structure varying spatially along the cylinder axis and which was superseded by the onset of a time dependent instability whereby the cellular structure translated along the cylinder axis. The onset of the instability was a function of the Deborah and Weissenburg numbers where the Weissenburg

number is a characteristic flow shear rate non-dimensionalized with the fluid relaxation time.

The configuration of vortex shedding from a cylinder in Newtonian flow with base bleed was studied experimentally by Cadot & Kumar (2000) and Cadot (2001). The injection of water and the injection of an aqueous PEO solution into the cylinder wake showed that injecting a viscoelastic solution increased the streamwise distance between vortices and reduced the intensity of the vorticity.

Vortex shedding from a cylinder for a range of shear-thinning fluids was investigated by Coelho & Pinho (2003*a*,*b*, 2004) over a wide range of Reynolds numbers. A decrease in vortex shedding frequency was noted for fluid elasticity but was found to increase for shear-thinning. Their Fig. 1 (Coelho & Pinho, 2003*b*) appears to show vortex shedding at $\mathrm{Re} < 40$, which would also imply a significant destabilization of the wake for the shear-thinning elastic fluids. The separation of the boundary layer from the cylinder was delayed for increasing fluid elasticity with the strongest effect at Reynolds numbers between 50 and 100.

1.4.1 Other studies of interest

Investigations of inertial instabilities with low fluid elasticity other than von Kármán vortex shedding could be instructive as to what might be important in vortex shedding from a cylinder for a viscoelastic fluid.

The investigation by Stokes *et al.* (2001*a* and 2001*b*) into vortex breakdown in a cylindrical cavity with a rotating lid using polymer solutions showed that low fluid elasticity stabilized the flow. The stabilization of the flow was attributed to a mixture of viscoelastic normal stresses and an increase in the extensional viscosity of the polymer fluids. For the Taylor–Couette geometry with low concentration aqueous PEO solutions ($M = 8 \times 10^6$ g/mol) Crumeyrolle *et al.* (2002) showed that the onset of Taylor vortices and wavy Taylor vortices was stabilized for small amounts of polymer. However at higher concentrations the flow was destabilized due to shear-thinning.

Therefore for two centrifugal instabilities with large inertia, low viscoelasticity has shown a stabilizing effect due to the normal forces and the increase in extensional viscosity while shear-thinning acts to destabilize system.

1.5 Summary

Two-dimensional laminar vortex shedding from a cylinder in a uniform Newtonian flow has been well documented experimentally and models have been developed that describe certain key aspects of the phenomena observed. Non-Newtonian fluids show various behaviours that distinguish them from the Newtonian model and for constant viscosity polymer solutions these are notably the presence of normal stresses and a non-Newtonian extensional viscosity. Previous investigations into the non-Newtonian cylinder wake using polymer solutions have shown that for increasing polymer concentration the shedding frequency decreases. A decrease in the critical Reynolds number is also apparent in several studies and a new instability at low Reynolds numbers is found for sufficiently elastic fluids.

Chapter 2

The Landau models

This chapter introduces the model equations that will be used to analyze the stability of vortex shedding from a cylinder. A comprehensive introduction to linear and non-linear stability is given by Drazin & Reid (1981). Here and in the following an asterisk denotes quantities that are non-dimensional with the cylinder diameter d, the diffusion time $d^2\rho/\eta$, and the fluid density ρ.

2.1 The Landau equation

The stability of a flow is assessed by examining the temporal and spatial response of some suitably non-dimensionalized fluctuating quantity $\mathbf{u}^*$ which is written

$$\mathbf{u}^*(\mathbf{x}^*, t^*) = A^*(t^*) f(\mathbf{x}^*, t^*) + \text{complex conjugate}, \tag{2.1}$$

where t^* is the time, $\mathbf{x}^*$ is the spatial repartition and $A^*(t^*)$, the complex amplitude of the perturbation, is dependent on the perturbation growth rate s^* and the perturbation frequency ω^*:

$$A^*(t) = u_0^* \exp[(s^* + \mathrm{i}\omega^*)t^*]. \tag{2.2}$$

For a linear stability analysis we write the linear growth rate $s^*_{\text{lin}} = \sigma^*_{\text{r}}$ and the linear frequency $\omega^*_{\text{lin}} = \sigma^*_{\text{i}}$. The behaviour of the complex perturbation magnitude $|A^*|$ is thus governed by the sign of σ^*_{r}. For all $\sigma^*_{\text{r}} < 0$ the fluctuation decays and the flow is stable while for all $\sigma^*_{\text{r}} > 0$ the fluctuation grows and the flow is unstable. The case $\sigma^*_{\text{r}} = 0$ describes a neutrally stable flow and the fluctuation neither grows nor decays. σ^*_{r} is a function of a critical flow parameter upon which the flow stability is dependent. This formulation of $|A^*|$ is useful to describe the perturbation behaviour at small times but is not accurate for $t^* \to \infty$.

To model the behaviour at large as well as small times Landau (Landau & Lifchitz, 1989) proposed the empirical formulation of the perturbation magnitude $|A^*|$:

$$\frac{\mathrm{d}|A^*|^2}{\mathrm{d}t^*} = 2\sigma_\mathrm{r}^*|A^*|^2 - l^*|A^*|^4, \tag{2.3}$$

where l^* is the Landau constant and Eq. (2.3) is known as the Landau equation. At small times $|A^*|$ is small and σ_r^* governs the response of the amplitude as in Eq. (2.2) but at $t^* \to \infty$ the quartic term which is controlled by l^* becomes important.

The Landau constant l^* plays a fundamental role in the nature of the bifurcation when σ^* passes through zero. When l^* is positive the bifurcation is said to be 'supercritical' while for $l^* < 0$ the bifurcation is said to be 'subcritical'. These two cases each have their own characteristic behaviour (Drazin & Reid, 1981). Laminar 2-D vortex shedding from a bluff body has been shown to correspond to a supercritical bifurcation (Mathis *et al.*, 1984; Provansal *et al.*, 1987; Schumm *et al.*, 1994). Thus the perturbation amplitude at large times (the saturated amplitude) is written:

$$|A^*|_\mathrm{sat} = \sqrt{\frac{2\sigma^*}{l^*}}. \tag{2.4}$$

2.2 The Stuart–Landau equation

Stuart (1958, 1960) used the model of weakly non-linear hydrodynamic stability to show that the complex perturbation amplitude (2.2) obeyed:

$$\frac{\mathrm{d}A^*(t^*)}{\mathrm{d}t^*} = (\sigma_\mathrm{r}^* + \mathrm{i}\sigma_\mathrm{i}^*)A^*(t) - (l_\mathrm{r}^* + \mathrm{i}l_\mathrm{i}^*)|A^*|^2A^*(t), \tag{2.5}$$

Equation (2.5), called the Stuart–Landau (SL) equation, assumes that the flow is 2-D and gives the time dependance of the instability but not the spatial repartition. It should be noted that σ_r^* and σ_i^* must be independent of the location in the flow as must the ratio $l_\mathrm{r}^*/l_\mathrm{i}^*$, although l_r^* may change with the location. Differentiating the complex amplitude (2.2) with respect to time we write:

$$\frac{\mathrm{d}A^*(t^*)}{\mathrm{d}t^*} = s^*A^*(t^*) + \mathrm{i}\omega^*A^*(t^*), \tag{2.6}$$

The real and imaginary parts of Eq. (2.6) can be equated with the real and imaginary parts of Eq. (2.5) to express the the non-linear growth rate s^* and the non-linear frequency ω^* of the perturbation:

$$s^* = \sigma_\mathrm{r}^* - l_\mathrm{r}^*|A^*|^2, \tag{2.7a}$$

$$\omega^* = \sigma_\mathrm{i}^* - l_\mathrm{i}^*|A^*|^2. \tag{2.7b}$$

For vortex shedding from a bluff body the linear growth rate is proportional to $\mathrm{Re} - \mathrm{Re_c}$. Therefore when Re is less than some critical value $\mathrm{Re_c}$, $A^*(t^*)$ decays, while for $\mathrm{Re} > \mathrm{Re_c}$, $A^*(t^*)$ increases. Thus we can approximate the coefficients in Eqs. (2.7) by their Taylor expansions about $\mathrm{Re_c}$:

$$\sigma_\mathrm{r}^* = [\mathrm{Re} - \mathrm{Re_c}]\frac{\mathrm{d}\sigma_\mathrm{r}^*}{\mathrm{dRe}}(\mathrm{Re_c}) + O(|\mathrm{Re} - \mathrm{Re_c}|^2), \tag{2.8a}$$

$$\sigma_\mathrm{i}^* = \sigma_\mathrm{i}^*(\mathrm{Re_c}) + [\mathrm{Re} - \mathrm{Re_c}]\frac{\mathrm{d}\sigma_\mathrm{i}^*}{\mathrm{dRe}}(\mathrm{Re_c}) + O(|\mathrm{Re} - \mathrm{Re_c}|^2), \tag{2.8b}$$

$$l_\mathrm{r}^* + il_\mathrm{i}^* = [l_\mathrm{r}^* + il_\mathrm{i}^*](\mathrm{Re_c}) + O(|\mathrm{Re} - \mathrm{Re_c}|). \tag{2.8c}$$

Combining Eqs. (2.7) and (2.8) we can write for $t^* \to \infty$:

$$\begin{aligned} |A^*|_\mathrm{sat} &= \sqrt{\frac{\sigma_\mathrm{r}^*}{l_\mathrm{r}^*}} \\ &= \left[\frac{1}{l_\mathrm{r}^*(\mathrm{Re_c})}\frac{\mathrm{d}\sigma_\mathrm{r}^*}{\mathrm{dRe}}(\mathrm{Re_c})\right]^{1/2}[\mathrm{Re} - \mathrm{Re_c}]^{1/2} \\ &= (k_1[\mathrm{Re} - \mathrm{Re_c}])^{1/2}, \end{aligned} \tag{2.9a}$$

$$\begin{aligned} \omega_\mathrm{sat}^* &= \sigma_\mathrm{i}^* - l_\mathrm{i}^*|A^*|_\mathrm{sat}^2 \\ &= \sigma_\mathrm{i}^*(\mathrm{Re_c}) - \left[\frac{l_\mathrm{i}^*}{l_\mathrm{r}^*}(\mathrm{Re_c})\frac{\mathrm{d}\sigma_\mathrm{r}^*}{\mathrm{dRe}}(\mathrm{Re_c}) - \frac{\mathrm{d}\sigma_\mathrm{i}^*}{\mathrm{dRe}}(\mathrm{Re_c})\right][\mathrm{Re} - \mathrm{Re_c}] \\ &= \sigma_\mathrm{i}^*(\mathrm{Re_c}) + k_2[\mathrm{Re} - \mathrm{Re_c}], \end{aligned} \tag{2.9b}$$

where k_1 and k_2 are introduced to simplify the presentation. Accepted values for the coefficients in Eqs. (2.9) for vortex shedding from a cylinder determined from experimental studies for laminar 2-D vortex shedding from a cylinder (Albarède & Monkewitz, 1992; Monkewitz *et al.*, 1996; Monkewitz, 1996) are:

$$\mathrm{Re_c} = 48.5 \pm 0.5 \tag{2.10a}$$

$$\sigma_\mathrm{r}^* = (0.21 \pm 0.005)(\mathrm{Re} - \mathrm{Re_c}) \tag{2.10b}$$

$$\sigma_\mathrm{i}^* = (33.6 \pm 0.3) + (0.64 \pm 0.02)(\mathrm{Re} - \mathrm{Re_c}) \tag{2.10c}$$

$$l_\mathrm{i}^*/l_\mathrm{r}^* = -(2.9 \pm 0.45) \tag{2.10d}$$

$$k_2 = 0.20 \pm 0.05. \tag{2.10e}$$

The SL model has been used with great success to describe the behaviour of von Kármán shedding from a circular cylinder and good agreement between experimental results has been found for high aspect ratio cylinders.

2.3 The complex Ginzburg–Landau equation

Although the 2-D SL model was found to be widely applicable, the influence of three-dimensional aspects, such as a finite cylinder aspect ratio L^* and non-parallel vortex shedding modes, were well documented for vortex shedding from a cylinder (Williamson, 1988*a*; Lee & Budwig, 1991; Norberg, 1994). To account for these 3-D phenomena Albarède & Monkewitz (1992) developed a model with weak spanwise variation using the complex Ginzburg–Landau (GL) equation. Thus the GL model allows a variation in the complex amplitude of the perturbation in z^*:

$$\frac{\partial A^*}{\partial t^*} = (\sigma_{\mathrm{r}}^* + \mathrm{i}\sigma_{\mathrm{i}}^*)A^* + (\mu_{\mathrm{r}}^* + \mathrm{i}\mu_{\mathrm{i}}^*)\frac{\partial^2 A^*}{\partial z^{*2}} - (l_{\mathrm{r}}^* + \mathrm{i}l_{\mathrm{i}}^*)|A^*|^2 A^*, \tag{2.11}$$

where $\mu^* = \mu_{\mathrm{r}}^* + \mathrm{i}\mu_{\mathrm{i}}^*$ is the diffusion coefficient and Eq. (2.11) is known as the spanwise GL equation. This representation can be thought of physically as a line source of SL oscillators with diffusive coupling.

The results of particular interest to the present work are the corrections for the finite aspect ratio of the cylinder which can be applied to the critical Reynolds number Re_{c} and the saturated vortex shedding frequency ω_{sat}^*:

$$\mathrm{Re}_{\mathrm{c}} = \mathrm{Re}_{\mathrm{c}0} + \left(\frac{\mu_r^*}{\sigma_{\mathrm{r}}^*}\right)\left(\frac{\pi}{L^*}\right)^2, \tag{2.12}$$

$$\omega_{\mathrm{sat}}^* = \omega_{\mathrm{sat}0}^* - \left(\mu_{\mathrm{i}}^* - \frac{l_{\mathrm{i}}^*\mu_r^*}{l_{\mathrm{r}}^*}\right)\left(\frac{\pi}{L^*}\right)^2, \tag{2.13}$$

where the the subscript 0 indicates values for an infinite aspect ratio cylinder. The coefficients μ_{r}^* and μ_{i}^* are dependent on the Reynolds number but values near the onset of vortex shedding from Monkewitz *et al.* (1996) are:

$$\mu_{\mathrm{r}}^* = 13 \pm 4 \tag{2.14}$$

$$\left(\mu_{\mathrm{i}}^* - \frac{l_{\mathrm{i}}^*\mu_{\mathrm{r}}^*}{l_{\mathrm{r}}^*}\right) = 24 \pm 2. \tag{2.15}$$

2.4 Summary

The 2-D SL and 3-D GL models that will be used to assess the stability of the cylinder wake have been presented as well as typical values of the model parameters for the cylinder wake that have been determined in previous experimental work.

Chapter 3

Polymer solution characterization

This chapter presents the relevant theoretical and practical aspects of characterizing and modeling polymer solutions as well as the experimentally determined properties of the fluids considered in this work.

The composition of the fluids is detailed initially (Section 3.1) and is followed by an overview of relevant models for polymer chains and polymer solutions (Section 3.2-3.4). The experimental procedures used to prepare and characterize the polymer solutions are given in Section 3.5 and finally the results of the characterization are presented and discussed in Section 3.6.

It should be noted that in this chapter all solution concentrations will be discussed in units of g/ml and not in wt% as used elsewhere in this thesis.

3.1 Composition of the solutions

The non-Newtonian liquids used in this work were polymer solutions which were for the most part dilute, meaning that interactions between individual polymer chains are considered unimportant.

Water was used as the solvent and high molecular weight polyethelyne oxide (PEO) chains were added in small quantities. Aqueous PEO solutions have been used previously in studies of non-Newtonian cylinder wakes (Gadd, 1966*a*; James & Accosta, 1970; Kalashnikov & Kudin, 1970; Usui *et al.*, 1980; Cadot & Kumar, 2000; Cadot, 2001) and solutions of this type are well discussed in the literature elsewhere (Brennen & Gadd, 1967; Tam & Tiu, 1989; Vlassopoulos & Schowalter, 1994; Dontula *et al.*, 1998; Tirtaatmadja *et al.*, 2005). Their relative popularity is because they show measurable viscoelastic effects while being inexpensive and easy to use. Aqueous PEO solutions have the additional advantage over other polymer solutions, for example aqueous polyacrylamide solutions, of showing relatively little shear-thinning at in-

termediate shear rates for low concentrations (Vlassopoulos & Schowalter, 1994). This allows viscoelastic effects to be examined independently of a shear rate dependent viscosity.

Solvent

Ordinary tap water was used as the solvent.

Polymer additive

Polyethelyne-oxide (PEO) is a water-soluble non-ionic synthetic polymer of chemical structure

$$\mathrm{H - (O - CH_2 - CH_2 -)_n\ OH.}$$

Water is a good solvent for PEO (Brandrup, 1989) meaning that the polymer chains are extended beyond their length in a theta solvent. Polymer chain degradation can be caused by oxidization; this effect increases with exposure to ultra-violet light as well as the presence of acids and heavy metal ions. High molecular weight PEO (greater than approximately 10^6 g/mol) can also be degraded by large mechanical stresses. Therefore when mixing PEO solutions it is important to keep applied stresses to a minimum.

The grade of PEO used, Polyox$^{\mathrm{TM}}$ WSR N12K, was supplied by The Dow Chemical Company. The manufacturer quoted a nominal polydisperse molecular weight of 10^6 g/mol. This was previously shown to be sufficiently high to introduce measurable non-Newtonian effects (Dontula *et al.*, 1998) yet still low enough to withstand reasonable mechanical stress and oxidization.

PEO chains have a repeat unit mass $m_0 = 44$ g/mol, an average bond length $l = 0.147$ nm and a characteristic ratio, the ratio between the mean square end-to-end distance of the unperturbed polymer chain $|r_0^2|$ and Nl^2 where N is the number of repeat units, $C_\infty = 4.1$ (Brandrup, 1989). Therefore for a molecular weight of 10^6 g/mol the number of repeat units $n \approx 22700$ and $|r_0^2| = C_\infty N l^2 \approx 2010$ nm^2.

3.2 Polymer characterization

3.2.1 Intrinsic viscosity

The intrinsic viscosity at zero shear rate $[\eta]_0$ is a measure of the polymer contribution to the solution viscosity and depends on the solvent, the polymer and the molecular weight of the polymer. $[\eta]_0$ can be determined using two

complementary methods: firstly with the relative viscosity, and secondly with the inherent viscosity.

$[\eta]_0$ from the relative viscosity

The relative viscosity η_{rel} of a solution can be expanded as a function of polymer concentration c and intrinsic viscosity $[\eta]_0$ in a Taylor series:

$$\eta_{\text{rel}} = \frac{\eta_0}{\eta_{\text{s}}} = 1 + [\eta]_0\ c + k'[\eta]_0{}^2 c^2 + \ldots, \tag{3.1}$$

where k' is the Huggins coefficient and $k' \approx 0.4$ for dilute polymer solutions. Neglecting terms of $O([\eta]_0^3 c^3)$ and higher and rewriting for the reduced viscosity η_{red} gives

$$\eta_{\text{red}} = \frac{\eta_{\text{rel}} - 1}{c} = [\eta]_0 + k'[\eta]_0{}^2 c. \tag{3.2}$$

Equation (3.2) is known as the Huggins equation and in the limit of zero concentration

$$[\eta]_0 = \lim_{c \to 0} \eta_{\text{red}}. \tag{3.3}$$

$[\eta]_0$ from the inherent viscosity

Alternatively we can use the inherent viscosity η_{inh} of the solution to find $[\eta]_0$. Using the approximation for small x, $\ln(1+x) = x - x^2/2$, we can show that

$$\ln\ \eta_{\text{rel}} = \ln\ (1 + \eta_{\text{sp}}) = \eta_{\text{sp}} - \frac{\eta_{\text{sp}}^2}{2}, \tag{3.4}$$

where the specific viscosity $\eta_{\text{sp}} = \eta_{\text{rel}} - 1$. Dividing through by c we can write,

$$\frac{\ln\ \eta_{\text{rel}}}{c} = \eta_{\text{inh}} = \frac{\eta_{\text{sp}}}{c} - \frac{c}{2}\left(\frac{\eta_{\text{sp}}}{c}\right)^2. \tag{3.5}$$

and substituting Eq. (3.2) in Eq. (3.5) gives

$$\eta_{\text{inh}} = [\eta]_0 + k''[\eta]_0{}^2 c + O([\eta]_0^4 c^3), \tag{3.6}$$

where the Kraemer coefficient $k'' = \left(k' - \frac{1}{2}\right)$ and Eq. (3.6) is known as the Kraemer equation. Again in the limit of zero concentration we find that

$$[\eta]_0 = \lim_{c \to 0} \eta_{\text{inh}}. \tag{3.7}$$

Therefore from Eqs (3.3) and (3.7) two independent values of the intrinsic viscosity can be calculated and the level of agreement between the two results gives an indication of the accuracy.

Reference	M_v (g/mol)	K (ml/g)	a	T (° C)
Brandrup (1989)	3×10^4	0.0499	0.67	25
Tirtaatmadja *et al.* (2005)	$3 \times 10^5 - 5 \times 10^6$	0.072	0.65	N/A

Table 3.1: Properties for dilute PEO solutions.

3.2.2 Molecular weight

There are three common definitions of the molecular weight, M, depending on how it is calculated: the *weight average* molecular weight, the *viscosity average* molecular weight and the *number average* molecular weight. The viscosity average molecular weight M_v will be used here as viscosity methods were used in the determination of M. For PEO the viscosity average molecular weight is close to, though slightly lower than, the weight average molecular weight.

The molecular weight of a polymer chain is related to the polymer chain length: the higher M_v, the longer the chain length. For monodisperse polymers, the standard deviation of M_v is very small for a large sample of polymer chains and the average M_v is representative of a given polymer chain. However for the polydisperse polymers used in this work there is a wide range of polymer chain lengths and it is only possible to consider an average molecular weight.

Using the Mark-Houwink equation, M_v is related to the intrinsic viscosity in the following way:

$$[\eta]_0 = K {M_v}^a, \tag{3.8}$$

where K and a are constants dependent on the polymer, the solvent and M_v. Values corresponding to PEO solutions are shown in Table 3.1.

A note on polymer chain degradation

Polymer chain degradation is accompanied by a drop in the solution shear viscosity because the shorter chains provide a smaller contribution to the solution viscosity. Therefore measuring η after a given period of time or after an applied mechanical stress, will signify whether ageing or mechanical degradation have taken place.

3.2.3 Solution concentration

The concentration c of a polymer solution is commonly expressed in either grammes per millilitre (g/ml), weight percent (wt%) or weight parts per million (wppm). In this chapter units of (g/ml) are used to facilitate comparisons with other results in the literature but elsewhere in the thesis units of (wt%) are used to simplify the presentation of the data, and

$$0.001 \text{ g/ml} = 0.1 \text{ wt\%}. \tag{3.9}$$

Solutions are generally divided into two classes: low concentration solutions and high concentration solutions. The concentration is considered low for $c[\eta]_0 <$ 1-5 and the interactions between polymer chains are weak. For high concentration solutions ($c[\eta]_0 > 5$) the polymer chains no longer move freely and interact strongly with neighbouring chains.

For a dilute polymer solution there are considered to be no interactions between individual polymer chains. Although there are several definitions of the upper concentration limit for a dilute solution, a value in the neighbourhood of

$$c = 1/[\eta]_0 \tag{3.10}$$

is generally accepted (Bird *et al.*, 1987*a*). Equation (3.10) will be used in the present work to define the maximum concentration for a dilute solution.

3.3 Molecular models for polymer solutions

Polymer solutions with low viscosity solvents and low polymer concentrations can be difficult to characterize using conventional rheometric techniques because of the small forces involved. Such solutions are often in the dilute or weakly semi-dilute concentration regimes and the interactions between individual polymer chains are taken to be negligible. If this assumption holds, the behaviour of a polymer chain is relatively easy to model. Therefore instead of measuring the macroscopic behaviour, the microscopic properties of a single polymer chain can be modeled and then used to calculate the global behaviour of the polymer solution.

There are various approaches to modelling polymer chains and the appropriate model is dependent on the polymer-solvent combination and the flow being considered. A thorough guide to polymer solution modelling can be found in Bird *et al.* (1987*a*,*b*) and in the following an overview of the key results for models relevant to the present study is given.

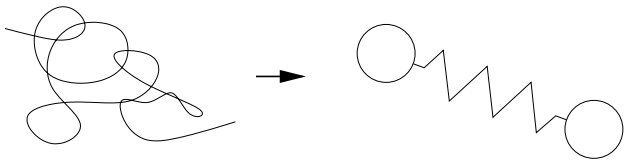

Fig. 3.1: The Oldroyd B model approximation of a polymer chain by an elastic dumbbell.

3.3.1 Suspensions of rigid spheres

Perhaps the most simple model for a polymer chain is a rigid sphere. Einstein (1906, 1911) showed that the viscosity η of a solution consisting of perfectly spherical bodies suspended in a Newtonian solvent of viscosity η_s is given by:

$$\eta = \eta_s \left(1 + \frac{5}{2}\varphi\right), \tag{3.11}$$

where the volume fraction of the spheres $\varphi = 4\pi n a^3/3$ and n is the number density (or the number of particles per unit volume). Interestingly, the change in viscosity is independent of the radius of the spheres and depends only on their total volume.

However, it is quickly seen that for the viscoelastic solutions used in this work the approximation of a polymer chain by a sphere is inadequate. The result is of some interest though as it gives an indication of the viscosity increase due to the addition of seeding particles in the fluids.

3.3.2 Oldroyd B model

A far more realistic model is the Oldroyd B model (Oldroyd, 1950) which uses a simple elastic dumbbell to represent a polymer chain as shown in Fig. 3.1. The extension of the polymer chain is accounted for by a non-bendable Hookean spring and the frictional drag of the polymer by the Stokes drag on the two dumbbell beads. The physical basis for this model is that the longest and therefore the most significant relaxation time of a polymer chain corresponds to just one spring. The solution viscosity η_{OB} and relaxation time λ_{OB} as a function of the polymer and solvent properties are given as:

$$\eta_{0_{\mathrm{OB}}} = \eta_s(1 + c[\eta]_0), \tag{3.12}$$

$$\lambda_{\mathrm{OB}} = \frac{[\eta]_0 \eta_s M_v}{\widetilde{N} k T}, \tag{3.13}$$

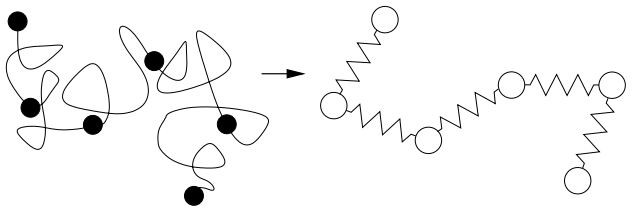

Fig. 3.2: Approximation of a polymer chain with a bead-spring model.

where $\widetilde{N}$ is Avogadaro's number and k is the Boltzmann constant. Also the first normal stress difference which is proportional to the square of the shear rate $\dot{\gamma}_{xy}$ can be written:

$$N_{1_{\mathrm{OB}}} = 2\lambda_{\mathrm{OB}}(\eta_0 - \eta_{\mathrm{s}})\dot{\gamma}_{xy}^2, \tag{3.14}$$

and the second normal stress difference $N_2 = 0$. The extensional viscosity $\eta_{\mathrm{ext}_{\mathrm{OB}}}$ is a function of the applied rate of extension $\dot{\gamma}_{xx}$.

$$\eta_{\mathrm{ext}_{\mathrm{OB}}} = \frac{2\eta_{\mathrm{s}}}{1 - 2\lambda_{\mathrm{OB}}\dot{\gamma}_{xx}} + \frac{\eta_{\mathrm{s}}}{1 + \lambda_{\mathrm{OB}}\dot{\gamma}_{xx}}. \tag{3.15}$$

Although the Oldroyd B model has some physical basis, there are limitations to its abilities to describe polymer solutions realistically. Eq. (3.12) shows that the viscosity is independent of shear rate and therefore does not take into any account shear-thinning effects. And the infinite extensibility of a Hookean spring gives the extension of an Oldroyd B polymer chain beyond its equilibrium state in shear flow as:

$$\frac{\langle r^2 \rangle}{\langle r_0^2 \rangle} = 1 + \frac{2}{3}\left(\lambda_{\mathrm{OB}}\dot{\gamma}_{xy}\right)^2, \tag{3.16}$$

while in reality a polymer chain can only be stretched out to a finite length.

3.3.3 Rouse and Zimm models

More sophisticated representations of a polymer chain can be constructed using several springs and beads in series, as shown in Fig. 3.2. The Rouse model (Rouse, 1953) consists of N spherical beads connected by $(N-1)$ Hookean springs. As in the Oldroyd B model, the drag of the polymer accounted for by the flow of solvent around the beads and the elasticity by the springs elements. This type of configuration gives a spectrum of $(N-1)$

relaxation times; for the j^{th} relaxation time when j is small we can write

$$\lambda_{\mathrm{R}_j} = \left(\frac{6}{\pi^2 j^2}\right) \lambda_{\mathrm{OB}_1}. \tag{3.17}$$

λ_{R_1} corresponds to the longest and most influential relaxation time and it is usual to approximate λ_{R} by λ_{R_1}.

The solution viscosity η_{R} is given by:

$$\eta_{\mathrm{R}} = \eta_{\mathrm{s}} \left[1 + \frac{\pi}{2}\left(\frac{nRTa}{S}\right)(N-1)^2\right], \tag{3.18}$$

where S is the Hookean spring constant and a is the bead radius. η_{R} is also independent of shear rate meaning that the Rouse model does not capture shear-thinning effects.

The Zimm model (Zimm, 1956) is similar to the Rouse model but also includes the hydrodynamic forces acting on each bead due to all the other beads in the chain. Like the Rouse model there is a spectrum of relaxation times but we shall only consider the longest relaxation time which is given by:

$$\lambda_{\mathrm{Z}} = \left(\frac{1}{\zeta(3\nu)}\right) \lambda_{\mathrm{OB}_1}, \tag{3.19}$$

where ζ is a function of ν, the exponent characterizing the scaling of the radius of gyration of a polymer chain with the M_{v}, and which has the limiting values of $\nu = 0.5$ and $\nu = 0.6$ corresponding to a theta solvent and a good solvent respectively. Tirtaatmadja *et al.* (2005) show that $\nu \approx 0.55$ for dilute PEO solutions which gives $1/\zeta(1.65) = 0.463$.

3.4 Continuum models for polymer solutions

For sufficiently concentrated aqueous PEO solutions the rheological properties can be measured directly. From these measurements, semi-empirical models can be fitted to the data to describe the bulk properties of the fluids.

3.4.1 Carreau model

The viscosity of many polymer solutions is a function of the applied shear rate $\dot{\gamma}_{xy}$. Aqueous PEO solutions exhibit shear-thinning behaviour, where the viscosity $\eta(\dot{\gamma}_{xy})$ decreases as the applied shear rate $\dot{\gamma}_{xy}$ increases. This is illustrated in Fig. 3.3. For low concentrations of PEO, the shear rates

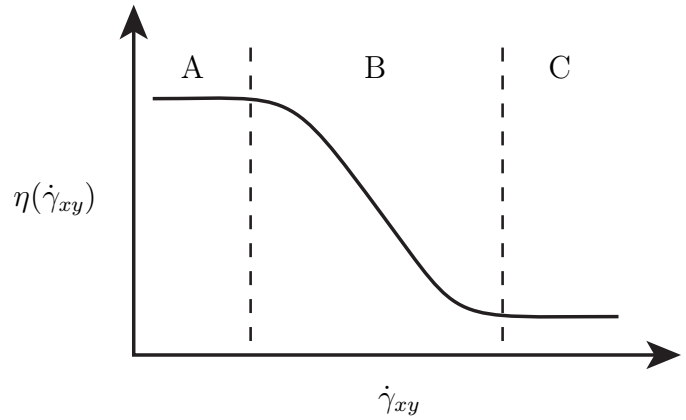

Fig. 3.3: Variation of solution viscosity $\eta(\dot{\gamma}_{xy})$ with shear rate $\dot{\gamma}_{xy}$ for a shear-thinning fluid: in region A, $\eta = \eta_0$ while in region B η falls as the shear rate increases. In region C the infinite shear viscosity η_∞ is reached.

over which the solution viscosity is constant (region A) can extend up to $\dot{\gamma}_{xy} = O(10^3\ \mathrm{s}^{-1})$ while for more concentrated PEO solutions shear-thinning (region B) can start at $\dot{\gamma}_{xy} = O(1\ \mathrm{s}^{-1})$. In region C the asymptotic viscosity at very high shear rates η_∞ is reached. For dilute PEO solutions this is taken to be zero (Bird *et al.*, 1987*a*).

Shear-thinning behaviour can be described using the semi-empirical Carreau model (Carreau, 1972) which gives describes η as a function of $\dot{\gamma}_{xy}$:

$$\frac{\eta - \eta_\infty}{\eta_0 - \eta_\infty} = \left[1 + (a\dot{\gamma}_{xy})^2\right]^{-b}. \tag{3.20}$$

The coefficients a and b are found by fitting Eq. (3.20) to experimental data.

3.4.2 Linear viscoelastic modelling

In the limit of small changes of displacements the relationship between the stress and the strain for any rheological behaviour can be represented analytically by a system of linear partial differential equations (Bird *et al.*, 1987*a*). Such representations can be considered to consist of Hookean spring and Newtonian dashpot elements arranged in various combinations. For example, considering the two limiting cases, the relationship between the stress and the strain in a perfect elastic solid can be modelled by a Hookean spring, while in a perfect fluid the relationship between stress and strain can be modelled by a dashpot (see Fig. 3.4). Any behaviour between these two extremes can be reduced to two equivalent canonical forms: the generalized Maxwell

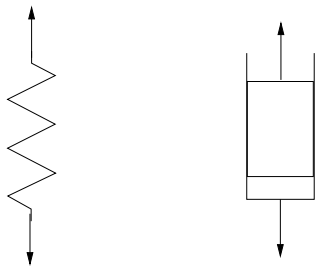

Fig. 3.4: Schematic representations of the relationship between the stress and strain for (a) a perfect solid and (b) a perfect fluid.

model and the generalized Kelvin model (Bird *et al.*, 1987*a*). As they are ultimately equivalent only the generalized Maxwell model will be presented here. The generalized Maxwell model consists of elementary units of a spring and a dashpot in series which are connected in parallel (see Fig. 3.5) and the shear stress $\sigma_{xy}(t)$ at time t is a function of the rate of deformation at all times $t' = [-\infty, t]$ and is written

$$\sigma_{xy}(t) = \sum_{i=1}^{n} \frac{\eta_i}{\lambda_i} \int_{-\infty}^{t} \exp\left[\frac{-(t-t')}{\lambda_i}\right] \dot{\gamma}_{xy}(t')\ dt', \tag{3.21}$$

for n basic units (modes) in parallel. The total solution viscosity η is given by the sum of η_i for $i = 1...n$, and the total solution relaxation time, λ, by the sum of λ_i for $i = 1...n$.

It is instructive to use this model to measure the response of a viscoelastic fluid to small amplitude oscillatory shear:

$$\gamma_{xy}(t') = \gamma_{xy0} \exp(\mathrm{i}\omega t'), \tag{3.22}$$

where γ_{xy0} is sufficiently small for linearity to apply. Substituting Eq. (3.22) into Eq. (3.21) the response of the fluid can be written as the function of the storage modulus G' and the loss modulus G'':

$$\sigma_{xy}(t) = (G' + \mathrm{i}G'')\gamma_{xy}(t). \tag{3.23}$$

The storage modulus is in phase with the applied shear and represents the solid-like behaviour of the material, while the loss modulus is $\pi/2$ rad out of phase with the applied shear and represents the fluid-like behaviour of the

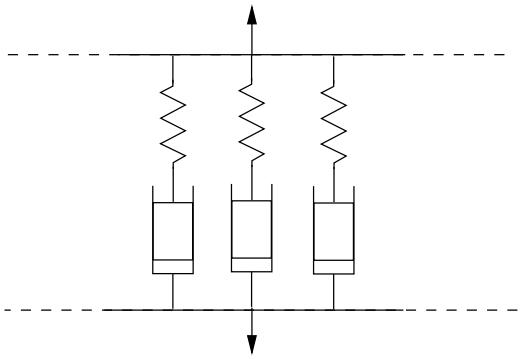

Fig. 3.5: Schematic representation of the generalized Maxwell model.

material. For linear oscillatory shear flow, the storage and loss moduli at the j^{th} frequency, G'_j and G''_j respectively, are written

$$G'_j = \sum_{i=1}^{n} \frac{\eta_i \lambda_i \omega_j^2}{1 + \omega_j^2 \lambda_i^2}, \tag{3.24}$$

$$G''_j = \sum_{i=1}^{n} \frac{\eta_i \omega_j}{1 + \omega_j^2 \lambda_i^2}, \tag{3.25}$$

with the total solution storage and loss moduli, G' and G'', equal to the sum of G'_i and G''_i respectively. η and λ can then be found numerically by finding the values of η_i and λ_i, for $i = 1...n$, which minimize the difference, χ^2, between the experimentally measured loss and storage moduli, $G'(\omega)$ and $G''(\omega)$, and those calculated for the generalized Maxwell model at j independent frequencies, $\omega_j, j = 1...m$:

$$\chi^2 = \left[\sum_{j=1}^{m} \left(G'(\omega_j) - G'_j\right)\right]^2 + \left[\sum_{j=1}^{m} \left(G''(\omega_j) - G''_j\right)\right]^2. \tag{3.26}$$

Eq. (3.26) is ill-posed and notoriously difficult to solve; several approaches are discussed in the literature (e.g. Syed Mustapha & Phillips, 2000; Jensen, 2002) although there is no 'fail safe' numerical technique. A simulated annealing algorithm similar to that of Jensen (2002) was used due to its relative insensitivity to initial estimates of the parameters and its ability to avoid generating non-physical negative values of η and λ.

3.4.3 Method of reduced variables

Polymer solution properties depend not only on the concentration of the solution but also on the temperature at which the measurements are performed. It is possible to collapse experimental data for different temperatures and concentrations however, using the method of reduced variables developed from empirical and theoretical considerations (Ferry, 1980; Tam & Tiu, 1989). Practically speaking, this technique allows a single set of data covering a wide range of variable space to be constructed from several smaller sets of data which individually cover smaller ranges of variable space. This is useful for improving the quality of data fitting and to have an understanding of how changes in parameters affect a range of concentrations instead of just one particular solution.

For viscosity data the reduced shear rate $\hat{\dot{\gamma}}_{xy}$ and reduced viscosity $\hat{\eta}$ are found using the following transformations:

$$\hat{\dot{\gamma}}_{xy} = \dot{\gamma}_{xy}\left[\frac{(\eta_0 - \eta_s)_T}{(\eta_{0\mathrm{ref}} - \eta_s)_{T_{\mathrm{ref}}}}\left(\frac{T_{\mathrm{ref}}}{T}\right)\right], \tag{3.27}$$

$$\hat{\eta} = \eta\left(\frac{\eta_{0\mathrm{ref}}}{\eta_0}\right), \tag{3.28}$$

where the subscript 'ref' corresponds to some reference data set with respect to which the data is reduced and the subscript T refers to values at temperature T.

Data from linear oscillatory measurements can also be treated in a similar manner. The reduced storage modulus $\hat{G}'$, the reduced loss modulus $\hat{G}''$ and the reduced oscillation frequency $\hat{\omega}$ are written

$$\hat{G}' = G'\left(\frac{M_{\mathrm{v}}}{c\widetilde{N}kT}\right), \tag{3.29}$$

$$\hat{G}'' = G''\left(\frac{M_{\mathrm{v}}}{c\widetilde{N}kT}\right), \tag{3.30}$$

$$\hat{\omega} = \omega\left[\frac{M_{\mathrm{v}}(\eta_0 - \eta_s)}{c\widetilde{N}kT}\right]. \tag{3.31}$$

3.5 Experimental techniques

3.5.1 Preparation of the solutions

To characterize the polymer solutions two stock solutions of approximately 0.002 g/ml and 0.015 g/ml were made by sprinkling the required quantity of

PEO on to the surface of the water and leaving it in a sealed container for 3 days at room temperature after which time it was visually homogenous. To ensure that the stock solution was homogenous it was gently stirred by hand and left for a further 24 hours. Different concentrations were then made by diluting the stock solutions with water and leaving for another 24 hours. Viscosity measurements on a test solution showed that after five days the stock solutions had lost the heterogenous 'network' effect seen in freshly prepared solutions (Hinch & Elata, 1979).

When mixing solutions for the cylinder flow facility, the installation was first filled with approximately 3 m^3 of water and a known mass of PEO was sprinkled on to the free surface of the tunnel. The 'sprinkling' effect was important to prevent agglomeration of the polymer which would give an inhomogeneous solution. The mixture was then left to dissolve and homogenize for five days, during which the pump was left running at 10 revolutions per minute which gave a freestream velocity of about 2 mms^{-1}. This promoted mixing but was sufficiently low to avoid mechanical degradation. The concentration of the solutions was calculated from the mass of PEO added to the mass of solvent and was checked by comparing the viscosity of the tunnel solution with a previously determined concentration-viscosity relationship (see Section 3.6.3).

3.5.2 Viscosity measurements

Two methods were used to measure the viscosity of the solutions. Firstly, Schott Ubelohde capillary tubes were used to measure solution viscosities for $c \in [0\ \text{g/ml}, 0.006\ \text{g/ml}]$ because of the high level of accuracy for solutions with shear rate independent viscosities fluids. A water bath was used to keep the solutions at a constant temperature to within ± 0.1°C during the measurements, which were performed at 8°C, 15°C and 25°C. The viscosity was found from the average of 10 measurements for each fluid at each temperature. The measurements for each data series typically agreed to within 0.2%.

For more concentrated solutions, $c \in [0.0025\ \text{g/ml}, 0.015\ \text{g/ml}]$, a Bohlin CVOR-150 rheometer with a double gap concentric cylinders apparatus was used in order to measure solution viscosities as a function of the applied shear rate. Measurements were performed in the shear rate range 0.01-150 s^{-1}, depending on the solution, and the solutions were held at a constant temperature to within ± 0.1°C using a water-jacket. Viscosities were measured at 5°C, 15°C and 25°C and the average viscosity-shear rate relationship was taken from 5 runs for each fluid and each temperature. Measurements typically

agreed to within 3% for solutions of 0.0025 g/ml with improved accuracy for more concentrated solutions.

For each solution used in the cylinder facility the viscosity was measured at several temperatures between 20°C and 25°C in order to determine the viscosity as an accurate function of the temperature. This was important in order to calculate the Reynolds number precisely.

3.5.3 Linear oscillatory measurements

The Bohlin CVOR 150 rheometer with a cone and plate setup of 60 mm diameter and 2° was used for oscillatory tests to measure G' and G'' in the frequency range 0.01–10 Hz at temperatures of 5° C, 15° C and 25° C for solutions in the concentration range $c \in [0.0075 \text{ g/ml}, 0.015 \text{ g/ml}]$. The normal stress difference N_1 was too small to be measured accurately.

The viscoelastic response as a function of the applied stress indicated that a stress magnitude $\sigma_{xy0} = 0.001$ Pa was within the approximations of linear deformation at 0.01, 0.1, 1 and 10 Hz. Therefore using this value for the applied stress, G' and G'' were measured as a function of the frequency and the average results were found from three series of measurements for each fluid at each temperature using a fresh sample for each measurement. The number of oscillation cycles used to calculate G' and G'' was adapted to the applied frequency. At high frequencies 10 cycles were used to give an accurate measurement while at low frequencies only half a cycle was used to avoid evaporation of the fluid due to the large times needed. A comparison between measurements performed starting at 10 Hz and decreasing the applied frequency and by starting at 0.01 Hz and increasing the applied frequency indicated that evaporation of the fluid did not noticeably affect the results.

3.6 Results

3.6.1 Solvent properties

The viscosity of water measured using a capillary viscometer was found to agree with standard tables for fresh water to within 1% over the temperature range 5–25°C. The density was taken to be equal to 1000 kg/m^3.

3.6.2 Intrinsic viscosity

Measurements with the capillary viscometer were used to find both the reduced and the inherent viscosities η_{red} and η_{inh}. The measurements were performed at 25°C to be close to the conditions of the tunnel and to enable comparison with other polymer data found at this temperature (Brandrup, 1989). Figure 3.6 shows that both η_{red} and η_{inh} are well described by a linear fit, each of which gives an estimate of $[\eta]_0$ and k' (see Eqs. (3.2) and (3.6)). The values found are shown in Table 3.2 and $[\eta]_0$ agrees well between both methods which indicates that the fitting hypotheses were justified. The intrinsic viscosity is also in fair agreement with the data from Tirtaatmadja *et al.* (2005) for PEO of $M_{\text{v}} = 10^6$.

The influence of shear-thinning on the capillary tube measurements can be estimated from the velocity profile for Poiseuille flow in a pipe of radius a. In cylindrical coordinates, where r and z are the radial and axial coordinates respectively, the velocity profile $u(r)$ and the shear rate in the capillary tube $\dot{\gamma}_{zr}(r)$ are written:

$$u(r) = \frac{\Delta P}{4\eta}(a^2 - r^2), \tag{3.32}$$

$$\dot{\gamma}_{zr}(r) = \frac{\mathrm{d}u_r}{\mathrm{d}r} = \frac{-2r\Delta P}{4\eta} = \frac{-2r\rho h g}{4\eta}, \tag{3.33}$$

where ΔP is the pressure drop between the ends of the pipe, the difference in height between the entrance and exit of the pipe h was 0.165 m and g is the acceleration due to gravity. The maximum shear rate occurs at the capillary wall where $r = a$. For example, a solution of 0.0002 g/ml with a kinematic viscosity of $\eta/\rho = 1.121$ cSt at 25°C measured using a capillary tube of radius $a = 0.53$ mm, measured this gives $(\dot{\gamma}_{zr})_{\max} = 382\ \text{s}^{-1}$. As will be shown in Section 3.6.3 this gives a good indication that shear-thinning in

Source	$[\eta]_0$ (ml/g)	k' (g/ml)
Reduced viscosity	520	0.40
Inherent viscosity	527	0.42
Tirtaatmadja *et al.* (2005)	572	-

Table 3.2: Values of $[\eta]_0$ and k' for water-PEO solutions at 25°C found from linear fits of Eqs. (3.2) and (3.6) as shown in Fig. 3.6. The value of $[\eta]_0$ given by Tirtaatmadja *et al.* (2005) for PEO $M_{\text{v}} = 10^6$ is shown for comparison.

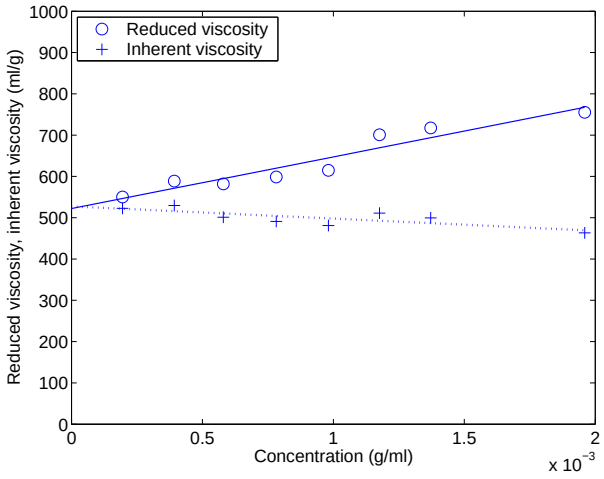

Fig. 3.6: The reduced viscosity η_{red} and the inherent viscosity η_{inh} as a function of polymer concentration c. The values found at $c = 0$ from the linear fits give estimates of the intrinsic viscosity $[\eta]_0$ (Eqs. (3.2) and (3.6)).

the capillary tube measurements was negligible and that the measured value of η is a close approximation of η_0.

Taking the average of the intrinsic viscosity found from the reduced and inherent viscosities $[\eta]_0 = 523.5$, Eq. (3.8) gives M_{v} equal to 1.03×10^6 g/mol using the constants given in Brandrup (1989) or 0.87×10^6 g/mol using the constants from Tirtaatmadja *et al.* (2005), both of which are in reasonable agreement with the value of 1×10^6g/mol quoted by the manufacturer. Using the criteria that polymer solutions are dilute for $[\eta]_0 c < 1$ (Eq. (3.10)), these solutions can therefore be considered dilute for concentrations of less than 0.0019 g/ml.

3.6.3 Viscosity

The solution viscosity as a function of the polymer concentration at 25°C is shown in Fig. 3.7. Viscosity measurements from both the capillary tubes and the double gap concentric cylinders techniques are presented and are in excellent agreement. For $c < 0.001$ g/ml the Oldroyd B model (see Eq. (3.12)):

$$\eta_{0_{\text{OB}}} = \eta_{\text{s}}(1 + 523c), \tag{3.34}$$

describes the increase in viscosity closely. The underestimation of the viscosity for $c > 0.001$ g/ml is expected because Eq. (3.34) does not use include the

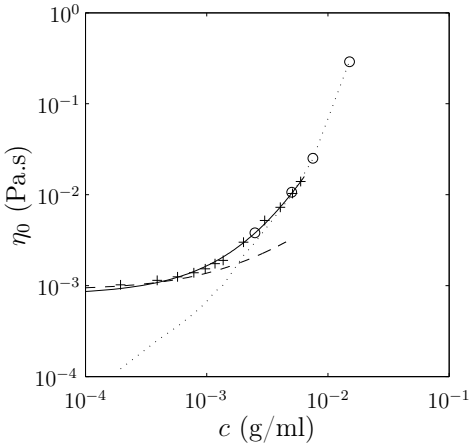

Fig. 3.7: Zero shear viscosity η_0 as a function of the polymer concentration c at 25°C. Symbols: + capillary viscometer; ∘ double gap viscometer; − − − Oldroyd B model Eq. (3.34); − power law fit Eq. (3.36); ··· 1 mode Maxwell model Eq. (3.35).

second order term that is used to find $[\eta]_0$ from Eqs. (3.2) and (3.6). The one-mode Maxwell model fitted to data from the linear oscillatory measurements (see Section 3.6.4):

$$\eta_{0_{\mathrm{M}}} = 1.02(\eta_0 - \eta_{\mathrm{s}}), \tag{3.35}$$

fits the data well for $c > 0.005$ g/ml. This is to be expected as the model was fitted to solutions with $c > 0.0075$ g/ml.

We can also establish an empirical relationship between the solution zero shear viscosity and the polymer concentration. Thus η_0 at 25°C for concentrations between 0.0003 g/ml and 0.006 g/ml is well represented by the power law:

$$c = 4.257 \times 10^{-2}(\eta_0)^{0.3549} - 3.377 \times 10^{-3}, \tag{3.36}$$

and Eq. (3.36) can be used to estimate the concentration of a solution with a known zero shear viscosity η_0.

The reduced shear rate $\hat{\dot{\gamma}}_{xy}$ and the reduced viscosity $\hat{\eta}(\hat{\dot{\gamma}}_{xy})$ from the double gap measuring apparatus, are shown in Fig. 3.8. The solution of concentration 0.015 g/ml at 5°C ($\eta_0 = 0.617$ Pa.s) was used as the reference data set and the data collapse well for the concentrations measured $c \in [0.0025\ \mathrm{g/ml}, 0.015\ \mathrm{g/ml}]$. There is some scatter at low shear rates because of the small forces involved.

Fitting a Carreau model (Eq. (3.20)) to the data in a least squares sense yields the coefficients $a = 0.642$ and $b = 0.0992$ and represents $\hat{\eta}(\hat{\dot{\gamma}}_{xy})$ well

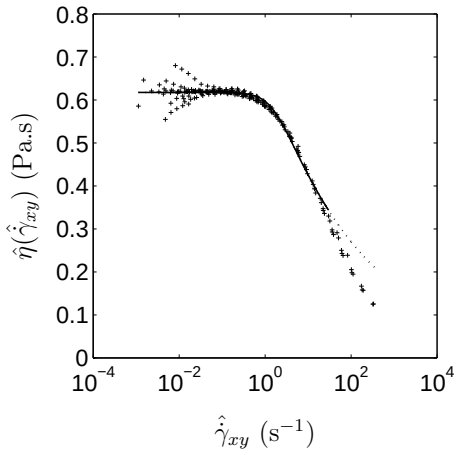

Fig. 3.8: Reduced viscosity $\hat{\eta}(\hat{\dot{\gamma}}_{xy})$ as a function of the reduced shear rate $\hat{\dot{\gamma}}_{xy}$ for temperatures $T = 5$–$25°C$ and concentrations $c = 0.0025$-0.015 g/ml. The reference data set used is $c = 0.015$ g/ml at 5°C. The Carreau model fit, (—) for $\hat{\dot{\gamma}}_{xy} < 30$ s^{-1} and $(\cdots)$ for $\hat{\dot{\gamma}}_{xy} > 30$ s^{-1}, is given by Eq. (3.37).

over reduced shear rates $\hat{\dot{\gamma}}_{xy} = 1$–$30$ s^{-1}. At higher shear rates the model overestimates the viscosity as shown by the dotted line in Fig. 3.8. The viscosity as a function of shear rate $\eta(\dot{\gamma}_{xy})$ for a PEO-water solution can be found by re-scaling the data for the temperature and η_0:

$$\eta(\dot{\gamma}_{xy}) = \eta_0 \left[1 + \left(1.04 \ (\eta_0 - \eta_s) \frac{278}{T} \ \dot{\gamma}_{xy} \right)^2 \right]^{-0.099} . \tag{3.37}$$

Using Eq. (3.37) the amount of shear-thinning undergone by a given solution with a known zero shear viscosity η_0 at a known shear rate $\dot{\gamma}_{xy}$ can be estimated.

3.6.4 Fluid relaxation time

The relaxation times for the Oldroyd B, Rouse and Zimm models are calculated from Eqs. (3.12), (3.17) and (3.19) respectively and are shown in Table 3.3. It is important to note that the relaxation times for these models are independent of the polymer concentration and due to the dilute solution assumption (Eq. (3.10)) are valid for solution concentrations of less than 0.0019 g/ml.

Solution relaxation times were also calculated by fitting the storage modulus G' and the loss modulus G'' to linear oscillatory strain measurements

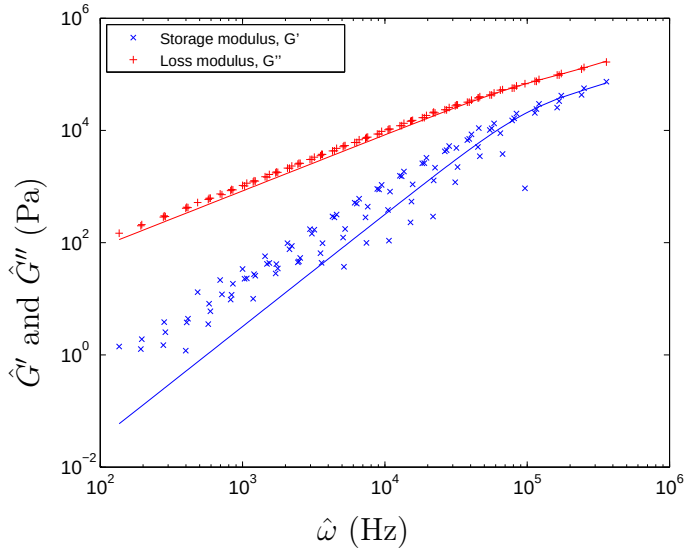

Fig. 3.9: Reduced storage and loss moduli for T=5–25°C and c = 0.0075–0.015 g/ml.

as explained in Section 3.4.2. Figure 3.9 shows the reduced storage modulus $\hat{G}'$ and the reduced loss modulus $\hat{G}''$ as a function of the reduced oscillation frequency $\hat{\omega}$ (see Eqs. (3.29)–(3.31)) for solutions of concentration 0.0075-0.015 g/ml measured in the temperature range 5–25°C. The data are reduced with respect to the solution with concentration $c = 0.015$ g/ml at a temperature of 5°C. The scatter in the storage modulus data is due to the extremely small forces measured and generally the degree of collapse is good.

The results obtained from fitting 1, 2, 3 and 4 mode Maxwell models to the whole normalized data set using a simulated annealing technique are presented in Table 3.4. Initially, as the number of modes i fitted to the data increases, 'useful' relaxation times λ_i and viscosities η_i are added. However, after a certain point, when higher modes are fitted the extra viscous and

Model	λ (s)
Oldroyd B	2.0×10^{-4}
Rouse	1.2×10^{-4}
Zimm	0.93×10^{-4}

Table 3.3: Micro-scale model relaxation times for dilute PEO-water solutions at 25°C.

	Number of modes fitted:			
	1	2	3	4
λ_1 (s^{-1})	1.60×10^{-6}	7.65×10^{-6}	1.71×10^{-5}	1.71×10^{-5}
η_1 (Pa.s)	0.65	0.39	0.23	0.23
λ_2 (s^{-1})	–	4.43×10^{-7}	3.44×10^{-6}	3.44×10^{-6}
η_2 (Pa.s)	–	0.44	0.32	0.32
λ_3 (s^{-1})	–	–	7.90×10^{-20}	5.65×10^{-17}
η_3 (Pa.s)	–	–	0.33	0.16
λ_4 (s^{-1})	–	–	–	1.34×10^{-15}
η_4 (Pa.s)	–	–	–	0.17
λ_{total} (s^{-1})	1.60×10^{-6}	8.09×10^{-6}	2.05×10^{-5}	2.05×10^{-5}
η_{total} (Pa.s)	0.65	0.84	0.88	0.88

Table 3.4: 1, 2, 3 and 4 mode Maxwell model relaxation times and viscosities fitted to the reduced data in Fig. 3.9.

elastic pairs consist of negligible components and increasing the number of modes further results in spurious values, for example when an additional mode is more important than the first mode. In Fig. 3.9 the three mode model is shown for comparison with the experimental data and fits the data well at high frequencies. However, fitting to the complete range of data tends to bring a good quality fit for high frequencies, but a lower quality fit to the lower end of the frequency range. Figure 3.10 shows the lower two decades of oscillatory data fitted with a one mode model, with $\lambda_1 = 1.05 \times 10^{-5}$ s and $\eta_1 = 1.02$ Pa.s, which represents the reduced loss modulus and reduced storage modulus in this region well. Therefore using the relationships (3.29)–(3.31) to re-scale the Maxwell relaxation time λ_{M} and viscosity η_{M}, this one mode model gives:

$$\lambda_{\text{M}} = 1.05 \times 10^{-5} \left(\frac{M(\eta_0 - \eta_s)}{cRT} \right), \tag{3.38}$$

$$\eta_{\text{M}} = 1.01 \left(\eta_0 - \eta_s \right). \tag{3.39}$$

As can be seen from Eq. (3.38), the relaxation time is dependent on solution concentration, unlike the Oldroyd B and Rouse models, with lower relaxation times for lower values of η_0. To estimate the quality of the Maxwell model,

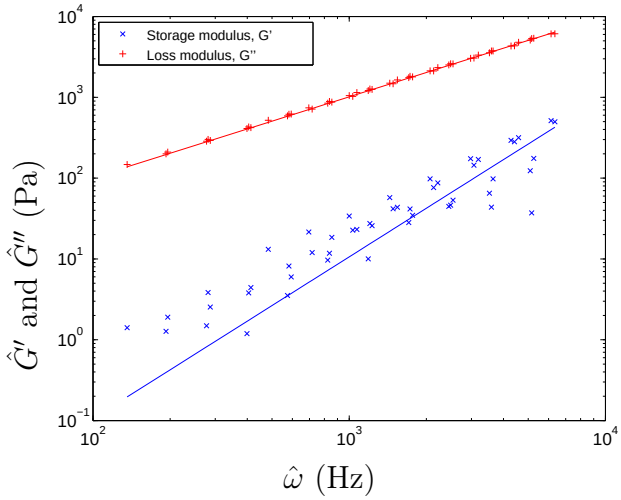

Fig. 3.10: Reduced storage and loss moduli for T=5–25°C and $c = 0.0075$–0.015 g/ml for reduced frequency range $\hat{\omega} \in [10^2 \text{ Hz}, 10^4 \text{ Hz}]$.

one can examine how well Eq. (3.39) models the solution viscosity. However we can quickly see from Eq. (3.39) that the one mode model is applicable only where $\eta_0 - \eta_s \approx 1/1.02$ which suggests a concentration rage of 0.005–0.01 g/ml at 25°C. This is expected because the Maxwell model is fitted to data over this range. λ_M for a concentration of 0.003 g/ml is equal to 4.25×10^{-3} s which is an order of magnitude greater than the relaxation times predicted by the bead-spring models. However because the Maxwell model represents the viscosity poorly at low concentrations it is hard to justify the use of λ_M at lower concentrations. Therefore, in the following work, the Zimm relaxation time will be used because it is considered to be based upon the most accurate hydrodynamic model.

3.7 Summary

The measuring techniques used to characterize the PEO-water solutions are appropriate as they show a high level of agreement with each other for a wide range of concentrations, temperatures, shear rates for the viscosity data and frequencies, temperatures and concentrations for the oscillatory data. This is supported by the good level of agreement with estimates of $[\eta]_0$ from other work and the molecular weight is found to be near the manufacturers quoted value.

The Carreau model fitted to the viscosity-shear rate data gives an accurate description of the data for reduced shear rates of less than 30 s^{-1} and can be used to estimate the level of shear-thinning. The Oldroyd B model is seen to represent the viscosity-concentration behaviour well at concentrations lower than 0.001 g/ml. For more concentrated solutions a single mode Maxwell model fitted to linear oscillatory data provides an accurate relationship between viscosity and concentration, but is not representative of the polymer solutions at concentrations below 0.005 g/ml. This is to be expected because the model was derived from more concentrated solutions.

Quantifying the fluid elasticity is notoriously tricky for low viscosity dilute polymer solutions. After fitting a multi-mode Maxwell model to linear oscillatory measurements it can be seen that more accurate results are possible by fitting a relevant, smaller portion of the data with a single mode. However the data are still poorly fitted below $c = 0.005$ g/ml. The Oldroyd B, Rouse and Zimm models all give relaxation times that are of the same order. For dilute polymer solutions the Zimm model offers the most accurate hydrodynamic model of a polymer solution (although arguably this does not necessarily mean that it should give the most representative λ) and is commonly used elsewhere in the literature (Tam & Tiu, 1989; Tirtaatmadja *et al.*, 2005). Therefore $\lambda_Z = 0.93 \times 10^{-4}$ will be used in the following work.

Chapter 4

Experimental set up

The presentation of the experimental set up is divided into two parts. The first section introduces and characterizes the new LMF experimental facility for studying the cylinder wake and the second section describes the measuring techniques used to study the cylinder wake.

4.1 Test facility

4.1.1 Overview

A closed-loop tunnel with a volume of 3 m^3 was used to investigate the cylinder wake; a plan view of the installation is shown in Fig. 4.1. The test section of height $H = 200$ mm, width $W = 150$ mm and length equal to 600 mm was equipped with a 'chimney' to provide access to the test section with the tunnel filled. In front of the test section a parabolic contraction with an area ratio of 12:1 was used to reduce the boundary layer thickness and decrease the relative magnitude of streamwise velocity fluctuations in the freestream. A false ceiling sitting flush with the test section upper wall was inserted through the chimney to eliminate the free surface and change in boundary layer in the test section. Here and in the following the 'outside' test section wall refers to the wall that is on the exterior part of the loop, while the 'inside' test section wall refers to the wall that is on the interior part of the loop.

Grids were placed at the pump exit to inhibit the formation of large flow structures and prevent their intermittent separation, as well as after the two elbows preceding the test section to smooth out irregularities in the velocity profile. A honeycomb after the test section prevented swirl from the pump affecting the flow upstream.

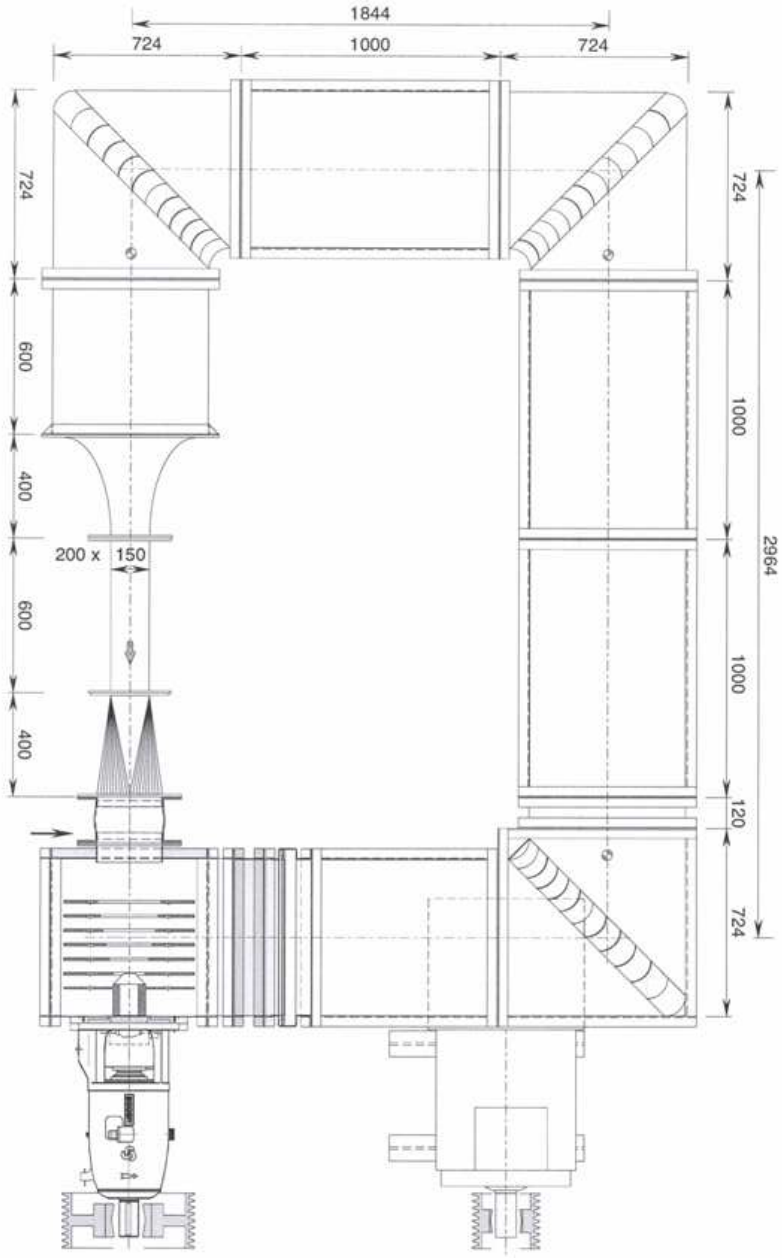

Fig. 4.1: Plan view of the hydrodynamic loop (fluid circulates in the anti-clockwise direction). The test-section is in the centre at the bottom and the pump is in the bottom right hand corner. All dimensions are in mm.

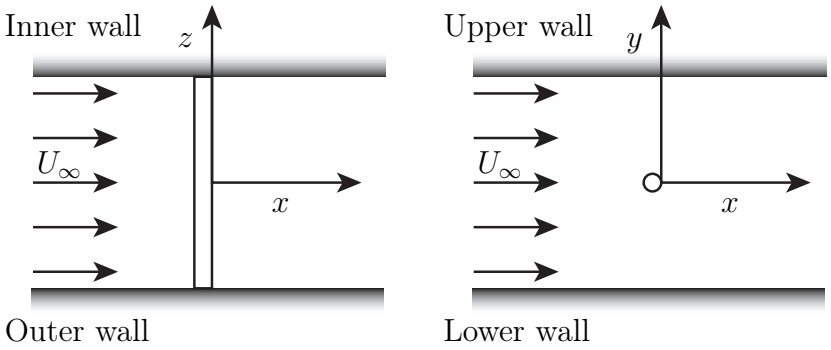

Fig. 4.2: Plan view (left) and side view (right) of the cylinder in the test section showing the location of the origin.

To avoid mechanical degradation of the polymer solutions a pump based on the design by Tesla (Tesla, 1913) was used. This type of pump employs rotating flat discs to entrain the fluid, the absence of blades reducing the shear rates applied to the fluid as it passes through the pump.

The plan view and side view sketch of the test section in Fig. 4.2 illustrates the location of the axes used in this work. The streamwise coordinate x is positive in the downstream direction, the transverse coordinate y is positive in the 'up' direction and the spanwise coordinate z is positive pointing from the outer to inner wall. The origin $(x, y, z) = (0, 0, 0)$ is located on the centreline at the trailing edge of the cylinder and at the midspan of the cylinder length.

4.1.2 Test section flow quality

Velocity profiles for the empty test section were measured using laser Doppler anemometry (LDA). The aim was to have a 'top-hat' velocity profile, i.e. a uniform velocity across the central region with thin boundary layers at the walls, and low free stream turbulence in the part of the test section containing the cylinder.

Freestream velocity, U_∞

Freestream velocity profiles for the empty test section measured in the vertical centre-plane at $z = 0$ mm, $x = -18$ mm are shown in Fig. 4.3. Across the central part of the test section U_∞ was constant to within 1% for all fluids at all speeds. There is a small mean transverse velocity of the order of $0.01U_\infty$

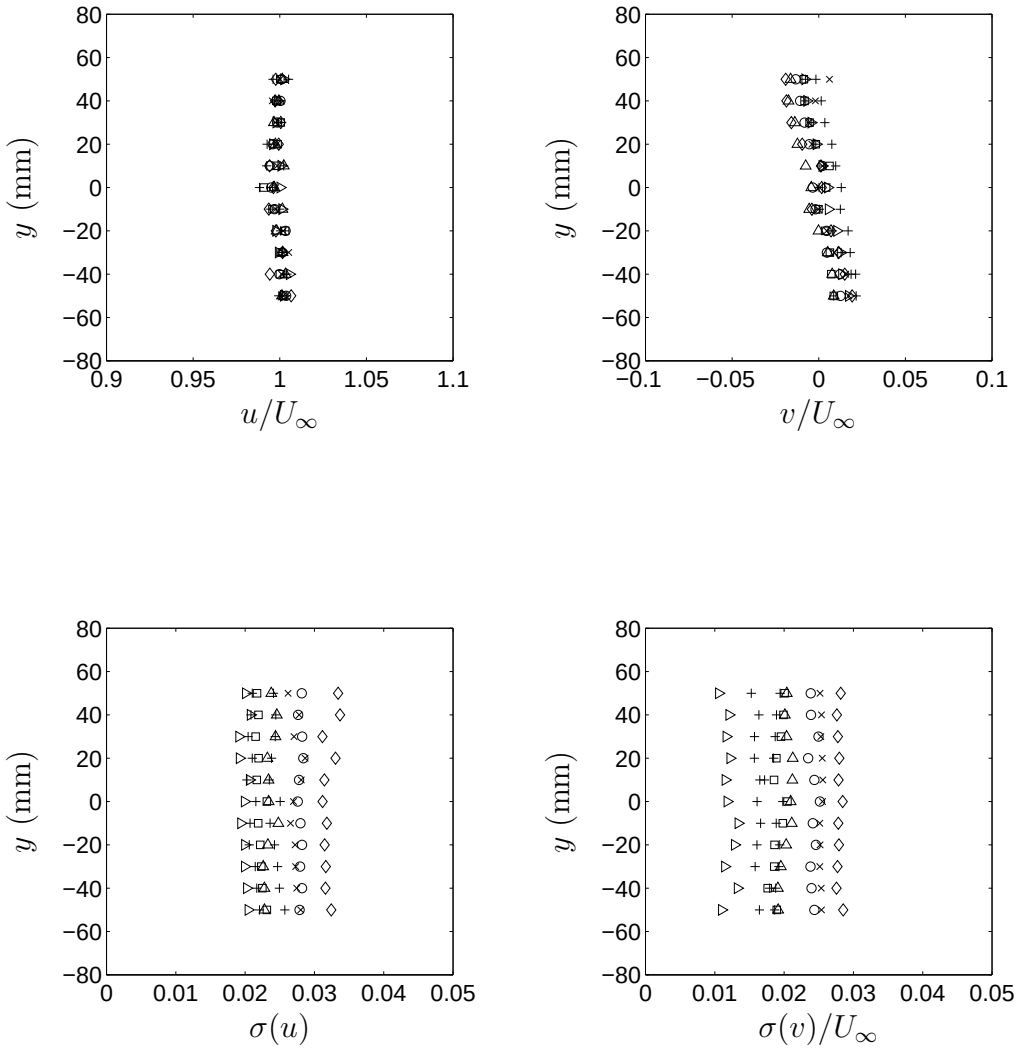

Fig. 4.3: Velocity profiles for the empty test section at $x = -18$ mm and $z = 0$ mm. Symbols: $\times$ water, $U_\infty = 0.015\,\mathrm{ms}^{-1}$; + water, $U_\infty = 0.031\,\mathrm{ms}^{-1}$; $\Diamond$ PEO 1000, $U_\infty = 0.034\,\mathrm{ms}^{-1}$; $\Box$ PEO 1000, $U_\infty = 0.083\,\mathrm{ms}^{-1}$; $\circ$ PEO 1500, $U_\infty = 0.049\ \mathrm{ms}^{-1}$; + PEO 1500, $U_\infty = 0.082\ \mathrm{ms}^{-1}$; $\triangle$ PEO 2900, $U_\infty = 0.055\ \mathrm{ms}^{-1}$; $\triangleright$ PEO 2900, $U_\infty = 0.114\ \mathrm{ms}^{-1}$.

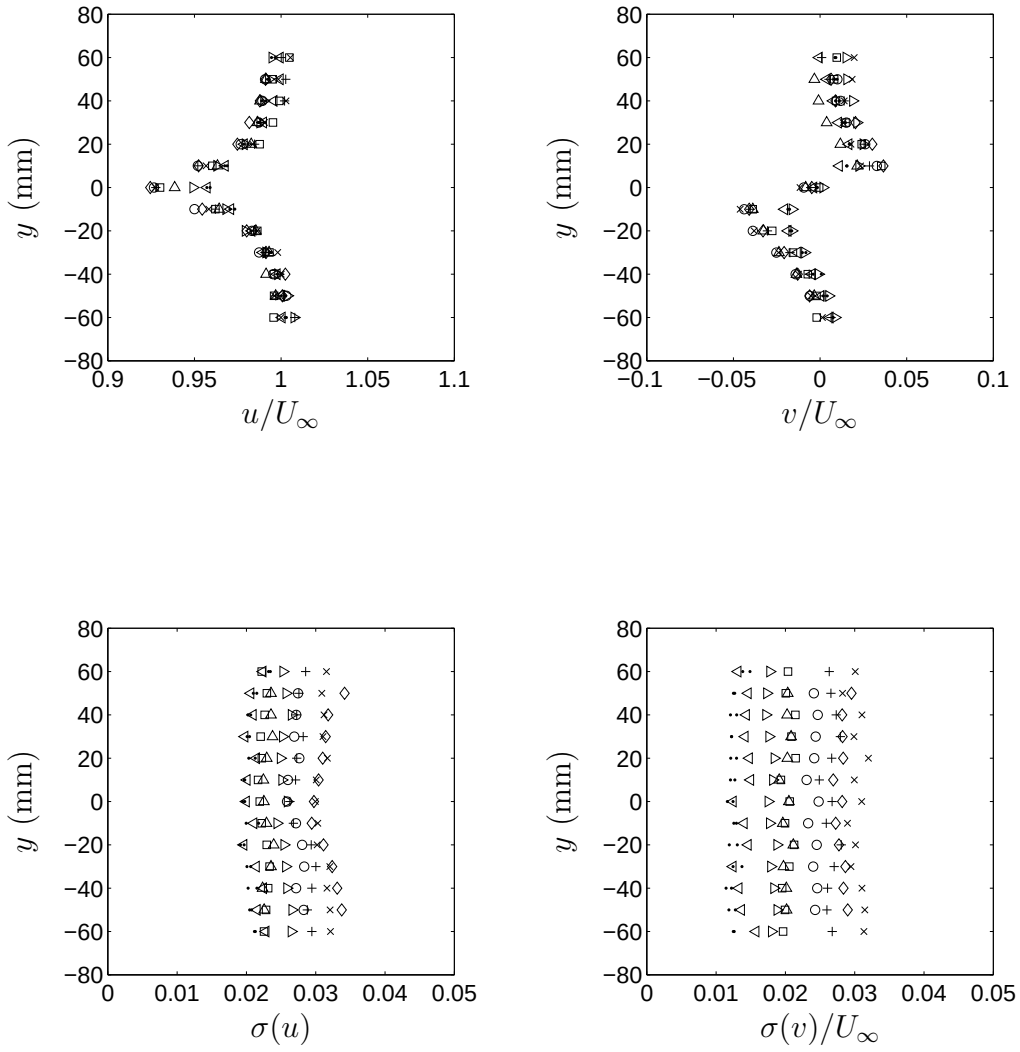

Fig. 4.4: Velocity profiles for the test section with the cylinder in place at $x = -18$ mm and $z = 0$ mm. Symbols: $\times$ water, $U_\infty = 0.015$ ms^{-1}; $+$ water, $U_\infty = 0.031$ ms^{-1}; $\Diamond$ PEO 1000, $U_\infty = 0.034$ ms^{-1}; $\square$ PEO 1000, $U_\infty = 0.083$ ms^{-1}; $\circ$ PEO 1500, $U_\infty = 0.049$ ms^{-1}; $+$ PEO 1500, $U_\infty = 0.082$ ms^{-1}; $\triangle$ PEO 2900, $U_\infty = 0.055$ ms^{-1}; $\triangleright$ PEO 2900, $U_\infty = 0.114$ ms^{-1}; $\triangleleft$ PEO 2900, $U_\infty = 0.150$ ms^{-1}.

towards the centre of the tunnel. This is because the velocity field has not yet quite recovered after the contraction at the entrance of the test section. The freestream turbulence components $\sigma(u)/U_\infty$ and $\sigma(v)/U_\infty$ are constant across the centre of the test section and less than 3% although the intensity decreases with increasing tunnel speed. Most of the spectral content was concentrated in the frequency range 0.01–0.1 Hz.

Velocity profiles at the same location with the cylinder and end-plates in the test section (4.4) also collapse independently of tunnel speed and polymer concentration. The mean streamwise and transverse components are clearly affected by the presence of the cylinder even at this upstream location. There is a small dip in $\sigma(u)/U_\infty$ at the centre of the test section in front of the cylinder, but apart from this the freestream turbulence is unchanged.

Boundary layers

The velocity boundary layer thickness, δ, was found from velocity measurements close to the test section walls, where δ is defined as the distance normal to the wall at which the velocity is equal to $0.99U_\infty$. Streamwise and transverse velocity profiles are shown in Fig. 4.5 for the outer and inner side wall boundary layers in the horizontal centre-plane at three streamwise locations for water. The measurements were made at a Reynolds number of 45 based on the cylinder diameter and, given the change in velocity profile with x, suggest that the boundary layer measured upstream is representative of the boundary layer at the cylinder. The value of δ at this Reynolds number was the maximum used ($\delta_{\max}$) and was approximately 30 mm for the vertical test section walls. Therefore, in order to minimize the influence of the side wall boundary layers on the experiments, a distance of $1.5\delta_{\max}$ was left between the test section side walls and the region of the cylinder span investigated, giving an effective cylinder length of 60 mm.

At higher Reynolds numbers the boundary layer thickness decreases and the dependance of δ on Re for water is shown in Fig. 4.6. We see that for a given location

$$\delta \propto \frac{1}{\sqrt{U_\infty}},$$

which is what one would expect for a laminar boundary layer Schlichting (1968). Figure 4.6 also shows that δ was 2–3 mm larger on the test section wall on the inside of the loop than the test section wall on the outside of the loop.

Velocity measurements near the top and bottom walls at $x = -15$ mm, $z = 0$ mm are presented in Fig. 4.7. The data were measured further away from the wall than for the side wall boundary layers to avoid obstructing the

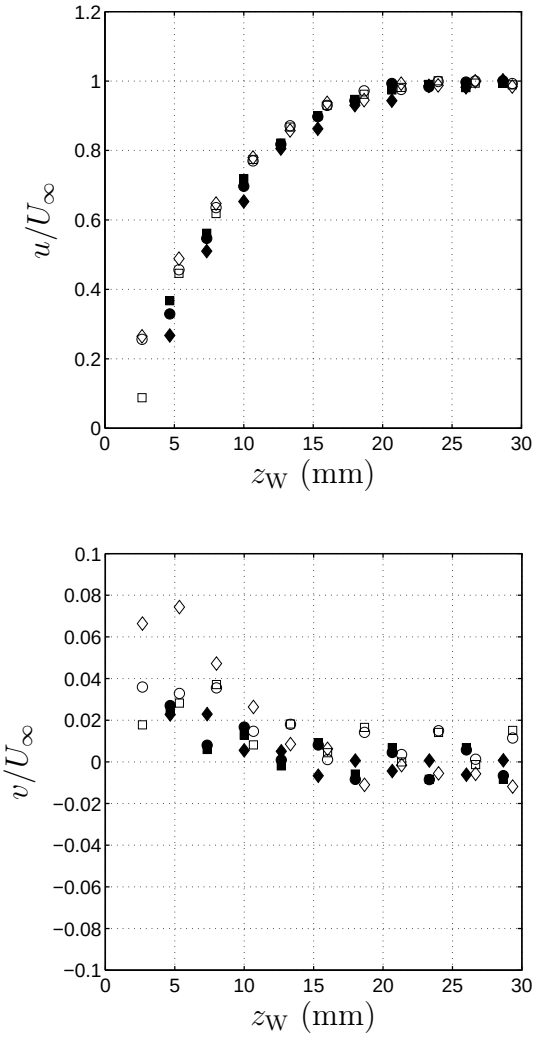

Fig. 4.5: Streamwise and transverse velocities u/U_∞ and v/U_∞ as a function of the distance from the wall z_W ($z_W = W/2 - z$ for the inner wall and $z_W = W/2 + z$ for the outer wall). Measurements are for water at $y = 0$ mm and $U_\infty = 0.012$ ms^{-1} for the empty test section. Symbols: $\Diamond$ $x = -21$ mm; $\Box$ $x = -42$ mm; $\circ$ $x = -63$ mm where empty symbols represent the outside wall boundary layer and filled symbols the inner wall boundary layer.

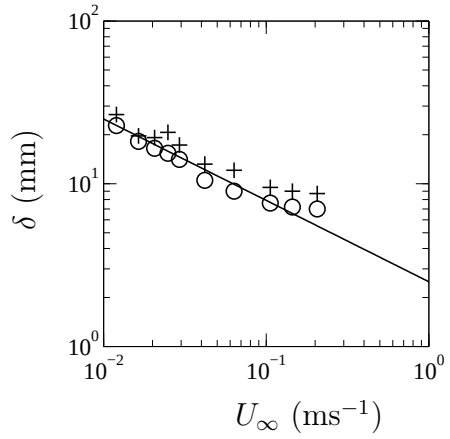

Fig. 4.6: δ as a function of U_∞, outer wall, $\circ$; inner wall, $+$. The straight line is proportional to $U_\infty^{-0.5}$.

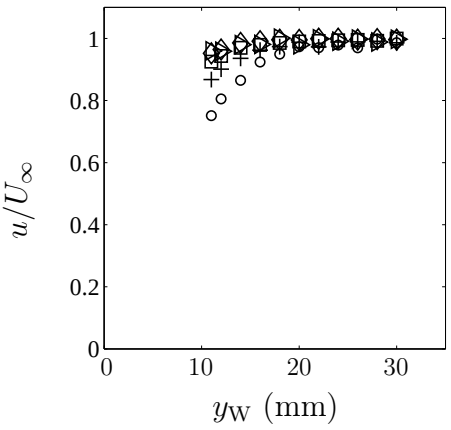

Fig. 4.7: Streamwise velocity u/U_∞ as a function of the distance from the upper wall $y_W = H/2 - y$ measured at $z = 0$ mm, $x = -15$ mm for the empty test section. Symbols: $\circ$ $U_\infty = 0.015$ ms^{-1}; $+$ $U_\infty = 0.019$ ms^{-1}; $\square$ $U_\infty = 0.024$ ms^{-1}; $\Diamond$ $U_\infty = 0.031$ ms^{-1}; $\triangleright$ $U_\infty = 0.035$ ms^{-1}.

LDA beams for the vertical velocity component. $\delta_{\max}$ was also 30 mm for the top and bottom walls and the boundary layer had a displacement thickness,

δ^*, defined as:

$$\delta^* = \int_0^\infty \left(1 - \frac{u}{U_\infty}\right) dy,$$

equal to 8 mm. Using δ^*, the effective blockage ratio for the test section with the cylinder b_{eff} can be calculated:

$$b_{\text{eff}} = \frac{d}{H - 2\delta^*}.$$

The maximum value of b_{eff} was 0.0163, corresponding to just a Reynolds number based on the cylinder diameter of 50. At the highest U_∞ of 0.2 ms^{-1}, b_{eff} was reduced to 0.0156.

4.1.3 Cylinder setup

The stainless steel cylinder of diameter $d = 3$ mm was aligned normal to U_∞ in the horizontal centre plane of the test section and situated 100 mm downstream of the test section entrance. The cylinder spanned the width of the test section although its effective length L, taken as the distance between the end cylinders (see below), was 60 mm giving an effective aspect ratio, L/d, of 20. The alignment of the cylinder with the freestream was assured via an adjustable mounting on the side wall.

In general, small asymmetries in the boundary conditions mean that parallel vortex shedding does not occur naturally behind a cylinder. A variety of techniques have been proposed to manipulate the cylinder ends to induce parallel vortex shedding, including angled end plates (Williamson, 1988*a*), transverse upstream cylinders (Hammache & Gharib, 1989), and end cylinders in combination with end plates (Eisenlohr & Eckelmann, 1989).

For these experiments the best method to produce parallel shedding was found to be a combination of end cylinders of diameter $d_e = 1.5d$ and length 15 mm and Plexiglas end plates of length $10d$ and thickness 1 mm. The end plates were positioned immediately downstream and at the mid-span of the end cylinders and were angled slightly outwards with $\theta_1, \theta_2 \in [0°, 2°]$, as shown in Fig. 4.8. In practice this meant fixing one end plate and making small adjustments to the angle of the other until parallel shedding was observed. The end plates were held in position from above using stainless steel supports 1 mm thick by 5mm wide and this set up did not create any measurable asymmetry in the upstream velocity profile about the centre-plane as can be seen in Fig. 4.4.

The above technique for imposing parallel vortex shedding was evaluated by comparing the Strouhal–Reynolds number relationship with that obtained

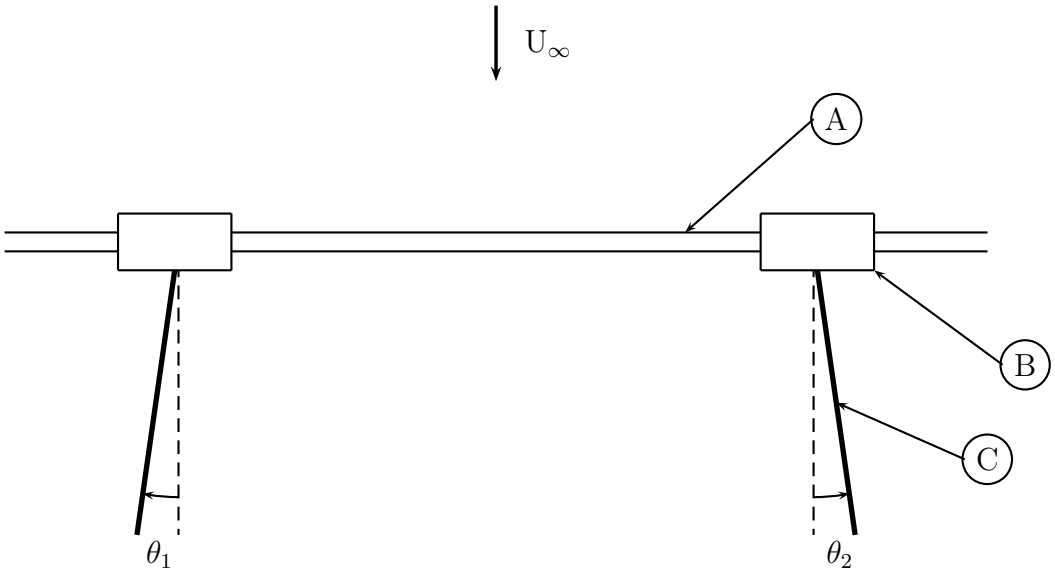

A - Cylinder, $d = 3$mm
B - End-cylinder, $d_e = 4.5$mm
C - End-plate, length = 30 mm

Fig. 4.8: Schematic of cylinder set up.

for two additional cases: firstly, end plates positioned downstream of the main cylinder and aligned at $\theta_1 \approx \theta_2 \approx 12^\circ$ but with no end cylinders, as described in Williamson (1988*a*), and secondly end plates positioned in front of the main cylinder and aligned at $\theta_1 \approx \theta_2 \approx 2^\circ$, again with no end cylinders (after Hammache & Gharib, 1989). The Strouhal–Reynolds number relationship was identical for all three configurations implying that the end cylinders did not alter the shedding frequency, but more fine-tuning was required to achieve parallel shedding for the techniques without end cylinders.

4.2 Measuring apparatus

4.2.1 Hydrogen bubble wire

Hydrogen bubbles were used to perform flow visualizations of the cylinder wake to check that the vortices were shed parallel to the cylinder. The bubbles were created by electrolysis, which separates water into hydrogen at a cathode and oxygen at an anode. A stretched stainless steel wire with a diameter of 70 μm and length of 50 mm served as the cathode and the

anode was a block of graphite placed after the pump, far downstream of the test section. Using an insulated brass sting, the hydrogen bubble wire was held parallel to the cylinder axis $5d$ downstream of the cylinder to avoid interfering with the attached shear layers and the mean recirculation region which are both important in the development of vortex shedding from a bluff body (Griffin, 1995).

A potential difference of 15 V between the cathode and the anode created sufficient bubbles and no salt was added to improve the conductivity of the solutions as this would change the properties of the polymer solutions (Tam & Tiu, 1989). The visualizations were clearest when the bubble wire was held slightly above the centre plane of the cylinder and injected bubbles into only one half of the vortex street.

4.2.2 Laser Doppler Anemometry

A Dantec Dynamics two component laser Doppler anemometry (LDA) system was used to measure flow velocities in the test section. The beams were focussed using a 310 mm achromatic lens which gave a measuring volume 75 μm in diameter and 0.63 mm long. A motorized traverse was used to move the LDA optical head along the x-, y- and z-axes with an accuracy of 0.1 mm in combination with a manual rotational degree of freedom about the y-axis. A comprehensive overview of the theoretical and practical aspects of LDA is provided by Durst *et al.* (1976).

The LDA signal for each velocity component was processed by a Dantec Burst Analyzer and the processed data were sent to a computer for analysis and storage. The flow was seeded with 5 μm diameter PPE particles (density $=$1005 kg/m^3) also supplied by Dantec Dynamics and enough were added to give a data rate between 10 and 20 Hz.

To verify that enough bursts were used in calculating the mean velocity $\bar{u}$ and the standard deviation $\sigma(u)$ a test was performed to examine their convergence for 5000 bursts. Fig. 4.9 shows that $\bar{u}$ converges to within less than 0.5% of the mean value for 5000 bursts after only 1000 bursts while $\sigma(u)$ needs 4000 bursts to converge to within 1% of the standard deviation for 5000 bursts.

In order to measure v very close to the trailing edge of the cylinder, the laser head was rotated about the y-axis by 10°. Due to the unequal optical path of the horizontal velocity component beams, measurements for u could not be performed at the same time.

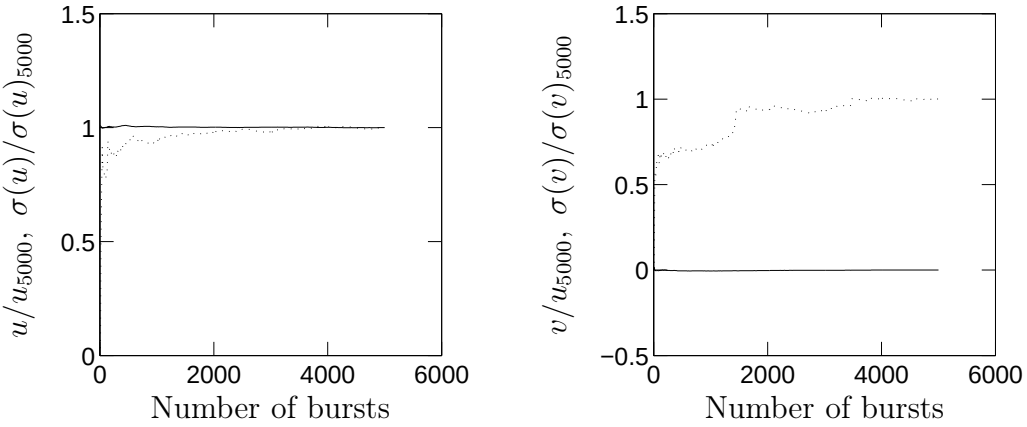

Fig. 4.9: Left: convergence of the mean streamwise velocity to the value after 5000 bursts u/u_{5000} $(-)$ and the standard deviation to the value after 5000 bursts $\sigma(u)/\sigma(u)_{5000}$ $(\cdots)$. Right: convergence of the mean transverse velocity v/u_{5000} $(-)$ and the standard deviation $\sigma(v)/\sigma(v)_{5000}$ $(\cdots)$ with increasing number of bursts.

4.2.3 Hot film Anemometry

The signal from a TSI Model 1054 Constant Temperature Anemometer connected to a 1210-20W hot film probe placed in the cylinder wake was used to measure vortex shedding frequencies as well as to provide the wake signal for the phase-averaged PIV technique. Details on the technical aspects of hot film anemometry can be found in Bruun (1995).

The hot film probe was inserted into the cylinder wake $10d$ downstream of the cylinder to avoid interfering with the formation of the cylinder wake and to get a clean and accurate signal, as discussed by Paranthoën *et al.* (1999). The signal was low pass filtered at 20 Hz to remove high frequency noise and recorded for 1800 s at a sampling rate of 512 Hz with a National Instruments data acquisition card, well above the Nyquist frequency of the vortex shedding which was in the range 0.75–10 Hz. The wake frequency was calculated by FFT after dividing the wake signal into records of 30000 samples with 50% overlap and multiplying each record with a Hanning window. The frequency resolution was better than 0.007 Hz and the power spectrum was found by averaging over all the records.

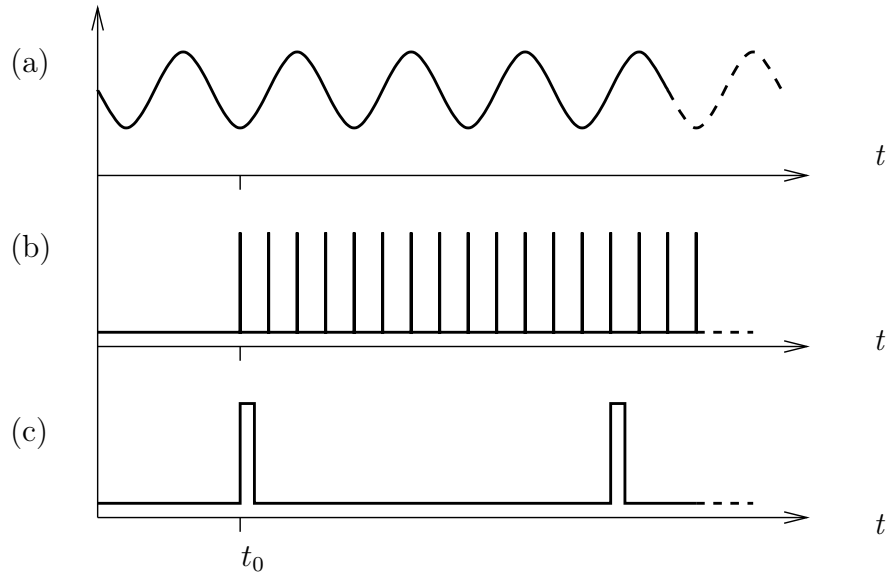

Fig. 4.10: Synchronization of signals for phase averaged PIV; (a) wake signal from hot film, (b) TTL signal at 10Hz triggering camera and (c) image pair recording time signal.

4.2.4 Particle Image Velocimetry

Cross-correlation particle image velocimetry (PIV) was used to measure the velocity field in the cylinder wake and in order to obtain information over the entire vortex shedding cycle a phase-averaging technique was used.

Set up

The same laser and camera set up was used as that described in Ursenbacher (2000). A twin pulsed Nd-Yag laser from Quantel was used to create two light sheets in quick succession with the time between the two, Δt, set between 0.001 s and 0.01 s, depending on U_∞. The flow was seeded with 20 μm diameter PPE particles supplied by Dantec Dynamics and enough were added to obtain approximately 10 particles in each PIV processing interrogation window (Keane & Adrian, 1990). A Kodak Megaplus ES1.0 camera running in triggered double exposure mode was used to capture pairs of images which were then processed using MATLAB and the MatPIV code for MATLAB developed by J.K. Sveen (Sveen, 2004).

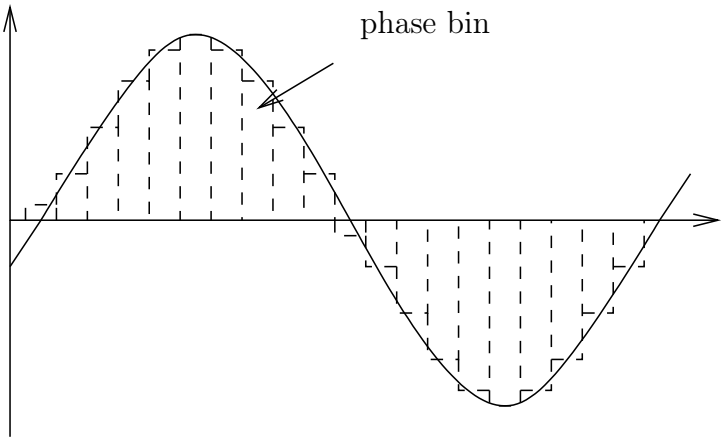

Fig. 4.11: Division of the vortex shedding cycle into the phase bins used for phase averaged PIV.

Phase-averaging technique

The following signals, illustrated in Fig. 4.10, were recorded to perform the phase-averaging:

(a) The hot film signal from the cylinder wake, recorded on a PC at 512 Hz.

(b) The TTL signal used to trigger the camera at 1 Hz, also recorded on the same PC as in (a) and starting at time t_0.

(c) The time at which the image pairs from the camera were read by the computer which was different to the PC used to record signals (a) and (b), also starting at time t_0.

After the data were collected the three signals described above were aligned to match each image pair with the fluctuating wake signal. The phase position for each image pair could then be computed using the local wavelength which was found from the local zero crossing points of the wake signal. The vortex shedding cycle was divided into 20 phase bins, as shown in Fig. 4.11, and the average velocity field was found for each bin.

To estimate how many images per bin would be needed, a test was performed which showed that for images with a particle density of 10 particles per interrogation window, 100 image pairs were required in order for the

mean velocity for a phase bin to converge, which implies a total of at least $20 \times 100 = 2000$ image pairs to cover the whole cycle.

Image pre-treatment

The mean image was subtracted from all the images to reduce the effects of reflections, shadows and other artifacts which might be detrimental to the PIV treatment.

PIV analysis

More information on cross correlation PIV in general and the MatPIV code in particular can be found in Raffel *et al.* (1998) and Sveen (2004) respectively. The PIV processing used to analyze the cylinder wake and the test case discussed below included the following:

- multi-pass processing — each image pair was processed 3 times using interrogation windows of 64×64 px, 32×32 px and again 32×32 px, each time the displacements found were used to calculate the local offset of the interrogation windows for the next pass.
- 50% overlap of the interrogation windows in both the x and y directions giving a vector every 16 px.
- windowing — a 2-D cosine window was applied to each interrogation window before the FFT used in the cross correlation, as suggested in Ursenbacher (2000).
- filtering of the vector field by comparison with the median of the surrounding vectors — vectors considered to be false, commonly known as 'outliers', were recalculated by using a method equivalent to a Lagrangian cubic interpolation. For each analysis the outliers made up less than 10% of the vector field and had a homogenous spatial distribution.

Post-processing

A calibration image of evenly spaced lines was taken for each data series with the PIV camera *in situ* to calculate the optical distortion of the images due to the lens and perspective effects. Quadratic functions for the distortion in x as a function of x and y and the distortion in y as a function of x and y were found. These functions were used to displace the centres of the PIV vectors as well as to change the vector angles and magnitudes. This resulted

in non-monotonically spaced vector fields which were re-sampled on to an evenly spaced grid using the Matlab 'griddata' command, which is based on a Delaunay triangulation technique.

The following standard finite difference masks were used to calculate the vorticity field $\boldsymbol{\omega}$, shear rate field $\dot{\gamma}_{xy}$, and rate of extension field $\dot{\gamma}_{xx}$ from the PIV velocity field $\mathbf{u} = u\mathbf{e}_x + v\mathbf{e}_y$ (Raffel *et al.*, 1998):

$$\boldsymbol{\omega} = u\mathbf{e}_x * \frac{1}{8\Delta Y}\begin{bmatrix} -1 & -2 & -1 \\ 0 & 0 & 0 \\ 1 & 2 & 1 \end{bmatrix} + v\mathbf{e}_y * \frac{1}{8\Delta X}\begin{bmatrix} -1 & 0 & 1 \\ -2 & 0 & 2 \\ -1 & 0 & 1 \end{bmatrix}, \quad (4.1)$$

$$\dot{\gamma}_{xy} = u\mathbf{e}_x * \frac{1}{8\Delta Y}\begin{bmatrix} 1 & 2 & 1 \\ 0 & 0 & 0 \\ -1 & -2 & -1 \end{bmatrix} + v\mathbf{e}_y * \frac{1}{8\Delta X}\begin{bmatrix} -1 & 0 & 1 \\ -2 & 0 & 2 \\ -1 & 0 & 1 \end{bmatrix}, \quad (4.2)$$

$$\dot{\gamma}_{xx} = v\mathbf{e}_y * \frac{1}{8\Delta Y}\begin{bmatrix} 1 & 2 & 1 \\ 0 & 0 & 0 \\ -1 & -2 & -1 \end{bmatrix} + u\mathbf{e}_x * \frac{1}{8\Delta X}\begin{bmatrix} -1 & 0 & 1 \\ -2 & 0 & 2 \\ -1 & 0 & 1 \end{bmatrix}, \quad (4.3)$$

where $*$ indicates a convolution and ΔX and ΔY are the distance in x and the distance in y respectively between two neighbouring vectors.

Assessment of PIV algorithm

To estimate the errors inherent in the PIV analysis and to ensure that the algorithm was suitable, synthetic images of a velocity field with strain rates and displacements similar to those found in the cylinder wake were analyzed.

The test velocity field was a single vortex cell from a Taylor vortex array, Taylor (1923), an example of which is shown in Fig. 4.12. For a Taylor vortex array the stream function, $\Psi(x, y)$, is given by:

$$\Psi(x, y) = \Psi_0 \sin\left(\frac{\pi x}{d_T}\right) \sin\left(\frac{\pi y}{d_T}\right), \quad (4.4)$$

where Ψ_0 is the vortex strength and d_T the vortex diameter. Values of $d_T =$ 256 px and $\Psi_0 = 2048/\pi$ px^{2}s^{-1} were used, giving a maximum velocity of 8 pxs^{-1} between two images. The resulting peak vorticity was 0.196 s^{-1}, which corresponds closely to the vorticities encountered in the cylinder wake.

The series of 64 realistic synthetic image pairs measuring 256×256 px was created using the algorithm detailed in Ursenbacher (2000). The images had an average distribution of 10 particles per 32×32 px interrogation window, which was similar to the particle density in the images for the cylinder wake. After analysis with MatPIV, the mean velocity and vorticity fields for the 64 image pairs, $\bar{\mathbf{u}}_{\mathrm{PIV}}$ and $\bar{\boldsymbol{\omega}}_{\mathrm{PIV}}$, were calculated.

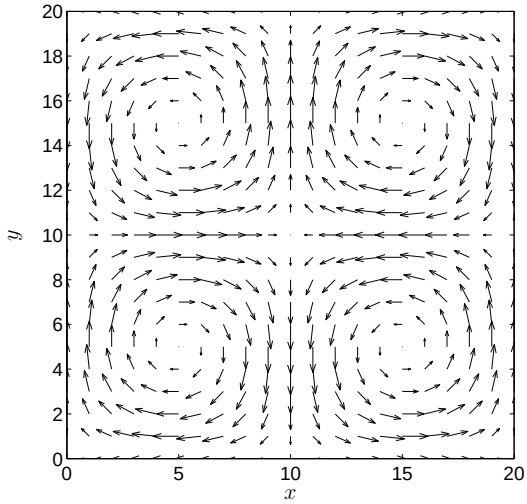

Fig. 4.12: Velocity field for a 4 cell Taylor vortex array (arbitrary scale).

Fig. 4.13 (a) shows slices through the centre of the velocity fields $\mathbf{u}$ and $\bar{\mathbf{u}}_{\mathrm{PIV}}$. In the regions with large displacements it can be seen that the velocities calculated from PIV are approximately 2% less than the theoretical values. An underestimation of the velocity field is to be expected because the PIV algorithm performs a spatial average over an interrogation window and thus cannot detect local peak velocities. The corresponding vorticity fields, $\boldsymbol{\omega}$ and $\bar{\boldsymbol{\omega}}_{\mathrm{PIV}}$, are shown in Fig. 4.13 (b). The peak vorticity is captured well by MatPIV and errors in the vorticity are also of the order of 4%.

The spatial distribution of percentage error in $\bar{\mathbf{u}}_{\mathrm{PIV}}$ is homogenous as can be seen in Fig. 4.13 (c). However the spatial distribution of the percentage error in $\bar{\boldsymbol{\omega}}_{\mathrm{PIV}}$ is greater where the vorticity is lower, as shown in Fig. 4.13 (d). This is to be expected because the vorticity is found by calculating the local difference in velocities and errors are relatively more important when the velocity gradient is small.

Fig. 4.13 (e) shows that for 64 image pairs, the percentage error is always less than 10% — this is excepting the centre of the vortex where the theoretical velocity is zero and therefore any non-zero velocity calculated from the PIV processing will give an infinite percentage error. The mean percentage error for 64 image pairs is 1.7% and 2.5% for $\bar{\mathbf{u}}_{\mathrm{PIV}}$ and $\bar{\boldsymbol{\omega}}_{\mathrm{PIV}}$ respectively. As can be seen in Fig. 4.13 (f) the mean error decreases for averaging over increasing numbers of results from PIV calculations; the mean error in the velocity field is always less than that in the vorticity field which is to be expected given that the vorticity is a differential quantity calculated using a finite difference method and errors become relatively larger.

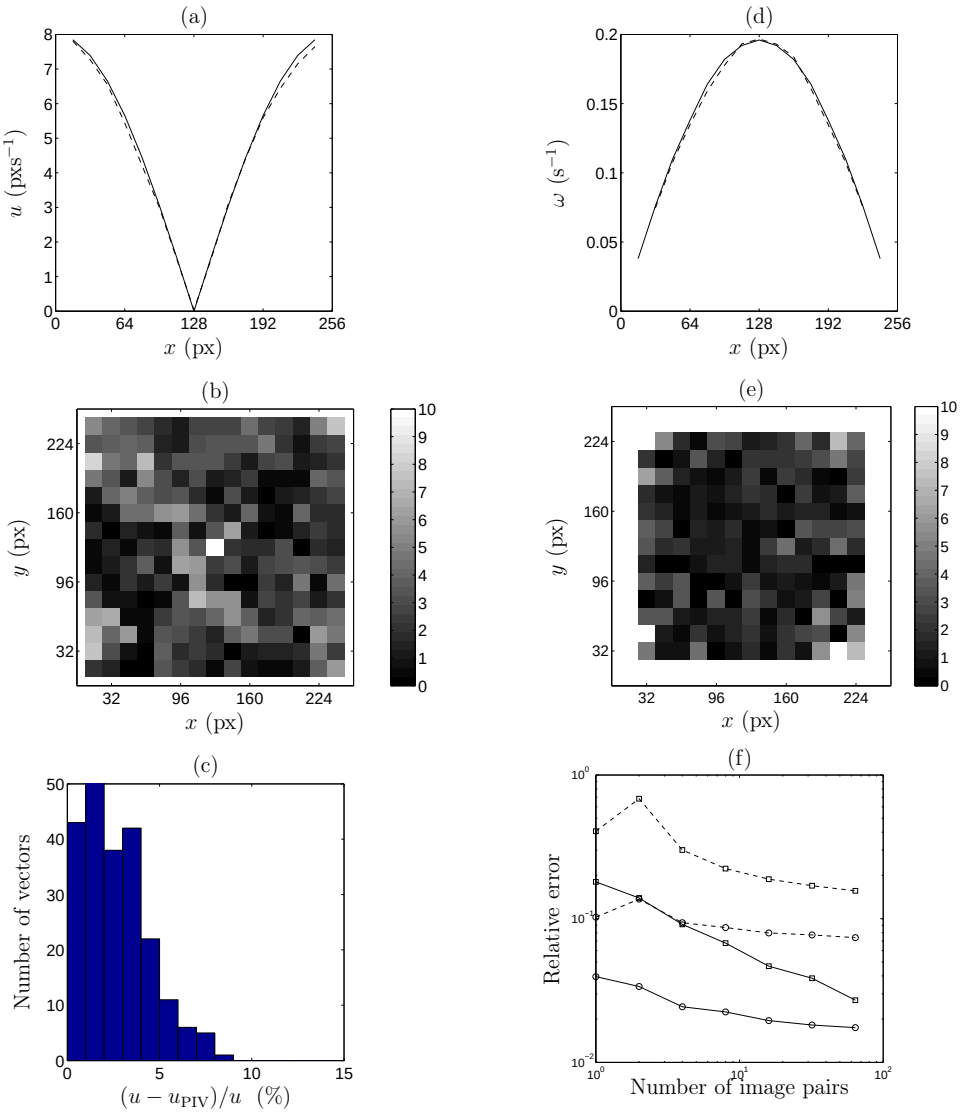

Fig. 4.13: (a) True (—) and calculated (−−) velocity profile through the vortex centre. (b) Spatial distribution of percentage error in the calculated velocity. (c) Histogram of percentage error in the calculated velocity. (d) True (—) and calculated (−−) vorticity profile through the vortex centre. (e) Spatial distribution of percentage error in the calculated vorticity. (f) Convergence of velocity (○) and vorticity (□) with increasing number of image pairs for MatPIV (—) and VISIFlow (−−). programs.

For comparison the percentage error using another PIV processing program, Visiflow, is also shown for the same PIV treatment in Fig. 4.13 (f). The percentage errors are an order of magnitude greater than those when using MatPIV, showing that Visiflow is ill-adapted to processing velocity fields of this type.

In conclusion, MatPIV appears to be well suited to performing phase averaged PIV analysis for images with moderate velocity gradients. With sufficient averaging the mean error in the velocity field can be reduced to less than 2% and the mean error in the vorticity field to 2.5%. Although the error is slightly higher than that for LDA measurements ($< 1\%$), PIV has the advantage of allowing a whole velocity field to be captured at once.

Chapter 5

Results and discussion of results

In the following chapter results for the cylinder wake are presented and discussed. Initially the quality of the polymer solutions (5.1) and the vortex shedding (5.2) is shown. Following this, the changes in wake stability (5.3) and vortex shedding frequency (5.4) are analyzed in relation to the polymer solution concentration. Measurements for the time average flow fields from LDA and PIV measurements (5.6.1 and 5.6.2) are then examined and lastly the phase-averaged PIV results (5.6.3) are commented on.

5.1 Fluids studied

The cylinder wake was investigated for water and four non-Newtonian aqueous PEO solutions. Experiments were conducted at temperatures in the range $21 - 25°C$. Once the polymer solutions were visually homogenous, typically $5 - 8$ days after adding the PEO to the water, the solution viscosity was measured every two days to monitor the polymer degradation. Over a one month period (the time needed to mix a polymer solution and perform measurements) the solution viscosity at 25°C decreased by 2%.

The polymer solution concentrations were calculated in two ways: firstly from the mass of polymer in relation to the mass of solvent and secondly by comparing the viscosity of the fluid with a previously determined viscosity-concentration relationship (see Fig. 3.7 and Eq. (3.36)). The results from the two methods are shown in Table 5.1 and are in good agreement for all the solutions. Because the viscosity-concentration relationship Eq. (3.36) is dependent on the polymer chain length this suggests that the mixing method did not degrade the polymer chains. The concentrations given by the viscosity measurements will be used hereafter as they give the fairest estimate of the effective polymer concentration. To simplify the presentation of the

Fluid name	m_{PEO} kg	$\nu_0(25°\mathrm{C})$ cSt	c from m_{PEO} (wt%)	c from η_0 (wt%)
PEO 500	1.500	1.20	0.052	0.054
PEO 1000	3.098	1.65	0.101	0.100
PEO 1500	4.499	2.12	0.145	0.141
PEO 2900	9.031	4.36	0.291	0.281

Table 5.1: Mass of PEO m_{PEO} added to the solvent and kinematic viscosity ν_0 of the polymer solutions and the corresponding concentrations c.

data, throughout the following chapter fluid concentrations will be discussed in units of percent by weight (wt%).

For each fluid, the temperature-viscosity relationship was determined for the temperature range 20-25°C in order to use the correct viscosity in calculations with the data.

5.2 Vortex shedding quality

The aim of this work was to study the nominally two-dimensional cylinder wake and therefore only parallel vortex shedding was investigated. This was ensured via the procedure explained in Chapter 4.1.3. Figure 5.1 shows typical hydrogen bubble visualizations of vortex shedding behind the cylinder for water and PEO 1500. The vortex shedding quality was the same for both the Newtonian and the polymer fluids. For downstream distances $x^* < 10$ the vortex lines are straight and parallel to the cylinder implying that the spanwise velocity is approximately zero. For $x^* > 10$, the wake starts to decay from the edges inwards and the vortex lines become less uniform across the span.

5.3 Stability of the wake

The critical Reynolds number $\mathrm{Re_c}$ is found by fitting the Stuart–Landau (SL) proportionality $|A|^2 \propto \mathrm{Re} - \mathrm{Re_c}$ (see Chapter 2) to the saturated instability amplitude. For laminar vortex shedding the instability amplitude is characterized by the transverse velocity fluctuation amplitude $|v|$. This was measured using LDA and is subsequently referred to in the non-dimensional form $|v^*| = |v|/(\nu_0/d)$.

The usual way to determine $\mathrm{Re_c}$ by measuring $|v^*|$ at a fixed location in the wake for all Reynolds numbers (e.g. Mathis *et al.*, 1984; Provansal

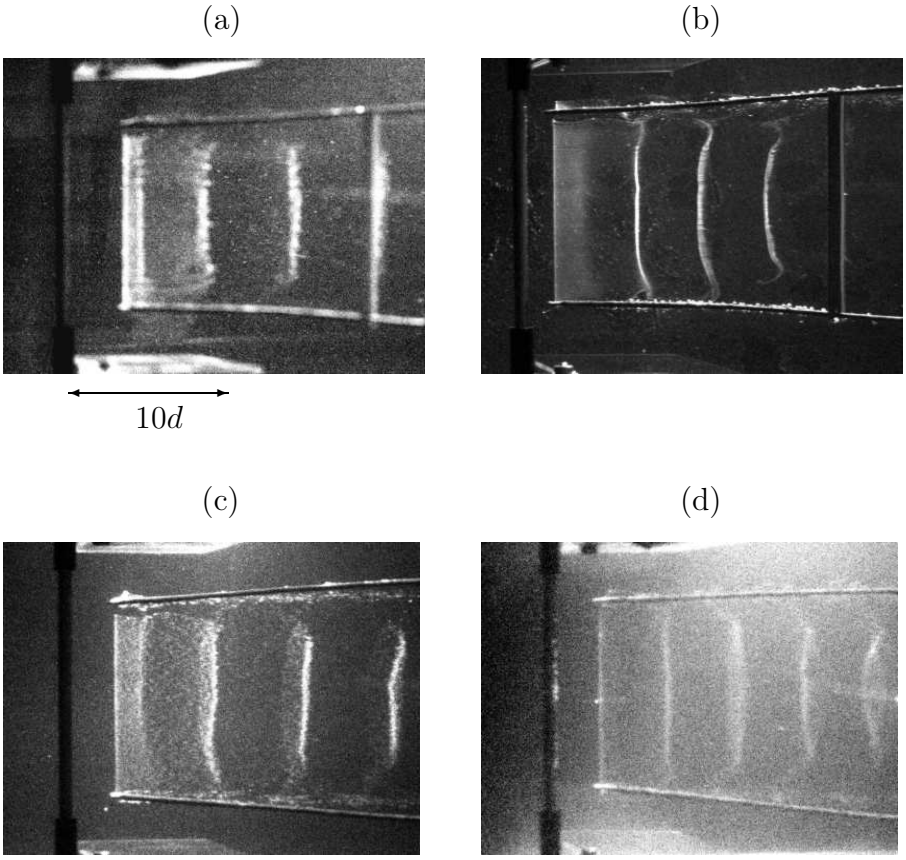

Fig. 5.1: Hydrogen bubble visualizations of von Kármán vortices behind the cylinder, plan view. The flow is from left to right and the shadow of the cylinder is visible on the left: (a) water, Re = 58, (b) water, Re = 115, (c) PEO 1500, Re = 62, (d) PEO 1500, Re = 95.

et al., 1987; Schumm *et al.*, 1994) is employed here. $|v^*|$ was measured at $(x^* = 7.5, y^* = 0, z^* = 0)$ because just after the onset of vortex shedding $|v^*|$ was close to $|v^*|_{\max}$ at this location, and by measuring the largest value of $|v^*|$ the relative error was minimized. Other workers have used similar locations in the wake, for example, for the coordinate system used in the present study, Mathis *et al.* used $(x^* = 4.5, y^* = 0)$ and Schumm *et al.* used $(x^* = 10, y^* = 1)$.

Figure 5.2 shows the dependance of $|v^*|^2$ on Re after the onset of vortex

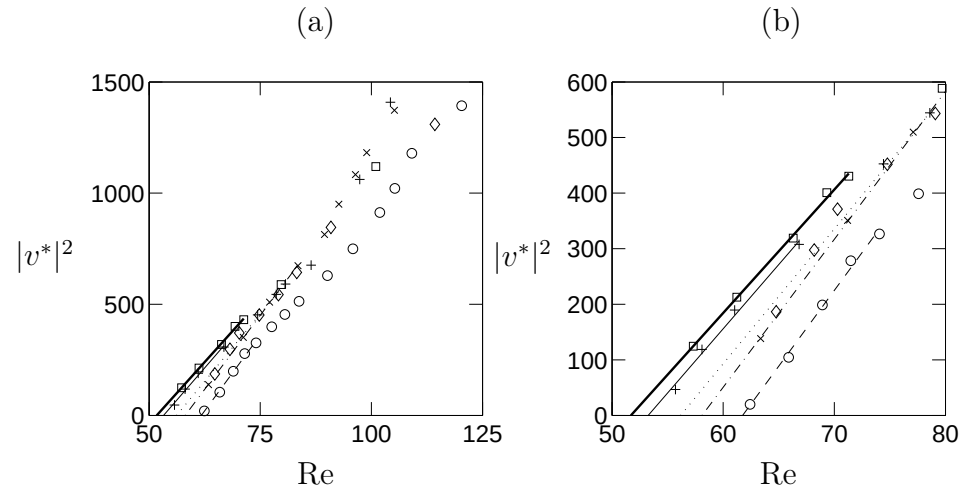

Fig. 5.2: (a) $|v^*|^2$ versus Re and (b) detailed view of $|v^*|^2$ versus Re near to the onset of vortex shedding. Symbols for (a) and (b): $\square$ water; + PEO 500; $\Diamond$ PEO 1000; $\times$ PEO 1500; $\bigcirc$ PEO 2900; with fits $|v^*|^2 = k_1(\mathrm{Re} - \mathrm{Re_c})$: - water; $-$ PEO 500; $\cdots$ PEO 1000; $- \cdot -$ PEO 1500; $--$ PEO 2900 (see Table 5.2 for fit coefficients).

shedding for water and the polymer solutions. The SL saturated amplitude equation (Eq. 2.9a):

$$|v^*|^2 = k_1(\mathrm{Re} - \mathrm{Re_c}), \tag{5.1}$$

was fitted to the data in a least squares sense near the onset of vortex shedding and extrapolated backwards to find $\mathrm{Re_c}$ at $|v^*|^2 = 0$. $\mathrm{Re_c}$ and k_1 for each fluid are shown in Table 5.2.

How far Eq. (5.1) is valid after the onset of vortex shedding is not well defined. Mathis *et al.* and Schumm *et al.* showed that for their experimental

Fluid	$\mathrm{Re_c}$	k_1
Water	51.7	22.2
PEO 500	53.3	23.1
PEO 1000	56.2	24.3
PEO 1500	58.1	26.6
PEO 2900	61.8	27.2

Table 5.2: Linear fit coefficients for Eq. (5.1) from Fig. 5.2.

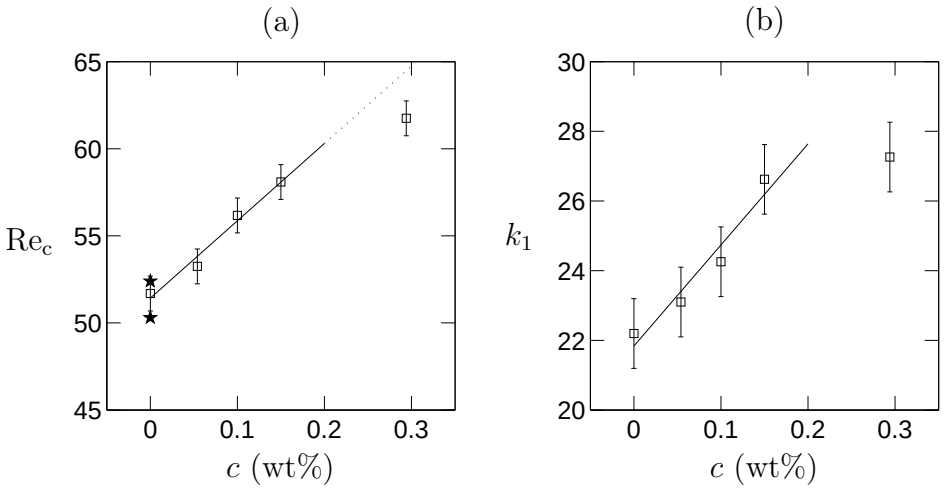

Fig. 5.3: Dependance of (a) $\mathrm{Re_c}$ on c and (b) k_1 on c, where c is the polymer concentration. The linear fits are given by Eqs. (5.2) and (5.3) respectively and in (a) ★ indicates predictions of the Newtonian value by the GL model for $L^* = 20$.

set ups the SL model was applicable at least for $\mathrm{Re} \in [\mathrm{Re_c}, \mathrm{Re_c} + 15]$ while Peschard *et al.* (1999) who used a cylinder of small aspect ratio showed that for their data the SL model was valid up to $\mathrm{Re} = \mathrm{Re_c} + 50$. In the present work, due to the relatively low velocity resolution of the facility, the range $[\mathrm{Re_c}, \mathrm{Re_c} + 25]$ was used to ensure there were enough data to give an accurate fit. For PEO 2900 the interval was reduced to $[\mathrm{Re_c}, \mathrm{Re_c} + 15]$ as $|v^*|^2$ was no longer linear with $\mathrm{Re} - \mathrm{Re_c}$ above this. The errors in calculating $\mathrm{Re_c}$ and k_1 were $\pm 1\%$ and $\pm 4\%$ respectively.

The critical Reynolds number and k_1 as a function of the solution polymer concentration c are shown in Fig. 5.3. For a Newtonian fluid, the critical Reynolds number predicted by the complex Ginzburg–Landau (GL) model (Chapter 2, Eq. (2.12)) for a cylinder of aspect ratio $L^* = 20$ is $\mathrm{Re_c} = 50.1$ using the coefficients from Monkewitz *et al.* (1996) and $\mathrm{Re_c} = 52.4$ using the linear regression from Fig. 6 in Albarède & Monkewitz (1992). These indicate the range of expected values and agree well with $\mathrm{Re_c} = 51.7$ for water. For the dilute solutions ($c < 0.19$ wt%, Eq. (3.10)) the dependence of $\mathrm{Re_c}$ on c is well described by:

$$\mathrm{Re_c} = 51.4 + 44.4c, \tag{5.2}$$

and the dependence of k_1 on c is given by:

$$k_1 = 21.8 + 29.1c. \tag{5.3}$$

Although the coefficient $k_1 = \sigma_r^*/l_r^*$ includes the growth rate of the instability σ_r^*, its value is also dependent on the coefficient l_r^* which changes with the quantity measured ($|v^*|$or $|u^*|$) and also with the location in the wake where the measurements are performed. As such, the precise behaviour of k_1 is of limited interest here.

The increase in critical Reynolds number with concentration indicates that adding small amounts of PEO to a Newtonian solvent stabilizes vortex shedding in the cylinder wake. This agrees with the linear stability analysis of free shear layers by Azaiez & Homsy (1994) where fluid elasticity was reported to decrease flow instability due to the actions of the non-Newtonian normal forces. Using the approximation of the peak shear rates in the flow past a cylinder presented below, the Oldroyd B model can be used to give an idea of the importance of normal stresses. Using λ_Z the normal stresses are $O(1\%)$ of the shear stresses. However, if it is acknowledged that the peak shear stresses are probably a factor of 2 greater than the approximation below (this is realistic) and in combination with an effective relaxation time that is $O(10\lambda_Z)$ (Tirtaatmadja *et al.*, 2005), then the normal stresses are likely to be $O(10\%)$ of the shear stresses. Normal stresses would then appear to be a satisfactory source of such large changes ($O(10\%)$) to the critical Reynolds number.

$\mathrm{Re_c}$ for PEO 2900 shows a reduction in this trend, however. Estimating the shear rates in the flow past the cylinder shows that the drop in $\mathrm{Re_c}$ for PEO 2900 coincides with the appearance of shear-thinning. The peak shear rates in the flow past a cylinder occur in the cylinder boundary layer where the local velocities are greatest and the shear layer is thinnest. This can be approximated by:

$$(\dot{\gamma}_{xy})_{max} = \frac{U_e}{\delta},$$

where U_e is the local velocity external to the boundary layer and δ is the boundary layer thickness. The local velocity on the cylinder given by potential theory (see Appendix B) is $U_e = 2U_\infty \sin\theta$, where θ is the angle measured from the leading edge of the cylinder about the cylinder axis. The greatest value of U_e occurs at $\theta = \pi/2$, which corresponds to the shoulder of the cylinder and for PEO 2900 at $\mathrm{Re} = \mathrm{Re_c}$ is approximately 0.18 $\mathrm{ms^{-1}}$. The boundary layer thickness at this location for PEO 2900 at $\mathrm{Re} = \mathrm{Re_c}$ and a cylinder with a diameter of 3mm is 0.76 mm from the Blasius solution (Schlichting, 1968) and 0.80 mm by Thwaites' method (Thwaites, 1949)

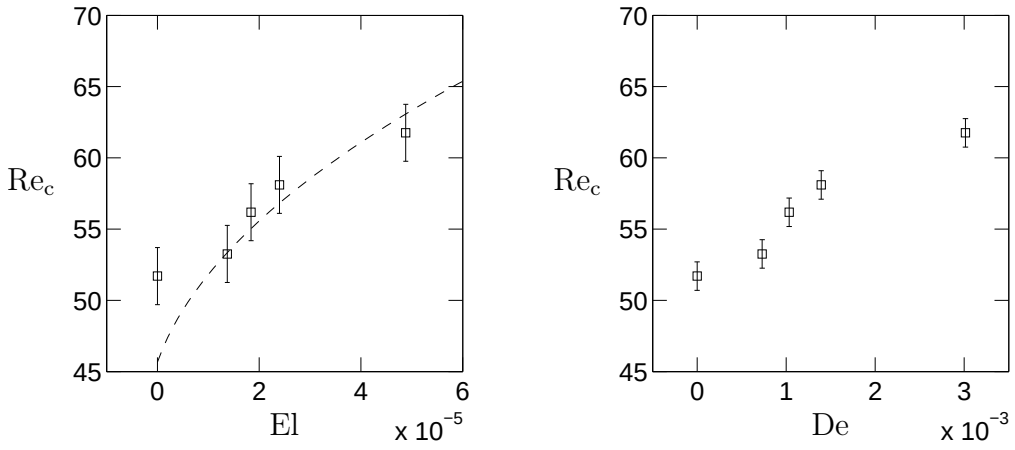

Fig. 5.4: $\mathrm{Re_c}$ versus the elasticity number El and $\mathrm{Re_c}$ versus the Deborah number at $\mathrm{Re_c}$, $\mathrm{De_c}$. The fit for $\mathrm{Re_c}$(El) $(--)$is given by Eq. (5.4).

(see Appendix B for details). Combining the values of U_e and δ at $\theta = \pi/2$ for PEO 2900 at $\mathrm{Re_c}$ we find $\dot{\gamma}_{\mathrm{xy}} \approx 225\ \mathrm{s}^{-1}$. From the viscosity-shear rate relation Eq. (3.37) established in Chapter 3, this corresponds to a drop in viscosity of 3% for PEO 2900. Performing the same estimate predicts a negligible reduction in viscosity for the other solutions.

The reduction in $\mathrm{Re_c}$ for PEO 2900 in relation to Eq. (5.2) is equal to 4%. This is the same order as the drop in viscosity in the boundary layer and it seems reasonable to attribute the relative decrease in $\mathrm{Re_c}$ to shear-thinning effects. Shear-thinning, as well as reducing the fluid viscosity, is predicted to delay the separation of the boundary layer on a cylinder (Serth & Kiser, 1967; Lin & Chern, 1979) and this will clearly change the dynamics of the wake. Thus the exact mechanism by which shear-thinning decreases the critical Reynolds number is not certain.

The change in stability in relation to PEO concentration for vortex shedding has been discussed briefly in previous experimental work. Kalashnikov & Kudin (1970) comment that the value of Re where vortices first appear decreases for the polymer solutions. These therefore implies a *decrease* in critical Reynolds number for increasing PEO concentration. The higher molecular weight PEO chains used in this previous studies could well have caused shear-thinning to occur for lower concentrations and at lower shear rates thus de-stabilizing the flow. Although it is not mentioned explicitly, Fig. 3 from Usui *et al.* (1980) indicates various changes in $\mathrm{Re_c}$ as a function of polymer concentration and cylinder diameter. Although one should be cautious in interpreting other data, a scenario where the wake is stabilized due to normal

forces and then destabilized at higher shear rates due to shear-thinning is consistent with the results presented by Usui *et al.* (1980).

The similarity between the behaviour shown in Fig. 5.3 (a) and the stability map of Crumeyrolle *et al.* (2002) for Taylor–Couette flow is noteworthy. Although the Taylor–Couette system is unstable due to centrifugal forces, unlike the wake which is unstable due to shear forces, there is qualitative agreement on the effects of small concentrations of high M_v PEO.

Figure 5.4 shows $\mathrm{Re_c}$ in relation to the elasticity number El as well as $\mathrm{Re_c}$ in relation to the Deborah number at the onset of vortex shedding, $\mathrm{De_c}$. The increase in $\mathrm{Re_c}$ with $\mathrm{El} = \eta\lambda/(d^2\rho)$ is dependent only on the polymer concentration c, where η and λ are functions of c and d and ρ are constant, and it should be possible to find the relationship between El and $\mathrm{Re_c}$. However, the assumption that λ is independent of concentration for dilute solutions is problematic because this means that El scales only with η. $\mathrm{El} \propto \eta$ leads to a value of El for water that is of the same order as El for the polymer solutions, and which is not physically representative. This can be seen by the dotted line in Fig. 5.4 which was calculated from the definition of El, the behaviour of $\mathrm{Re_c}$ with c Eq. (5.2) and the dependence of η_0 on c from the Huggins equation (3.2) and is given by:

$$\mathrm{Re_c} = 51.4 + 10.6\left[\left(0.2 + 0.8\mathrm{El}\frac{d^2\rho}{\lambda\eta_\mathrm{s}}\right)^{1/2} - 1\right]. \tag{5.4}$$

A more precise description of λ would allow an experimental assessment of the suggestion from Azaiez & Homsy (1994) that the increase in stability in a shear layer due to fluid elasticity is dependent only on El.

The increase in $\mathrm{Re_c}$ for increasing Deborah number (5.4) is in qualitative agreement with the numerical work of Sahin & Owens (2004). However the expected relation between $\mathrm{Re_c}$ and De is unclear from the present experiments because De is a function of U_∞ and is therefore varying as Re crosses the critical threshold.

Summary of results for the wake stability

The critical Reynolds number for water is in good agreement with previous experiments and the predicted value from the GL model for an aspect ratio of 20. For dilute polymer solutions $\mathrm{Re_c}$ increases linearly with concentration, the physical reasons for which will be discussed in Section 5.6.2. However, shear-thinning is found to destabilize the flow and the destabilization is proportional to the reduction in viscosity.

5.4 Vortex shedding frequency

The vortex shedding frequency f was found by performing a FFT on the velocity signal from a 1D hot film probe, as described in Sec. 4.2.3, placed at $(x^* = 7.5, y^* = 1)$.

Frequency power spectra

Figure 5.5 shows examples of the power spectra for the Newtonian and non-Newtonian cylinder wakes. The fundamental frequency peak is more than 3 decades above the background noise and is sharp giving a well defined vortex shedding frequency. The background noise decays at high frequencies due to the low pass filter applied to the signal as explained in Section 4.2. The frequency resolution of the spectra was 0.0039 Hz giving 0.7% error for the lowest frequencies measured for water, and 0.04% error for the highest frequencies measured for PEO 2900.

Some of the spectra show additional frequency peaks at the fundamental frequency of the pump motor ($0.4-2$ Hz) and higher harmonics. These could not be filtered as they are of the same order as the wake shedding frequency but are easily detectable as electronic noise as they are very sharp.

For $70 < \mathrm{Re} < 110$ some of the spectra had side-bands indicating modulation of the wake signal. However, the power in the side-bands is at least two decades less than the power in the main frequency peak and is therefore small. This effect is probably due to the low aspect ratio of the cylinder and the relative proximity of the cylinder ends, which was previously reported to cause side-bands in the power spectrum (Williamson, 1989).

At $\mathrm{Re} > 100$, the spectra for PEO 1500 and PEO 2900 show secondary frequency peaks. This phenomenon is probably due to the edges of the wake and the end-cylinders introducing additional frequencies. However the main vortex shedding frequency is not measurably affected and it is impossible to say whether the additional frequencies are due to fluid elasticity or some quirk of the experimental set up.

Non-dimensionalization of f

The vortex shedding frequency is commonly expressed in two non-dimensional forms. The first of these, f^*, is obtained by non-dimensionalizing with the viscous diffusion time d^2/ν_0:

$$f^* = \frac{f d^2}{\nu_0}. \tag{5.5}$$

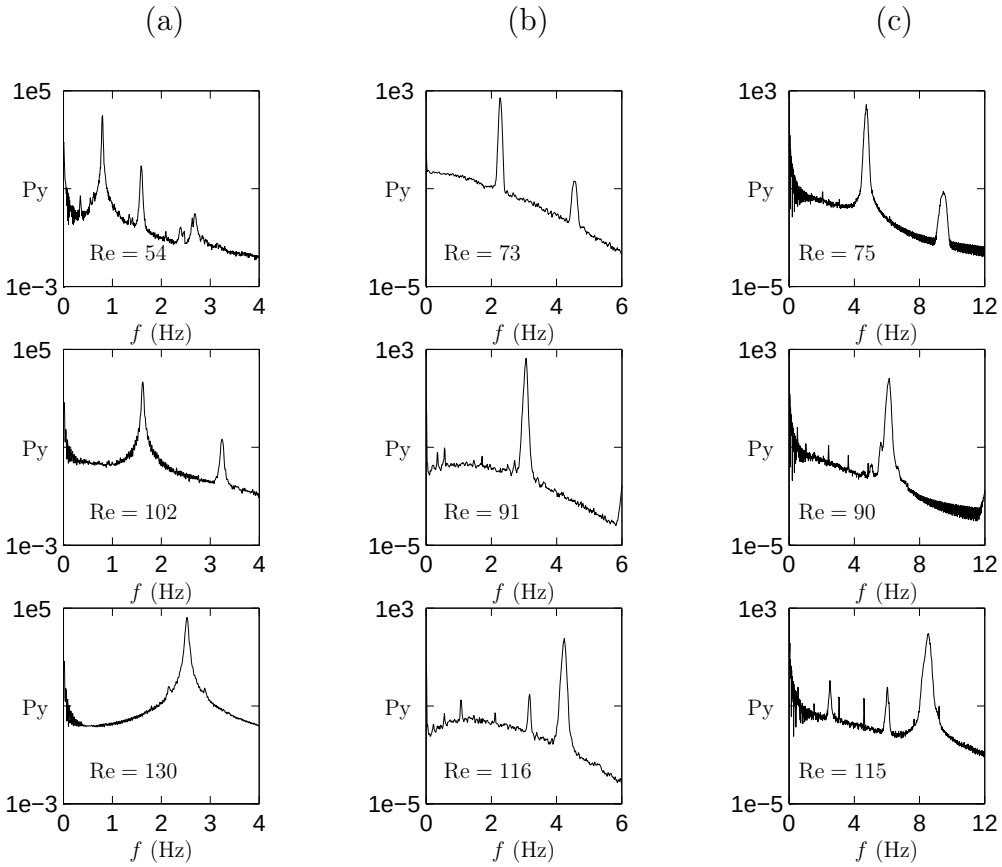

Fig. 5.5: Vortex shedding power spectra. Column: (a) water; (b) PEO 1500; and (c) PEO 2900.

f^* is sometimes referred to as the Roshko number and is the appropriate non-dimensional form of the instability frequency in the SL and GL models. The second non-dimensional form of the frequency is the Strouhal number St where f is multiplied by the inertial time scale d/U_∞:

$$\mathrm{St} = \frac{fd}{U_\infty} \left(= \frac{f^*}{\mathrm{Re}} \right). \tag{5.6}$$

5.4.1 Spanwise variation of f

The frequency measured at $(x^* = 5, y^* = 1, z^* = -3.3, 0, 3.3)$ using the hot film probe was constant for all three positions to within experimental error at all Reynolds numbers and for all fluids. The spectra at $z^* = \pm 3.3$ were noisier however, showing secondary frequency peaks similar to those in Fig. 5.5, Re

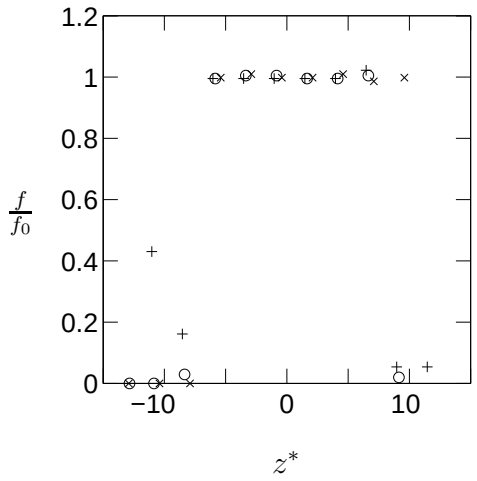

Fig. 5.6: Vortex shedding frequency f normalized by the frequency at $z = 0$, f_0, measured in the spanwise direction. The data are for water and were measured using LDA at $(x^* = 5, y^* = 0)$: + Re=57; x Re=70; o Re=112.

Fluid	Quadratic fit	Re range
Water	$f^* = -2.29 + 0.150\mathrm{Re} + 3.25 \times 10^{-4}\mathrm{Re}^2$	$[51.7, 155]$
PEO 500	$f^* = -2.24 + 0.142\mathrm{Re} + 3.66 \times 10^{-4}\mathrm{Re}^2$	$[53.3, 133]$
PEO 1000	$f^* = -1.37 + 0.126\mathrm{Re} + 4.16 \times 10^{-4}\mathrm{Re}^2$	$[56.2, 152]$
PEO 1500	$f^* = -1.32 + 0.126\mathrm{Re} + 3.88 \times 10^{-4}\mathrm{Re}^2$	$[58.1, 145]$
PEO 2900	$f^* = -2.25 + 0.143\mathrm{Re} + 2.85 \times 10^{-4}\mathrm{Re}^2$	$[61.8, 121]$

Table 5.3: f^*– Re relationship for water and PEO solutions, see Figs. 5.7 (a) and (b).

= 116. The spectra at $z^* = 0$ did not have these, so it is probable that the secondary peaks are due to the edges of the wake and the end-cylinders.

To have a more complete understanding of the spanwise variation in f, frequency measurements were performed using LDA for water and are presented in Fig. 5.6 where f is normalized by the frequency f_0 obtained at $z = 0$. The error in these measurements is greater than for the hot film but the data show that for $z^* \in [-6.7, 6.7]$ the vortex shedding frequency is constant, outside of which there is no clear frequency peak.

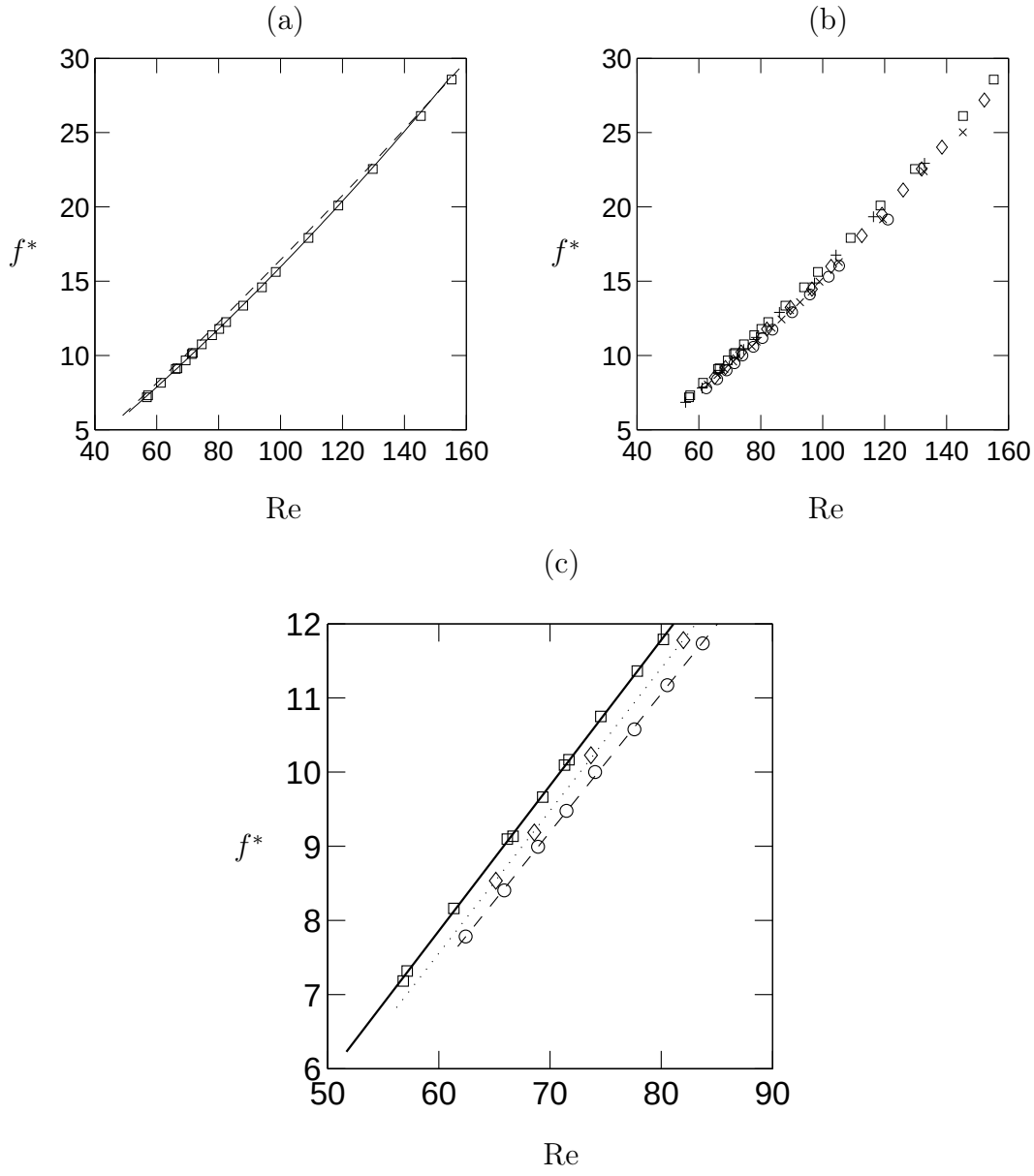

Fig. 5.7: Non-dimensional shedding frequency f^* vs. Re: (a) water, – Eq. (5.7); –– Williamson (1989); (b) water and polymer solutions with symbols: □ water; + PEO 500; ◊ PEO 1000; × PEO 1500; ◯ PEO 2900; (c) blow-up of (b) with linear fits: - water; ··· PEO 1000; –– PEO 2900 (see Table 5.4 for fit coefficients).

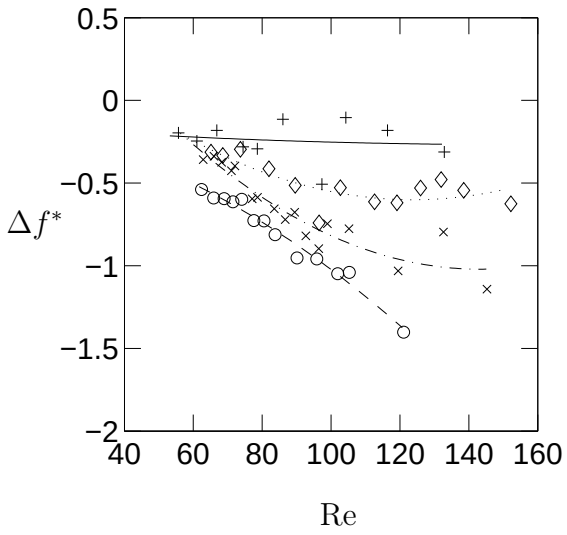

Fig. 5.8: Polymer solution shedding frequency minus the Newtonian shedding frequency Δf^* versus Re: symbols the same as Fig. 5.7; with quadratic fits: − PEO 500; ··· PEO 1000; − · − PEO 1500; −− PEO 2900.

5.4.2 Roshko number, f^*

$\mathbf{Re_c \leq Re \leq (Re_c + 100)}$

Figure 5.7 (a) shows the dependence of f^* on Re for water. The data describe a continuous relationship for all Reynolds numbers, a recognized characteristic of parallel vortex shedding (Williamson, 1989), and are well represented by the quadratic function:

$$f^* = -2.29 + 0.150\mathrm{Re} + 3.25 \times 10^{-4}\mathrm{Re}^2 \tag{5.7}$$

for Reynolds numbers in the interval $[51.7, 155]$. Experimental results from Williamson (1989) for a cylinder of $L^* = O(100)$ are shown for comparison and are slightly above the present data as expected for the larger aspect ratio. Figure 5.7 shows f^* as a function of Re for the polymer fluids as well as for water. The data for the polymer solutions are well described by the corresponding quadratic functions given in Table 5.3.

The change in f^* between the polymer solutions (subscript P) and water (subscript N) $\Delta f^* = f^*_{\mathrm{P}} - f^*_{\mathrm{N}}$ is shown in Fig. 5.8. At a given Reynolds number the shedding frequency decreases with increasing polymer concentration. This agrees with the reduction in vortex shedding frequency for

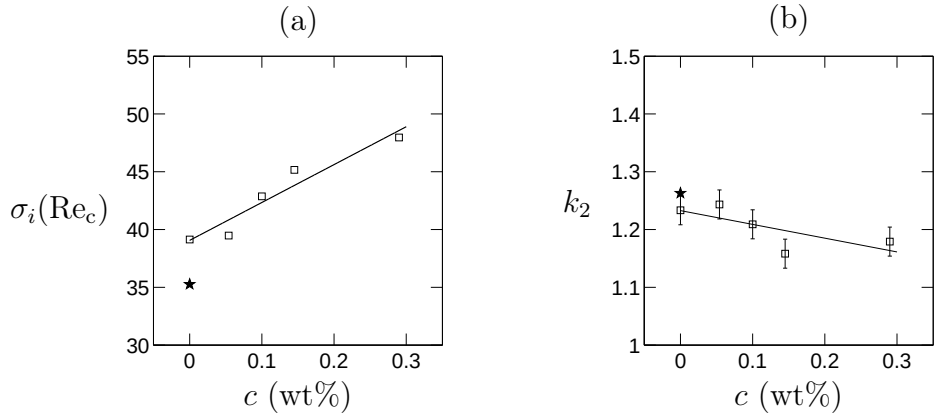

Fig. 5.9: Dependance of (a) $\sigma_i(\mathrm{Re_c})$ and (b) k_2 on c with ★ indicating the Newtonian values commonly used in the GL model. The linear fits are given by Eqs. (5.9) and (5.10).

aqueous PEO solutions previously observed by Gadd (1966*a*), Kalashnikov & Kudin (1970) and Usui *et al.* (1980). Figure 5.8 also shows that for a given polymer concentration Δf^* is dependent on Re.

All four polymer solutions show a similar trend immediately after the onset of vortex shedding, with Δf^* negative and decreasing further as Re increases. The exact behaviour of PEO 500 is unclear as the relative error ($\approx 50\%$) is higher than for the other fluids. However for PEO 1000 and PEO 1500 Δf^* clearly levels off after Re = 100, indicating that Δf^* does not continue to decrease indefinitely with increasing Re.

$\mathbf{Re_c \leq Re \leq (Re_c + 30)}$

For Reynolds numbers in the range $[\mathrm{Re_c}, \mathrm{Re_c}{+}30]$, Fig. 5.7 (c) shows that f^* is well represented by a linear function of Re for a given polymer concentration. Therefore the SL saturated frequency equation Eq. (2.9b) can be written:

$$\frac{\omega^*_{\mathrm{sat}}}{2\pi} = f^* = \frac{1}{2\pi}\left(\sigma^*_{\mathrm{i}}(\mathrm{Re_c}) + k_2(\mathrm{Re\text{-}Re_c})\right), \tag{5.8}$$

where the linear frequency at the onset of vortex shedding $\sigma^*_{\mathrm{i}}(\mathrm{Re_c})$ and the coefficient k_2 are found for each concentration and are shown in Table. 5.4. The error in calculating $\sigma^*_{\mathrm{i}}(\mathrm{Re_c})$ is $\pm 2\%$. For water $\sigma_{\mathrm{i}}(\mathrm{Re_c})^* = 39.2$ which is in fair agreement with the value of $\omega^*_{\mathrm{sat}} = 37.0$ found from the GL model (Eq. (2.13)) for a cylinder with $L^* = 20$ at the onset of vortex shedding.

Fluid	$k_2/(2\pi)$	$\sigma_{\mathrm{i}}^*(\mathrm{Re_c})/(2\pi)$
Water	0.196	6.23
PEO 500	0.198	6.32
PEO 1000	0.192	6.87
PEO 1500	0.184	7.14
PEO 2900	0.188	7.63

Table 5.4: Frequency fit coefficients to data in Fig. 5.7(c).

Figure 5.9 (a) shows that over the concentration range investigated the linear vortex shedding frequency at the onset of vortex shedding $\sigma_{\mathrm{i}}^*(\mathrm{Re_c})$ increases linearly with increasing polymer concentration and the relationship is given by:

$$\sigma_i^*(\mathrm{Re_c}) = 39.1 + 32.8c. \tag{5.9}$$

The gradient k_2 (Fig. 5.9 (b)) decreases with increasing polymer concentration, following:

$$k_2 = 1.23 - 0.249c. \tag{5.10}$$

k_2 for water is in fair agreement with the value of 1.26 calculated from the data in Monkewitz *et al.* (1996). Combining Eqs. (5.2), (5.9) and (5.10) the saturated shedding frequency can be expressed as the following function of polymer concentration and Reynolds number:

$$f^*(\mathrm{Re}, c) = \frac{1}{2\pi}\left[(1.23\mathrm{Re} - 24.0) - (7.80 + 0.249\mathrm{Re})c + 11.1c^2\right]. \tag{5.11}$$

Valid for $\mathrm{Re} \in [\mathrm{Re_c}, \mathrm{Re_c} + 30]$ and $c \in [0, 0.15\ \mathrm{wt\%}]$, Eq. (5.11) illustrates the reduction in f^* with increasing polymer concentration at a fixed value of Re.

5.4.3 Strouhal number

Figure 5.10 (a) shows the Newtonian St-Re relationship for the present work alongside results from Roshko (1954), Williamson (1989) and König *et al.* (1990). The current data fall below the other results at all values of Re. This is due to the short aspect ratio used in the current experiments; the other studies shown in Fig. 5.10 used cylinders with an aspect ratio greater than 80. Comparable reductions in St as a function of Re for cylinders with

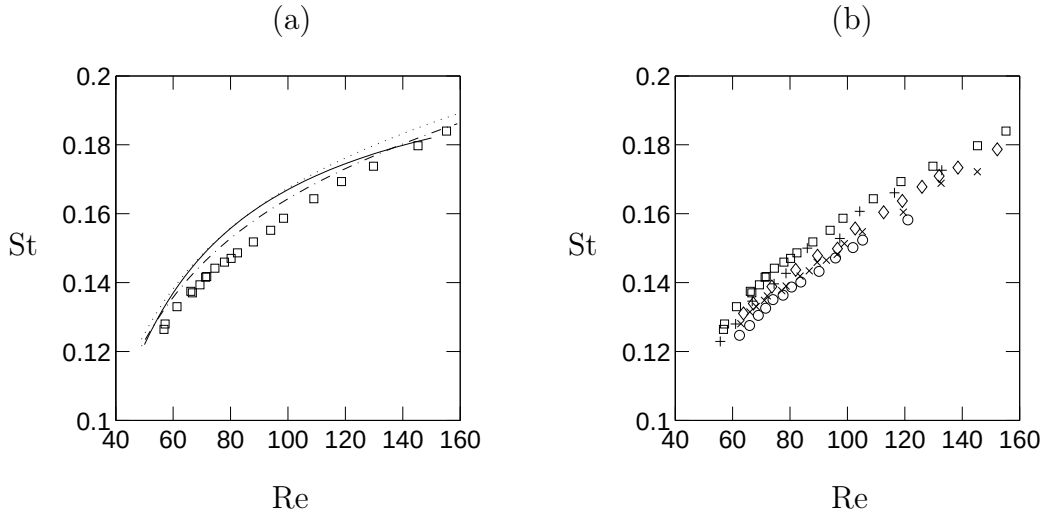

Fig. 5.10: St versus Re: comparison with results for water □ with experimental data from − Roshko (1954), − · − Williamson (1989) and ··· König *et al.* (1990).

similarly short aspect ratios have been documented by Williamson (1989) and Norberg (1994).

The St-Re relationship for the polymer solutions alongside the Newtonian data for the present work are shown in Fig. 5.10. Having already seen the effect of polymer concentration on f^*, it is no surprise to see that the Strouhal number as a function of Re decreases with increasing polymer concentration.

Usui *et al.* (1980) found that for Reynolds numbers $[50, 150]$ the change in Strouhal number $\Delta\mathrm{St} = \mathrm{St_P} - \mathrm{St_N}$ for polymer solutions was well described by the following power law functions of the Deborah number and the non-dimensional group $(d/\sqrt{\lambda\nu_0})$:

$$\Delta\mathrm{St} = -\,0.203\mathrm{De}^{0.32}, \tag{5.12}$$

$$\Delta\mathrm{St} = -\,0.59\left(\frac{d}{\sqrt{\lambda\nu_0}}\right)^{-0.56} \tag{5.13}$$

where $(d/\sqrt{\lambda\nu_0})$ is equal to $\mathrm{El}^{-1/2}$. Recalling that $\mathrm{St} = f^*/\mathrm{Re}$ and using Eq. (5.11), the Huggins formulation of the viscosity Eq. (3.2) and $\mathrm{El} =$

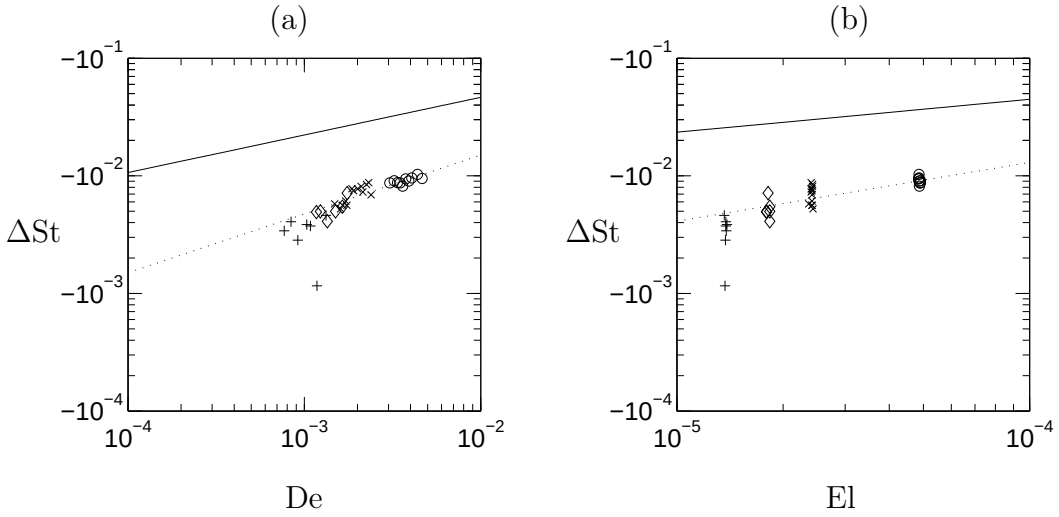

Fig. 5.11: $\Delta\mathrm{St} = \mathrm{St_P} - \mathrm{St_N}$ versus (a) De and (b) El. Symbols: + PEO 500; ◊ PEO 1000; × PEO 1500; ◯ PEO 2900; with fits proposed by Usui *et al.* (1980) −, given in Eqs. (5.12) and (5.13), and fits to present data ⋯ Eqs. (5.17) and (5.18).

$\eta\lambda/(d^2\rho)$, we can write St as a function of the polymer concentration:

$$\begin{aligned} 2\pi\mathrm{St} = &\left(1.23 - \frac{24.0}{\mathrm{Re}}\right) \\ &- \left(\frac{7.80}{\mathrm{Re}} + 0.249\right) \frac{(0.2 + 0.8\mathrm{El}\xi)^{1/2} - 1}{0.8[\eta]_0} \\ &+ \left(\frac{11.1}{\mathrm{Re}}\right) \frac{(0.2 + 0.8\mathrm{El}\xi) - 2\,(0.2 + 0.8\mathrm{El}\xi)^{1/2} + 1}{(0.8[\eta]_0)^2}, \end{aligned} \tag{5.14}$$

where $\xi = d^2\rho/(\lambda\eta_\mathrm{s})$. Eq. (5.14) suffers from the same drawback as Eq. (5.4), namely that there is a non-zero elasticity number for the Newtonian solution. This makes it difficult to use such a formulation to study the change in St with polymer concentration, especially where the concentration approaches zero.

However, inspection of Eq. (5.11) reveals that the term that is second order in concentration is at most 5% of the first order term. This suggests that the change in frequency is essentially linearly dependent on the polymer concentration and allows us to hypothesize that $\Delta\mathrm{St} \propto c$. Next, by propos-

ing that λ is independent of concentration for the polymer concentrations studied, and therefore implying that El $\propto c^2$, we can write:

$$\Delta\text{St} \propto \text{El}^{1/2}, \tag{5.15}$$

and it follows that for a constant Reynolds number

$$\Delta\text{St} \propto \text{De}^{1/2}. \tag{5.16}$$

Relationships (5.15) and (5.16) are fitted to the data and yield:

$$\Delta\text{St} = -1.3\text{El}^{1/2}, \tag{5.17}$$

$$\Delta\text{St} = -0.15\text{De}^{1/2}. \tag{5.18}$$

Figure 5.11 shows that they represent the data well for Reynolds numbers up to 100, beyond which the SL model is no longer applicable. From the above reasoning we would expect Eq. (5.18) to be different for each Reynolds number. However, in practise the change in Re only alters ΔSt by 20% for this range of data, which is of the same order as the errors in the data. Figure 5.11 shows that the trends are in fair agreement with those of Usui *et al.* (1980). The reduction in Strouhal number is smaller in the current work because lower molecular weight PEO was used, providing a lower fluid elasticity.

Summary of results for the vortex shedding frequency

The frequency-Reynolds number relationship is continuous across a wide range of Reynolds numbers, supporting the assumption of parallel vortex shedding. The non-dimensional frequency f^* for water agrees closely with previous work. f^* decreased with increasing polymer concentration and the change in f^* was dependent on the Reynolds number. There was no marked change in behaviour for PEO 2900 in relation to the other polymer solutions suggesting that shear thinning does not affect the instability frequency. The relationships between the Strouhal number and the Deborah and elasticity numbers were determined for the Reynolds numbers up to 100.

5.5 LDA velocity profiles

The downstream evolution of the von Kármán vortex street was characterized by measuring $|v^*|$ on the centreline at Reynolds numbers between 50 and 150. The spanwise distribution of $|v^*|$ was also investigated.

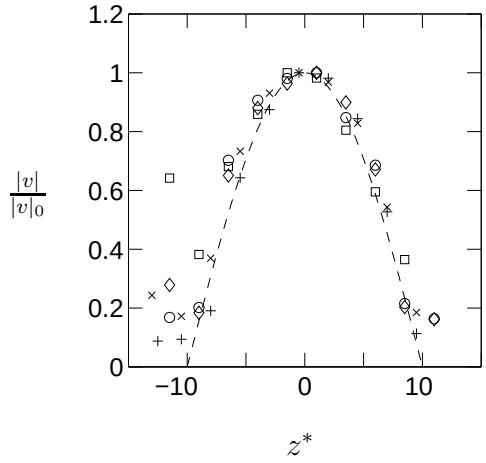

Fig. 5.12: Spanwise variation of $|v|/|v|_0$ for water: + Re=62; x Re=84; $*$ Re=109; and for PEO 1500: □ Re=120. Cosine half period shown by $--$.

5.5.1 Spanwise $|v^*|$ profiles

Figure 5.12 shows the spanwise variation of $|v^*|$ measured at $(x^* = 5, y^* = 0)$ for Reynolds numbers $[50, 150]$. The measurements for water and the polymer fluids show that parallel vortex shedding gives a symmetric distribution of $(|v^*|/|v^*|_0)$ about $z^* = z/d = 0$, where $|v^*|_0$ is the velocity at $z^* = 0$, and is well represented by half a cosine period. In order to measure the strongest velocity signal with the least interference from the edges of the wake, all LDA measurements were made at $z^* = 0$, or near to this for PIV, where the velocity field was measured at $z^* = 1.7$.

5.5.2 Streamwise $|v^*|$ profiles on the centreline

The downstream evolution of $|v^*|$ along the wake centreline $(y^* = 0, z^* = 0)$ is shown in Figs. 5.13–5.15 for water and the polymer solutions over a range of Reynolds numbers. The transverse velocity fluctuation profiles show two trends as Re increases for all the fluids: firstly the maximum value $|v^*|_{\max}$ increases, and secondly the position of $|v^*|_{\max}$, $x^*_{\max}$, moves upstream towards the trailing edge of the cylinder.

Two comparisons of $|v^*|$ profiles at a given Reynolds number are shown in Fig. 5.16. Close to the onset of vortex shedding at $\mathrm{Re} - \mathrm{Re_c} \approx 15$ the profiles are similar for all the fluids; the differences between the profiles can reasonably be attributed to small variations in the Reynolds number.

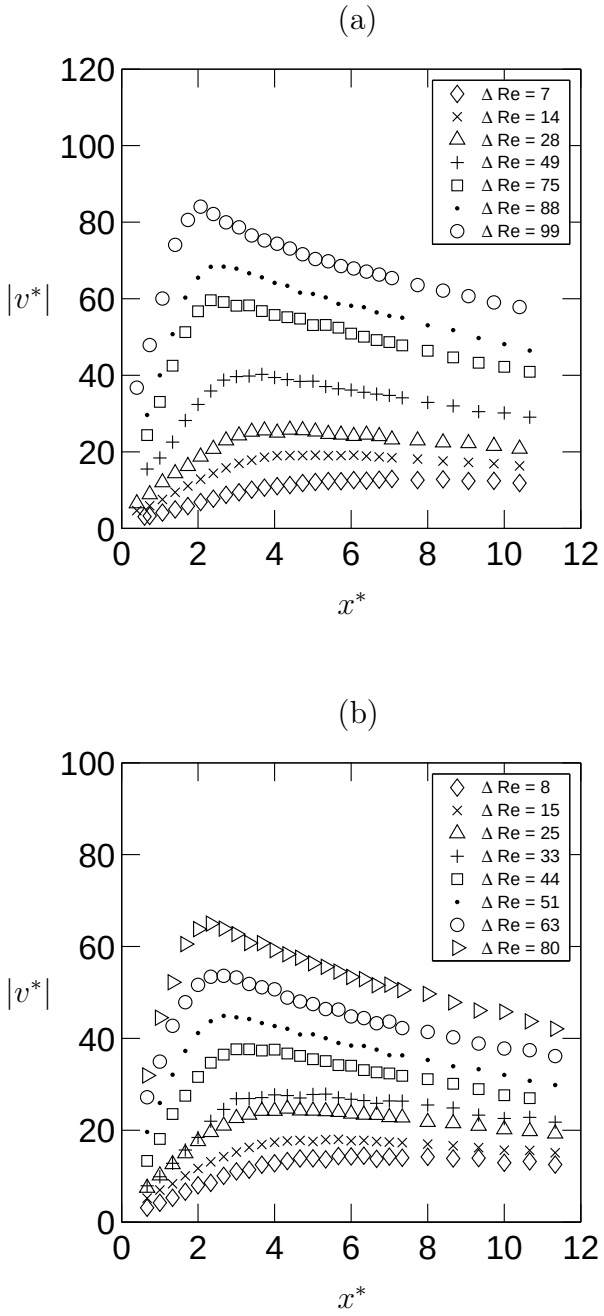

Fig. 5.13: $|v^*|$ profiles on the centreline for (a) water (b) PEO 500, where $\Delta\mathrm{Re} = \mathrm{Re} - \mathrm{Re_c}$.

(a)

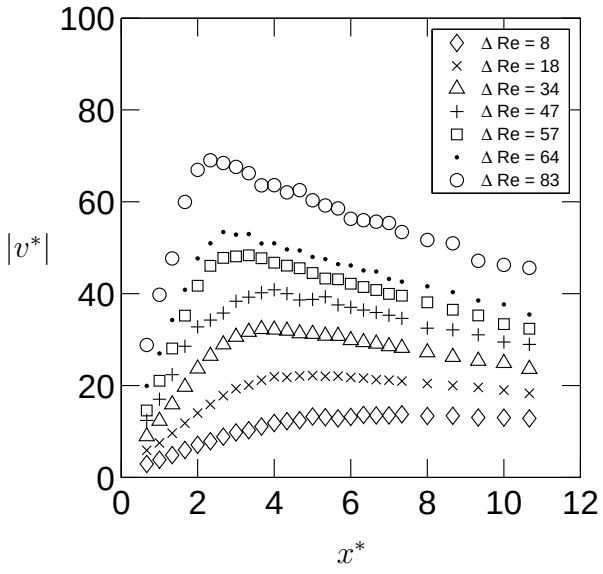

(b)

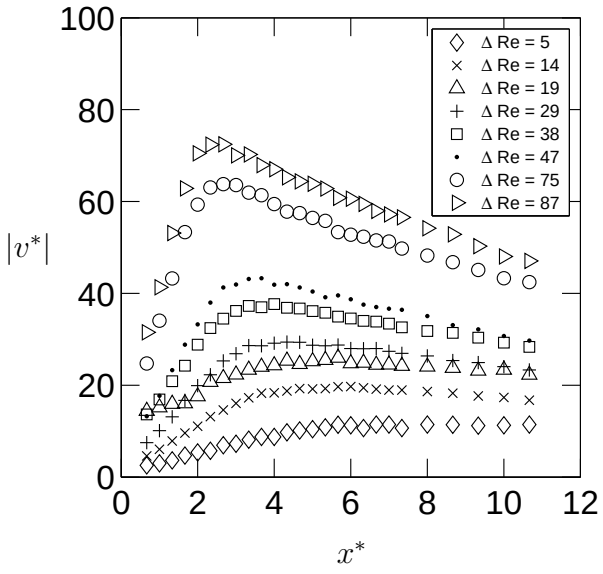

Fig. 5.14: $|v^*|$ profiles on the centreline for (a) PEO 1000 and (b) PEO 1500, where $\Delta\mathrm{Re} = \mathrm{Re} - \mathrm{Re_c}$.

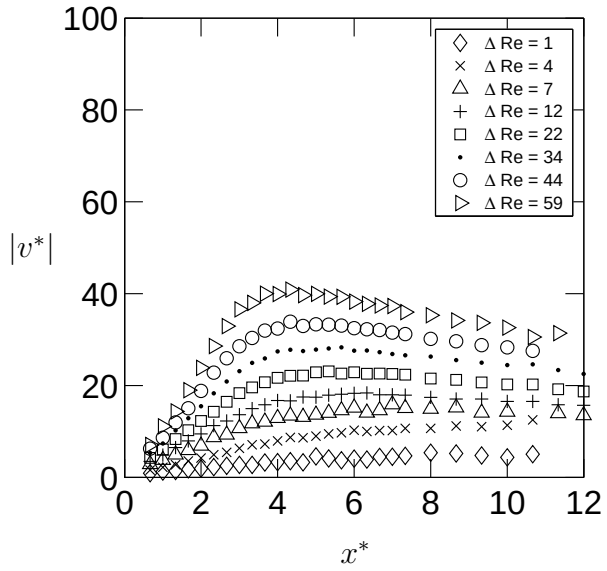

Fig. 5.15: $|v^*|$ profile on the centreline for PEO 2900, where $\Delta\mathrm{Re} = \mathrm{Re} - \mathrm{Re_c}$.

However, at $\mathrm{Re} - \mathrm{Re_c} \approx 45$, the $|v^*|$ profile for PEO 2900 falls significantly below those for the dilute solutions and water which are similar.

As discussed in Section 5.3 shear-thinning effects were non-negligible for PEO 2900 at the onset of vortex shedding. For increasing Reynolds number these would have become even more important and could well explain the altered $|v^*|$ profiles for PEO 2900 in comparison to the other fluids. It is unlikely that the change can be attributed to increasing fluid elasticity: no change is detected for the PEO 1500 profiles even at the higher Reynolds numbers where the fluid elasticity as measured by the Deborah number is of the same order for PEO 1500 and PEO 2900.

The dependence of $|v^*|_{\max}$ on Re is shown in Fig. 5.17. $|v^*|_{\max}$ for PEO 2900 falls below the other results at higher Reynolds numbers. The data for water and the dilute polymer solutions follow two distinct behaviours. For $\mathrm{Re} - \mathrm{Re_c} \in [0, 40]$ the growth of $|v^*|_{\max}$ is proportional to the square root of $\mathrm{Re} - \mathrm{Re_c}$:

$$|v^*|_{\max} = 5.32(\mathrm{Re} - \mathrm{Re_c})^{1/2}, \tag{5.19}$$

following the scaling suggested by the SL model. The scaling of $|v^*|_{\max}$ with $(\mathrm{Re})^{1/2}$ was originally proposed by Goujon-Durand *et al.* (1994) for data

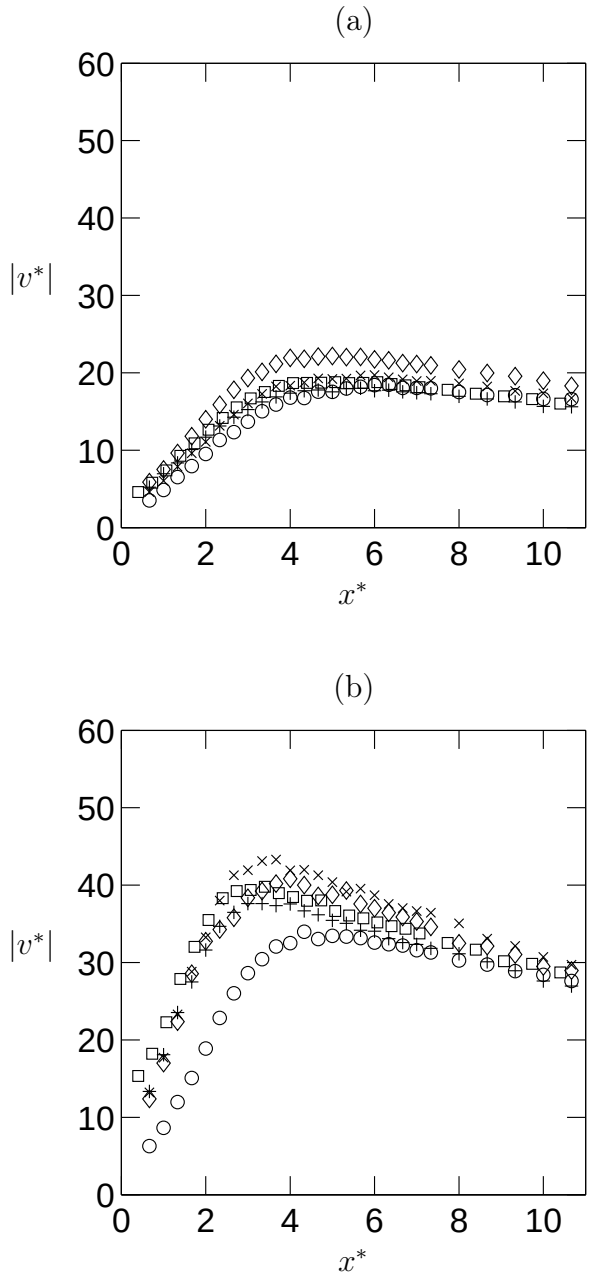

Fig. 5.16: Comparison between $|v^*|$ profiles along the centreline for (a) Re $\in$ $[\mathrm{Re_c} + 13, \mathrm{Re_c} + 19]$ and (b) Re $\in$ $[\mathrm{Re_c} + 44, \mathrm{Re_c} + 49]$. Symbols: $\square$ water; $+$ PEO 500; $\Diamond$ PEO 1000; $\times$ PEO 1500; $\bigcirc$ PEO 2900.

from the wake of a trapezoidal cylinder for $\mathrm{Re} = [\mathrm{Re_c}, 1.58\mathrm{Re_c}]$. The present results show that at Reynolds numbers $[40, 100]$, $|v^*|_{\max}$ saturates and grows linearly with U_∞ giving:

$$|v^*|_{\max} = 0.83(\mathrm{Re} - \mathrm{Re_c}). \tag{5.20}$$

The dependence of $x^*_{\max}$ on Re is shown in Fig. 5.18. At low Reynolds numbers $x^*_{\max}$ is ill-defined because the gradient $\mathrm{d}|v^*|/\mathrm{d}x^*$ near $|v^*|_{\max}$ is very shallow which accounts for a certain amount of scatter in the data. An inverse square root relationship for $x^*_{\max}$ versus Re was suggested by Goujon-Durand *et al.* (1994). This introduces the problem that in the limit of small values of $\mathrm{Re} - \mathrm{Re_c}$, $x^*_{\max} \to \infty$. This is clearly not physical as $x^*_{\max}$ located at infinity implies an infinitely extended perturbation. Losses due to viscosity mean that in reality there must be some finite value of $x^*_{\max}$ at small values of $\mathrm{Re} - \mathrm{Re_c}$. The data are well fitted for Reynolds numbers $\mathrm{Re} - \mathrm{Re_c} = [0, 40]$ by:

$$x^*_{\max} = [0.035(\mathrm{Re} - \mathrm{Re_c})^{1/2} + 0.049]^{-1}, \tag{5.21}$$

implying that for $\mathrm{Re} - \mathrm{Re_c} \to 0$, $x^*_{\max} \to 20.4$.

Taking into account the change in behaviour of $|v^*|_{\max}$ as a function of Re at $\mathrm{Re} - \mathrm{Re_c} > 40$, one might reasonably assume a corresponding change in behaviour for $x^*_{\max}$ as a function of Re at $\mathrm{Re} - \mathrm{Re_c} > 40$. In the same way that $|v^*|_{\max}$ saturates with U_∞, $x^*_{\max}$ saturates with U_∞ too and is well fitted by the relationship:

$$x^*_{\max} = 0.98 + 118(\mathrm{Re} - \mathrm{Re_c})^{-1}. \tag{5.22}$$

Eq (5.22) asymptotes to 0.98 for $\mathrm{Re} \to \infty$. This is closer to the cylinder than other studies have indicated, but one can reasonably expect another change in the behaviour of $x^*_{\max}$ with $\mathrm{Re} - \mathrm{Re_c}$ at the onset of three-dimensional vortex shedding at $\mathrm{Re} = 180$, at which point Eq. (5.22) gives $x^*_{\max} = 1.9$.

The data for PEO 2900 do not closely follow the behaviours described by Eqs. (5.19)–(5.22). Although for low values of $\mathrm{Re} - \mathrm{Re_c}$ the agreement is good between the dilute solutions and water, for $\mathrm{Re} - \mathrm{Re_c} > 20$ the data behave as if the actual Reynolds number were lower than that given by $U_\infty d/\nu_0$. This means that the effects of shear-thinning cannot simply be accounted for by replacing the zero shear viscosity with an effective local viscosity which is a function of the local shear rate, as this would imply a higher effective Reynolds number.

Furthermore the changes seen for PEO 2900 cannot be shown to correspond to a single (lower) effective Reynolds number. For example, the

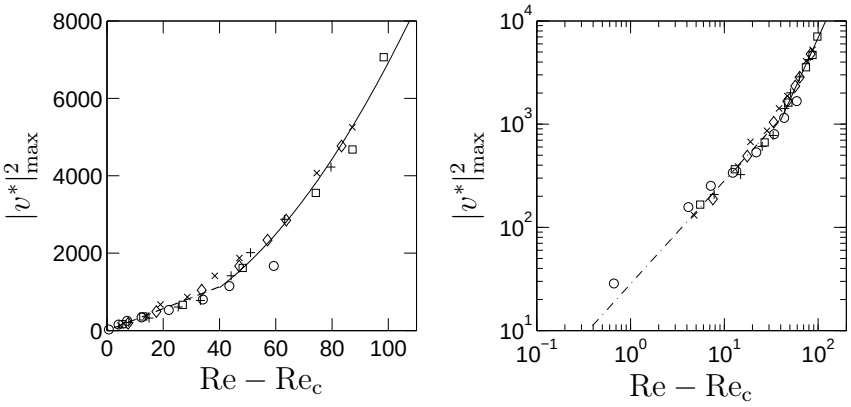

Fig. 5.17: $|v^*|^2_{\max}$ versus Re. Symbols: □ water; + PEO 500; ◊ PEO 1000; × PEO 1500; ◯ PEO 2900; with fits: $- \cdot -$ for $\mathrm{Re} - \mathrm{Re_c} < 40$ given by Eq. (5.19) and $-$ for $\mathrm{Re} - \mathrm{Re_c} > 40$ given by Eq. (5.20).

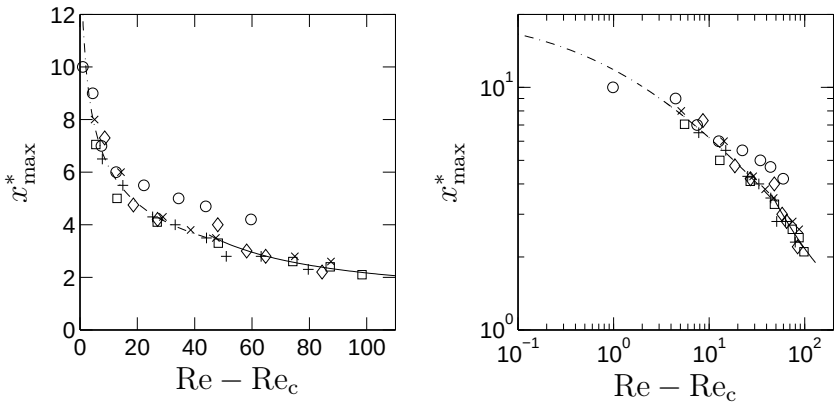

Fig. 5.18: $x^*_{\max}$ versus Re. Symbols: □ water; + PEO 500; ◊ PEO 1000; × PEO 1500; ◯ PEO 2900; with fits: $- \cdot -$ for $\mathrm{Re} - \mathrm{Re_c} < 40$ given by Eq. (5.21) and $-$ for $\mathrm{Re} - \mathrm{Re_c} > 40$ given by Eq. (5.22).

value of $|v^*|$ for PEO 2900 at $\mathrm{Re} = \mathrm{Re_c} + 60$ is equivalent to the data at $\mathrm{Re} = \mathrm{Re_c} + 45$ for the other fluids. However, examination of $x^*_{\max}$ shows that the value for PEO 2900 at $\mathrm{Re} = \mathrm{Re_c} + 60$ is equivalent to a Reynolds number of $\mathrm{Re} = \mathrm{Re_c} + 25$ for the other solutions. Thus the change in the location of the maximum velocity fluctuations and the change in velocity fluctuation amplitude cannot simply be parameterized by Re.

Summary of results for LDA measurements

The transverse velocity fluctuation profiles along the centreline for water and the dilute polymer solutions exhibit similar maximum values which occur at the same locations. The profiles for PEO 2900, however, show a reduced fluctuation amplitude in relation to the other fluids. Furthermore they show an even stronger trend for $x^*_{\max}$ to be further downstream than seen for the other fluids.

5.6 PIV velocity fields

Results from mean and phase-averaged PIV measurements are shown for water, PEO 1500 and PEO 2900 at Re $\approx$ $\mathrm{Re_c}$ + 6 and Re $\approx$ $\mathrm{Re_c}$ + 50. Firstly, data are presented for the streamwise and transverse velocity fluctuation amplitudes $|u^*|$ and $|v^*|$, the time-averaged streamwise and transverse velocities $\bar{u}$ and $\bar{v}$, the time-averaged vorticity $\bar{\omega}$ and the time-averaged shear and extensional stress $\bar{\sigma}_{xy}$ and $\bar{\sigma}_{xx}$, where an overbar signifies a time-averaged quantity. These results will then be used to explore the stability of the mean flow which will be followed by an examination of the vortex shedding cycle using the phase-averaged PIV measurements. The following non-dimensionalizations will be used :

$$
\begin{aligned}
|u^*| &= |u| \left(\frac{d}{\nu_0}\right), & |v^*| &= |v| \left(\frac{d}{\nu_0}\right), \\
u^* &= \frac{u}{U_\infty}, & v^* &= \frac{v}{U_\infty}, \\
\omega^* &= \omega \left(\frac{d}{U_\infty}\right), & & \\
\sigma^*_{xy} &= \sigma_{xy} \left(\frac{d}{U_\infty \eta_0}\right), & \sigma^*_{xx} &= \sigma_{xx} \left(\frac{d}{U_\infty \eta_0}\right).
\end{aligned}
$$

To simplify the presentation of the data, fluid stresses will be discussed in terms of the total shear stress and the average mean extensional stress:

$$
\begin{aligned}
\sigma^*_{xy} + \sigma^*_{yx} &= (\sigma_{xy} + \sigma_{yx}) \frac{d}{U_\infty \eta_0}, \\
0.5(\sigma^*_{xx} - \sigma^*_{yy}) &= 0.5(\sigma_{xx} - \sigma_{yy}) \frac{d}{U_\infty \eta_0}.
\end{aligned}
$$

5.6.1 Time averaged velocity fields

Re $\approx$ $\mathrm{Re_c}$ + 6: velocity fluctuation amplitudes

The mean streamwise and transverse velocity fluctuations $|u^*|$ and $|v^*|$ are shown in Fig. 5.19 and Fig. 5.20 for the three fluids studied. The Reynolds numbers corresponding to the measurements are $\mathrm{Re_c}$+4.8 for water, $\mathrm{Re_c}$+8.1 for PEO 1500 and $\mathrm{Re_c}$ + 6.5 for PEO 2900. The intensity and distribution of fluctuations is proportional to the distance above $\mathrm{Re_c}$ which explains the differences between the measurements for the three fluids. In this light, the three sets of data are in good agreement with each other and also with the velocity fields of Nishioka & Sato (1978) and Paranthoën *et al.* (1999).

Table 5.5 gives the values of $|v^*|_{\max}$ and $x^*_{\max}$ found from the PIV data. The values of $|v^*|_{\max}$ are in good agreement with the fit from the LDA measurements (Eq. (5.20)). The PIV results, however, give values of $x^*_{\max}$ that are 0.5–1 lower than the predictions from Eq. (5.22). As discussed previously, the precise location of $|v^*|_{\max}$ close to the onset of vortex shedding is ill-defined because of the shallow gradient $\partial|v^*|/\partial x^*$ and the streamwise distance where $|v^*|$ is greater than $0.99|v^*|_{\max}$ is indicated as the error.

Comparing Figs. 5.19 and 5.20 we can see that $|v^*|_{\max}$ is greater than $|u^*|_{\max}$, which justifies the use of $|v^*|$ rather than $|u^*|$ to find $\mathrm{Re_c}$ in Section 5.2. Furthermore $|v^*|_{\max}$ is on the centreline which is simpler to locate than the regions of maximum $|u^*|$ which are at $y^* \approx 0.75$.

In the region of $(x^* = 6, y^* = 3)$ there is some error due to light reflected from the hot film probe, for example, in Fig. 5.19(a). The flow is not physically perturbed but the error is introduced during the PIV cross correlation process. As explained in 4.2.4, the images were cleaned by subtracting the average image. Although this reduced the effects of reflections, it did not remove them completely.

$\mathbf{Re \approx Re_c + 6}$: mean velocities

Figure 5.21 shows the mean streamwise flow velocity $\bar{u}^*$ for water, PEO 1500 and PEO 2900. The contour $\bar{u}^* = 0.7$ shows that the wake for water develops over the longest streamwise distance and the wake for PEO 1500 over the shortest. Also the velocity overshoot $\bar{u}^* = 1.1$ is smaller for water than for the other two fluids. However, these differences are small and consistent with the variation in $\mathrm{Re} - \mathrm{Re_c}$ between the three sets of measurements.

The location of the mean free stagnation point in the wake x^*_{SP} and the location of minimum u, $x^*_{\min}$, are shown in Table 5.5. The values were determined by a linear interpolation of u^* and $\partial u^*/\partial x^*$ on the centreline to find $u^* = 0$ and $\partial u^*/\partial x^* = 0$. x^*_{SP} is plotted as a function of $\mathrm{Re} - \mathrm{Re_c}$ in Fig. 5.26 and agrees well with the measurements of Nishioka & Sato (1978) and Paranthoën *et al.* (1999). The data show a slight trend of decreasing x^*_{SP} and $x^*_{\min}$ with increasing concentration. However, the decrease in x^*_{SP} and $x^*_{\min}$ with polymer concentration is small and is likely to be due to an alignment error in the data rather than the influence of polymer additives. Given that the width of a PIV interrogation window is $0.12d$ and the alignment of the reference target for the PIV measurements was accurate to $\pm 0.05d$, it is reasonable to expect an error of ± 0.1 in x^*.

The mean transverse velocity $\bar{v}^*$ fields (Fig. 5.22) indicate that there is an asymmetry in the flow between the top and bottom half of the vortex street. Examining the maximum and minimum of $\bar{v}^*$ we can see that the magnitude

of $\bar{v}^*_{\max}$ is about $0.04U_\infty$ greater than that of $\bar{v}^*_{\min}$ and that $\bar{v}^*_{\max}$ is up to $1.5d$ further downstream than $\bar{v}^*_{\min}$. The phenomenon is present in all the data, suggesting that it is not an artefact of the velocity field alignment. However, the effect becomes smaller with increasing concentration, which corresponds to an increase in U_∞. This asymmetry could be partly due to the presence of the hot film probe and the vertical supports holding the end-plates (see Section 4.1.3). These are only present in the top half of the test section and the decrease in local cross-sectional area that they cause is approximately 4%. This would tend to create a higher velocity in the upper half of the test section.

$\mathbf{Re \approx Re_c + 6}$: mean vorticity and stresses

The mean non-dimensional vorticity $\bar{\omega}^*$ is shown in Fig. 5.23 and is similar for all 3 fluids. The maximum magnitude of $\bar{\omega}^*$ occurs at the streamwise location measured nearest to the cylinder and $y^* \approx \pm 0.7$. This is coherent with the expectation that maximum vorticity occurs in the cylinder boundary layers which detach from the cylinder at $y^* \approx \pm 0.5$.

The mean shear stresses are shown in Fig. 5.24. The maximum mean shear rates $\bar{\dot{\gamma}}_{xy}$ measured in the wake were 11.5 s^{-1}, 33.8 s^{-1} and 67.3 s^{-1} for water, PEO 1500 and PEO 2900 respectively. These values are shown in Table 5.5 for comparison with estimates of the shear rate U_e/δ at the shoulder of the cylinder calculated using the procedure outlined in Appendix B. The shear rates measured in the separated shear layer are approximately 25% of the estimated values in the attached boundary layer. While the theoretical value for PEO 2900 indicates that there was a 6% reduction in η in the cylinder boundary layer, shear-thinning effects were not large enough to alter the velocity distribution in the wake significantly. From the Oldroyd B model for the normal stresses (Eq. (3.14)), the maximum normal stresses for the region measured using PIV are approximately 0.3% and 1% of the peak shear stress for PEO 1500 and PEO 2900, respectively.

Figure 5.25 shows the mean extensional stresses $0.5(\bar{\sigma}^*_{xx} - \bar{\sigma}^*_{yy})$. The regions where the extensional stresses are highest coincide with the regions where the mean shear stress is close to zero and vice versa. $\bar{\sigma}_{zz} = (\bar{\sigma}_{xx} + \bar{\sigma}_{yy})$ is equal to zero to within experimental accuracy indicating that there is no significant velocity gradient normal to the x-y plane. The Oldroyd B model (Eq.(3.15)) predicts no significant change in the extensional viscosity at these extension rates.

Fluid	Re	$\lvert v^*\rvert_{\max}$		$x^*_{\max}$		x^*_{SP}	$x^*_{\min}$	$\dot{\gamma}_{xy}$ (s^{-1})	U_e/δ (s^{-1})		η/η_0
		PIV	Eq. 5.20	PIV	Eq. 5.22				Blasius	Thwaites	
Water	$\mathrm{Re_c}+4.8$	11.1	11.7	7.0 ± 1	7.95	2.2	0.8	11.5	47.5	44.7	–
PEO 1500	$\mathrm{Re_c}+8.1$	17.2	15.1	5.5 ± 1	6.70	2.1	0.7	33.8	143	132	1.00
PEO 2900	$\mathrm{Re_c}+6.5$	15.8	13.6	6.6 ± 1	7.23	2.0	0.6	67.3	302	279	0.94
Water	$\mathrm{Re_c}+54.3$	44.6	45.1	2.9 ± 0.5	3.15	1.5	0.7	24.7	108	101	–
PEO 1500	$\mathrm{Re_c}+49.9$	46.4	41.4	3.0 ± 0.5	3.34	1.5	0.6	65.2	296	273	0.99
PEO 2900	$\mathrm{Re_c}+47.2$	37.4	39.2	3.7 ± 0.5	3.48	1.8	0.7	129	607	561	0.86

Table 5.5: Results from PIV data: maximum transverse velocity fluctuations $\lvert v^*\rvert_{\max}$ and location of maximum transverse velocity fluctuations $x^*_{\max}$ and comparison with fits from LDA data; location of mean free stagnation point x^*_{SP} and location of minimum velocity U in the wake $x^*_{\min}$; approximate shear rate at cylinder shoulder based on the exterior velocity from potential theory $U_\mathrm{e} = 2U_\infty$ and the boundary layer thickness δ given by the Blasius solution (Schlichting, 1968, pp. 154–160) and the method of Thwaites (Thwaites, 1949); local reduction in viscosity η/η_0 due to shear rate at cylinder shoulder.

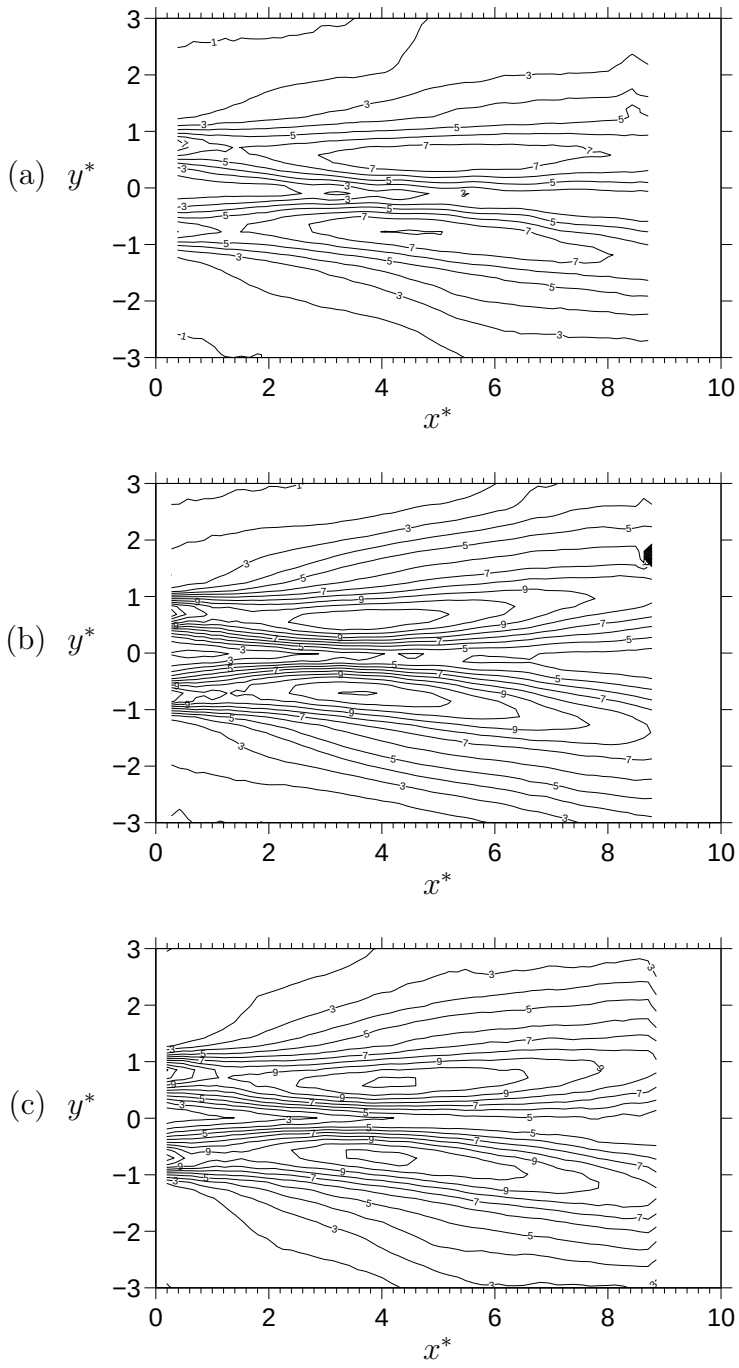

Fig. 5.19: Streamwise velocity fluctuations $|u^*|$ at Re $\approx$ Re$_c$ + 6 for (a) water, (b) PEO 1500 and (c) PEO 2900.

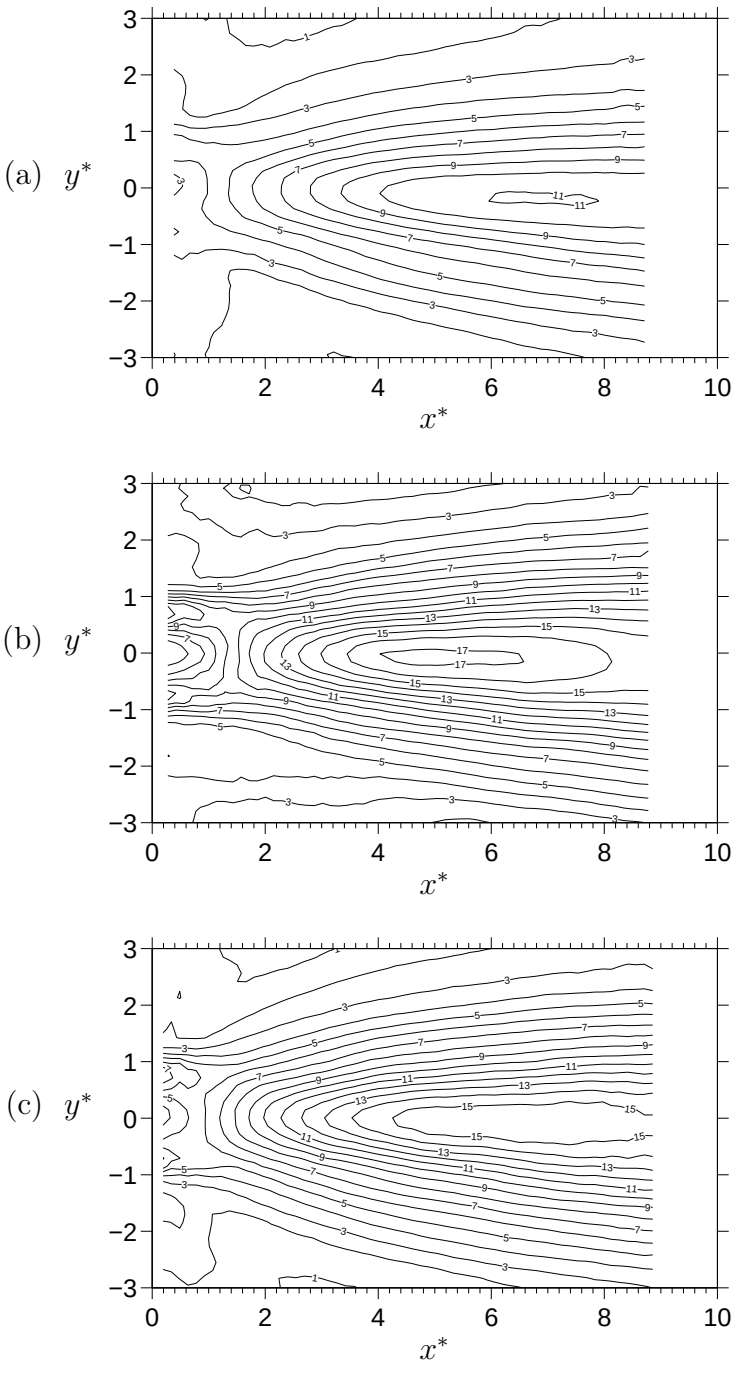

Fig. 5.20: Transverse velocity fluctuations $|v^*|$ at $\mathrm{Re} \approx \mathrm{Re_c} + 6$ for (a) water, (b) PEO 1500 and (c) PEO 2900.

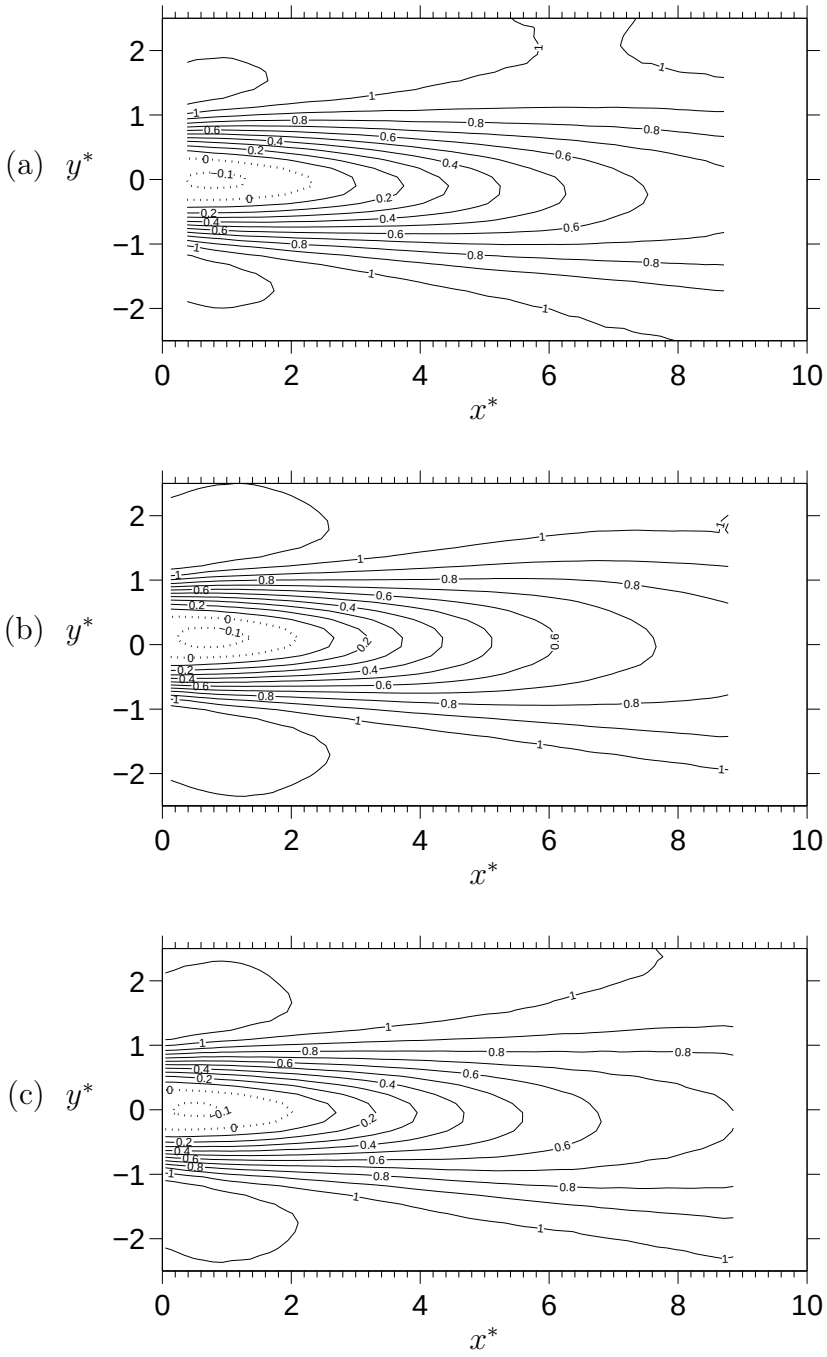

Fig. 5.21: Mean streamwise velocity $\bar{u}^*$ at Re $\approx$ Re$_c$ + 6 for (a) water, (b) PEO 1500 and (c) PEO 2900. Full lines indicate $\bar{u}^* > 0$ and dotted lines indicate $\bar{u}^* \leq 0$.

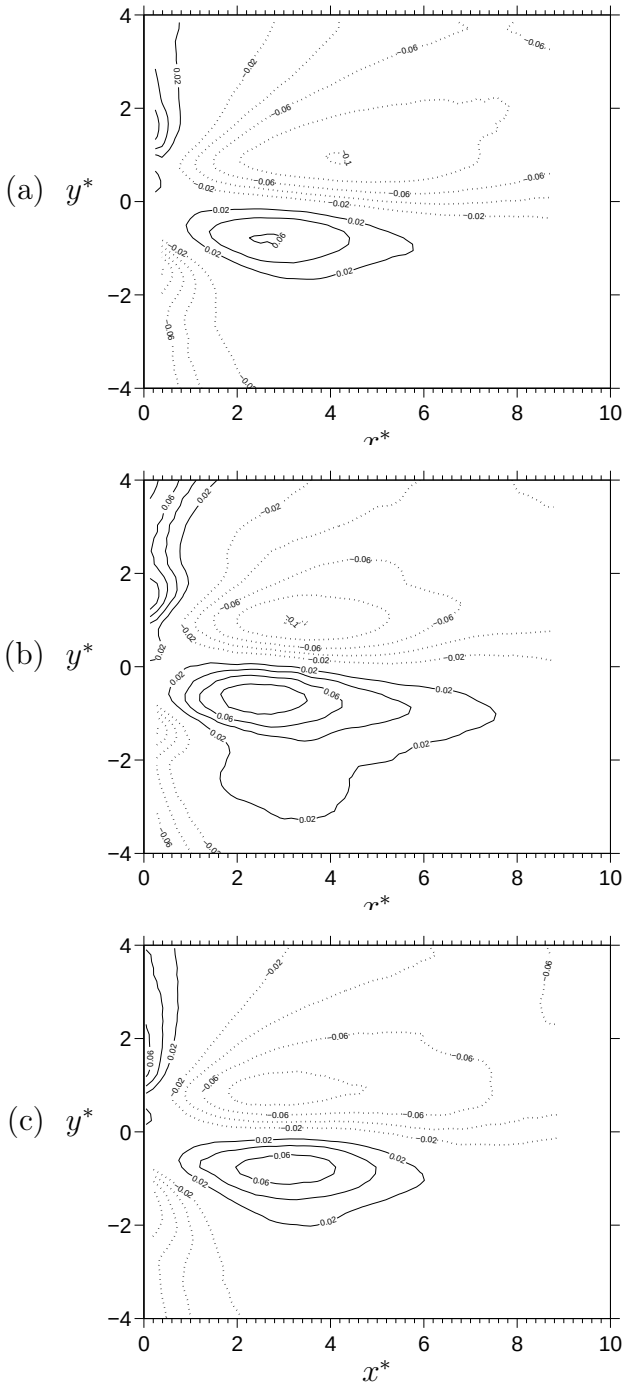

Fig. 5.22: Mean transverse velocity $\bar{v}^*$ at Re $\approx$ Re$_c$ + 6 for (a) water, (b) PEO 1500 and (c) PEO 2900. Full lines show $\bar{v}^* > 0$ and dotted lines show $\bar{v}^* < 0$.

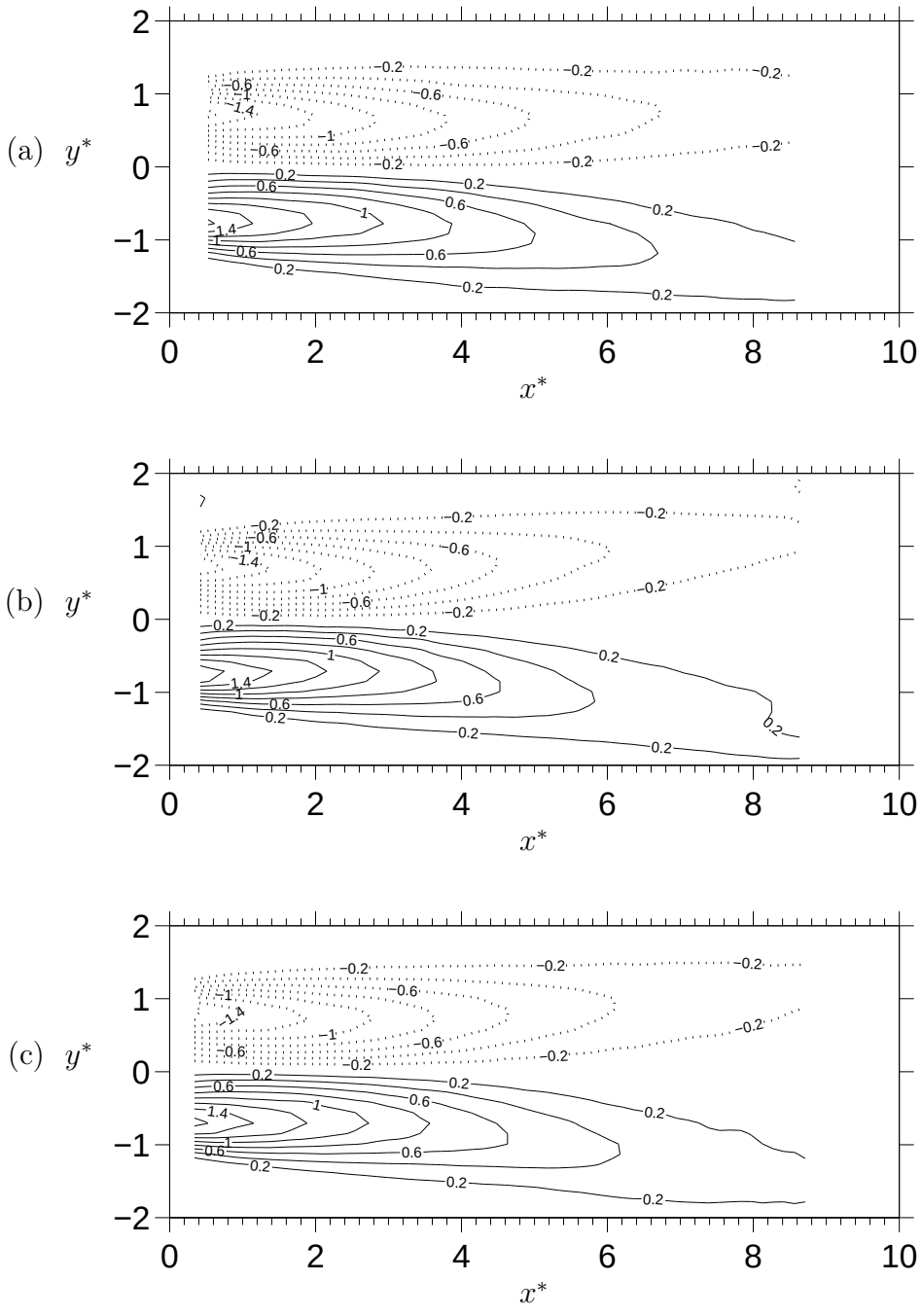

Fig. 5.23: Mean vorticity $\bar{\omega}^*$ at Re $\approx$ Re$_c$ + 6 for (a) water, (b) PEO 1500 and (c) PEO 2900. Full lines show $\bar{\omega}^* > 0$ and dotted lines show $\bar{\omega}^* < 0$.

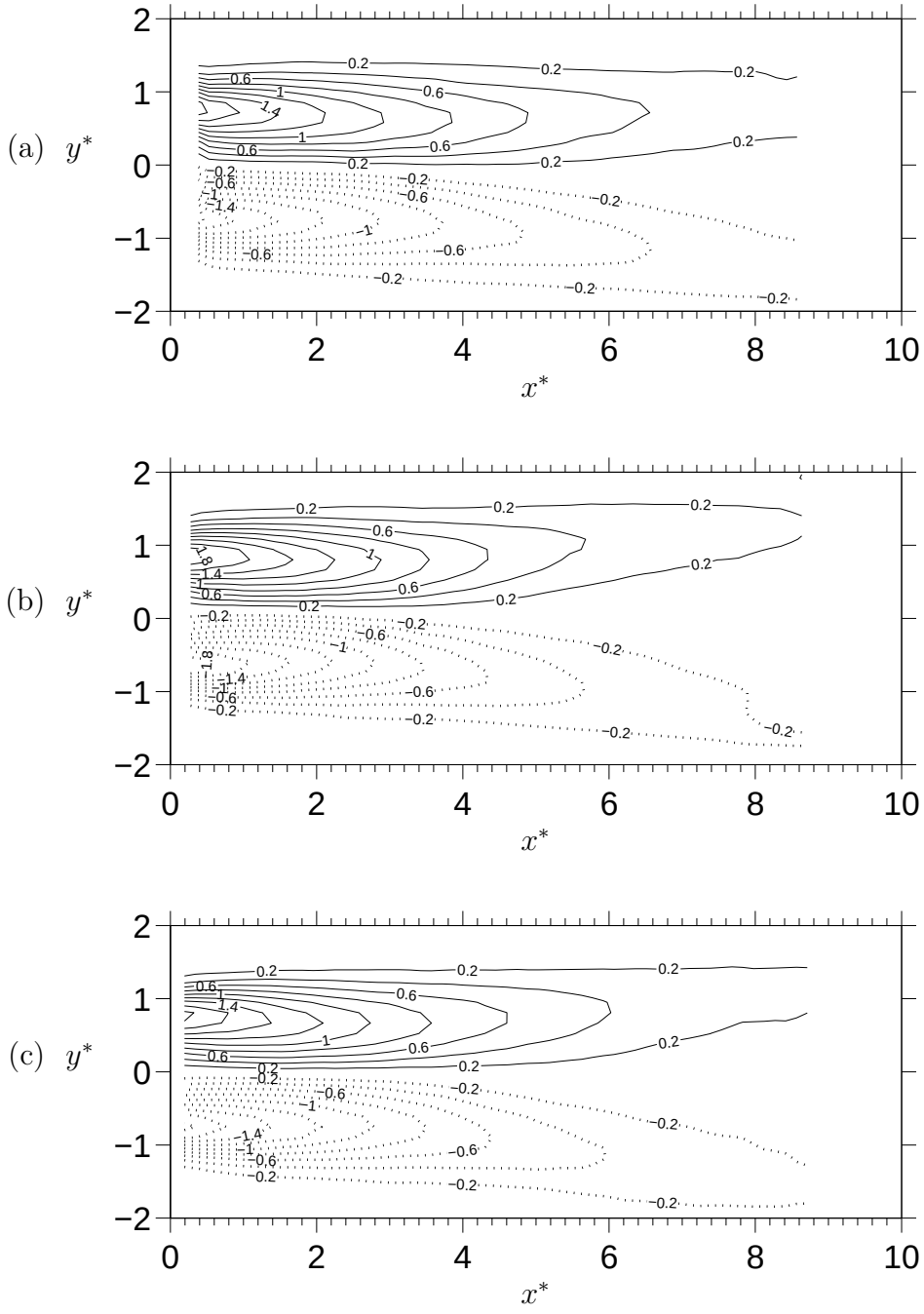

Fig. 5.24: Mean shear rate $\bar{\sigma}^*_{xy} + \bar{\sigma}^*_{yx}$ at Re $\approx$ Re$_c$ + 6 for (a) water, (b) PEO 1500 and (c) PEO 2900. Full lines show $\bar{\sigma}^*_{xy} + \bar{\sigma}^*_{yx} > 0$ and dotted lines show $\bar{\sigma}^*_{xy} + \bar{\sigma}^*_{yx} < 0$.

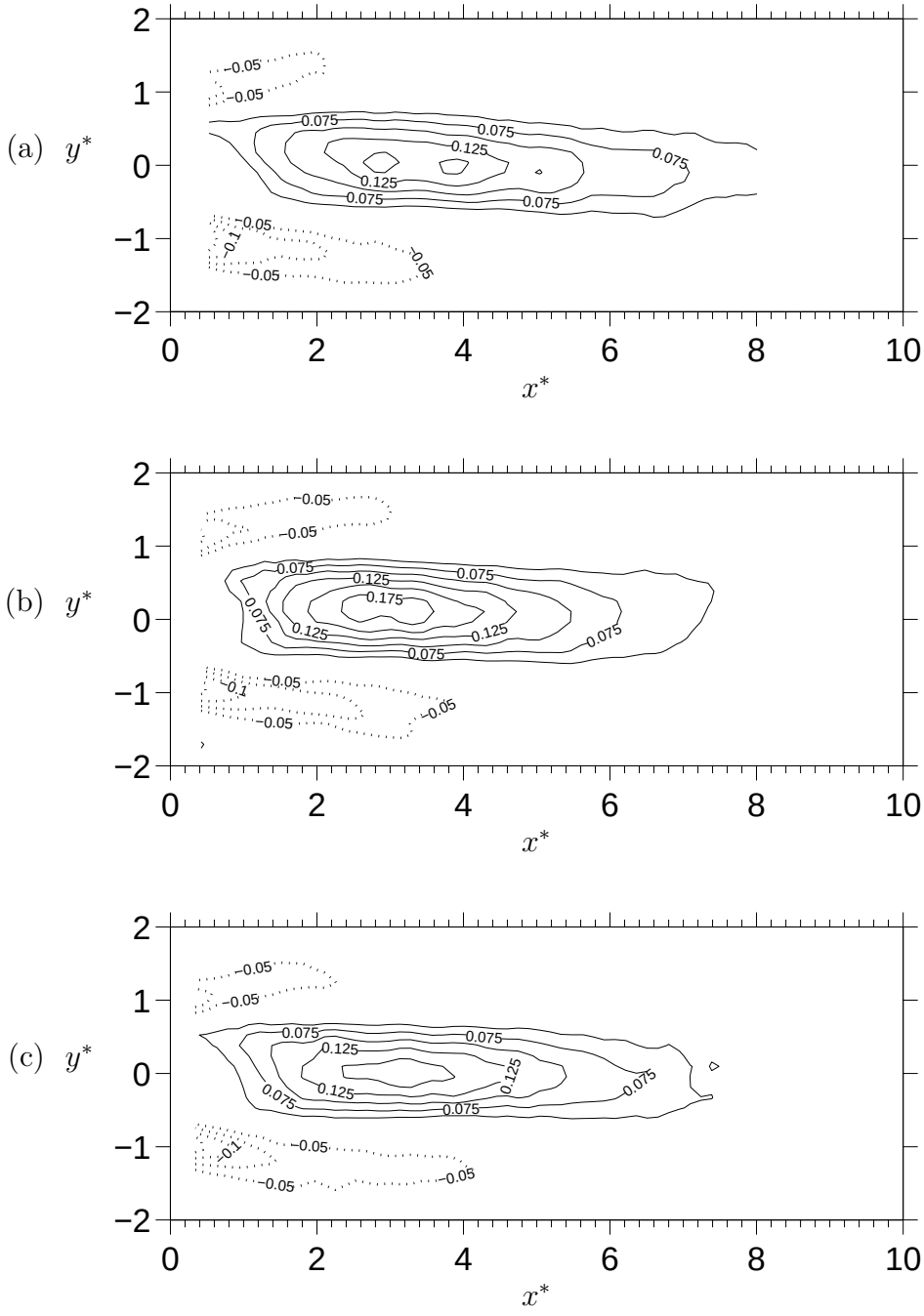

Fig. 5.25: Mean rate of extension $0.5(\bar{\sigma}^*_{xx} - \bar{\sigma}^*_{yy})$ at Re $\approx$ Re$_c$ + 6 for (a) water, (b) PEO 1500 and (c) PEO 2900. Full lines show $0.5(\bar{\sigma}^*_{xx} - \bar{\sigma}^*_{yy}) > 0$ and dotted lines show $0.5(\bar{\sigma}^*_{xx} - \bar{\sigma}^*_{yy}) < 0$.

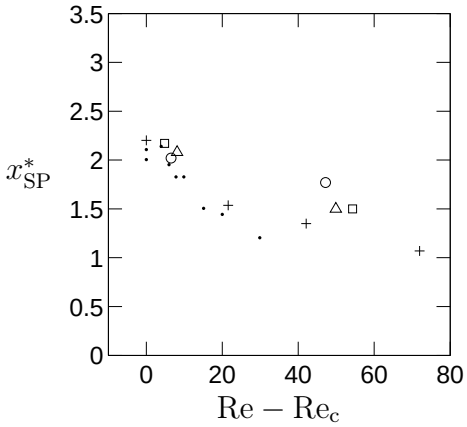

Fig. 5.26: Location of the mean free stagnation point x^*_{SP}. Symbols: □ water; △ PEO 1500; ◯ PEO 2900; · Paranthoën *et al.* (1999); + Nishioka & Sato (1978). The data from other studies have been plotted in terms of the coordinate system used in the present work.

$\mathbf{Re \approx Re_c + 50}$: velocity fluctuation amplitudes

$|u^*|$ and $|v^*|$ at $\mathrm{Re} \approx \mathrm{Re_c} + 50$ for water, PEO 1500 and PEO 2900 are shown in Figs. 5.31 and 5.32. The exact values of Re for the three fluids are $\mathrm{Re_c} + 54.3$ for water, $\mathrm{Re_c} + 49.9$ for PEO 1500 and $\mathrm{Re_c} + 47.2$ for PEO 2900. The location and the magnitude of $|v^*|_{\max}$ for water and PEO 1500 are very close (the values are given in Table 5.5), which is to be expected because the difference between the two values of $\mathrm{Re} - \mathrm{Re_c}$ is only 9%. As previously seen for the LDA measurements, $|v^*|_{\max}$ for PEO 2900 is lower and $x^*_{\max}$ is further downstream in comparison to the other fluids. Similarly to $\mathrm{Re} \approx \mathrm{Re_c} + 6$, values of $|v^*|$ from the PIV data are closer to the cylinder than for the LDA measurements. The range of x^* where $|v^*| > 0.99|v^*|_{\max}$ is shown as the uncertainty and suggests that the two sets of results are in good agreement. Some error due to reflections from the hot film are visible at $(x^* = 8, y^* = 2.5)$ similar to the PIV measurements at $\mathrm{Re} \approx \mathrm{Re_c} + 6$.

Figure 5.32 shows that at $x^* < 0.5$ the transverse velocity fluctuations in the shear layers leaving the cylinder are altered for the polymer solutions. PEO 1500 and PEO 2900 exhibit local peaks in $|v^*|$ at $y \approx \pm 0.75$ where there are none for water. This is also illustrated in the cross section velocity profiles shown in Fig. 5.27. The transverse velocity fluctuations for the polymer solutions are concentrated over a narrower region and the gradients

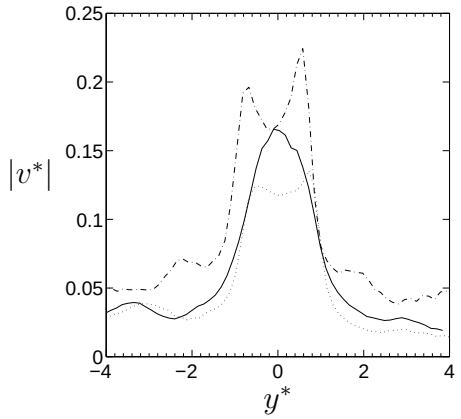

Fig. 5.27: Transverse slice through the $|v^*|$ field at $x^* = 0.5$ for Re $\approx$ Re$_c$+50. Symbols: – water; $- \cdot -$ PEO 1500; $\cdots$ PEO 2900.

are steeper. The peaks for PEO 2900 are smaller than for PEO 1500 which corresponds to the overall reduction in $|v^*|$ at this concentration. For the polymer solutions, the large shear rates near where the boundary layer detaches from the cylinder induce significant normal stresses acting towards the cylinder and these are thought to cause the redistribution of $|v^*|$. There is no significant change in $|u^*|$, although the normal stresses would not necessarily act in the same way on the streamwise velocity fluctuations which are perpendicular to the normal forces.

The reduction in velocity fluctuations for PEO 2900 occurs throughout the measured velocity field. Because the instability perturbations originate in the separated shear layers it is reasonable to assume that any global changes in the perturbation field originate in this region. The two major non-Newtonian effects acting in the shear layers are shear-thinning and normal forces. As previously seen for the LDA data, PEO 2900 is the only fluid to exhibit a measurable reduction in $|v^*|$. This effect correlates with the predicted onset of shear-thinning in the cylinder boundary layer which might suggest that the two are linked. The possible mechanism for reduced perturbations due to shear-thinning could be that a lower viscosity results in a lower transmission of stresses ($\sigma_{xy} = \eta\dot{\gamma}_{xy}$).

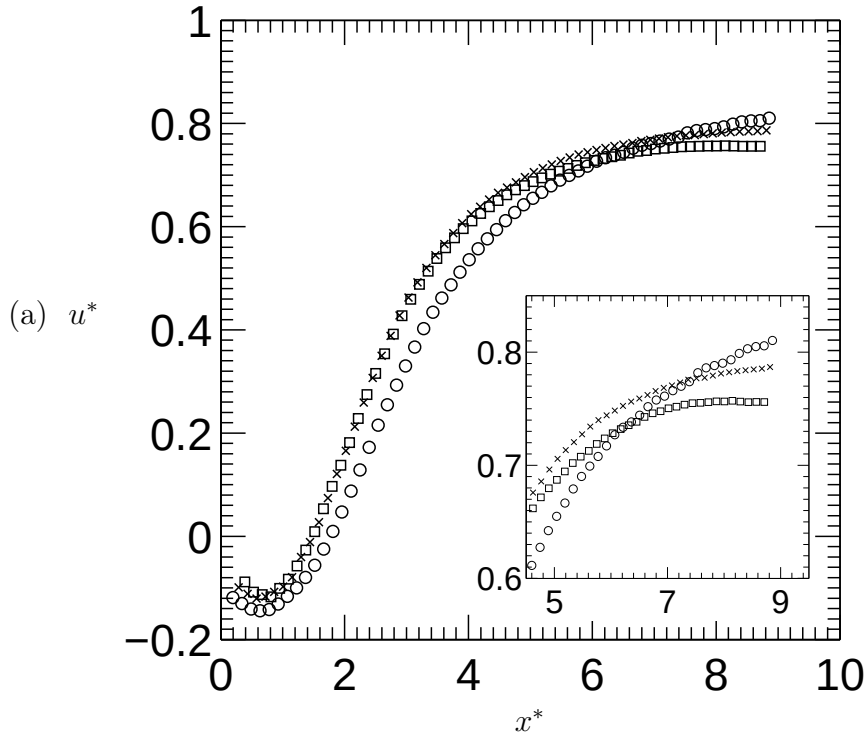

Fig. 5.28: Streamwise time-averaged velocity profiles on the centreline in the wake of a cylinder. Symbols: □ water; × PEO 1500; ◯ PEO 2900.

$\mathbf{Re \approx Re_c + 50}$: mean velocities

The mean non-dimensionalized streamwise velocity $\bar{u}^*$ is shown in Fig. 5.33. Near to the cylinder, for $x^* < 2$, PEO 2900 displays significant differences compared to the two other fluids. Table 5.5 and Fig. 5.26 show that for PEO 2900 x^*_{SP} is located further downstream and that the negative streamwise velocity on the centreline is greater. The downstream shift in x^*_{SP} matches with the downstream shift seen in x^*_{max}.

Further downstream, the development of the wake on the centreline at $x^* > 7$ is different for both PEO 1500 and PEO 2900 compared to the Newtonian case. The recovery of u^* to its freestream value is quicker for increasing polymer concentration. This can be seen in the centreline u^* profiles in Fig. 5.28, where u^* is approximately 6% greater for PEO 1500 and 8% greater for PEO 2900 compared to water. This bears a resemblance to the flows observed for the steady wakes of spheres (and bubbles) falling (rising)

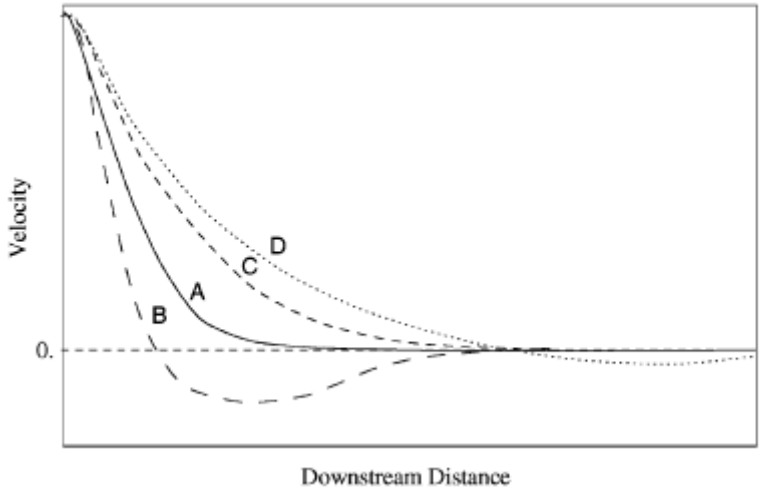

Fig. 5.29: Sketch of different streamwise velocity profiles on the centreline behind a sphere from Harlen (2002): 'A' corresponds to a Newtonian velocity profile while 'B', 'C' and 'D' indicate various experimentally observed non-Newtonian velocity profiles.

in polymer solutions. There are several behaviours identified for spheres moving through viscoelastic fluids (Sigli & Coutanceau, 1977; Hassager, 1979; Bisgaard, 1983) which are thought to depend on the solution used in the experiments, and these are summarized in Fig. 5.29 from Harlen (2002). As the sphere falls through the fluid, sometimes a 'negative wake' is observed, where the streamwise velocity in the wake has a component which is in the opposite direction to the motion of the sphere. This creates an overshoot in the velocity profile compared to the Newtonian fluid, illustrated by profiles 'B' and 'D' in Fig. 5.29.

The downstream increase in u for a polymer fluid in relation to the Newtonian case is explained by the polymer chains not parallel to the x-axis transferring streamwise momentum from the outer wake to the core wake region, as illustrated in Fig. 5.30 (also from Harlen (2002)). This seems reasonable because polymer chains in shear flow do not remain oriented to the principal direction of motion but rather they tumble while stretching and contracting (Liu, 1989; Smith *et al.*, 1999). Although the cylinder wake is unsteady in these experiments and the experimental conditions are not identical, a transfer of momentum via the dynamics of the polymer chains provides a possible explanation for the higher streamwise velocities at the centre of the wake for polymer solutions compared to a Newtonian fluid.

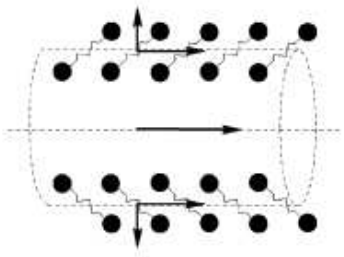

Fig. 5.30: Schematic of mechanism creating a 'negative wake' effect. Polymer chains not aligned parallel to the x-axis transfer streamwise momentum from the outer wake to the inner wake region. From Harlen (2002).

The distribution of the mean non-dimensional transverse velocity $\bar{v}^*$ is less asymmetric at $\mathrm{Re} = \mathrm{Re_c} + 50$ than for $\mathrm{Re} = \mathrm{Re_c} + 6$. The upper and lower halves of the vortex street develop in a spatially similar manner and the magnitude of the upper velocity is approximately 3% greater than for the lower half. This supports the previous observation that the difference between the two halves of the vortex street is reduced with increasing freestream velocity.

$\mathbf{Re \approx Re_c + 50}$: mean vorticity and stresses

The changes in velocity distribution for PEO 2900 compared to PEO 1500 and water are also apparent in the non-dimensional vorticity $\bar{\omega}^*$, shear stress $\bar{\sigma}_{xy}$ and extensional stress $\bar{\sigma}_{xx}$ fields, Figs. 5.35–5.37. The maximum measured values of $\bar{\dot{\gamma}}_{xy}$ are 65.2 s^{-1} and 129 s^{-1} for PEO 1500 and PEO 2900, respectively. These are not high enough to provoke significant shear-thinning in the region measured: for PEO 2900, 129 s^{-1} corresponds to a reduction in η of 1%. As previously discussed, the shear rates nearer the cylinder are much higher however. The shear rate estimated from the boundary layer thickness and local velocity at the shoulder of the cylinder (see Table 5.5) suggests that was high enough to reduce η by at least 10% for PEO 2900. This lends strong support to the hypothesis that shear-thinning was responsible for the changes in the cylinder wake velocity field.

The maximum rate of extension $\bar{\dot{\gamma}}_{xx}$ for PEO 2900 is approximately 17 s^{-1} and the Oldroyd B model predicts a 1% increase in the extensional viscosity η_{ext} for this level. Although this is only an indication, it would suggest that for these data changes in η_{ext} in the wake region probably had only a very small effect, but were on the verge of becoming significant. However, elsewhere in the flow round the cylinder, the changes in extensional viscosity

may have been more significant and detailed survey of the whole flow would be needed to give a more accurate picture.

Summary of results for time average PIV data

The PIV data near the onset of vortex shedding agree well with each other and with the LDA measurements. The higher Reynolds number data suggest that the shear-thinning causes the observed reduction in transverse velocity fluctuations in the wake for PEO 2900. Normal stresses are thought to create a redistribution of $|v^*|$ close to the cylinder observed at $\mathrm{Re} \approx \mathrm{Re}_c + 50$. Also a streamwise velocity overshoot is observed in the wake and a comparison is made to the negative wake for viscoelastic flow past spheres.

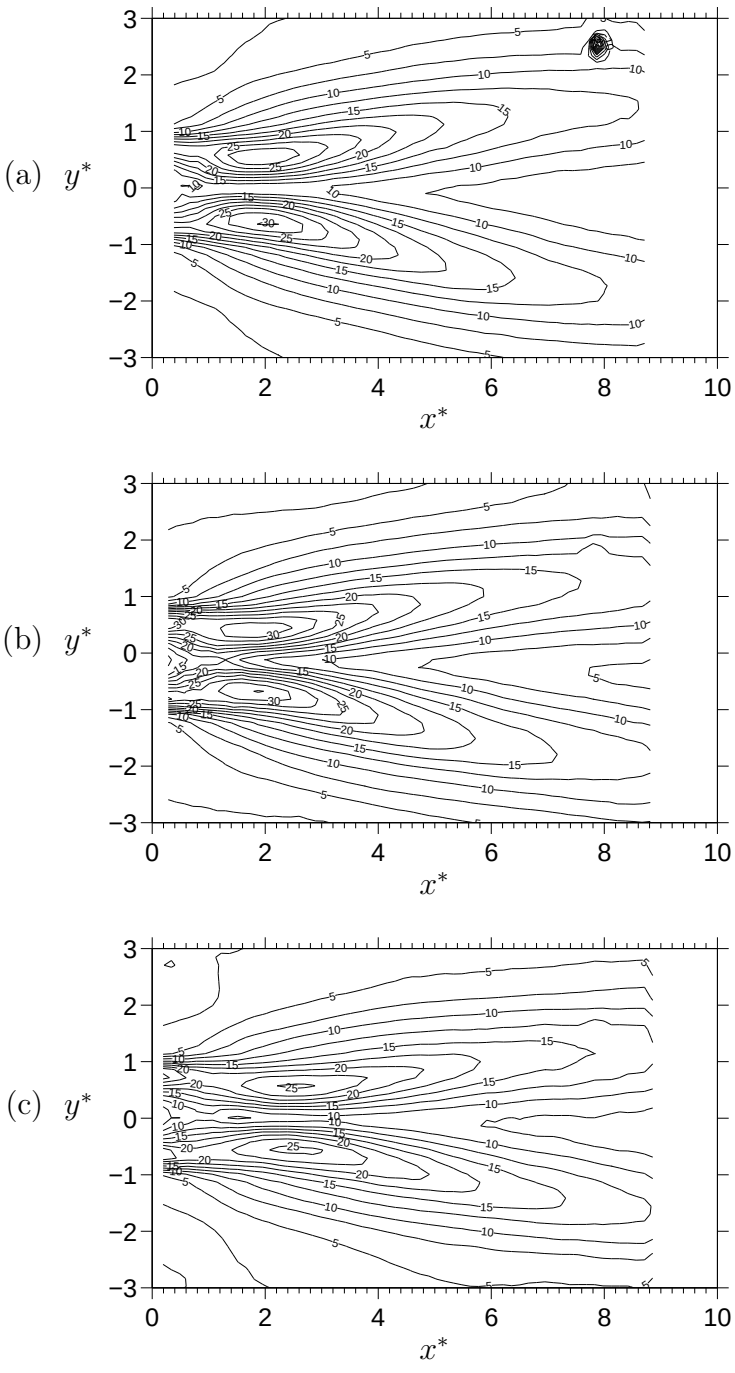

Fig. 5.31: Streamwise velocity fluctuations $|u^*|$ at Re $\approx$ Re$_c$ + 50 for (a) water, (b) PEO 1500 and (c) PEO 2900.

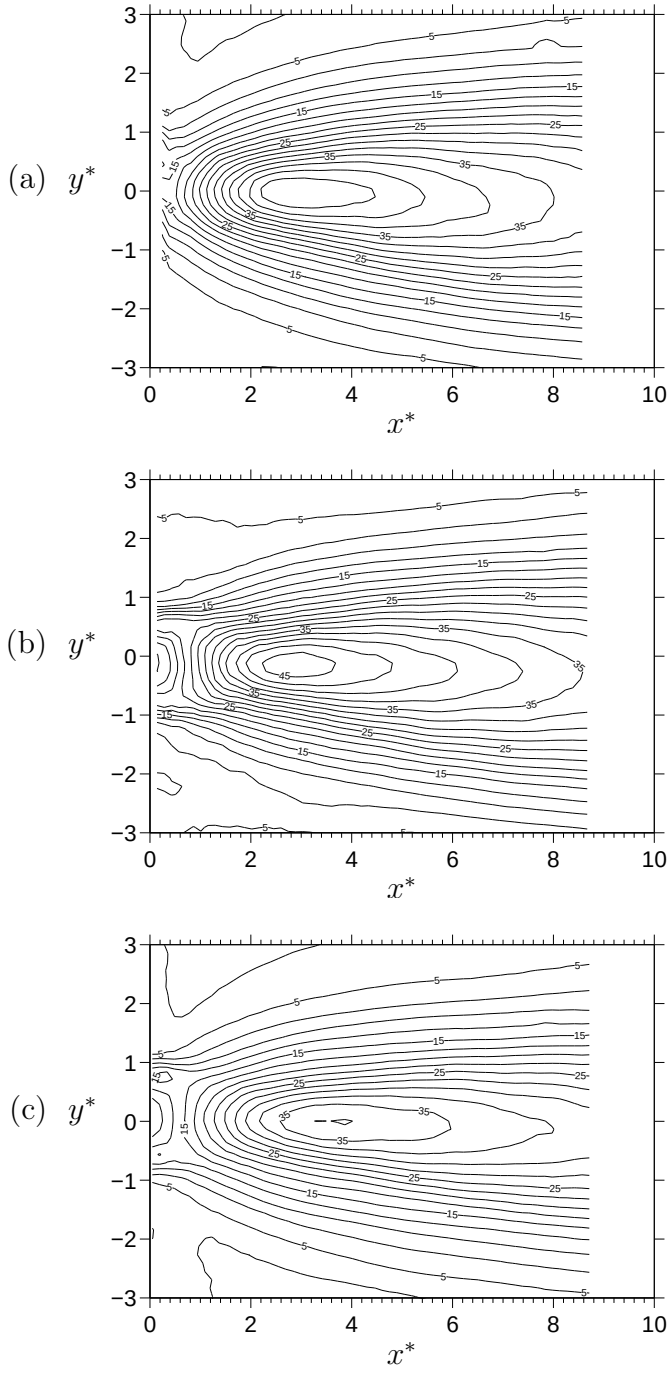

Fig. 5.32: Transverse velocity fluctuations $|v^*|$ at Re $\approx$ Re$_c$ +50 for (a) water, (b) PEO 1500 and (c) PEO 2900.

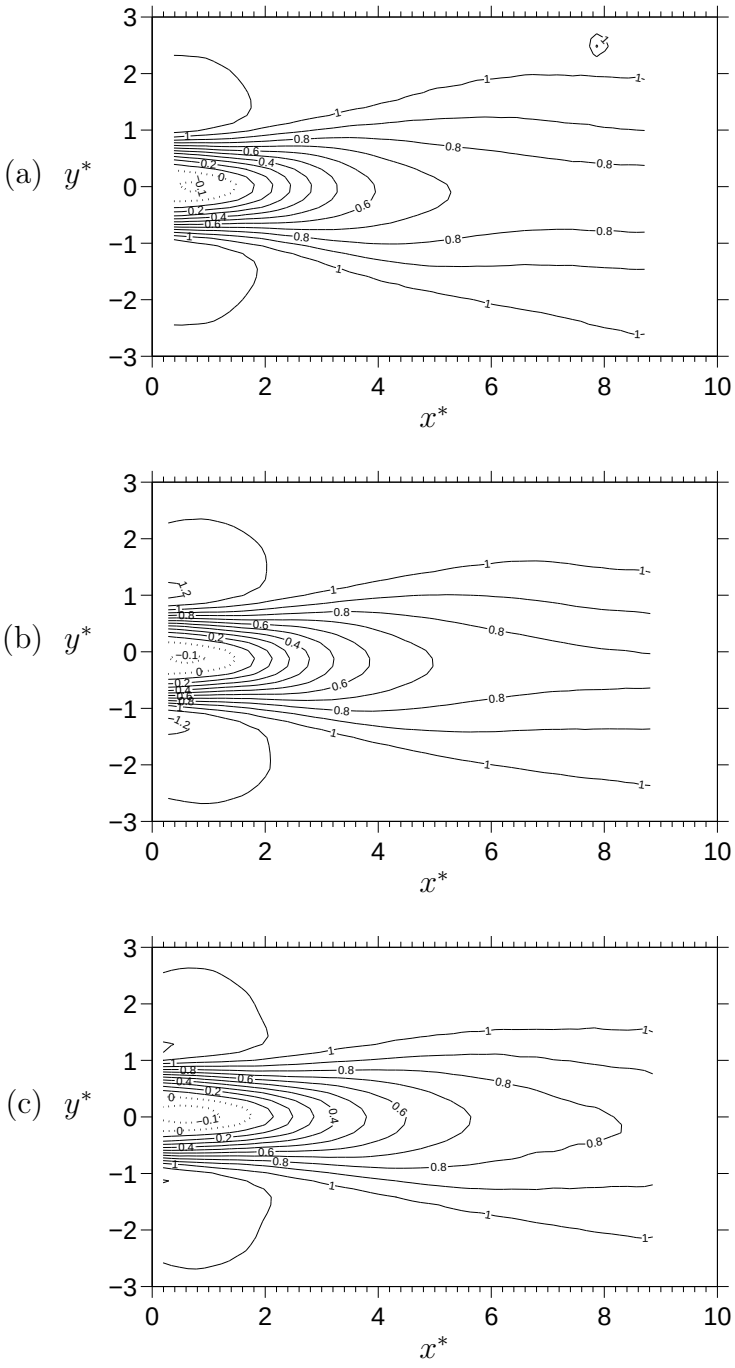

Fig. 5.33: Mean streamwise velocity $\bar{u}^*$ at Re $\approx$ Re$_c$ + 50 for (a) water, (b) PEO 1500 and (c) PEO 2900. Full lines indicate $\bar{u}^* > 0$ and dotted lines indicate $\bar{u}^* \leq 0$

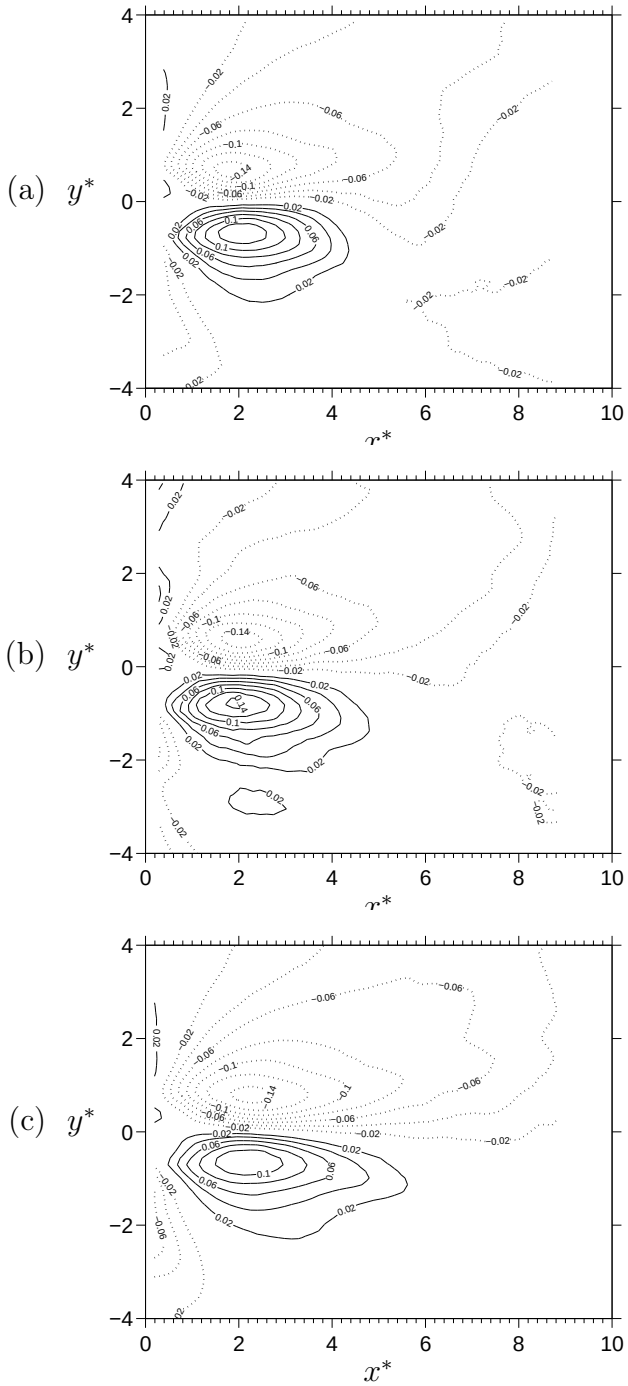

Fig. 5.34: Mean transverse velocity $\bar{v}^*$ at Re $\approx$ Re$_c$ + 50 for (a) water, (b) PEO 1500 and (c) PEO 2900. Full lines show $\bar{v}^* > 0$ and dotted lines show $\bar{v}^* < 0$.

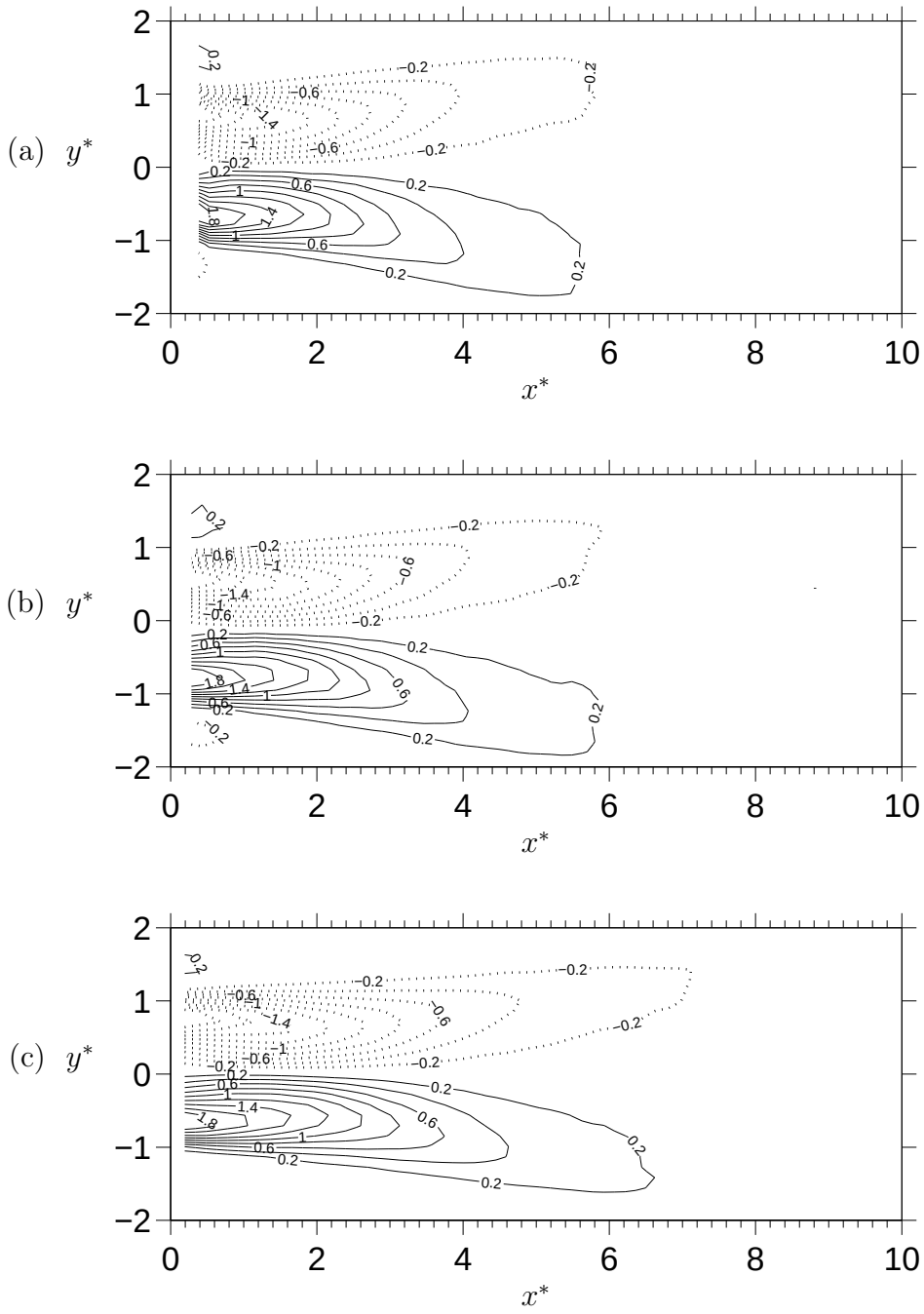

Fig. 5.35: Mean vorticity $\bar{\omega}^*$ at $\mathrm{Re} \approx \mathrm{Re_c} + 50$ for (a) water, (b) PEO 1500 and (c) PEO 2900. Full lines show $\bar{\omega}^* > 0$ and dotted lines show $\bar{\omega}^* < 0$.

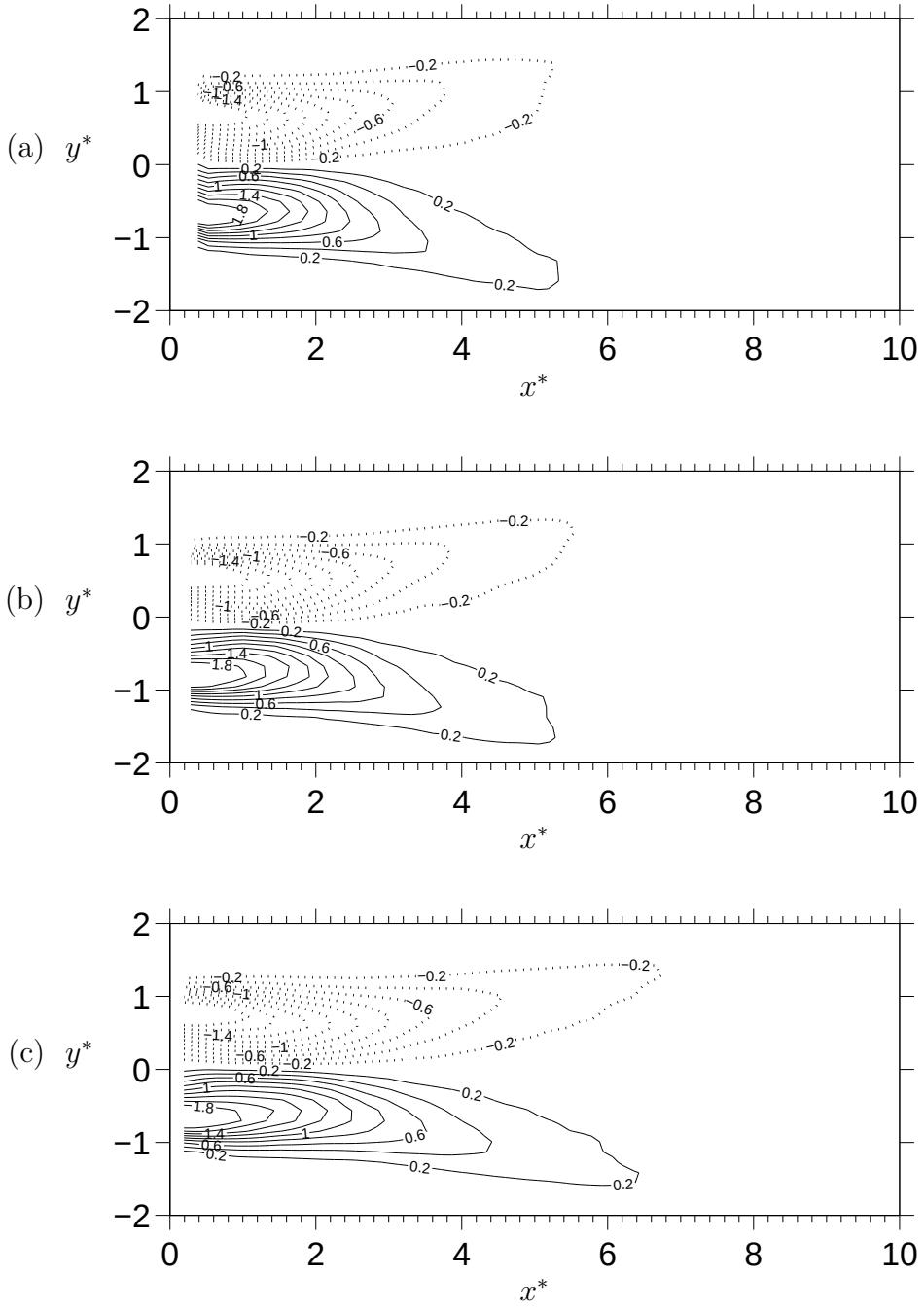

Fig. 5.36: Mean shear rate $\bar{\sigma}^*_{xy} + \bar{\sigma}^*_{yx}$ at Re $\approx$ Re$_c$ + 50 for (a) water, (b) PEO 1500 and (c) PEO 2900. Full lines show $\bar{\sigma}^*_{xy} + \bar{\sigma}^*_{yx} > 0$ and dotted lines show $\bar{\sigma}^*_{xy} + \bar{\sigma}^*_{yx} < 0$.

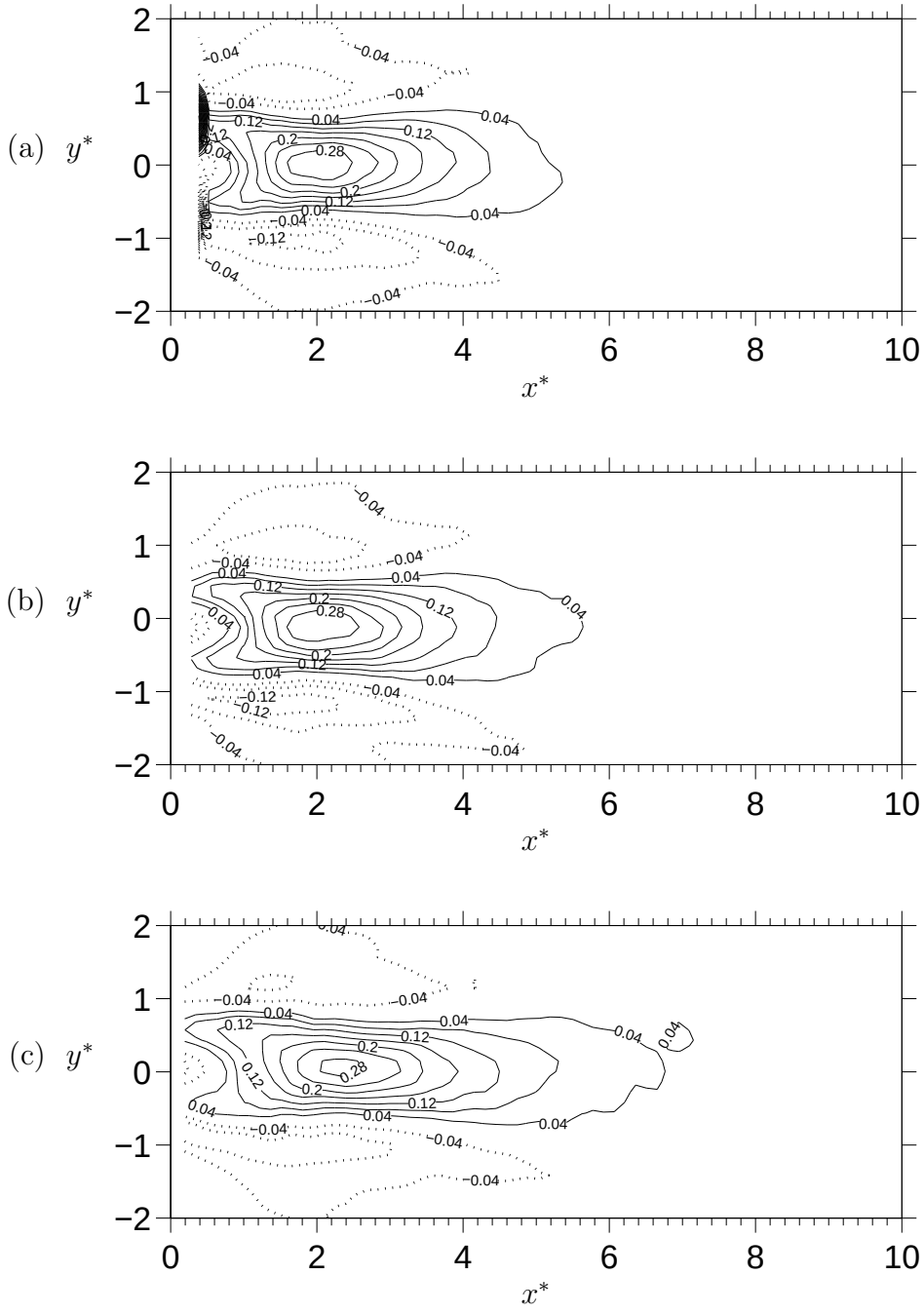

Fig. 5.37: Mean rate of extension $0.5(\bar{\sigma}^*_{xx} - \bar{\sigma}^*_{yy})$ at Re $\approx$ Re$_c$ + 50 for (a) water, (b) PEO 1500 and (c) PEO 2900. Full lines show $0.5(\bar{\sigma}^*_{xx} - \bar{\sigma}^*_{yy}) > 0$ and dotted lines show $0.5(\bar{\sigma}^*_{xx} - \bar{\sigma}^*_{yy}) < 0$.

5.6.2 Mean flow stability properties

Examination of the transverse $\bar{u}(y)$ velocity profiles as a function of the downstream distance provides information on the passage from convective to absolute stability in the wake of a bluff body (Monkewitz & Nguyen, 1987; Monkewitz, 1988). As discussed by Monkewitz & Nguyen the area of most importance for wake stability is that of mean recirculation downstream of the bluff body. In the following analysis two parameters that play an important role in the wake stability will be considered. The first of these is the velocity ratio Λ, defined as:

$$\Lambda = \frac{\bar{u}_{\mathrm{CL}} - \bar{u}_{\mathrm{max}}}{\bar{u}_{\mathrm{CL}} + \bar{u}_{\mathrm{max}}},$$

where $\bar{u}_{\mathrm{CL}}$ is the velocity on the wake centreline and $\bar{u}_{\mathrm{max}}$ refers to the maximum value of u. Λ provides a measure of the the mean recirculation in the wake, with $\Lambda = -1$ corresponding to a wake $\bar{u}_{\mathrm{CL}} = 0$ and $\Lambda < -1$ indicating $\bar{u}_{\mathrm{CL}} < 0$. Due to the limited spatial resolution of the PIV measurements the $\bar{u}(y)$ profiles were re-sampled using a standard low-pass interpolation technique as shown in Fig. 5.38. $\bar{u}_{\mathrm{max}}$ was found from the mean value of $\bar{u}_{\mathrm{max}}$ for $y^* < 0$ and $\bar{u}_{\mathrm{max}}$ for $y^* > 0$. Close to the cylinder the values given by $y^* < 0$ and $y^* > 0$ agreed to within $<0.5\%$ although for downstream distances $x > 5$ the difference between the two increased. The minimum value of $u(y)$ was used for $\bar{u}_{\mathrm{CL}}$.

The second quantity of interest is the vorticity thickness δ_ω which is defined as:

$$\delta_\omega = \frac{|\bar{u}_{\mathrm{max}} - \bar{u}_{\mathrm{CL}}|}{|\partial\bar{u}/\partial y|_{\mathrm{max}}} \tag{5.23}$$

and indicates the thickness of the shear layers. Figure 5.39 shows a typical $\partial\bar{u}/\partial y$ profile which is calculated using a second order finite difference scheme. To find $|\partial\bar{u}/\partial y|_{\mathrm{max}}$ the average value calculated for $y^* < 0$ and $y^* > 0$ was used. It is usual to introduce the characteristic length and velocity scale $y_{1/2}$ and $\bar{u}_{1/2}$ for each $\bar{u}(y)$ profile. The mean profile velocity $\bar{u}_{1/2}$ is defined as $(\bar{u}_{\mathrm{max}} + \bar{u}_{\mathrm{CL}})/2$ and the the local wake half width $y_{1/2}$ is given by the location at which $u(y_{1/2}) = \bar{u}_{1/2}$. $y_{1/2}$ was calculated by finding $\bar{u}_{1/2}$ for $y^* < 0$ and $y^* > 0$ and dividing the sum of the distance between them by two, as shown in Fig. 5.38. $\bar{u}_{1/2}$ and $y_{1/2}$ naturally give rise to the profile Reynolds number $\mathrm{Re_P} = \bar{u}_{1/2}y_{1/2}/\nu_0$.

$\mathbf{Re \approx Re_c + 6}$

Figure 5.41 shows the centreline velocity $\bar{u}_{\mathrm{CL}}$ for water, PEO 1500 and PEO 2900. As explained previously, close to the onset of vortex shedding

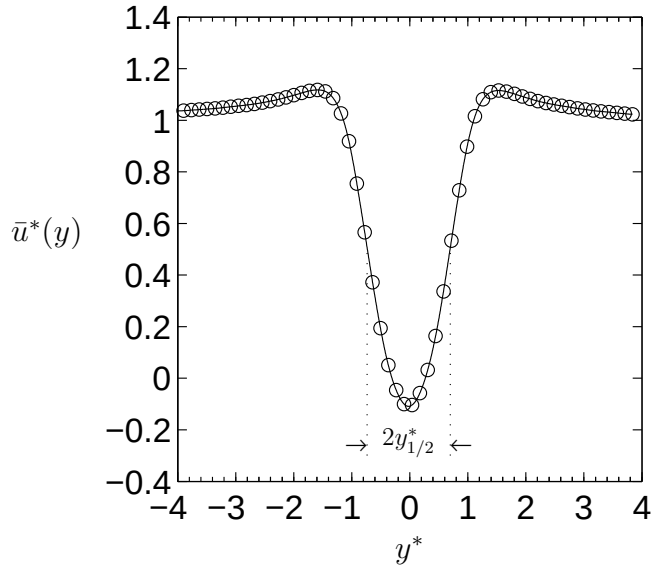

Fig. 5.38: $\bar{u}^*(y)$ profile at $x^*_{\min}$ for water, $\mathrm{Re} = \mathrm{Re_c} + 4.8$. Symbols: ◯ PIV data; — interpolated data.

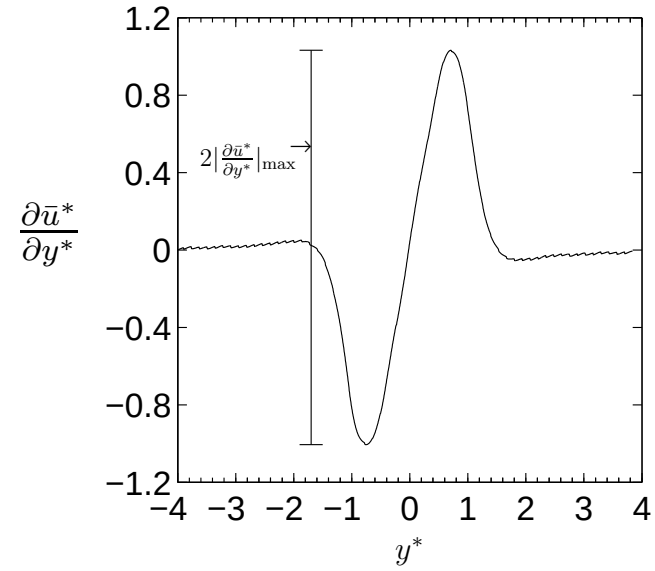

Fig. 5.39: Velocity gradient $\partial \bar{u}^*/\partial y^*$ for $\bar{u}(y)$ profile at $x^*_{\min}$ for water, $\mathrm{Re} = \mathrm{Re_c} + 4.8$.

Fluid	Re	$\mathrm{Re_P}$	$(\mathrm{Re_P})_{\mathrm{VK}}$	$\Lambda_{\min}$	$(\delta_\omega/y_{1/2})_0$	N^{-1}
Water	$\mathrm{Re_c}+4.8$	21.6	20.2	-1.24	1.06	0.536
PEO 1500	$\mathrm{Re_c}+8.1$	24.0	22.0	-1.25	1.09	0.554
PEO 2900	$\mathrm{Re_c}+6.5$	25.2	23.1	-1.22	1.12	0.573
Water	$\mathrm{Re_c}+54.3$	35	—	-1.22	1.01	0.505
PEO 1500	$\mathrm{Re_c}+49.9$	36.2	—	-1.22	1.04	0.524
PEO 2900	$\mathrm{Re_c}+47.2$	36.6	—	-1.28	1.07	0.540

Table 5.6: Mean streamwise velocity profile parameters.

the wake is sensitive to small changes in the distance from $\mathrm{Re_c}$ and the differences in the profiles are consistent with the different Reynolds numbers for the three fluids. The location of the mean free stagnation point x_{SP} is found by linearly interpolating to find where $\bar{u}_{\mathrm{CL}} = 0$ and the values found are given in Table 5.5. x_{SP} is similar for all three fluids with x_{SP} for water being slightly greater due to the lower Reynolds number.

A second order finite difference scheme was used to find $\partial\bar{u}^*/\partial x^*$, shown in Fig. 5.42. The location of maximum backflow in the wake $x_{\min}$ was found where $\partial u^*/\partial x^* = 0$ and the values found are given in Table 5.5. $x_{\min}$ is independent of polymer concentration to within the accuracy of the data.

Figure 5.43 illustrates the evolution of Λ with x^* and shows similar characteristics to $\bar{u}_{\mathrm{CL}}$. The mean free stagnation point corresponds to where $\Lambda = -1$ and the minimum values of the velocity ratio $\Lambda_{\min}$, which are given in Table 5.6, are the same to within experimental accuracy for the three fluids.

The dependence of the non-dimensional wake half width $y^*_{1/2}$ on x^* is shown in Fig. 5.44. For $x^* < 2$, $y^*_{1/2} = 0.72$ for all three fluids. Downstream from this point the wake increases in width, with a higher growth rate for a higher Reynolds number. There is good correspondence between the streamwise position where the wake starts to widen and the location of the mean free stagnation point x_{SP}.

Using $y^*_{1/2}$ the non-dimensional vorticity thickness $\delta_\omega/y_{1/2}$ can be calculated and is presented in Fig. 5.45. $\delta_\omega/y_{1/2}$ is proportional to the inverse of the profile shape parameter N, i.e. $\delta_\omega/y_{1/2} \propto N^{-1}$ (Monkewitz, 1988), and as such plays a key role in the linear stability of the Newtonian wake. Measured at the location of maximum backflow the data compare well with results presented in Table II in Monkewitz (1988). There is a small variation in $\delta_\omega/y_{1/2}$ and N^{-1} proportional to the polymer concentration (see Table 5.6), however the significance of this is questionable. The profiles are very similar in shape but appear to be mis-aligned in the streamwise direction. Applying a

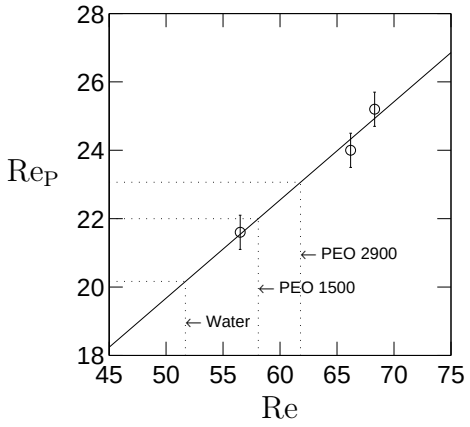

Fig. 5.40: Profile Reynolds number $\mathrm{Re_P}$ versus Re at $\mathrm{Re} \approx \mathrm{Re_c} + 6$. The dotted lines mark the critical Reynolds numbers for water, PEO 1500 and PEO 2900.

correction of $x^* = \pm 0.1$ is sufficient to make the trend linking $\delta_\omega / y_{1/2}$ with c disappear. Given that the non-dimensional width of a PIV interrogation window is $x^* = 0.12$ this is entirely plausible as the source of the observed differences. Thus it is highly likely that the trend is artificial and caused by small errors in the alignment of the data. Examining Fig. 5.47 in the region of $N^{-1} \sim 0.55$ suggests that a significant change in N^{-1}, and thus $\delta_\omega / y_{1/2}$, would be required to alter the wake stability. The absence of evidence for this change in the data implies that the wake stability is not altered by a change in the vorticity thickness.

The profile Reynolds numbers at $x_{\min}$ are also given in Table 5.6. Plotting $\mathrm{Re_P}$ as a function of Re, there is a fair suggestion of a linear relationship between the two quantities, as indicated in Fig. 5.40. This linear fit allows the critical profile Reynolds number at which the wake starts vortex shedding $(\mathrm{Re_P})_{\mathrm{VK}}$ to be estimated and these are given in Table 5.6. The value found for water $(\mathrm{Re_P})_{\mathrm{VK}} = 20.2$ is in fair agreement with that of 17.13 calculated in Monkewitz (1988) for the data of Nishioka & Sato (1978).

In Fig. 5.46, δ_ω / d illustrates how the shear layer width evolves downstream of the cylinder. For $x^* < 1$, δ_ω / d grows quickly and then changes rate growing more slowly after $x^* > 1$. Downstream from $x^* > 6$, some error is introduced in to the calculations by the hot film shadow.

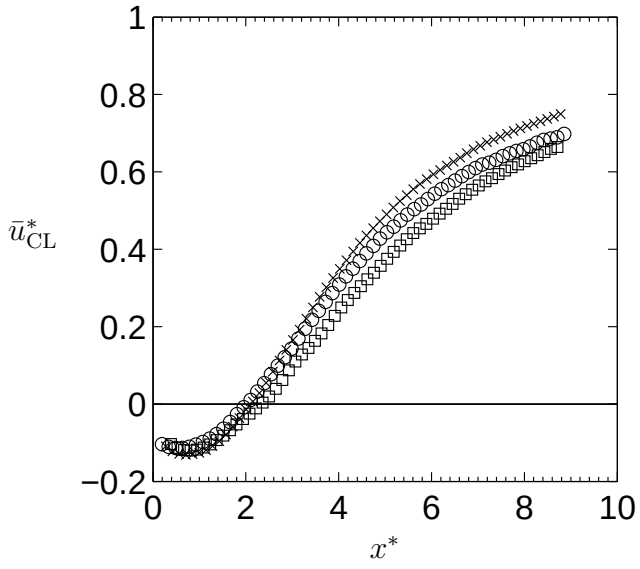

Fig. 5.41: Centre line velocity $\bar{u}^*_{\mathrm{CL}}$ versus x^* for $\mathrm{Re} \approx \mathrm{Re_c} + 6$. Symbols: □ water; × PEO 1500; ◯ PEO 2900.

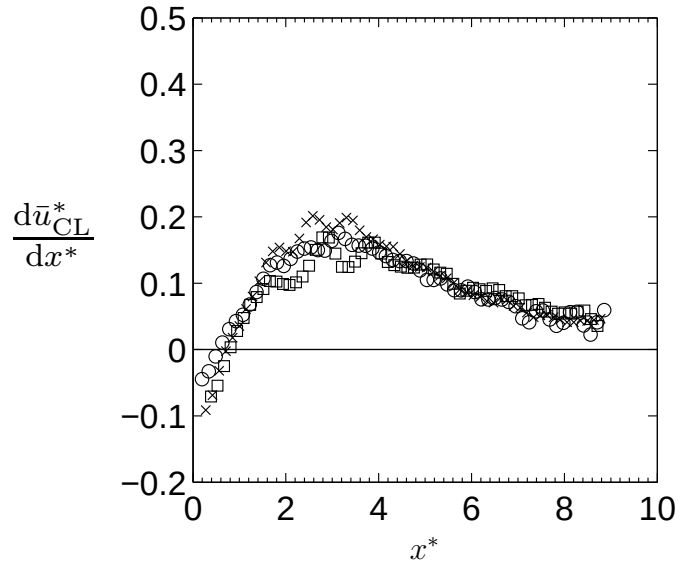

Fig. 5.42: Centre line velocity gradient $\mathrm{d}\bar{u}^*_{\mathrm{CL}}/\mathrm{d}x^*$ versus x^* for $\mathrm{Re} \approx \mathrm{Re_c} + 6$. Symbols: □ water; × PEO 1500; ◯ PEO 2900.

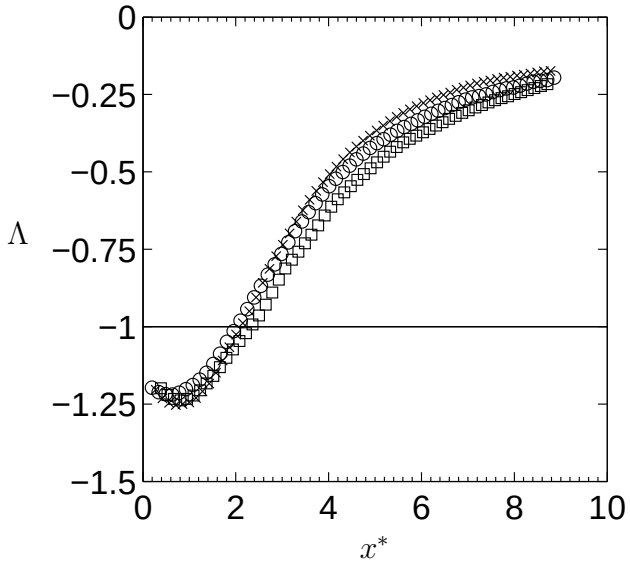

Fig. 5.43: Velocity ratio Λ versus x^* for $\mathrm{Re} \approx \mathrm{Re_c} + 6$. Symbols: □ water; × PEO 1500; ◯ PEO 2900.

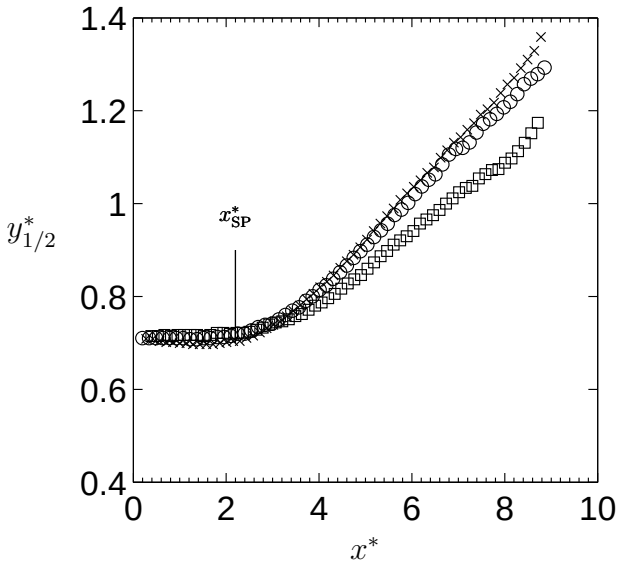

Fig. 5.44: Wake half width $y^*_{1/2}$ versus x^* for $\mathrm{Re} \approx \mathrm{Re_c} + 6$. Symbols: □ water; × PEO 1500; ◯ PEO 2900.

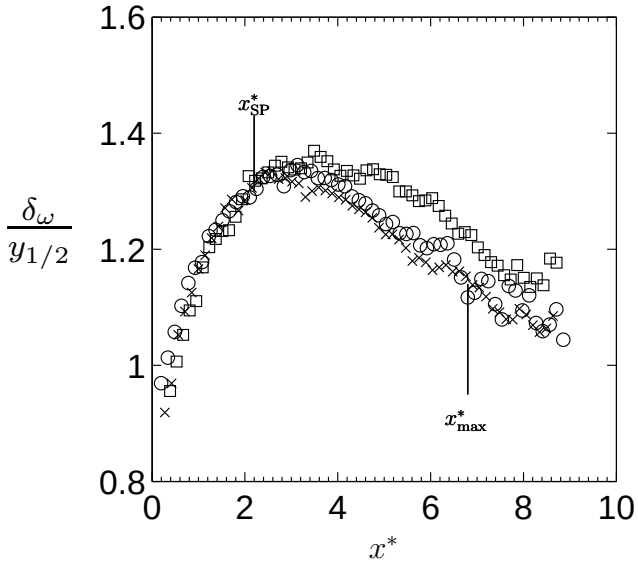

Fig. 5.45: Normalized vorticity thickness $\delta_\omega / y_{1/2}$ versus x^* for Re $\approx$ $\mathrm{Re_c} + 6$. Symbols: $\square$ water; $\times$ PEO 1500; $\bigcirc$ PEO 2900.

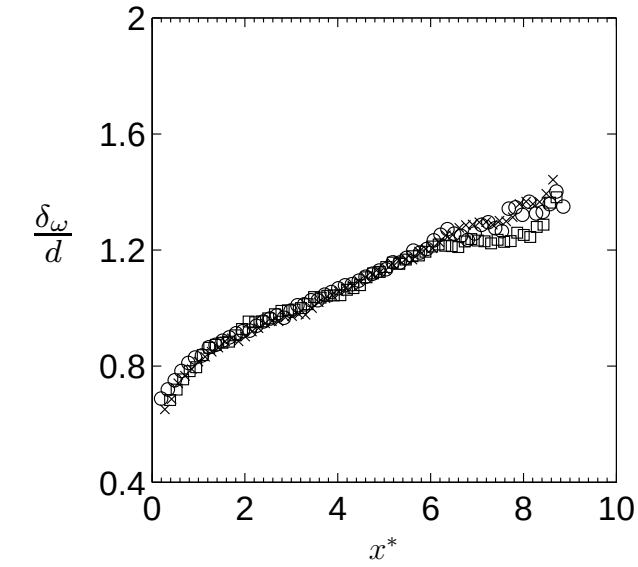

Fig. 5.46: Normalized vorticity thickness δ_ω / d versus x^* for Re $\approx$ $\mathrm{Re_c} + 6$. Symbols: $\square$ water; $\times$ PEO 1500; $\bigcirc$ PEO 2900.

$\mathbf{Re \approx Re_c + 50}$

As already mentioned, the difference in Reynolds number between the measurements for water, PEO 1500 and PEO 2900 is less significant at Re $\approx$ $\mathrm{Re_c}+49$ because of the relatively large distance above $\mathrm{Re_c}$. Figure 5.48 shows the centreline velocity $\bar{u}_{\mathrm{CL}}$ for the three fluids. The centreline velocity profile for PEO 2900 is appreciably different from that for water and PEO 1500. Not only is the mean free stagnation point located further downstream (see Table 5.5), but the backflow is significantly greater. The greater values of $\bar{u}^*$ for the polymer solutions at $x^* > 6$ illustrate the previously discussed velocity overshoot.

Figure 5.49 shows that the location of maximum backflow, i.e. where $\mathrm{d}\bar{u}^*_{\mathrm{CL}}/\mathrm{d}x^* = 0$, is similar for all three fluids, and is also similar to the results for Re $\approx \mathrm{Re_c} + 6$. This suggests that $x_{\min}$ is practically independent of the Reynolds number between the onset of vortex shedding and Re $\approx \mathrm{Re_c} + 49$ for the fluids studied.

The stronger negative velocity for PEO 2900 is well illustrated in Fig. 5.50. The values of $\Lambda_{\min}$ calculated are given in Table 5.6 and show that the measurements for water and PEO 1500 are in good agreement. Figure 5.47 illustrates the relative importance of Λ on the flow stability: stronger backflow leads to an earlier onset of instability. In comparison to the effect of N, Λ is far more efficient at changing the flow stability. The increase in Λ for PEO 2900 at Re $\approx \mathrm{Re_c} + 50$ is significant and suggests that there was a corresponding increase at Re $\approx \mathrm{Re_c} + 6$ for this fluid. Given the fairly small destabilization observed, Fig. 5.47 suggests that only a very small change in Λ would be required and this would almost certainly be undetectable given the level of uncertainty in the data. Therefore the destabilization of the wake observed for PEO 2900 by an increase in the centreline backflow seems probable. The physical mechanism for this increase is uncertain. Changes in the wake development due to shear thinning, such as a change in the boundary layer separation point on the cylinder, could be involved.

The behaviour of the non-dimensional wake half width is more complex than for Re $\approx \mathrm{Re_c} + 6$. Figure 5.51 shows that the wake for $x^* < x^*_{\mathrm{SP}}$ gets thinner, downstream from which it begins to grow until reaching a maximum width of $y^*_{1/2} = 1.2$ at $x^* \approx 6$. For $x^* > 6$ the wake decays and $y^*_{1/2}$ gradually contracts. Similar to the centreline velocity profile, $y^*_{1/2}$ for PEO 2900 takes a greater distance to develop compared to water and PEO 1500.

Figure 5.52 shows $\delta_\omega/y_{1/2}$ for Re $\approx \mathrm{Re_c} + 50$. The dependence of $\delta_\omega/y_{1/2}$ for $x^* < x^*_{\min}$ on polymer concentration can be removed by using the same re-alignment of the data as for Re $\approx \mathrm{Re_c} + 6$. Because the same spatial calibration was used for the measurements at both Reynolds numbers this

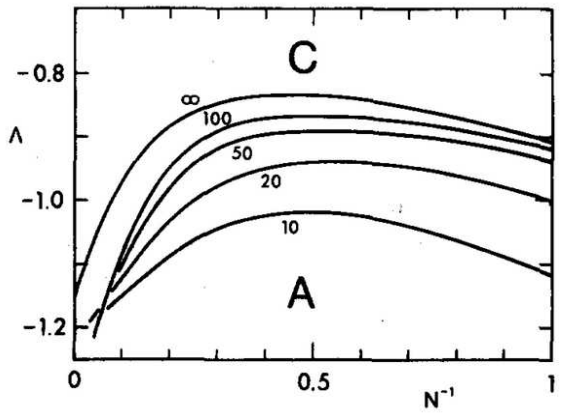

Fig. 5.47: Boundary for transition from convective to absolute instability as a function of Λ and shape factor N for various profile Reynolds numbers $\mathrm{Re_P}$. From Monkewitz (1988).

suggests that the observed differences are caused by a shift in the streamwise direction.

As previously stated, the change in $\delta_\omega/y_{1/2}$ required to alter the wake stability is relatively large and should be apparent beyond the uncertainty of the data. This is not apparent for any of the data, therefore it is unlikely that the stabilization and subsequent destabilization of the wake are due to changes in $\delta_\omega/y_{1/2}$.

δ_ω/d shows that the shear layers grow downstream of the cylinder but reach a maximum width at $x^* = 6$ for water and PEO 1500 and $x^* = 7.5$ for PEO 2900.

Summary of results for base flow stability analysis

Examination of the velocity ratio suggests that the destabilization of the wake for PEO 2900 is caused by an increase in the mean backflow on the centreline. Differences in measured values of vorticity thickness are thought to be caused by errors in the data alignment.

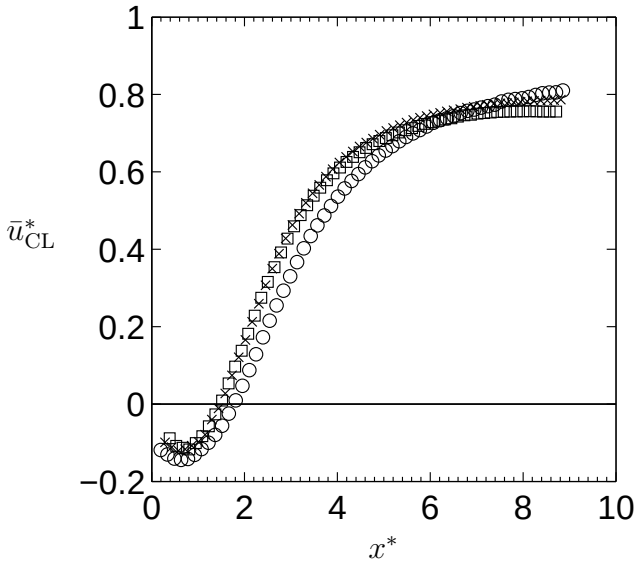

Fig. 5.48: Centreline velocity $\bar{u}^*_{\mathrm{CL}}$ versus x^* for $\mathrm{Re} \approx \mathrm{Re_c} + 50$. Symbols: □ water; × PEO 1500; ◯ PEO 2900.

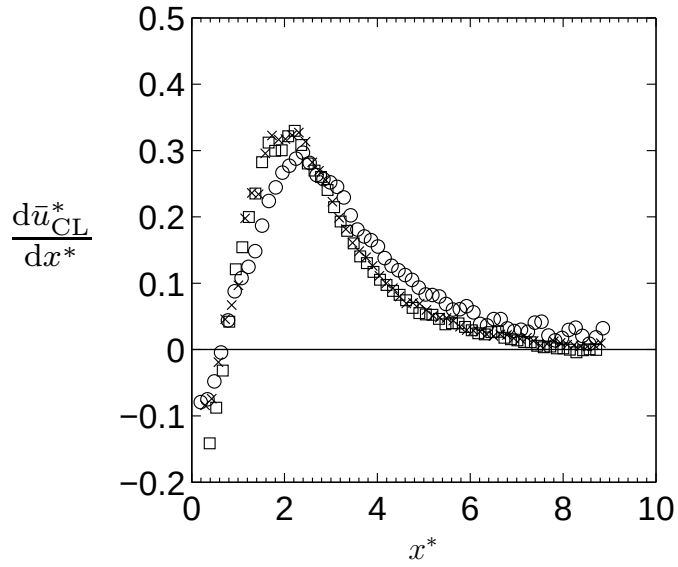

Fig. 5.49: Centreline velocity gradient $\mathrm{d}\bar{u}^*_{\mathrm{CL}}/\mathrm{d}x^*$ versus x^* for $\mathrm{Re} \approx \mathrm{Re_c} + 50$. Symbols: □ water; × PEO 1500; ◯ PEO 2900.

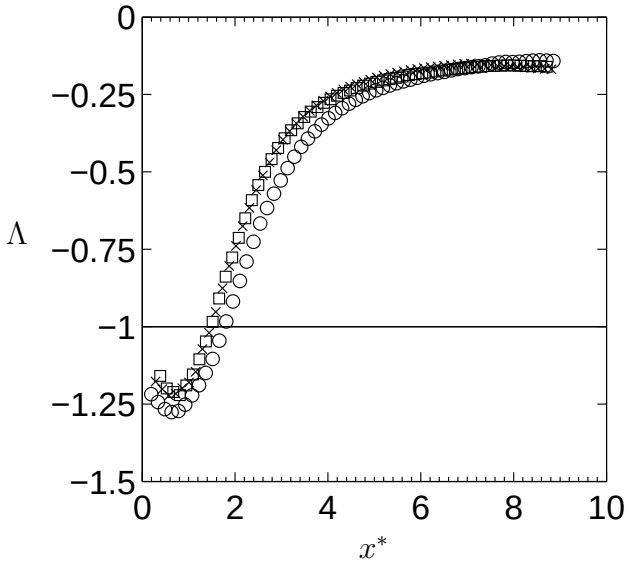

Fig. 5.50: Velocity ratio Λ versus x^* for $\mathrm{Re} \approx \mathrm{Re_c} + 50$. Symbols: □ water; × PEO 1500; ◯ PEO 2900.

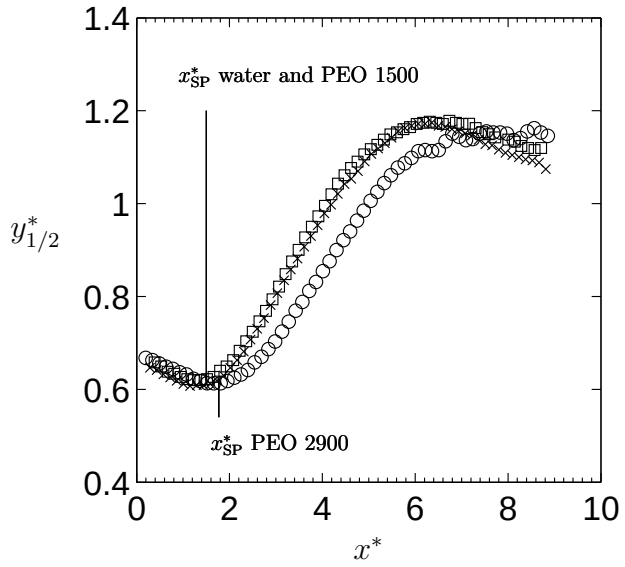

Fig. 5.51: Wake half width $y^*_{1/2}$ versus x^* for $\mathrm{Re} \approx \mathrm{Re_c} + 50$. Symbols: □ water; × PEO 1500; ◯ PEO 2900.

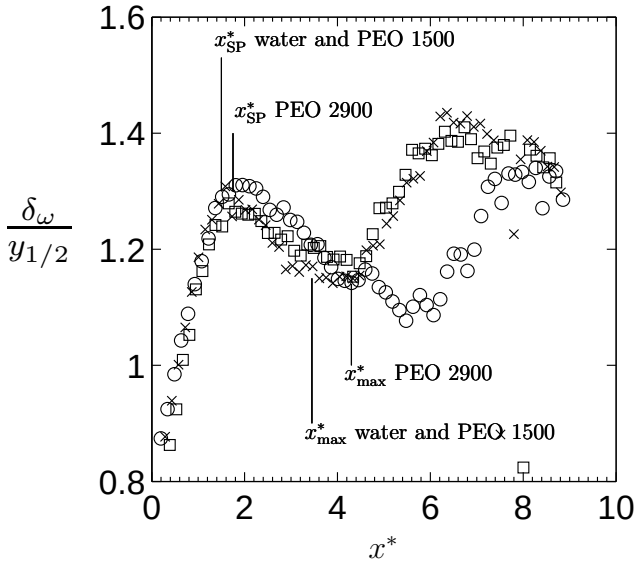

Fig. 5.52: Normalized vorticity thickness $\delta_\omega / y_{1/2}$ versus x^* for Re $\approx$ $\mathrm{Re_c} + 50$. Symbols: $\square$ water; $\times$ PEO 1500; $\bigcirc$ PEO 2900.

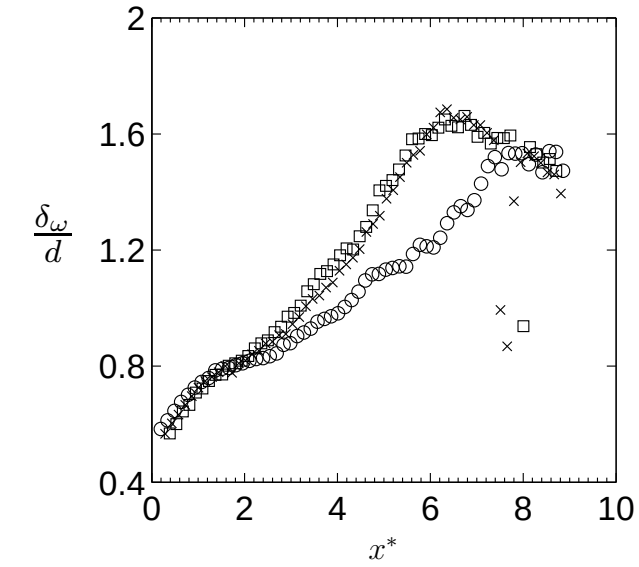

Fig. 5.53: Normalized vorticity thickness δ_ω / d versus x^* for Re $\approx$ $\mathrm{Re_c} + 50$. Symbols: $\square$ water; $\times$ PEO 1500; $\bigcirc$ PEO 2900.

5.6.3 Phase-averaged measurements

Velocity and stress fields

The phase-averaged PIV u^* and v^* fields were found using the procedure explained in Section 4.2.4. The velocity and stress fields, u^*, v^*, $\sigma^*_{xy} + \sigma^*_{yx}$ and $0.5(\sigma^*_{xx} - \sigma^*_{yy})$ at the same phase position ϕ_0 for $\mathrm{Re} \approx \mathrm{Re_c} + 6$ are shown in Figs. 5.54 and Figs. 5.55. The reference phase position ϕ_0 was chosen arbitrarily and a half cycle for each fluid at $\mathrm{Re} \approx \mathrm{Re_c} + 6$ and $\mathrm{Re} \approx \mathrm{Re_c} + 50$ is shown in Appendix A.

The phase-averaging technique was found to work well for water and PEO 1500 at $\mathrm{Re} \approx \mathrm{Re_c} + 6$ and for water and PEO 2900 at $\mathrm{Re} \approx \mathrm{Re_c} + 50$. However, the data for PEO 2900 at $\mathrm{Re} \approx \mathrm{Re_c} + 6$ and for PEO 1500 at $\mathrm{Re} \approx \mathrm{Re_c} + 50$ show significant decreases in the fluctuations of u and v, and therefore the stress fields too. This is not physically representative of the wake because the fluctuating magnitudes $|u^*|$ and $|v^*|$ in Section 5.6.1 show no corresponding decrease. The likely cause of the reduction in peak values is leakage from other phase bins, which would tend to bring the velocities fields for each phase position towards the mean field. This leakage is probably due to a polluted wake signal measured by the hot film. Background electronic noise in the laboratory is probably cause of this. Applying a band pass filter to the wake signal around the vortex shedding frequency improved the velocity fields but did not bring them to the same clarity as the other measurements.

However, four out of the six data sets offer accurate representations of the vortex shedding cycle. The peak values for the streamwise velocity and stress fields are located close to the cylinder and do not change significantly compared to the time average fields seen in Section 5.6.1. The local concentrations of velocity and stress in the wake are well illustrated, however, and the previously noted increase in magnitude of v^* for the upper half of the vortex street in relation to the lower half is clearly visible in Figs. A.3, A.4, A.11 and A.12.

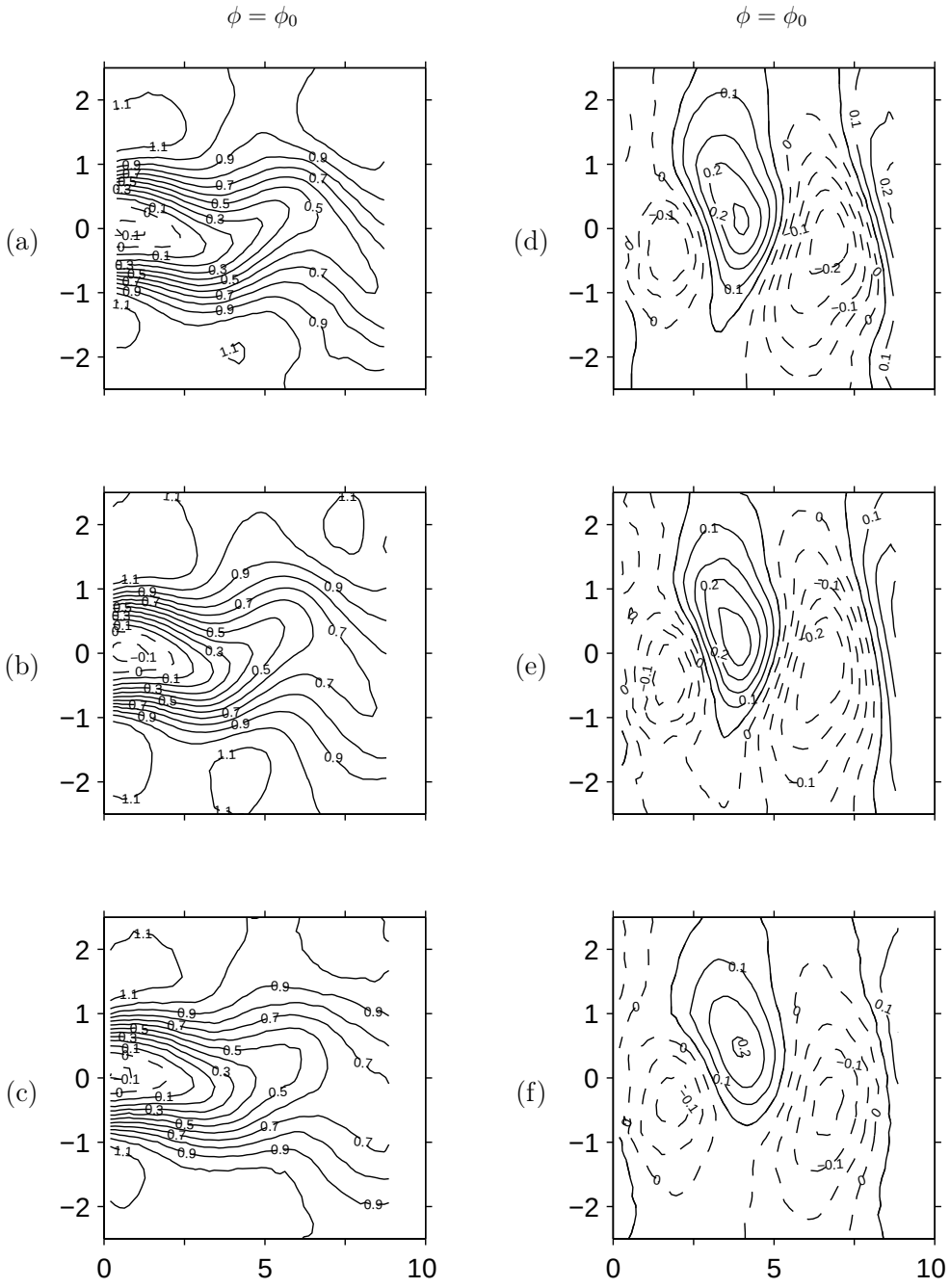

Fig. 5.54: u^* (a)–(c) and v^* (d)–(f) at $\phi = \phi_0$ for (a),(d) water at $\mathrm{Re} = \mathrm{Re_c} + 4.8$, (b),(e) PEO 1500 at $\mathrm{Re} = \mathrm{Re_c} + 8.1$ and (c),(f) PEO 2900 at $\mathrm{Re} = \mathrm{Re_c} + 6.5$. Lines: $--$ $u^* \leq 0$ and — $u^* > 0$, $--$ $v^* < 0$ and — $v^* > 0$. Axes: $x = x^*, y = y^*$.

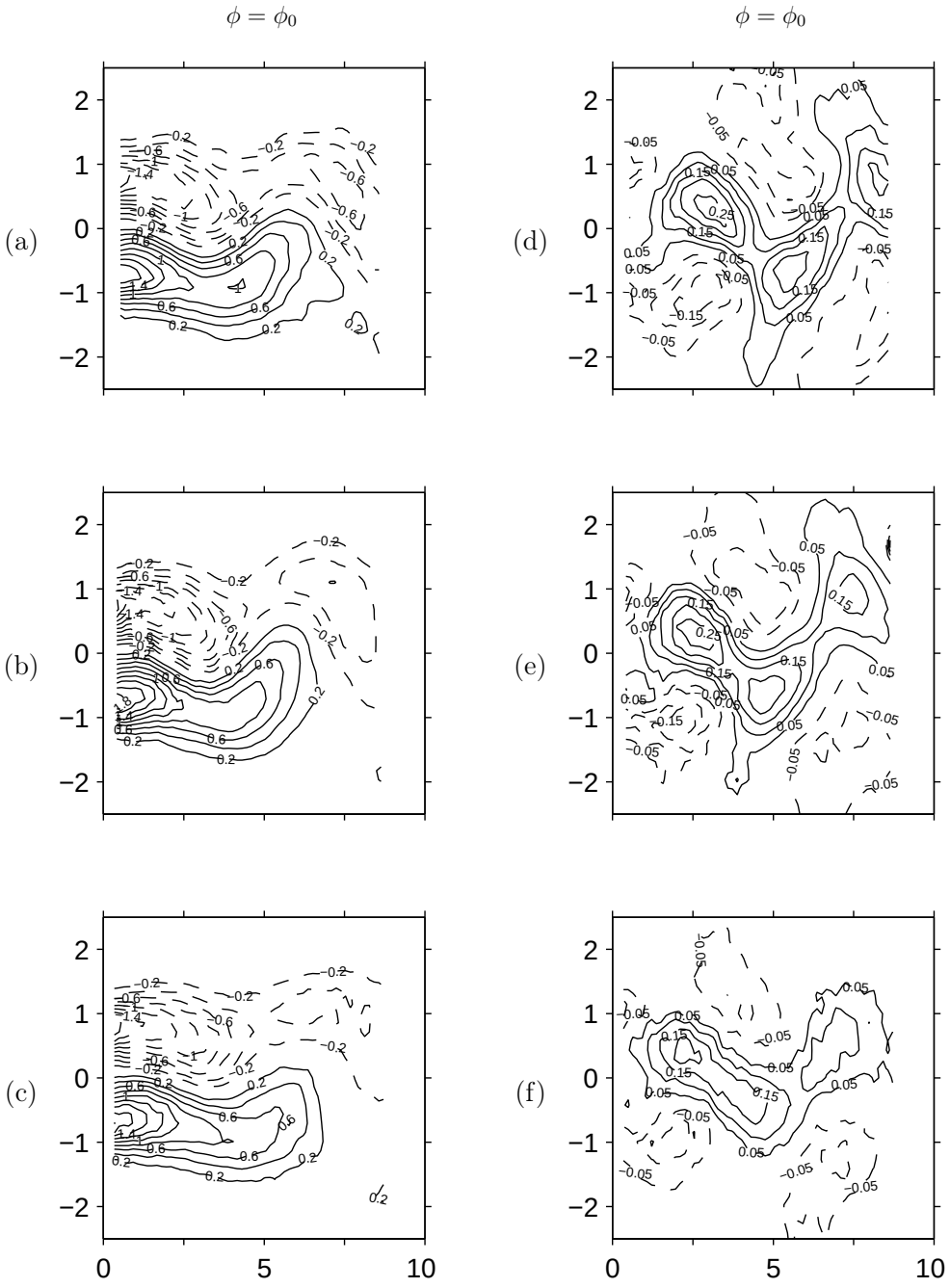

Fig. 5.55: $\sigma^*_{xy} + \sigma^*_{yx}$ (a)–(c) and $0.5(\sigma^*_{xx} - \sigma^*_{yy})$ (d)–(f) at $\phi = \phi_0$ for (a),(d) water at $\mathrm{Re} = \mathrm{Re_c} + 4.8$, (b),(e) PEO 1500 at $\mathrm{Re} = \mathrm{Re_c} + 8.1$ and (c),(f) PEO 2900 at $\mathrm{Re} = \mathrm{Re_c} + 6.5$. Lines: $- -$ $\sigma^*_{xy} + \sigma^*_{yx} < 0$ and — $\sigma^*_{xy} + \sigma^*_{yx} > 0$, $- -$ $0.5(\sigma^*_{xx} - \sigma^*_{yy}) < 0$ and — $0.5(\sigma^*_{xx} - \sigma^*_{yy}) > 0$.

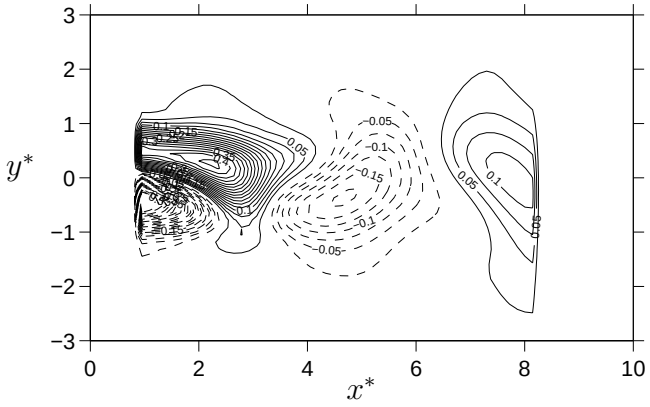

Fig. 5.56: Example Γ_1 field. Re $\approx$ Re$_c$ + 6 for water: $--$ $\Gamma_1 < 0$ and — $\Gamma_1 > 0$

Vortex convection speed

The vortex convection speed is determined by locating the centre of the vortices at each phase of the cycle and tracking the change in position with time. The decreased magnitudes noted in the velocity fields do not strongly affect the location of the vortices centres.

The dimensionless scalar function Γ_1 defined by Graftieaux *et al.* (2001) provides an efficient way of locating vortex centres. Γ_1 is defined as:

$$\Gamma_1(\mathrm{P}) = \frac{1}{N} \sum_S \frac{(\mathrm{PM} \wedge \mathbf{U}_\mathrm{M}) \cdot \mathbf{n}}{||\mathrm{PM}|| \cdot ||\mathbf{U}_\mathrm{M}||} = \frac{1}{N} \sum_S \sin \theta_\mathrm{M}, \tag{5.24}$$

where S is a rectangular domain surrounding the point P and contains N points M. θ_M is the angle between the velocity vector $\mathbf{U}_\mathrm{M}$ and the radius vector PM and $\mathbf{n}$ is the unit vector normal to the measurement plane. The size of the domain used to calculate Γ_1 does not greatly affect the location of the vortex Graftieaux *et al.* (2001) but using a larger domain acts as a low pass filter and reduces peak values. In this work a fixed domain size of 9×9 vectors was used in order to produce accurate results for the noisiest data. Γ_1 was calculated from the velocity field of each phase position of the phase-averaged velocity field, an example measurement is shown in Fig. 5.56, and the vortex centres were found manually.

The streamwise location of the vortex centre as a function of the phase ϕ for the three fluids at Re $\approx$ Re$_c$ + 6 and Re $\approx$ Re$_c$ + 50 is shown in Figs. 5.57 and 5.58, respectively. Data are presented for both the upper and lower halves of the vortex street and show that the vortex street evolves

Fluid	Re	c_{v}^*
Water	$\mathrm{Re} \approx \mathrm{Re_c} + 6$	0.77
PEO 1500	$\mathrm{Re} \approx \mathrm{Re_c} + 6$	0.82
PEO 2900	$\mathrm{Re} \approx \mathrm{Re_c} + 6$	0.83
Water	$\mathrm{Re} \approx \mathrm{Re_c} + 50$	0.88
PEO 1500	$\mathrm{Re} \approx \mathrm{Re_c} + 50$	0.90
PEO 2900	$\mathrm{Re} \approx \mathrm{Re_c} + 50$	0.83

symmetrically. Near to the cylinder the vortices are still attached to the cylinder shear layers and move downstream slowly. As they detach at $x^* \approx 2$, the vortices accelerate and then convect downstream at a constant speed. The non-dimensional vortex convection speed c_{v}^* is calculated from $\mathrm{d}x^*/\mathrm{d}\phi$:

$$c_{\mathrm{v}}^* = \frac{c_{\mathrm{v}}}{U_\infty} = \frac{1}{U_\infty}\left(\frac{\mathrm{d}x}{\mathrm{d}t}\right) = 2\pi\mathrm{St}\left(\frac{\mathrm{d}x^*}{\mathrm{d}\phi}\right).$$

The values found are given in Table 5.6.3 and for both Reynolds numbers c_{v}^* falls in the range 0.75–0.9. The error is of the order of 0.1 and the data are in fair agreement with the nearly constant value of 0.86 for the same Reynolds range from Williamson (1989).

Inaccuracies in the velocity fields from the phase averaging technique for the PEO solutions mean that the precision is not great enough to distinguish any trends in c_{v}^* with increasing polymer concentration. The convection velocity data give a good indication of the increasing error in the phase averaging technique due to higher freestream velocities and higher polymer concentrations.

The streamwise distance between an upper and lower vortex street vortex, which corresponds to half of the wavelength of the vortex street A, is also shown in Figs. 5.57 and 5.58. To within experimental precision, A is constant throughout the shedding cycle and there is no detectable change in the wavelength for increasing polymer concentration.

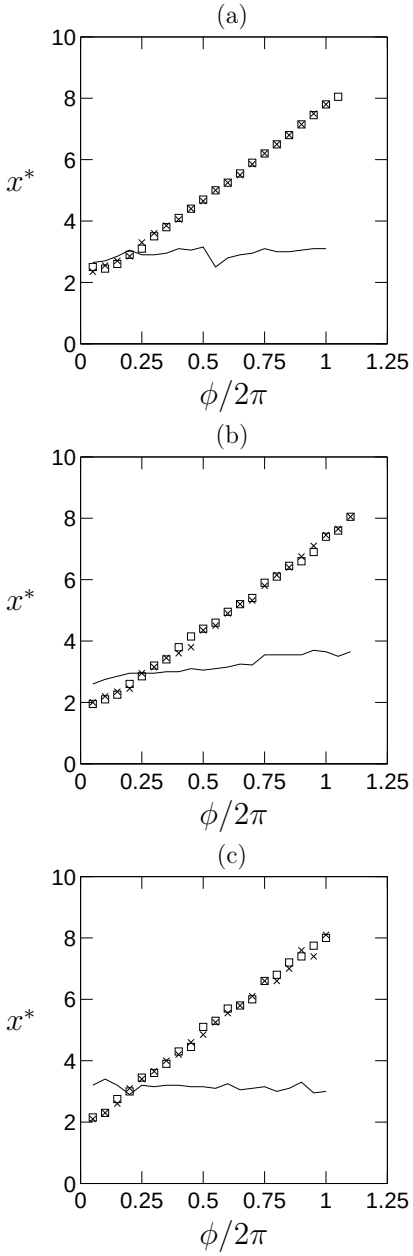

Fig. 5.57: Downstream location of vortex centre as a function of phase ϕ for (a) Water, (b) PEO 1500 and (c) PEO 2900 at $\mathrm{Re} \approx \mathrm{Re_c} + 6$. Symbols: $\square$ upper vortex; $\times$ lower vortex; — streamwise distance between upper and lower vortex centres $\equiv A/2$.

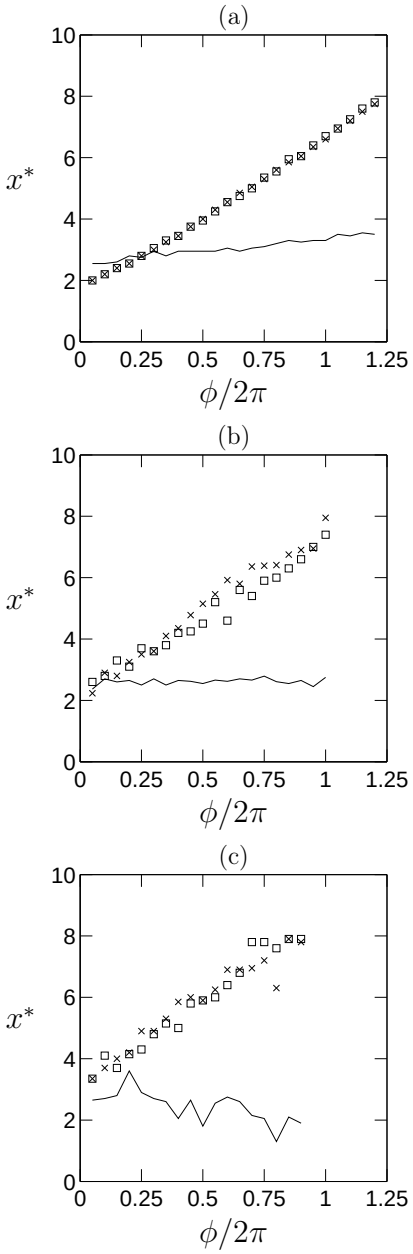

Fig. 5.58: Downstream location of vortex centre as a function of phase ϕ for (a) Water, (b) PEO 1500 and (c) PEO 2900 at $\mathrm{Re} \approx \mathrm{Re_c} + 50$. Symbols: $\square$ upper vortex; $\times$ lower vortex; — streamwise distance between upper and lower vortex centres $\equiv A/2$.

Chapter 6

Conclusions

Vortex shedding from a cylinder was studied for water and four low concentration aqueous PEO solutions. The Newtonian behaviour of the cylinder wake, including the critical Reynolds number Re_c the vortex shedding frequency as a function of the Reynolds number, and the mean and fluctuating velocity distributions, agreed well with previous investigations. Coefficients for the Stuart–Landau model were determined and using the corrections from the complex spanwise Ginzburg–Landau model were within the range of expected values.

The wake was stabilized by polymer additives and Re_c increased linearly with polymer concentration for constant viscosity solutions. Shear-thinning was thought to counteract this effect and reduce Re_c, which could explain the reductions in Re_c previously noted for vortex shedding from a cylinder. The destabilization observed for a shear-thinning viscosity was thought to be linked to a stronger back-flow in the mean recirculation region downstream of the cylinder. The vortex shedding frequency at a given value of Re decreased with increasing polymer concentration and is in good qualitative agreement with previous work on the cylinder wake with aqueous PEO solutions.

The transverse velocity fluctuation profiles measured using LDA showed that the addition of PEO does not significantly alter the maximum value nor the location of the maximum value of the velocity fluctuations, for concentrations of 0.15 wt% and lower. Shear-thinning was thought to cause a reduction in the fluctuation magnitudes at a given Reynolds number, however, and also cause the location of maximum fluctuations to move further downstream.

Soon after the onset of vortex shedding, small amounts of fluid elasticity did not produce measurable differences in the velocity field downstream of the cylinder. At higher Reynolds numbers, fluid elasticity was shown to redistribute the transverse velocity fluctuations in the attached shear layers,

possibly through the action of normal forces. Shear-thinning brought about a decrease in the amplitude of streamwise and transverse velocity fluctuations throughout the wake region, as well as causing a change the spatial repartition of shear rates and rates of extension. Also, an overshoot in the streamwise velocity was observed for the polymer solutions and an analogy was drawn to the negative wake for spheres settling in a viscoelastic liquid.

Phase-averaged PIV measurements showed that the vortex convection speed and the wavelength of the vortex shedding were constant to within experimental error and independent of polymer concentration.

Perspectives

This present work has shown that polymer additives can have both a stabilizing and a destabilizing effect on inertial shear layer instabilities. Further experimental studies using a variety of well characterized polymer solutions would give an improved understanding of the interplay between different non-Newtonian effects and flow stability. Significant changes in the fluctuating and mean velocity fields for PEO solutions have also been noted and are worthy of detailed investigation.

Appendix A

Phase averaged measurements

Phase averaged PIV data are presented for water, PEO 1500 and PEO 2900 over half a cycle at $\mathrm{Re} \approx \mathrm{Re_c} + 6$ and $\mathrm{Re} \approx \mathrm{Re_c} + 50$. The initial phase ϕ_0 is arbitrary but constant for the three fluids at a given Reynolds number.

$\mathrm{Re} \approx \mathrm{Re_c} + 6$	
Figures A.1 and A.2	Streamwise velocity $u^* = u/U_\infty$
Figures A.3 and A.4	Transverse velocity $v^* = v/U_\infty$
Figures A.5 and A.6	Shear stress $\sigma^*_{xy} + \sigma^*_{yx} = (\sigma_{xy} + \sigma_{yx})d/(U_\infty \eta_0)$
Figures A.7 and A.8	Extensional stress $0.5(\sigma^*_{xx} - \sigma^*_{yy}) = 0.5(\sigma_{xx} - \sigma_{yy})d/(U_\infty \eta_0)$

$\mathrm{Re} \approx \mathrm{Re_c} + 50$	
Figures A.9 and A.10	Streamwise velocity $u^* = u/U_\infty$
Figures A.11 and A.12	Transverse velocity $v^* = v/U_\infty$
Figures A.13 and A.14	Shear stress $\sigma^*_{xy} + \sigma^*_{yx} = (\sigma_{xy} + \sigma_{yx})d/(U_\infty \eta_0)$
Figures A.15 and A.16	Extensional stress $0.5(\sigma^*_{xx} - \sigma^*_{yy}) = 0.5(\sigma_{xx} - \sigma_{yy})d/(U_\infty \eta_0)$

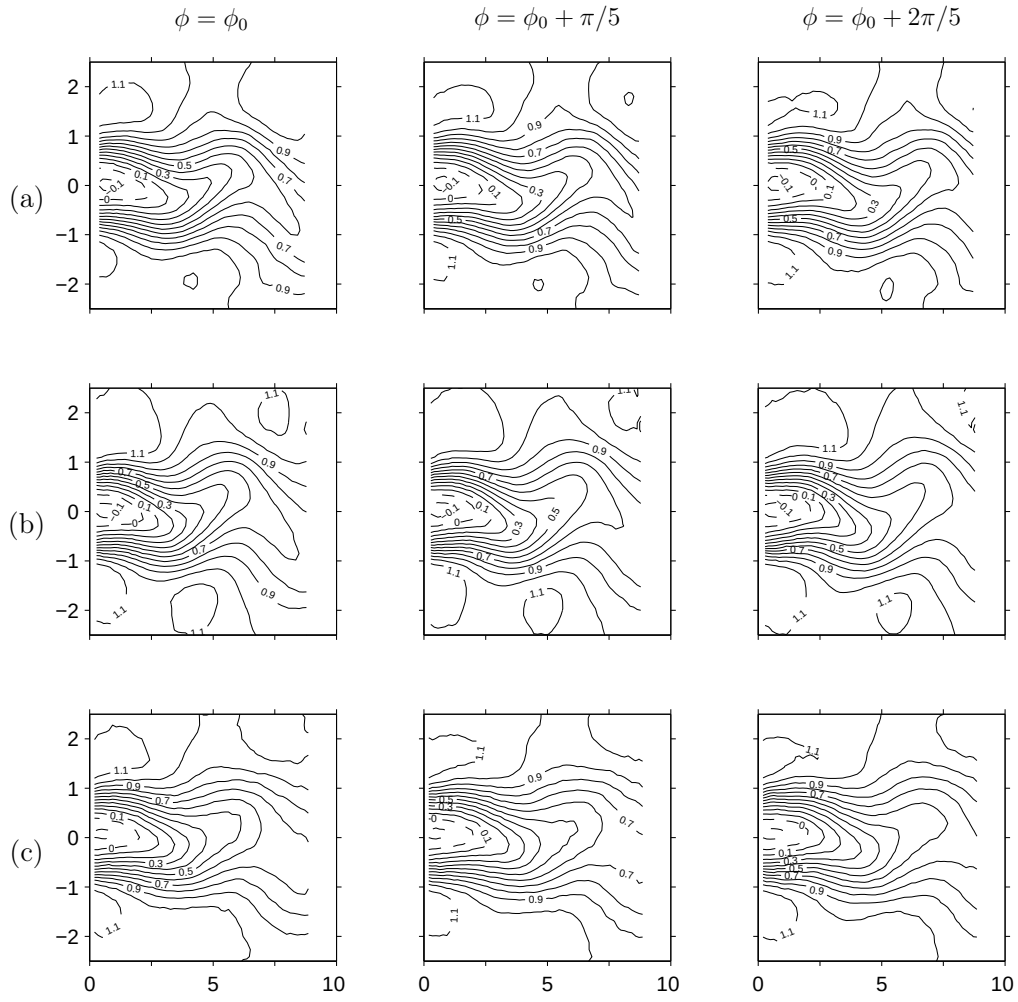

Fig. A.1: Streamwise velocity $u^* = u/U_\infty$ as a function of phase for (a) water at $\mathrm{Re} = \mathrm{Re_c} + 4.8$, (b) PEO 1500 at $\mathrm{Re} = \mathrm{Re_c} + 8.1$ and (c) PEO 2900 at $\mathrm{Re} = \mathrm{Re_c} + 6.5$. Lines: $- -$ $u^* \leq 0$ and — $u^* > 0$.

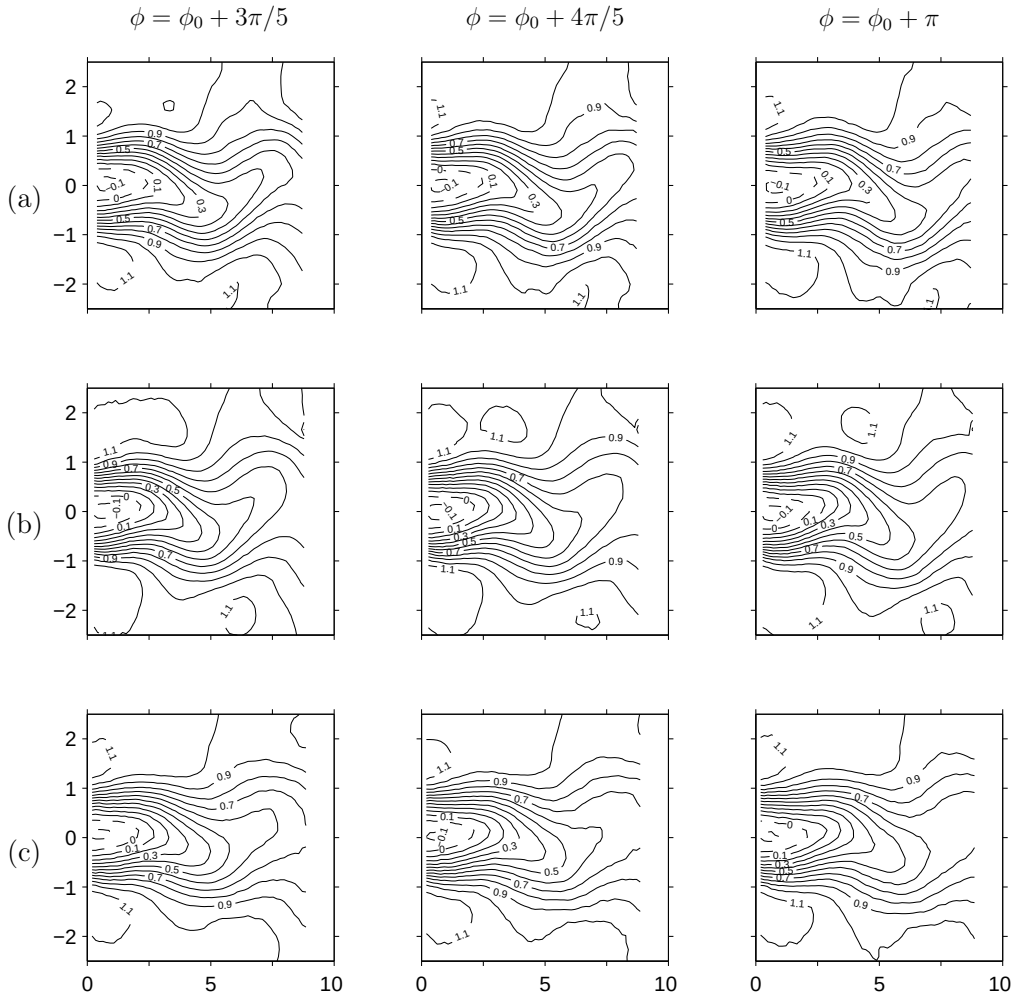

Fig. A.2: Streamwise velocity $u^* = u/U_\infty$ as a function of phase for (a) water at $\mathrm{Re} = \mathrm{Re_c} + 4.8$, (b) PEO 1500 at $\mathrm{Re} = \mathrm{Re_c} + 8.1$ and (c) PEO 2900 at $\mathrm{Re} = \mathrm{Re_c} + 6.5$. Lines: $- -$ $u^* \leq 0$ and — $u^* > 0$.

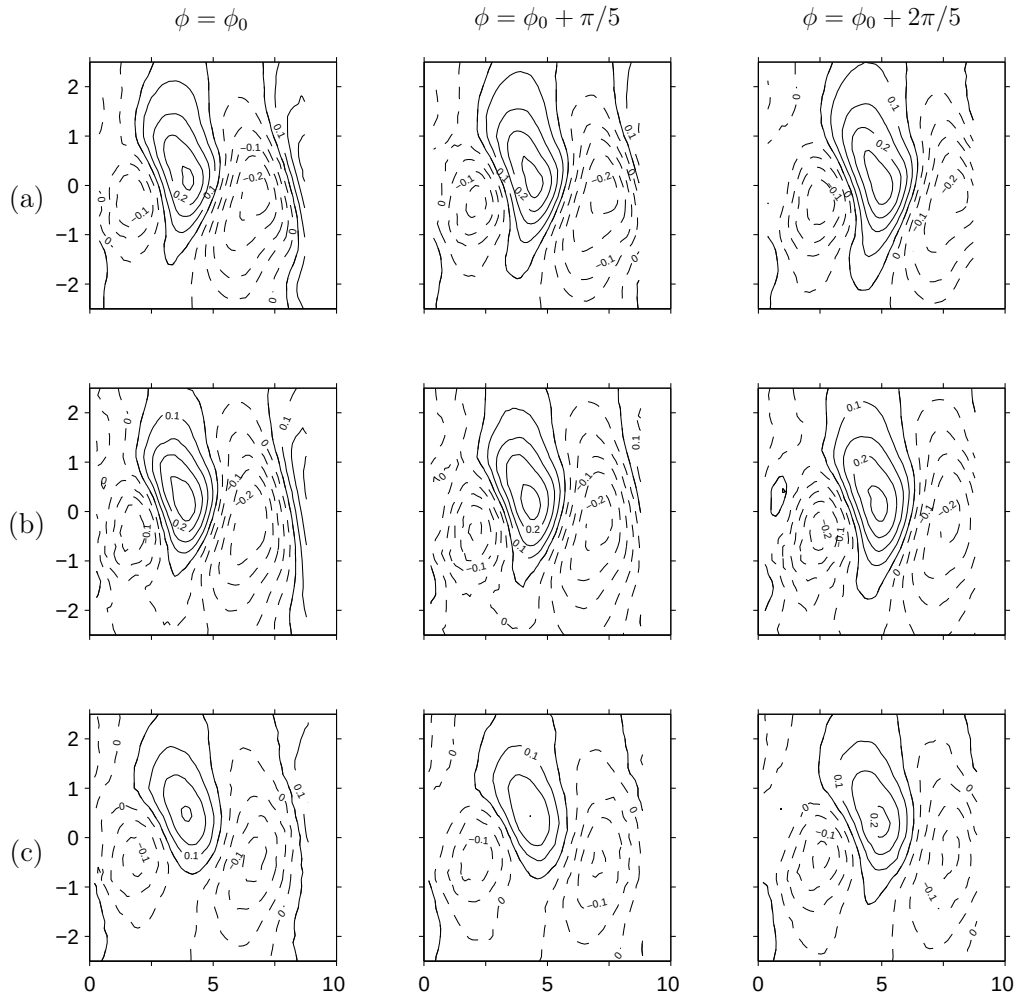

Fig. A.3: Transverse velocity $v^* = v/U_\infty$ as a function of phase for (a) water at $\mathrm{Re} = \mathrm{Re_c} + 4.8$, (b) PEO 1500 at $\mathrm{Re} = \mathrm{Re_c} + 8.1$ and (c) PEO 2900 at $\mathrm{Re} = \mathrm{Re_c} + 6.5$. Lines: $- -$ $u^* < 0$ and — $u^* > 0$.

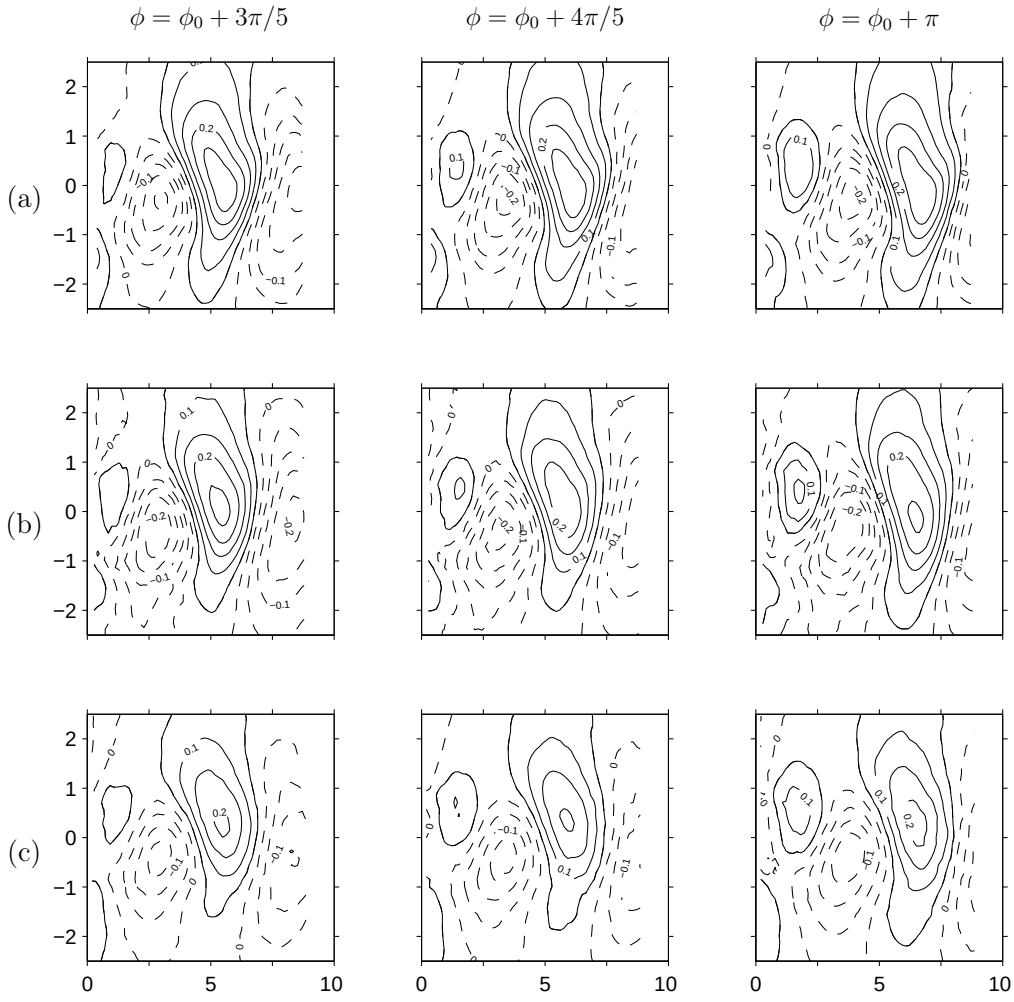

Fig. A.4: Transverse velocity $v^* = v/U_\infty$ as a function of phase for (a) water at $\mathrm{Re} = \mathrm{Re_c} + 4.8$, (b) PEO 1500 at $\mathrm{Re} = \mathrm{Re_c} + 8.1$ and (c) PEO 2900 at $\mathrm{Re} = \mathrm{Re_c} + 6.5$. Lines: $- -$ $u^* < 0$ and — $u^* > 0$.

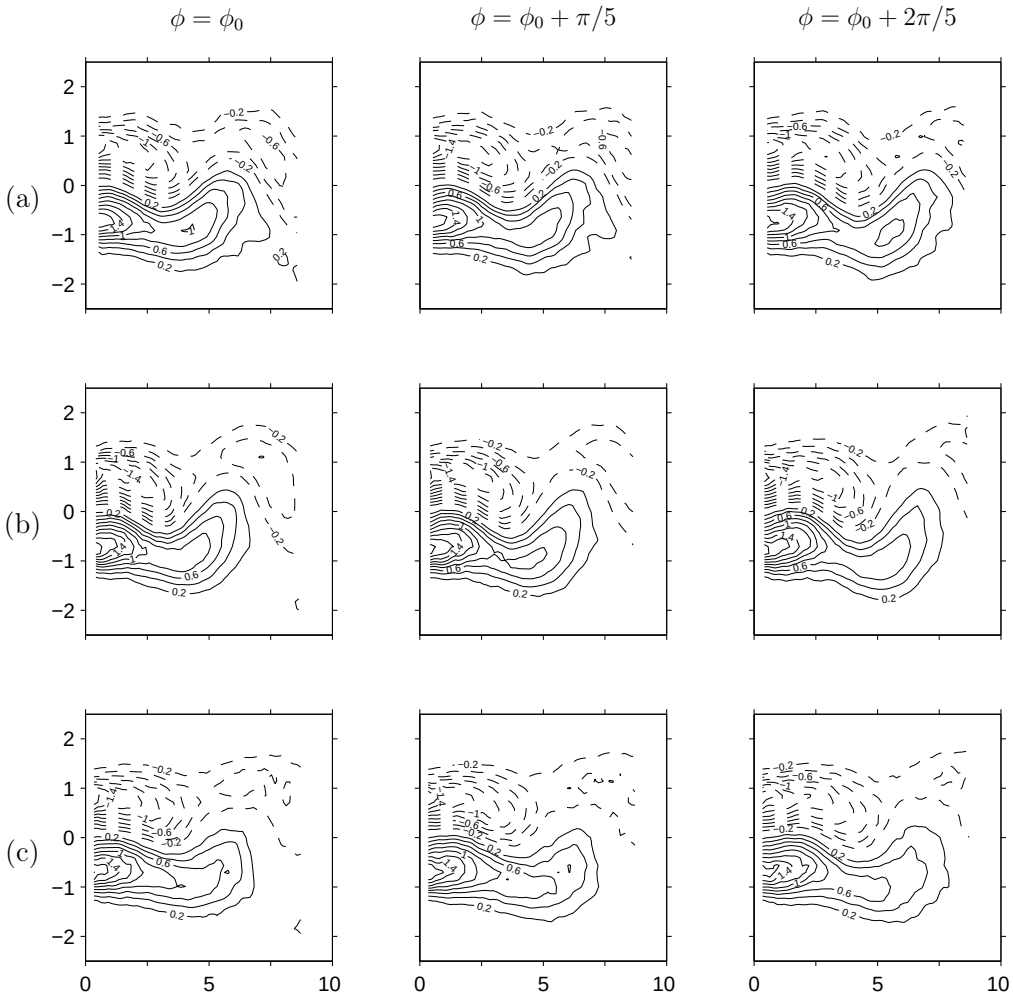

Fig. A.5: Shear stress $\sigma^*_{xy} + \sigma^*_{yx} = (\sigma_{xy} + \sigma_{yx})d/(U_\infty \eta_0)$ as a function of phase for (a) water at $\mathrm{Re} = \mathrm{Re_c} + 4.8$, (b) PEO 1500 at $\mathrm{Re} = \mathrm{Re_c} + 8.1$ and (c) PEO 2900 at $\mathrm{Re} = \mathrm{Re_c} + 6.5$. Lines: $- -$ $u^* < 0$ and — $u^* > 0$.

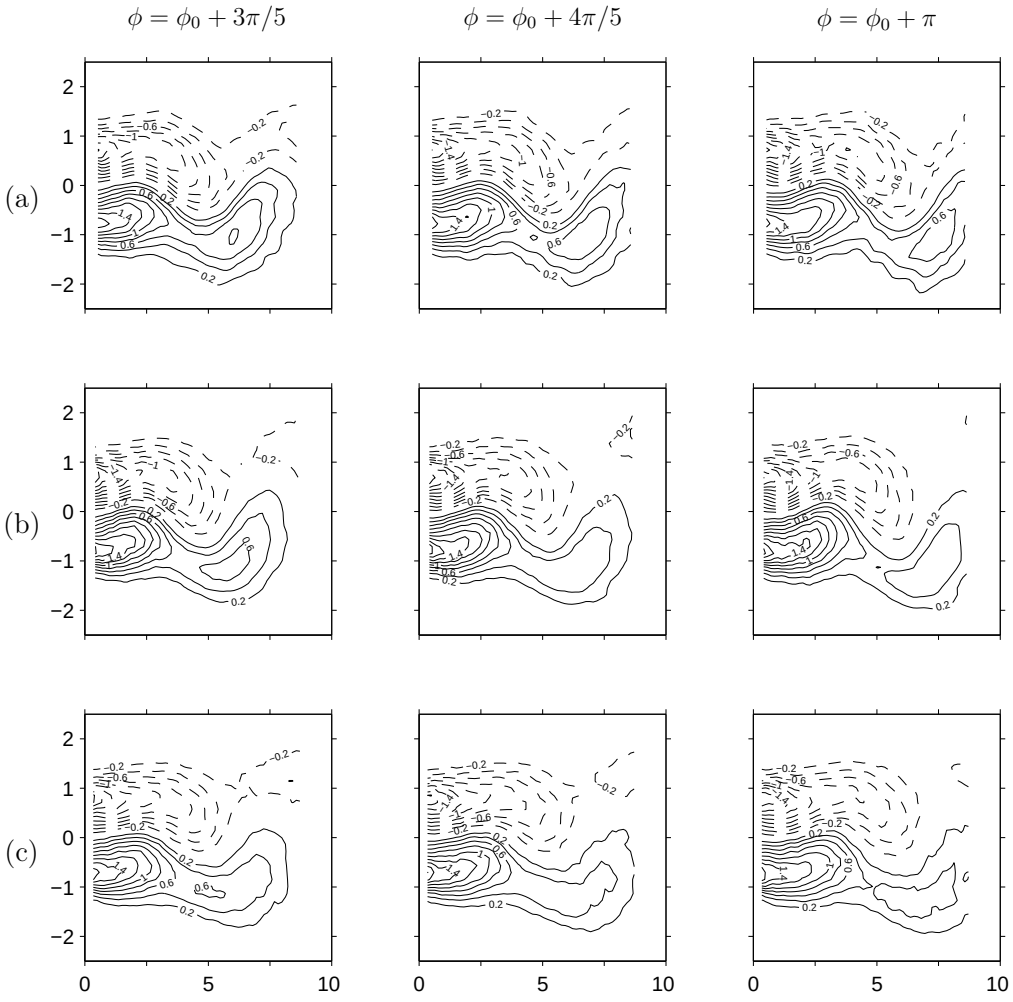

Fig. A.6: Shear stress $\sigma^*_{xy} + \sigma^*_{yx} = (\sigma_{xy} + \sigma_{yx})d/(U_\infty \eta_0)$ as a function of phase for (a) water at $\mathrm{Re} = \mathrm{Re_c} + 4.8$, (b) PEO 1500 at $\mathrm{Re} = \mathrm{Re_c} + 8.1$ and (c) PEO 2900 at $\mathrm{Re} = \mathrm{Re_c} + 6.5$. Lines: $- -$ $u^* < 0$ and — $u^* > 0$.

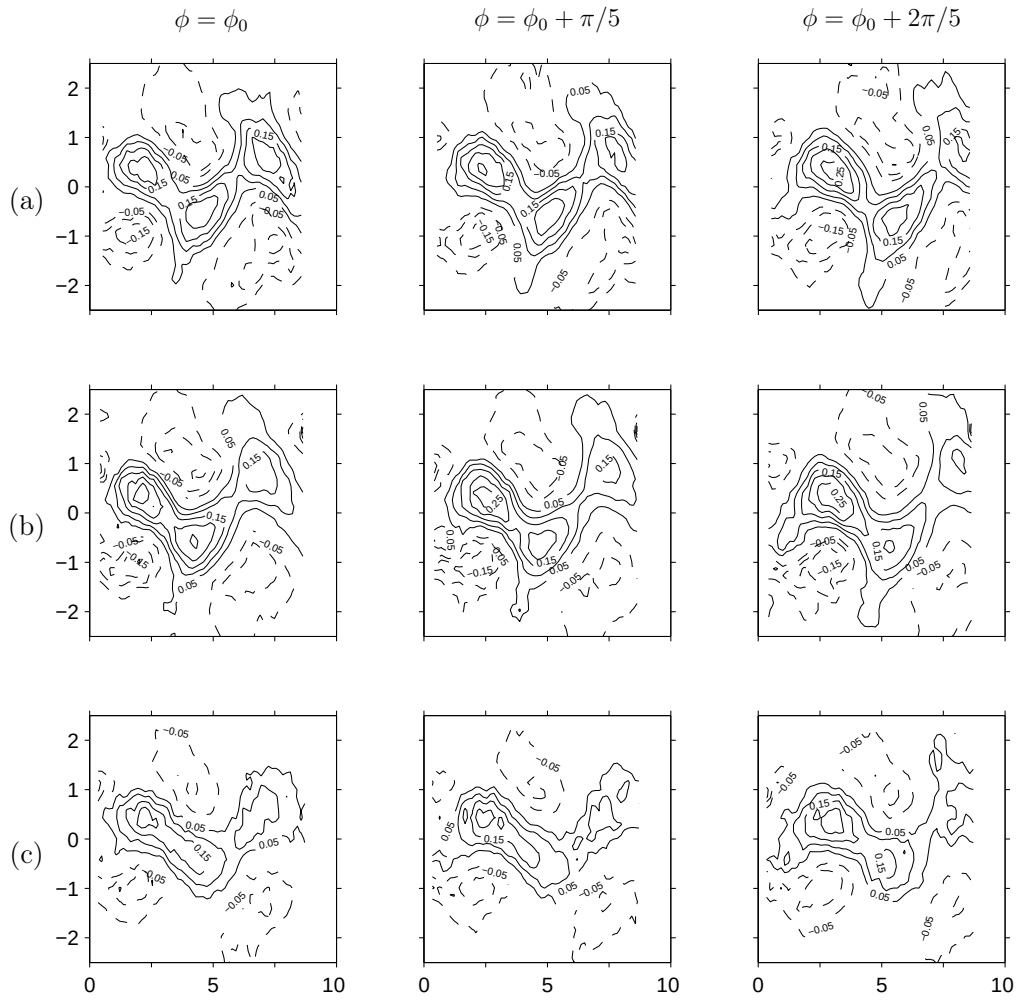

Fig. A.7: Extensional stress $0.5(\sigma^*_{xx} - \sigma^*_{yy}) = 0.5(\sigma_{xx} - \sigma_{yy})d/(U_\infty \eta_0)$ as a function of phase for (a) water at $\mathrm{Re} = \mathrm{Re_c} + 4.8$, (b) PEO 1500 at $\mathrm{Re} = \mathrm{Re_c} + 8.1$ and (c) PEO 2900 at $\mathrm{Re} = \mathrm{Re_c} + 6.5$. Lines: $- -$ $u^* < 0$ and — $u^* > 0$.

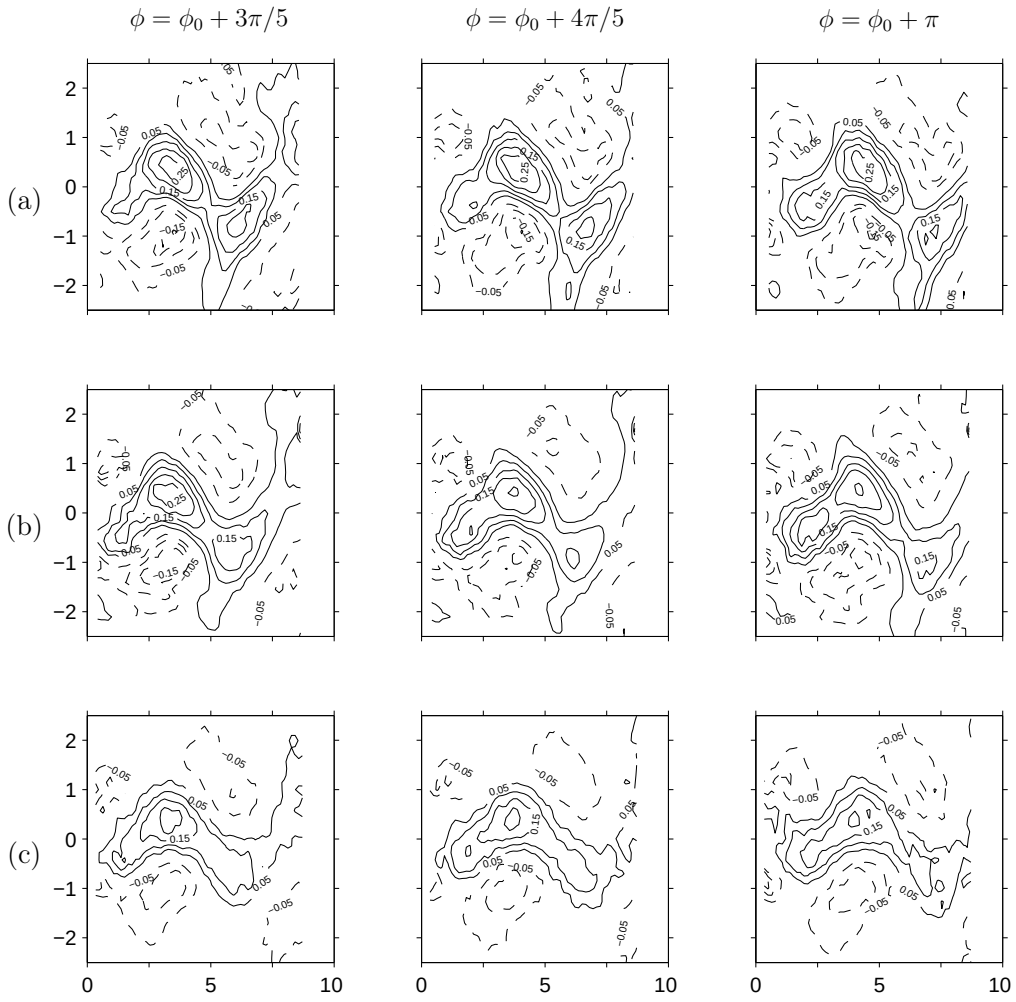

Fig. A.8: Extensional stress $0.5(\sigma^*_{xx} - \sigma^*_{yy}) = 0.5(\sigma_{xx} - \sigma_{yy})d/(U_\infty \eta_0)$ as a function of phase for (a) water at $\mathrm{Re} = \mathrm{Re_c} + 4.8$, (b) PEO 1500 at $\mathrm{Re} = \mathrm{Re_c} + 8.1$ and (c) PEO 2900 at $\mathrm{Re} = \mathrm{Re_c} + 6.5$. Lines: $- -$ $u^* < 0$ and — $u^* > 0$.

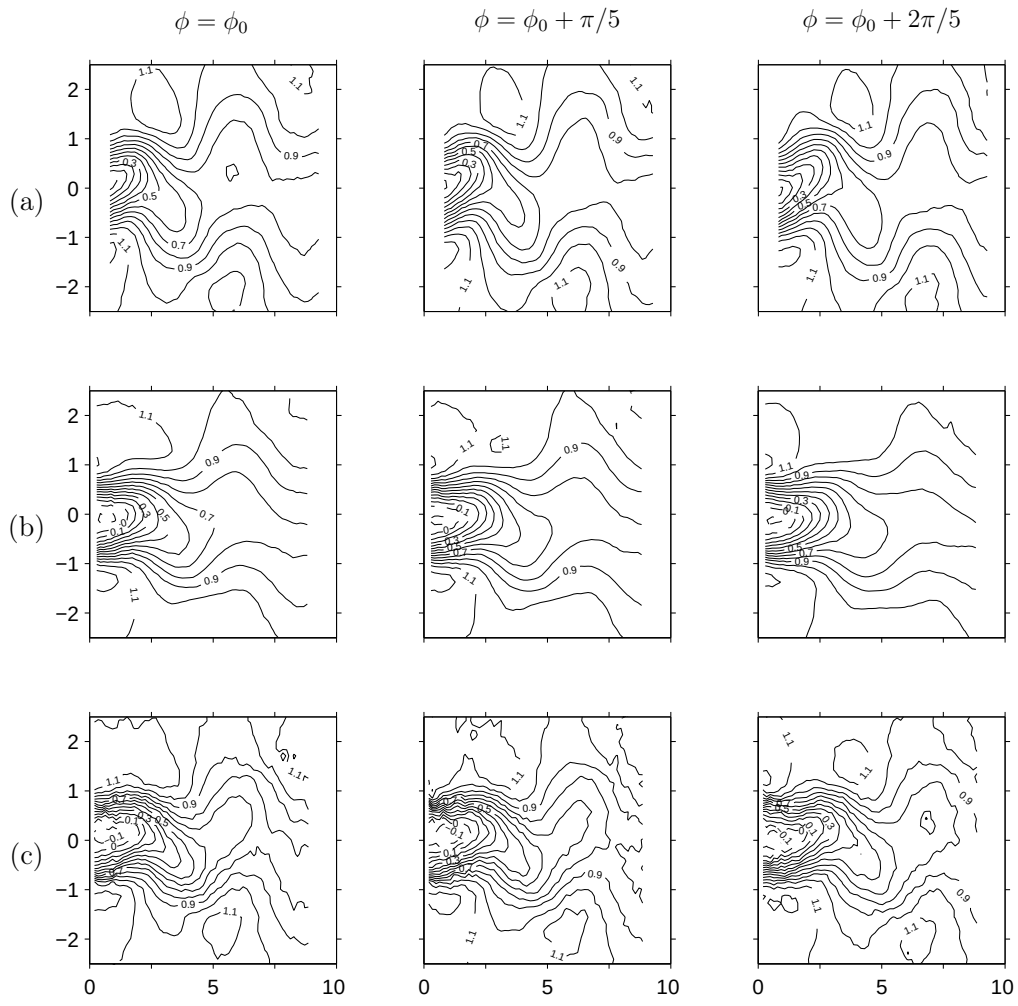

Fig. A.9: Streamwise velocity $u^* = u/U_\infty$ as a function of phase for (a) water at $\mathrm{Re} = \mathrm{Re_c} + 54.3$, (b) PEO 1500 at $\mathrm{Re} = \mathrm{Re_c} + 49.9$ and (c) PEO 2900 at $\mathrm{Re} = \mathrm{Re_c} + 47.2$. Lines: $- -$ $u^* \leq 0$ and — $u^* > 0$.

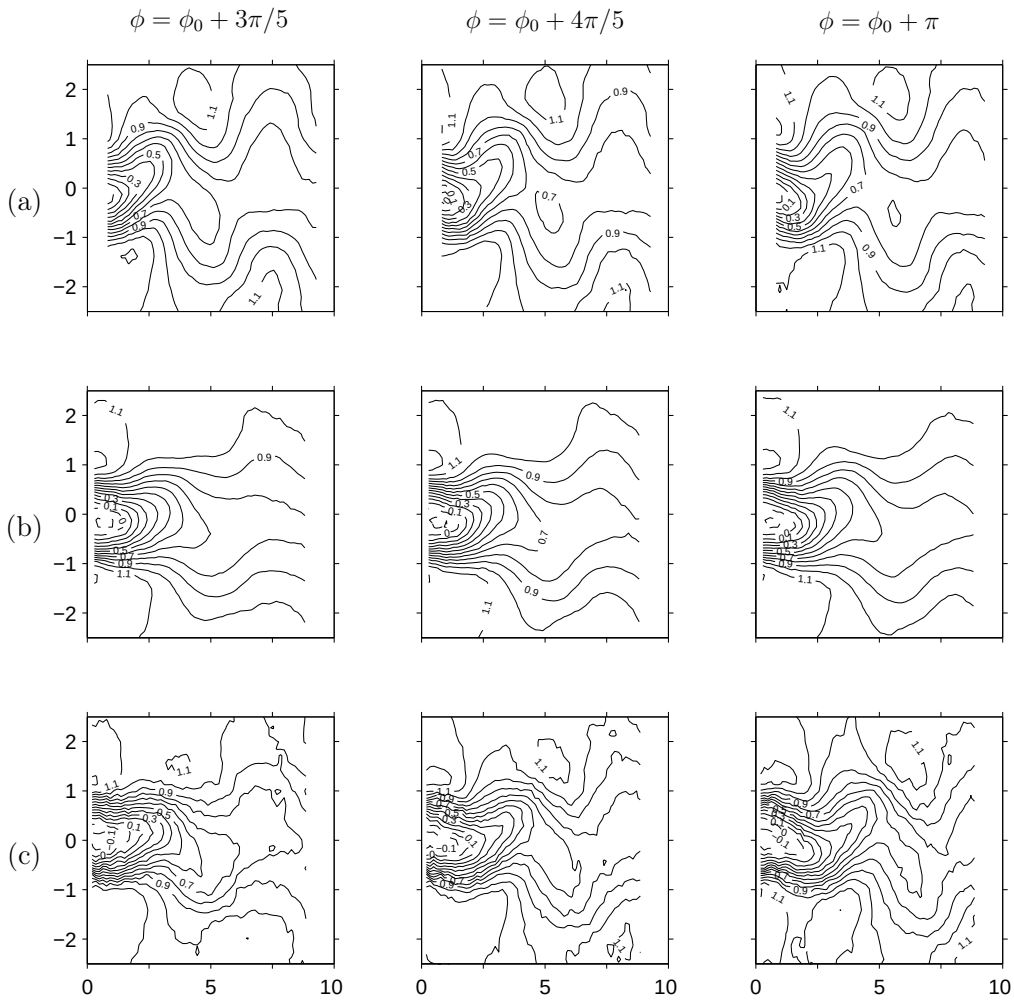

Fig. A.10: Streamwise velocity $u^* = u/U_\infty$ as a function of phase for (a) water at $\mathrm{Re} = \mathrm{Re_c} + 54.3$, (b) PEO 1500 at $\mathrm{Re} = \mathrm{Re_c} + 49.9$ and (c) PEO 2900 at $\mathrm{Re} = \mathrm{Re_c} + 47.2$. Lines: $- -$ $u^* \leq 0$ and — $u^* > 0$.

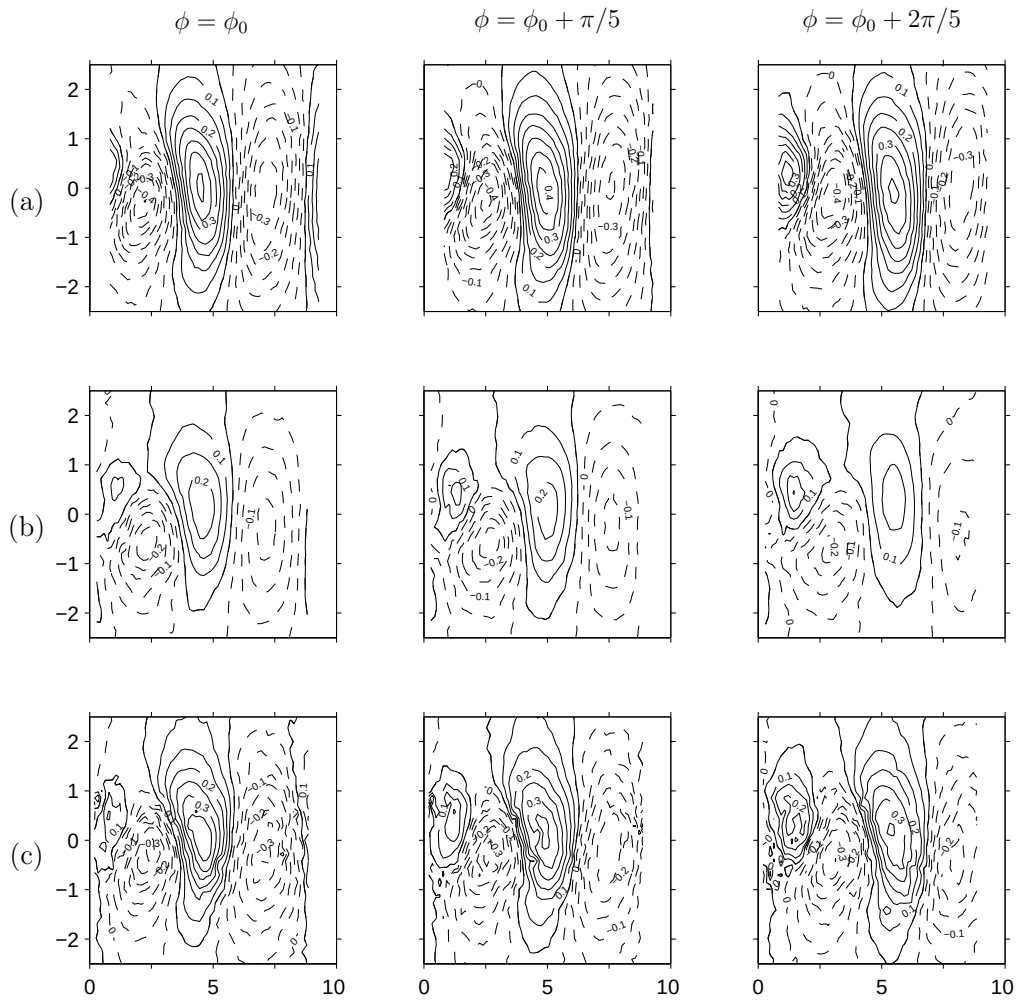

Fig. A.11: Transverse velocity $v^* = v/U_\infty$ as a function of phase for (a) water at $\mathrm{Re} = \mathrm{Re_c} + 54.3$, (b) PEO 1500 at $\mathrm{Re} = \mathrm{Re_c} + 49.9$ and (c) PEO 2900 at $\mathrm{Re} = \mathrm{Re_c} + 47.2$. Lines: $- -$ $u^* < 0$ and — $u^* > 0$.

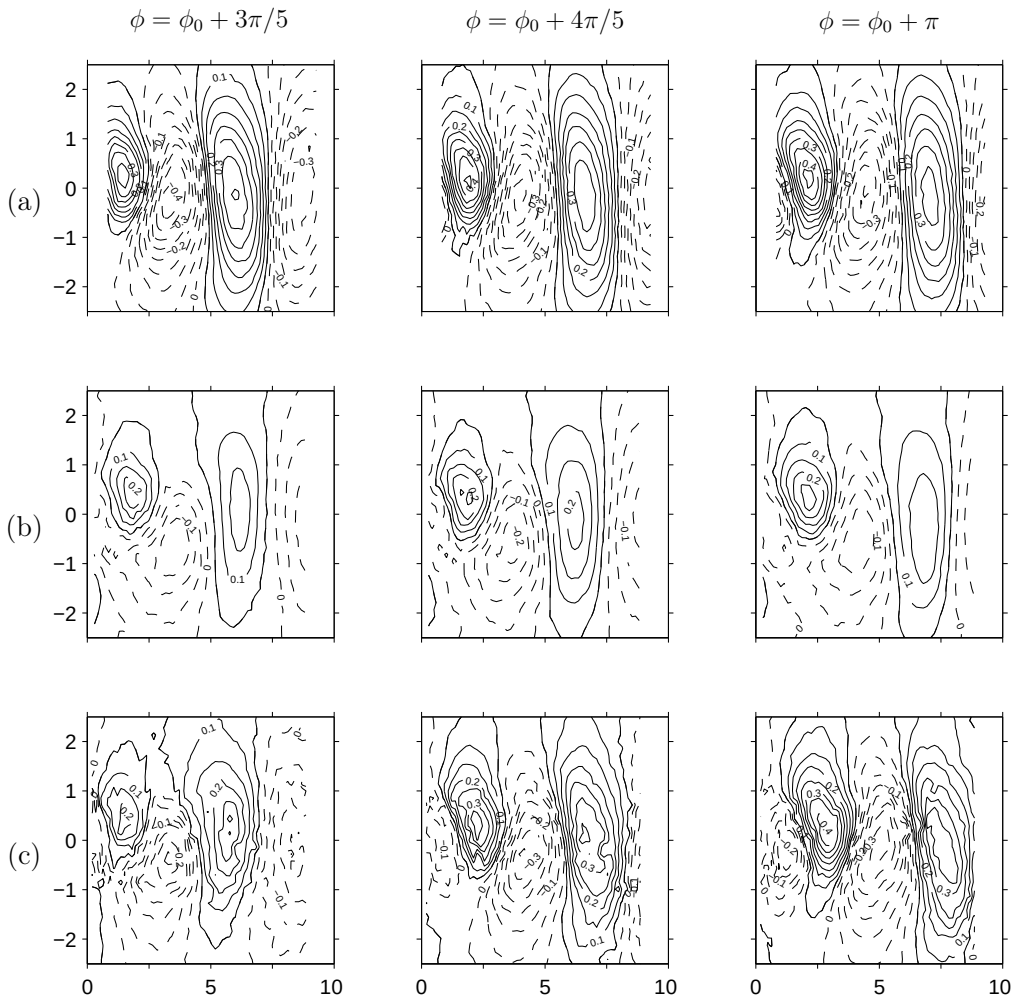

Fig. A.12: Transverse velocity $v^* = v/U_\infty$ as a function of phase for (a) water at $\mathrm{Re} = \mathrm{Re_c} + 54.3$, (b) PEO 1500 at $\mathrm{Re} = \mathrm{Re_c} + 49.9$ and (c) PEO 2900 at $\mathrm{Re} = \mathrm{Re_c} + 47.2$. Lines: $- -$ $u^* < 0$ and — $u^* > 0$.

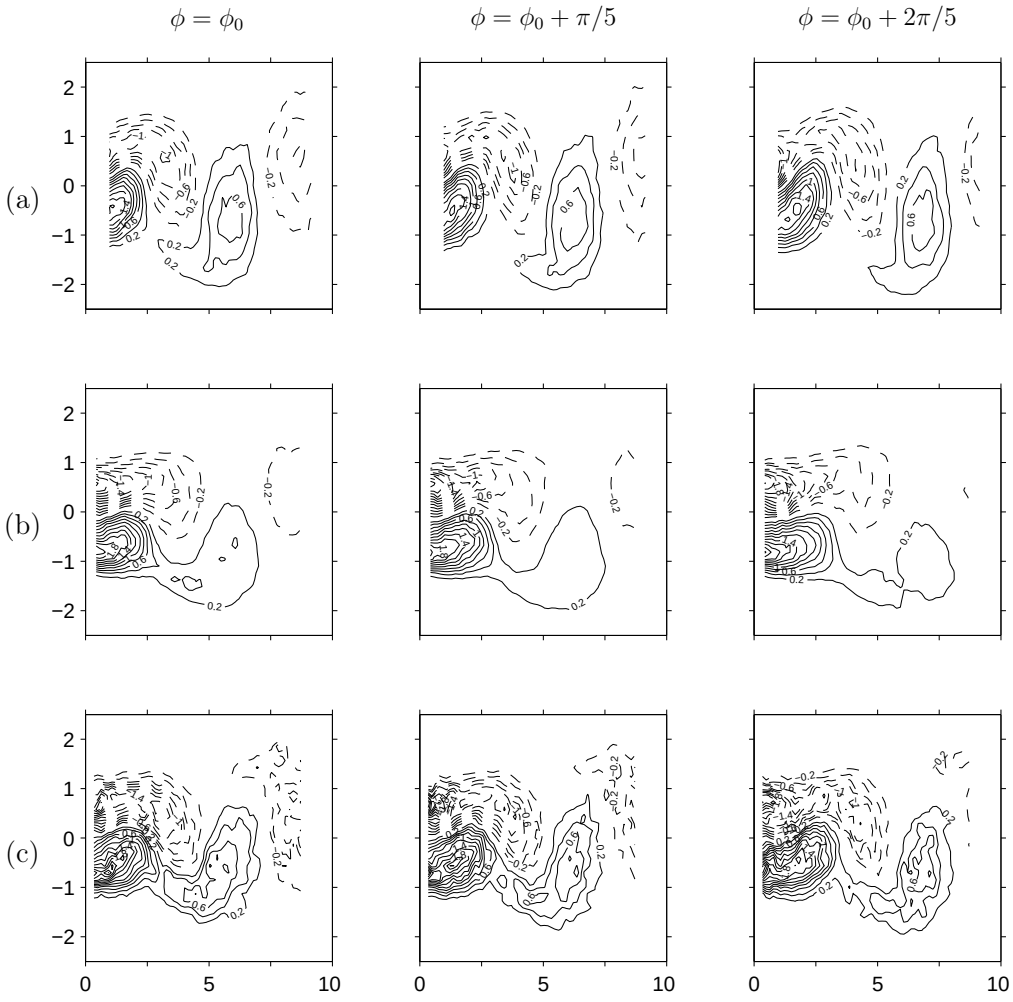

Fig. A.13: Shear stress $\sigma^*_{xy} + \sigma^*_{yx} = (\sigma_{xy} + \sigma_{yx})d/(U_\infty \eta_0)$ as a function of phase for (a) water at $\mathrm{Re} = \mathrm{Re_c} + 54.3$, (b) PEO 1500 at $\mathrm{Re} = \mathrm{Re_c} + 49.9$ and (c) PEO 2900 at $\mathrm{Re} = \mathrm{Re_c} + 47.2$. Lines: $- -$ $u^* < 0$ and — $u^* > 0$.

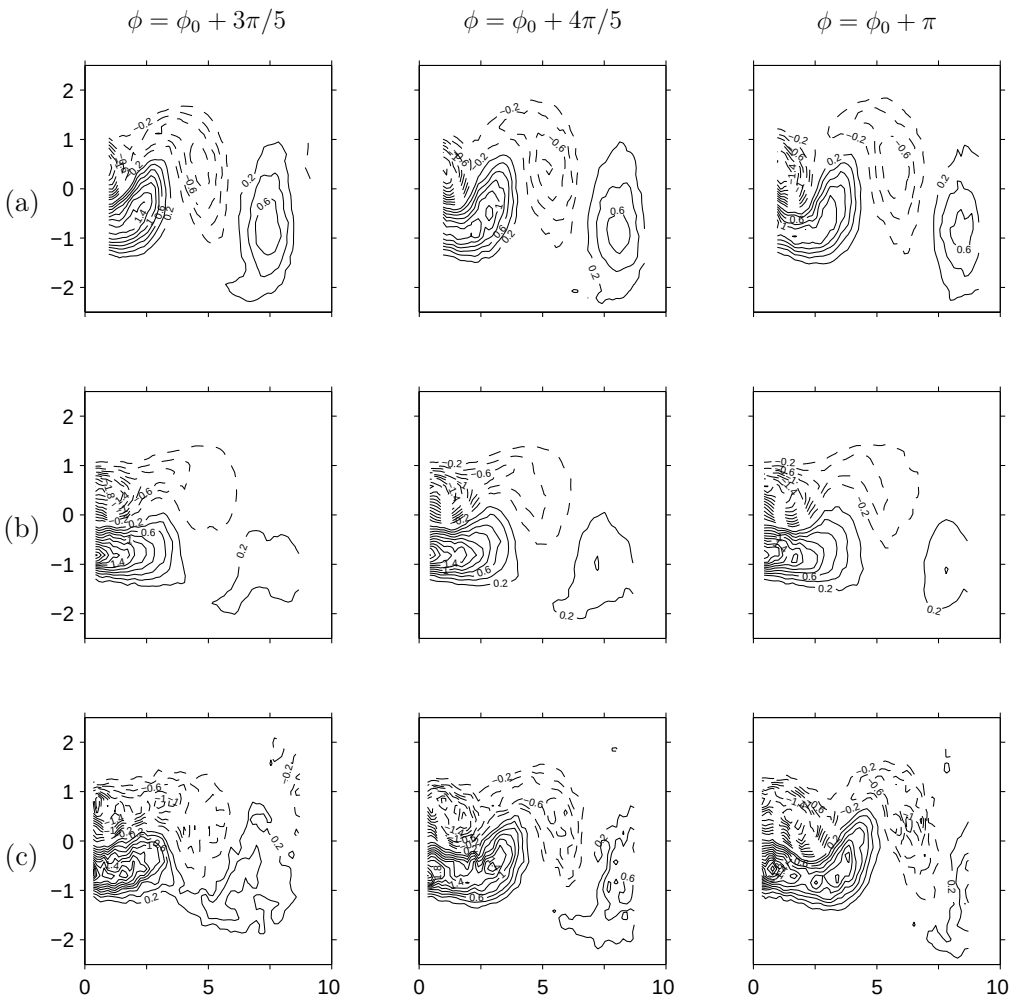

Fig. A.14: Shear stress $\sigma^*_{xy} + \sigma^*_{yx} = (\sigma_{xy} + \sigma_{yx})d/(U_\infty \eta_0)$ as a function of phase for (a) water at $\mathrm{Re} = \mathrm{Re_c} + 54.3$, (b) PEO 1500 at $\mathrm{Re} = \mathrm{Re_c} + 49.9$ and (c) PEO 2900 at $\mathrm{Re} = \mathrm{Re_c} + 47.2$. Lines: $- -$ $u^* < 0$ and — $u^* > 0$.

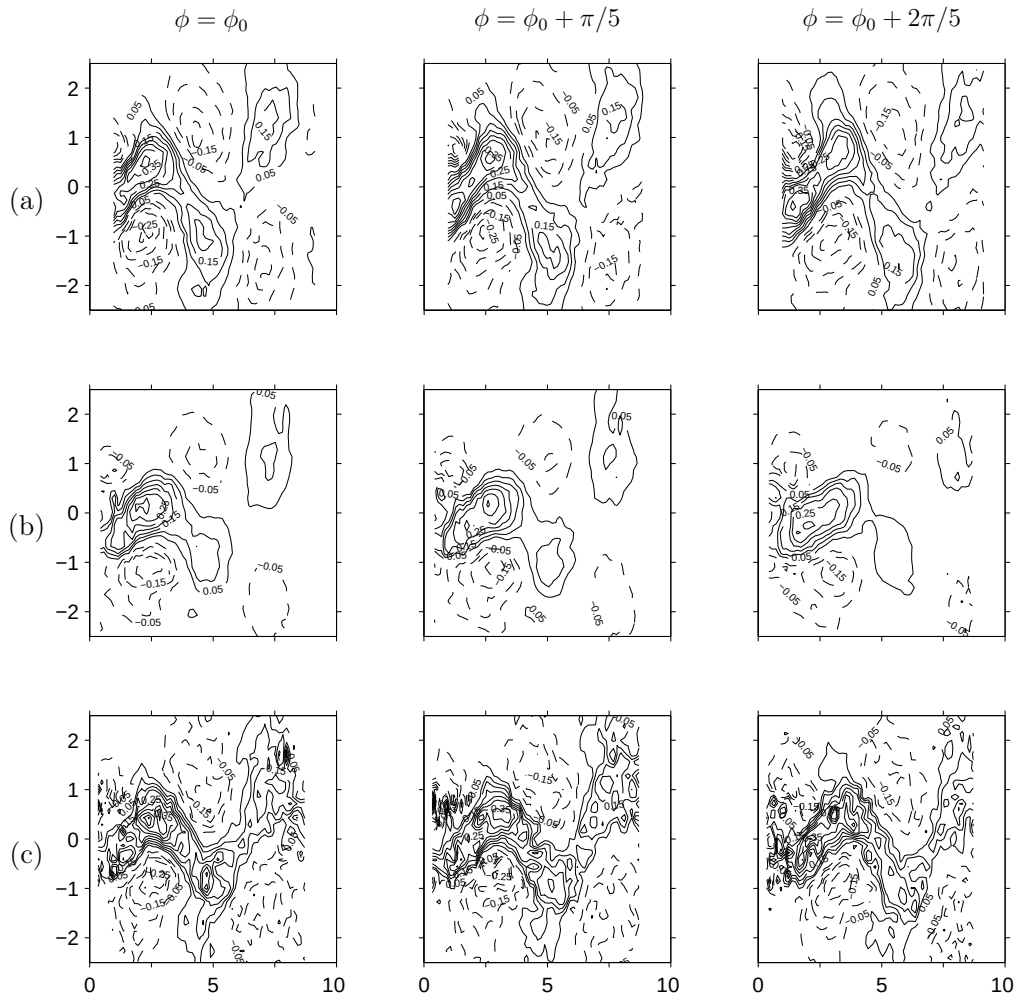

Fig. A.15: Extensional stress $0.5(\sigma^*_{xx} - \sigma^*_{yy}) = 0.5(\sigma_{xx} - \sigma_{yy})d/(U_\infty \eta_0)$ as a function of phase for (a) water at $\mathrm{Re} = \mathrm{Re_c} + 54.3$, (b) PEO 1500 at $\mathrm{Re} = \mathrm{Re_c} + 49.9$ and (c) PEO 2900 at $\mathrm{Re} = \mathrm{Re_c} + 47.2$. Lines: $- -$ $u^* < 0$ and — $u^* > 0$.

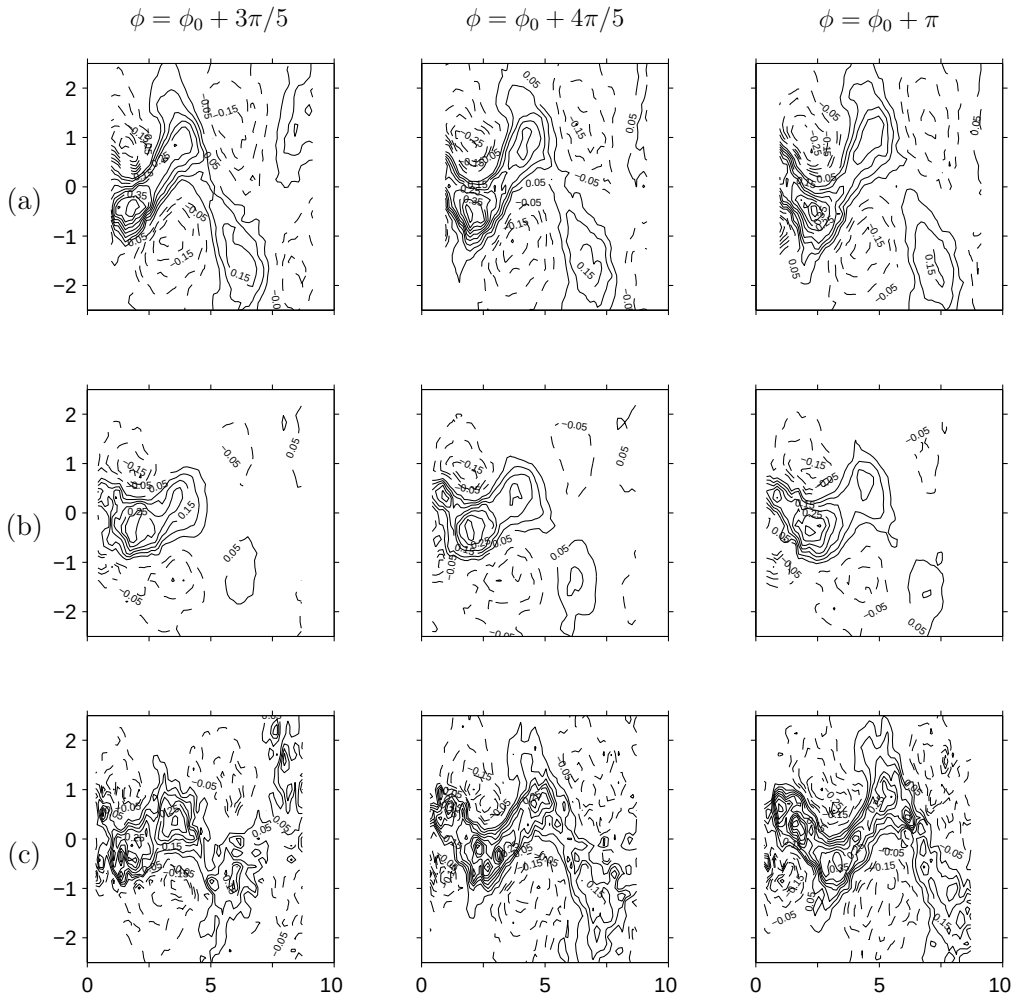

Fig. A.16: Extensional stress $0.5(\sigma^*_{xx} - \sigma^*_{yy}) = 0.5(\sigma_{xx} - \sigma_{yy})d/(U_\infty \eta_0)$ as a function of phase for (a) water at $\mathrm{Re} = \mathrm{Re_c} + 54.3$, (b) PEO 1500 at $\mathrm{Re} = \mathrm{Re_c} + 49.9$ and (c) PEO 2900 at $\mathrm{Re} = \mathrm{Re_c} + 47.2$. Lines: $- -$ $u^* < 0$ and — $u^* > 0$.

Appendix B

Results for two-dimensional incompressible flow past a cylinder

B.1 Flow past a cylinder: velocity potential

The velocity field (e.g. Anderson, 1991) near a cylinder of radius r can be estimated using the potential velocity for an inviscid, imcompressible, irrotational flow ϕ. In polar coordinates with the origin at the centre of the cylinder this is given by:

$$\phi = U_\infty r \cos\theta \ (r + a^2). \tag{B.1}$$

Thus the tangential and radial velocity fields u_θ and u_r in the flow past a cylinder (i.e. $r \geq a$) are:

$$u_\theta = \frac{1}{r}\frac{\partial \phi}{\partial \theta} = -U_\infty \sin\theta \ (1 + \frac{a^2}{r^2}), \tag{B.2}$$

$$u_r = \frac{\partial \phi}{\partial r} = U_\infty \cos\theta \ (1 - \frac{a^2}{r^2}). \tag{B.3}$$

B.2 Cylinder laminar boundary layer: Blasius series solution

The Blasius series solution for the two-dimensional incompressible boundary layer on a cylinder is described in detail in Schlichting (1968) pp.154-161.

In the following calculations we use the velocity field given by potential flow to approximate the pressure at the cylinder surface. To calculate the

maximum shear stress in the flow past a cylinder we examine the flow at the shoulder of the cylinder ($\theta = \pi/2$), where, according to the velocity field given by Eq. (B.2), the velocity magnitude is greatest. Assuming that the cylinder boundary layer changes thickness slowly in relation to the change in the velocity at the edge of the boundary layer u_e, this location represents the highest shear rates $\dot{\gamma}_{xy}$ in the flow past a cylinder. Using Fig. 9.6 in Schlichting (1968), at $\theta = \pi/2$ the boundary layer thickness δ_{99} is given by:

$$\delta_{99} = \frac{2.8d}{\sqrt{2\mathrm{Re}}}, \tag{B.4}$$

where d is the cylinder diameter. For example, for a cylinder of diameter 0.003 m at a Reynolds number of 60 the boundary layer thickness is:

$$\delta_{99} = \frac{2.8 \times 0.003}{\sqrt{2 \times 60}} = 7.67 \times 10^{-4} \text{ m}. \tag{B.5}$$

B.3 Cylinder laminar boundary layer: method of Thwaites

An alternative technique for calculating the thickness of a boundary layer on a cylinder comes from the method of Thwaites (Thwaites, 1949; Schlichting, 1968) which is based on the momentum equation approximations for the boundary layer.

Using Eq. (B.2) once more to describe the velocity field external to the boundary layer at the cylinder shoulder, we find the the boundary layer momentum thickness ϑ is equal to:

$$\vartheta = \sqrt{\frac{0.45\eta}{2\rho U_\infty}\left(\frac{8a}{15}\right)}, \tag{B.6}$$

where a is the cylinder radius. Noting that at $\theta = \pi/2$ the local streamwise velocity gradient $\partial u_e/\partial x$ is zero allows us to write:

$$\vartheta = \frac{37}{315}\,\delta_{99}, \tag{B.7}$$

and the boundary layer thickness is then given by:

$$\delta_{99} = \frac{2.95d}{\sqrt{2\mathrm{Re}}}. \tag{B.8}$$

Thus the boundary layer thickness from Eq. (B.8) is 5% greater than Eq. (B.4).

Curriculum vitae

Christopher James Pipe

Date and place of birth: 23.03.1979, Cuckfield (U.K.)

	Education
1995-1997	Brighton, Hove and Sussex VI College, Brighton (U.K.) 'A' levels
1997-2001	Imperial College of Science, Technology and Medicine, London (U.K.) MEng., Aeronautical Engineering
2001-2005	École Polytechnique Fédérale de Lausanne, Lausanne (C.H.) PhD, Laboratory of Fluid Mechanics (LMF), Supervisor: Prof P. A. Monkewitz

Bibliography

Albarède, P. & Monkewitz, P. A. 1992 A model for the formation of oblique shedding and "chevron" patterns in cylinder wakes. *Phys. Fluids A* **4** (4), 744–756.

Anderson, J. D. 1991 *Fundamentals of aerodynamics*, 2nd edn. McGraw-Hill.

Azaiez, J. & Homsy, G. M. 1994 Linear stability of free shear flow of viscoelastic liquids. *J. Fluid Mech.* **268**, 37–69.

Barnes, H. A., Hutton, J. F. & Walters, K. 1989 *An introduction to rheology*. Elsevier.

Batchelor, G. K. 1967 *An introduction to fluid mechanics*. Cambridge University Press.

Bird, R. B., Armstrong, R. C. & Hassager, O. 1987*a* *Dynamics of polymeric liquids: Volume 1 Fluid mechanics.*, 2nd edn. Wiley Interscience.

Bird, R. B., Curtiss, Armstrong, R. C. & Hassager, O. 1987*b* *Dynamics of polymeric liquids: Volume 2 Kinetic theory.*, 2nd edn. Wiley Interscience.

Bisgaard, C. 1983 Velocity fields around spheres and bubbles investigated by laser-Doppler anemometry. *J. Non-Newtonian Fluid Mech.* **12**, 283–302.

Boger, D. V. 1976 A highly elastic constant-viscosity fluid. *J. Non-Newtonian Fluid Mech.* **3**, 87–91.

Brandrup, J. 1989 *Polymer Handbook.*, 3rd edn. Wiley Interscience.

Brennen, C. 1970 Some cavitation experiments with dilute polymer solutions. *J. Fluid Mech.* **44**, 51–63.

BIBLIOGRAPHY

Brennen, C. & Gadd, G. E. 1967 Ageing and degradation in dilute polymer solutions. *Nature* **215**, 1368–1370.

Briggs, R. J. 1964 *Electron stream interaction with plasmas*. MIT Press, Cambridge, MA.

Bruun, H. H. 1995 *Hot-Wire Anemometry, Principles and Signal Analysis*. Oxford Science Publications.

Cadot, O. 2001 Partial roll-up of a viscoelastic Kármán street. *Eur. J. Mech. B-Fluids* **20**, 145–153.

Cadot, O. & Kumar, S. 2000 Experimental characterization of viscoelastic effects on two- and three-dimensional shear instabilities. *J. Fluid Mech.* **416**, 151–172.

Carreau, P. 1972 Rheological equations from molecular network theories. *Trans. Soc. Rheol.* **16** (1), 99–127.

Cheny, J.-M. & Walters, K. 1998 Rheological influences on the splashing experiment. *J. Non-Newtonian Fluid Mech.* **86**, 185–210.

Chomaz, J. M., Huerre, P. & Redekopp, L. G. 1988 Bifurcations to local and global modes in spatially developing flows. *Phys. Rev. Lett.* **60** (1), 25–28.

Coelho, P. M. & Pinho, F. T. 2003*a* Vortex shedding in cylinder flow of shear-thinning fluids I. Identification and demarcation of flow regimes. *J. Non-Newtonian Fluid Mech.* **110**, 143–176.

Coelho, P. M. & Pinho, F. T. 2003*b* Vortex shedding in cylinder flow of shear-thinning fluids II. Flow characteristics. *J. Non-Newtonian Fluid Mech.* **110**, 177–193.

Coelho, P. M. & Pinho, F. T. 2004 Vortex shedding in cylinder flow of shear-thinning fluids III. Pressure measurements. *J. Non-Newtonian Fluid Mech.* **121**, 55–68.

Coutanceau, M. & Bouard, R. 1977*a* Experimental determination of the main features of the viscous flow in the wake of a circular cylinder in uniform translation. Part 1. Steady flow. *J. Fluid Mech.* **79**, 231–256.

Coutanceau, M. & Bouard, R. 1977*b* Experimental determination of the main features of the viscous flow in the wake of a circular cylinder in uniform translation. Part 2. Unsteady flow. *J. Fluid Mech.* **79**, 231–256.

Crumeyrolle, O., Mutabazi, I. & Grisel, M. 2002 Experimental study of inertioelastic Couette–Taylor instability modes in dilute and semidilute polymer solutions. *Phys. Fluids* **14** (5), 1982–1688.

Dontula, P., Macosko, C. W. & Scriven, L. E. 1998 Model elastic liquids with water-soluble polymers. *AIChE J.* **44** (6), 1247–1255.

Drazin, P. G. & Reid, W. H. 1981 *Hydrodynamic stability*. Cambridge University Press.

Durst, F., Melling, A. & Whitelaw, J. H. 1976 *Principles and practice of laser-Doppler anemometry*. Academic Press.

Einstein, A. 1906 Eine neue Bestimmung der Moleküledimensionen. *Annalen Phys.* **19**, 289–306.

Einstein, A. 1911 Berichtigung zu meiner Arbeit: 'Eine neue Bestimmung der Moleküledimensionen'. *Annalen Phys.* **34**, 591–592.

Eisenlohr, H. & Eckelmann, H. 1989 Vortex splitting and its consequences in the vortex street wake of cylinders at low Reynolds number. *Phys. Fluids A* **1** (2), 189–192.

Ferry, J. D. 1980 *Viscoelastic properties of polymers.*, 3rd edn. Wiley Interscience.

Gadd, G. E. 1966*a* Effects of long-chain molecule additives in water on vortex streets. *Nature* **211**, 169–170.

Gadd, G. E. 1966*b* Reduction of turbulent friction in liquids by dissolved additives. *Nature* **212**, 874–877.

Gerrard, J. H. 1978 The wakes of cylindrical bluff bodies at low Reynolds numbers. *Philos. Trans. R. Soc. Lond. A* **288**, 351–382.

Goujon-Durand, S., Jenffer, P. & Wesfreid, J. E. 1994 Downstream evolution of the Bénard–von Kármán instability. *Phys. Rev. E* **50** (1), 308–313.

Graftieaux, L., Michard, M. & Grosjean, N. 2001 Combining PIV, POD and vortex identification algorithms for the study of unsteady turbulent swirling flows. *Meas. Sci. Technol.* **12**, 1422–1429.

Griffin, O. M. 1995 A note on bluff body vortex formation. *J. Fluid Mech.* **284**, 217–224.

Grove, A. S., Shair, F. H., Petersen, E. E. & Acrivos, A. 1964 An experimental investigation of the steady separated flow past a circular cylinder. *J. Fluid Mech.* **19**, 60–80.

Hammache, M. & Gharib, M. 1989 A novel method to promote parallel vortex shedding in the wake of circular cylinders. *Phys. Fluids A* **1**, 1611.

Harlen, O. G. 2002 The negative wake behind a sphere sedimenting through a viscoelastic fluid. *J. Non-Newtonian Fluid Mech.* **108**, 411–430.

Hassager, O. 1979 Negative wake behind bubbles in non-Newtonian liquids. *Nature* **279**, 402–403.

Hinch, E. J. & Elata, C. 1979 Heterogeneity of dilute polymer solutions. *J. Non-Newtonian Fluid Mech.* **5**, 411–425.

James, D. F. & Accosta, A. J. 1970 The laminar flow of dilute polymer solutions around circular cylinders. *J. Fluid Mech.* **42** (2), 269–288.

James, D. F. & Gupta, O. P. 1975 Drag on dilute circular cylinders in dilute polymer solutions. *Chem. Eng. Progress Symposium Series* **67** (111), 62–73.

Jensen, E. A. 2002 Determination of discrete relaxation spectra using simulated annealing. *J. Non-Newtonian Fluid Mech* **107**, 1–11.

Kalashnikov, V. N. & Kudin, A. M. 1970 Karman vortices in the flow of drag reducing polymer solutions. *Nature* **255**, 445–446.

von Kármán, T. 1911 über den mechanismus des widerstandes, den ein bewegter körper in einer flüssigkeit erfahrt. *Nachr. Ges. Wiss. Göttingen Math. Phys. Klasse* pp. 509–517.

Keane, R. D. & Adrian, R. J. 1990 Optimization of particle image velocimeters. 1.Double pulsed systems. *Meas. Sci. Technol.* **1** (11), 1202–1215.

Kim, B. K. & Telionis, D. P. 1989 The effect of polymer additives on laminar separation. *Phys. Fluids A* **1** (2), 267–273.

König, M., Eisenlohr, H. & Eckelmann, H. 1990 The fine structure in the Strouhal–Reynolds number relationship of the laminar wake of a circular cylinder. *Phys. Fluids A* **2** (9), 1607–1614.

Konuita, A., Adler, P. & Piau, J. 1980 Flow of dilute polymer solutions around circular cylinders. *J. Non-Newtonian Fluid Mech* **7**, 101–106.

Landau, L. D. & Lifchitz, E. M. 1989 *Physique théorique. Tome 6 : Mécanique des fluides*, 2nd edn. MIR.

Lee, T. & Budwig, R. 1991 A study of the effect of aspect ratio on vortex shedding behind circular cylinders. *Phys. Fluids A* **3**, 309–315.

Lin, F. N. & Chern, S. N. 1979 Laminar boundary layer flow of non-Newtonian fluid. *Int. J. Heat Mass Transfer* **22**, 1323–1329.

Liu, T. W. 1989 Flexible polymer chain dynamics and rheological properties in steady flows. *J. Chem. Phys.* **90**, 5826–5842.

Mathis, C., Provansal, M. & Boyer, L. 1984 The Benard–Von Karman instability: an experimental study near the threshold. *J. Physique Lett.* **45**, 483–316.

McKinley, G. H., Armstrong, R. C. & Brown, R. A. 1993 The wake instability in viscoelastic flow past confined circular cylinders. *Philos. Trans. R. Soc. Lond. A* **344**, 265–304.

Monkewitz, P. A. 1988 The absolute and convective nature of instability in two-dimensional wakes at low Reynolds numbers. *Phys. Fluids* **31** (5), 999–1006.

Monkewitz, P. A. 1996 Modeling of self-excited wake oscillations by amplitude equations. *Experimental Thermal and Fluid Science* **12**, 175–183.

Monkewitz, P. A. & Nguyen, L. N. 1987 Absolute instability in the near-wake of two-dimensional bluff bodies. *J Fluids Struct.* **1**, 165–184.

Monkewitz, P. A., Williamson, C. H. K. & Miller, G. D. 1996 Phase dynamics of Kármán vortices in cylinder wakes. *Phys. Fluids* **8** (1), 91–96.

Nishioka, M. & Sato, H. 1978 Mechanism of determination of the shedding frequency of vortices behind a cylinder at low Reynolds numbers. *J. Fluid Mech.* **89**, 49–60.

Norberg, C. 1994 An experimental investigation of the flow around a circular cylinder: influence of aspect ratio. *J. Fluid Mech.* **258**, 287–316.

Oertel, H. 1990 Wakes behind blunt bodies. *Annu. Rev. Fluid. Mech.* **22**, 539–564.

OLDROYD, J. G. 1950 On the formulation of rheological equations of state. *Proc. Roy. Soc. London. Ser. A.* **200**, 523–541.

PARANTHOËN, P., BROWNE, L. W. B., MASSON, S. L., DUMOUCHEL, F. & LECORDIER, J. C. 1999 Characteristics of the near wake of a cylinder at low Reynolds numbers. *Eur. J. Mech. B/Fluids* **18**, 659–674.

PESCHARD, I., LE GAL, P. & TAKEDA, Y. 1999 On the spatio-temporal structure of cylinder wakes. *Exp. Fluids* **26**, 188–196.

PROVANSAL, M., MATHIS, C. & BOYER, L. 1987 Bénard–von Kármán instability: transient and forced regimes. *J. Fluid Mech.* **182**, 1–22.

RAFFEL, M., WILLERT, C. & KOMPENHANS, J. 1998 *Particle Image Velocimetry*. Springer.

ROSHKO, A. 1954 Report no. 1191. *Tech. Rep.*. Nat. Adv. Comm. Aero. Wash.

ROSHKO, A. 1955 On the wake and drag of bluff bodies. *J. Aeronaut. Sci.* **22**, 124–132.

ROSHKO, A. 1961 Experiments on the flow past a circular cylinder at very high Reynolds numbers. *J. Fluid Mech.* **10**, 345–356.

ROUSE, P. E. 1953 A theory of the linear viscoelastic properties of dilute polymer solutions of coiling polymers. *J. Chem. Phys.* **21**, 1272–1280.

SAHIN, M. & OWENS, R. G. 2004 On the effects of viscoelasticity on two-dimensional vortex dynamics in the cylinder wake. *J. Non-Newtonian Fluid Mech.* **123**, 121–139.

SARPKAYA, T., RAINEY, P. G. & KELL, R. E. 1973 Flow of dilute polymer solutions about circular cylinders. *J. Fluid Mech.* **57**, 177–208.

SCHLICHTING, H. 1968 *Boundary layer theory*, 6th edn. McGraw-Hill.

SCHUMM, M., BERGER, E. & MONKEWITZ, P. A. 1994 Self excited oscillations in the wake of two-dimensional bluff bodies and their control. *J. Fluid Mech.* **271**, 17–53.

SERTH, R. W. & KISER, K. M. 1967 A solution of the two-dimensional boundary-layer equations for an Ostwald–deWaele fluid. *Chem. Eng. Sci.* **22**, 945–956.

Sigli, D. & Coutanceau, M. 1977 Effect of finite boundaries on the slow laminar isothermal flow of a viscoelastic fluid around a spherical obstacle. *J. Non-Newtonian Fluid Mech.* **2**, 1–21.

Smith, D. E., Babcock, H. P. & Chu, S. 1999 Single-polymer dynamics in steady shear flow. *Science* **283**, 1724–1727.

Smith, K. A., Merrill, E. W., Mickley, H. S. & Virk, P. S. 1967 Anamolous Pitot tube and hot film measurements in dilute polymer solutions. *Chem. Engng Sci.* **22**, 619–626.

Stokes, J. R., Graham, L. J. W., Lawson, N. J. & Boger, D. V. 2001*a* Swirling flow of viscoelastic fluids. Part 1. Interaction between inertia and elasticity. *J. Fluid Mech.* **429**, 67–115.

Stokes, J. R., Graham, L. J. W., Lawson, N. J. & Boger, D. V. 2001*b* Swirling flow of viscoelastic fluids. Part 2. Elastic effects. *J. Fluid Mech.* **429**, 117–153.

Stuart, J. T. 1958 On the non-linear mechanics of hydrodynamic stability. *J. Fluid Mech.* **4**, 1–21.

Stuart, J. T. 1960 On the non-linear mechanics of wave mechanics in stable and unstable parallel flows. *J. Fluid Mech.* **9**, 353–370.

Sveen, J. K. 2004 *An introduction to MatPIV v. 1.6.1*.

Syed Mustapha, S. M. F. D. & Phillips, T. N. 2000 A dynamic non-linear regression method for the determination of the discrete relaxation spectrum. *J. Phys. D: Appl. Phys.* **33**, 1219–1229.

Tam, K. C. & Tiu, C. 1989 Steady and dynamic shear properties of aqueous polymer solutions. *J. Rheol.* **33** (2), 257–280.

Taneda, S. 1956 Experimental investigation of the wakes behind cylinders and plates at low Reynolds numbers. *J. Phys. Soc. Japan* **11** (3), 302–307.

Taylor, G. I. 1923 On the decay of vortices in a viscous fluid. *Philos. Mag.* **46**, 671–674.

Tesla, N. 1913 United states patent office 1061142.

Thwaites, B. 1949 Approximate calculation of the laminar boundary layer. *Aeronaut. Quart.* **1**, 245–280.

BIBLIOGRAPHY

Tirtaatmadja, V., McKinley, G. H. & Cooper-White, J. J. 2005 Drop formation and breakup of low viscosity elastic fluids: effect of molecular weight and concentration. *Phys. Fluids* Submitted.

Tritton, D. J. 1959 Experiments on the flow past a circular cylinder at low Reynolds numbers. *J. Fluid Mech.* **6**, 547–567.

Ursenbacher, T. 2000 Traitement de vélocimétrie par images digitales de particules par une technique robuste de distortion d'images. PhD thesis, No. 2214, École Polytechnique Fédérale de Lausanne.

Usui, H., Shibata, T. & Sano, Y. 1980 Kármán vortex behind a circular cylinder in dilute polymer solutions. *J. Chem. Eng. Japan* **13** (1), 77–79.

Vlassopoulos, D. & Schowalter, W. R. 1994 Steady viscometric properties and characterization of dilute drag-reducing polymer solutions. *J Rheol.* **38** (5), 1427–1446.

Williamson, C. H. K. 1988*a* Defining a univeral and continuous Strouhal–Reynolds number relationship for the laminar vortex shedding of a circular cylinder. *Phys. Fluids* **31** (10), 2742–2744.

Williamson, C. H. K. 1988*b* The existence of two stages in the transition to three-dimensionality of a cylinder wake. *Phys. Fluids* **31** (11), 3165–3168.

Williamson, C. H. K. 1989 Oblique and parallel modes of vortex shedding in the wake of a circular cylinder at low Reynolds numbers. *J. Fluid Mech.* **206**, 579–627.

Williamson, C. H. K. 1996 Vortex dynamics in the cylinder wake. *Annu. Rev. Fluid. Mech.* **28**, 477–539.

Zimm, B. H. 1956 Dynamics of polymer molecules in dilute solution: viscoelasticity, flow birefringence and dielectric loss. *J. Chem. Phys.* **24**, 269–278.